Machine Learning and Optimization Models to Assess and Enhance System Resilience

By

Xiaoge Zhang

Dissertation

Submitted to the Faculty of the

Graduate School of Vanderbilt University

in partial fulfillment of the requirements

for the degree of

DOCTOR OF PHILOSOPHY

in

Interdisciplinary Studies: Systems Engineering and Operations Research

May 31st, 2019

Nashville, Tennessee

Approved:

Professor Sankaran Mahadevan

Professor Gautam Biswas

Professor Mark Ellingham

Professor Hiba Baroud

Dr. Kai Goebel

Dr. Shankar Sankararaman

To my wife, Jing Li

ACKNOWLEDGMENTS

Over the past five years, I have learnt a lot with the support of many precious friends, classmates, group members, university faculty, and family members. Reflecting on the past five years I have spent at Vanderbilt, there are countless valuable memories and moments I will keep in mind forever. The rich experience at Vanderbilt will be a lifelong treasure for my personal life and professional career development. The diverse culture and work environment with colleagues from all over the world has enabled me to learn and think about many problems from different perspectives. Herein, I would like to take this opportunity to thank all those who helped me to overcome the difficulties and challenges in my graduate study, and helped to make this dissertation a successful end.

First and foremost, I would like to express my heartfelt gratitude to my advisor Prof. Sankaran Mahadevan for all the dedication, diligence, patience, and rigor that he has devoted to mentoring me throughout my graduate study. He has taught me how to be a good researcher. Over the past five years, he has been an exemplary person for me to follow. The joy and enthusiasm he has for his research is contagious and motivational for me, even at the times of difficulties during Ph.D pursuit. I am deeply indebted to Dr. Mahadevan for his encouragement and enormous support during my Ph.D study. I am looking forward to opening a new chapter in our relationship for the rest of my professional career.

Besides my advisor, I would also like to gratefully acknowledge the other members of my Ph.D committee: Prof. Gautam Biswas, Prof. Mark Ellingham, Prof. Hiba Baroud as well as two external committee members Dr. Kai Goebel and Dr. Shankar Sankararaman, for their insightful comments and valuable feedback, but also for the constructive criticisms they raised which motivated me to deepen my research from different perspectives. Among many other things, I am thankful to Dr. Kai Goebel and Dr. Shankar Sankararaman for their mentorship during my internship at NASA Ames Research Center in the fall of 2016 and our fruitful collaboration thereafter.

I will forever be thankful to my former advisor Prof. Yong Deng at Southwest University (now at University of Electronic Science and Technology of China). Prof. Yong Deng has always been very helpful and supportive for my career development, and he has been a good teacher, mentor, and scientist. Without him, I would not have been to pursue my study at Vanderbilt.

It was a great experience to work with so many brilliant people at Vanderbilt University. In particular, I was lucky to work with Dr. Zhen Hu, who was the go-to person for most members of our risk and reliability research group. I would like to thank Dr. You Ling, Dr. Chen Liang, Dr. Guowei Cai, Dr. Chenzhao Li and Dr. Saideep Nannapaneni for their tireless support and helpful suggestions. I would also like to thank Paromita Nath for all the discussions in understanding and tackling challenging research problems. In addition, I would like to extend my appreciation to many colleagues and collaborators: Prof. Matthew Weinger, Prof. Nathan Lau, Dr. Abhinav Subramanian, Dr. Xinyang Deng, Dr. Daijun Wei, Chao Yan, Jin-Zhu Yu, Cai Gao, Thushara De Silva, Amy Jungmin Seo and Tianzi Wang (graduate students at Virginia Tech), Dennis Deardorff (graduate student at Virginia Tech, retired licensed nuclear power plant control room operator), and many others, in no particular order, for all the precious time we have spent together and all the fun we have had, without which this dissertation will not have been possible.

Lastly, I would like to thank my family for their boundless care, love and encouragement. Especially, I am deeply thankful to my wife for her selfless support and invaluable sacrifice she has made after I moved to USA. Without her constant encouragement, I could not have survived during the first year in face of the challenges from new culture and language.

The financial support for the research presented in this dissertation was from the following agencies (I) NASA University Leadership Initiative program (Grant No. NNX17AJ86A, Project Technical Monitor: Dr. Kai Goebel) through subcontract to Arizona State University (Principal Investigator: Dr. Yongming Liu); (II) the U.S. Department of Energy through a NEUP grant No. DENE 0008267 (Principal Investigator: Dr. Matthew Weinger, Vanderbilt University; Monitor: Dr. Bruce Hallbert, Idaho National Laboratory); and (III) the research internship at NASA Ames Research Center as mentioned above. Some of the numerical studies were conducted at the Advanced Computing Center for Research and Education (ACCRE) at Vanderbilt University. All these sources of support are gratefully acknowledged.

TABLE OF CONTENTS

LIST OF TABLES

Table Page

LIST OF FIGURES

Figure Page

Chapter 1

Introduction

1.1 Overview

Considering the socio-economic impact and independent nature of many large-scale complex systems in our daily life, it is critical to ensure that they are operated at a desirable performance level. To accomplish this goal, it is important to monitor the variation of system performance over time and diagnose malfunction events/faults as soon as possible for the purpose of taking corresponding actions to eliminate system malfunctions and maintaining system performance at the desirable level in the presence of different sources of aleatory and epistemic uncertainty. Specifically, aleatory uncertainty refers to the inherent natural variability in the system that is irreducible, while epistemic uncertainty represents the uncertainty caused by the lack of knowledge, which can be reduced by collecting more information. Typically, when the system works normally, a straightforward way to measure its performance is to model the different sources of uncertainty with appropriate distributions, then propagate such uncertainty sources through a system model, thereby projecting the input variables to the performance metric of the investigated system. However, if some disturbance or anomalous event happens to the system, one challenge arising here is that it is difficult to describe the operations of many real-world systems with mathematical and physical equations due to the complicated characteristics of system malfunctions or external extreme events, the partial loss of system functionalities, the involvement and decisions of human operators, and the lack of explicit relationships between the features elicited from heterogeneous data and the system performance.

In face of the disastrous effect caused by the unanticipated events, in this dissertation, we aim to assess and mitigate their impact on the performance of engineering systems from a resilience perspective such that the system performance can be restored to its original level

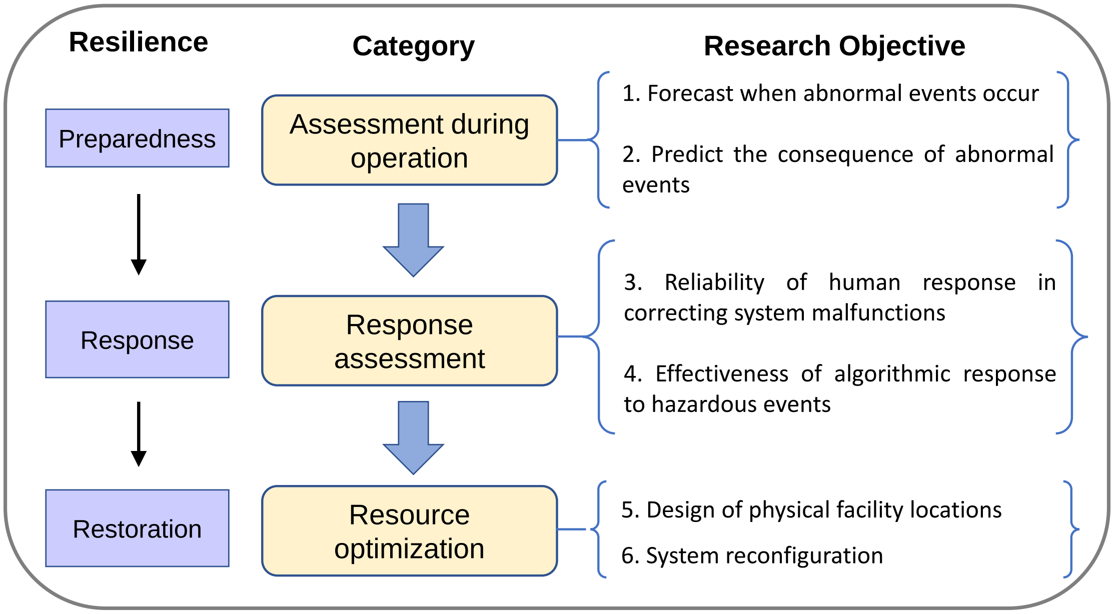
Resilience
Category
Research Objective
Preparedness
Assessment during operation
1. Forecast when abnormal events occur
2. Predict the consequence of abnormal events
Response
Response assessment
3. Reliability of human response in correcting system malfunctions
4. Effectiveness of algorithmic response to hazardous events
Restoration
Resource optimization
5. Design of physical facility locations
6. System reconfiguration

Figure 1.1: Structure of the dissertation

in a timely manner. From the standpoint of system life cycle, when a system is at the design stage, reliability analysis is usually conducted to evaluate the overall system performance by considering the condition of each component under uncertain environment [5, 6, 7]. While in this dissertation, as shown in Fig. 1.1, we primarily focus on investigating the measures that can be taken before, during, and after the occurrence of extreme events when the system is already in operation. Towards this end, six individual objectives have been pursued along this direction: I. Prior to the occurrence of anomalous events, we develop data-driven models to forecast when hazardous event might occur in the future, thereby increasing stakeholder's situation awareness; II. If a system malfunction has already happened, a hybrid model that blends multiple classification models is developed to predict the severity associated with the event consequence in terms of their risk levels; III. Since operators' experience and prior training plays a significant role in diagnosing and responding to off-nominal events, we develop a machine learning framework to measure the reliability of human operators in responding to malfunction events, based on multiple types of data collected from a human-in-the-loop experimental study; IV. Simulation data is used to characterize the performance of algorithmic response in managing an abnormal event; V. We investigate a design-for-resilience methodology, focusing on number and locations of centers that respond to a disastrous event; VI. We also investigate a system reconfiguration strategy for resilient response to the increased demands caused by an extreme event.

As shown in Fig. 1.1, the six measures described above aim to assess and enhance system resilience from different views. In particular, the first two measures focus on the construction of predictive models to forecast characteristics pertaining to anomalous events. Specifically, the former method emphasizes forecasting when the abnormal event is about to occur, while the latter focuses on predicting the outcome of hazardous event. The third and fourth actions center on characterizing the effectiveness of human and algorithmic responses in mitigating the impact of extreme event. The third action evaluates the reliability of human operators in responding to malfunction events, while the fourth action measures the effectiveness of a rerouting strategy in mitigating the impact of closure of a destination airport. The last two strategies aim to increase the resilience of engineering systems from an optimization point of view. The fifth strategy designs a resilient logistics service center distribution by accounting for the potential impact of natural disasters, while the last strategy optimizes the reconfiguration of an already existing traffic network to mitigate the system-wide congestion caused by the large-volume evacuation out of disaster-prone area.

To accomplish the aforementioned goals, we leverage state-of-the-art machine learning and optimization techniques to develop quantitative models for the investigated engineering systems, in which the complex patterns and the connections between system state variables are mined and represented in the data-driven models appropriately. In this regard, computational efficiency is a major concern when training machine learning models for system performance assessment. To address this challenge, several strategies have been implemented to improve the model efficiency. I. Data-driven global sensitivity analysis is performed to identify dominant input variables, so that the input variables with negligible effect on system performance are eliminated accordingly, thus significantly reducing the problem dimension; II. Correlation analysis among input variables is conducted. If the correlation coefficient between any two input variables is larger than a threshold, the two variables are assumed to carry similar information. In this case, only one of them needs to be retained as input to the model, thereby removing redundant variables. III. Resilient distributed big data techniques, e.g., Apache Spark, are utilized to process large volumes of raw data, from which significant features in the raw data can be derived in an efficient manner, thereby accelerating large-scale data processing; IV. We train deep learning models on GPU in the Advanced Computing Center for Research and Education (ACCRE) at Vanderbilt University. By doing this, the time needed for training each model is reduced substantially.

In the rest of this chapter, Section 1.2 briefly describes the proposed research objectives in this dissertation, and Section 1.3 introduces the organization of the dissertation section by section.

1.2 Research Objectives

The overall goal of the proposed research is to develop rigorous and efficient machine learning-based models for assessing system resilience and to leverage optimization models to strengthen the system's ability in withstanding extreme events. To achieve this goal, we investigate several possible measures that can be taken before, during, and after the occurrence of extreme events. Thus, six individual objectives are pursued in order to achieve the overall goal.

The first objective is to predict system behavior over time based on massive historical data and forecast when an anomalous event is about to happen in the future. The methodology is illustrated with a flight trajectory prediction problem in order to assess the safety of separation between aircraft in the air transportation system. A hybrid model blending one-step-ahead prediction from a trained deep feedforward neural network and 2-minutes-ahead prediction from a trained recurrent neural network is developed to forecast the future trajectories of multiple flights, where epistemic model prediction uncertainty is characterized following a Bayesian approach. Such multi-fidelity strategy achieves both accuracy and efficiency for safety assessment in realistic applications.

The second objective is to examine a wide variety of anomalous events from documented incident reports for the purpose of characterizing the risk associated with the consequence of hazardous events given an observed system malfunction. A hybrid model blending support vector machine and an ensemble of deep neural networks is developed to predict the severity associated with the consequence of abnormal aviation incidents. While the models developed in the first objective are based on numerical data, the models in the second objective are based on categorical and text data.

The third objective is to develop a machine learning framework so as to measure the reliability of human operators in eliminating off-nominal malfunction events. To achieve this goal, different malfunction events are injected into the system an an experimental study, and the heterogeneous data featuring operator response are collected. An empirical model fusing heterogeneous data is developed to quantify the operator's performance in responding to malfunction events.

The fourth objective is to evaluate the performance of response strategy in managing abnormal situations. The method is illustrated for an aircraft rerouting strategy in handling a disruptive event caused by the closure of a destination airport, in which the interactions among system components and the multiple sources of uncertainty arising at different stages are considered. With the data collected from a dynamic simulation mimicking the aircraft rerouting process, we train a support vector regression-based model to assess the effectiveness of this strategy in mitigating the impact of airport closure.

The fifth objective is to optimally design a service center configuration that is resilient in withstanding the impact of disruptive events. Specifically, we investigate a pre-disaster resilience-based design optimization approach for logistics service centers configuration. A bi-level program is formulated, and the impact of potential disruptive events is accounted for by the upper-level decision maker. The objective of the formulated bi-level program is to maximize the resilience of the service center configuration, thereby enhancing the ability of the system to withstand unexpected events.

The sixth objective focuses on system reconfiguration strategies of existing systems for achieving resilience when subjected to extreme events. Specifically, we optimize the operational resilience of a traffic network to mitigate the congestion caused by the large volume evacuation out of the disaster-prone zones when confronted with an extreme event. A bi-level mathematical optimization model is formulated to mitigate the incurred traffic congestion through two network reconfiguration schemes: contraflow (also referred to as lane reversal), and crossing elimination at intersections. The system reconfiguration strategies are optimized to maximize the resilience of the transportation network in withstanding the extreme event.

1.3 Organization of the Dissertation

The subsequent chapters of this dissertation will be devoted to the objectives proposed above.

Chapter 2 first defines system resilience in a quantitative manner, which will be used in Chapters 7 and 8 as the performance indicator. Next, Chapter 2 provides a brief introduction to several state-of-the-art machine learning algorithms, including: (1) support vector machine, (2) deep learning: deep feedforward neural network, recurrent neural network. Besides, a Bayesian neural network framework is introduced as a generic means to characterize model prediction uncertainty. Afterwards, we review uncertainty analysis that is used to quantify the uncertainties arising at different stages in complex systems. In parallel, global sensitivity analysis is introduced to measure the contribution of each random variable to system-level variability. Following the uncertainty analysis, a bi-level optimization program is introduced to characterize the interactions among different decision makers in order to increase system resilience. Finally, a unified big data analytics engine Apache

Spark is introduced to process large volumes of raw data in Chapter 2.

Chapter 3 focuses on the first objective: developing deep learning models to forecast the occurrence of abnormal events. The proposed methodology is illustrated with en-route flight trajectory prediction in the air transportation system in order to support en-route safety assessment. The following steps are pursued: (1) a unified big data engine Apache Spark is used to process large volume of raw data obtained from Federal Aviation Administration (FAA) in the Flight Information Exchange Model (FIXM) format; (2) two deep learning models are trained with historical flight trajectories to predict the future state of flight trajectory from different perspectives; (3) the two trained deep learning models are combined to achieve both accuracy and efficiency; and (4) the integrated model is used to forecast the trajectories of multiple flights, and then assess the safety between two flights based on separation distance.

Chapter 4 focuses on the second objective. It facilitates the "proactive safety" paradigm to increase system resilience with a focus on predicting the severity associated with the consequence of abnormal aviation events in terms of their risk levels. The following steps are pursued: (1) the incidents reported in the Aviation Safety Reporting System (ASRS) are categorized into five risk groups; (2) a support vector machine model is used to discover the relationships between the event synopsis in text format and event consequence; (3) an ensemble of deep neural networks is trained to model the associations between event contextual features and event outcomes, (4) an innovative fusion rule is developed to blend the prediction results from the two trained machine learning models; and (5) the prediction of risk level categories is extended to event-level outcomes through a probabilistic decision tree.

Chapter 5 focuses on the third objective. It analyzes the reliability of human operators in terms of their response to malfunction events. The following steps are pursued: (1) Simulator experimental data is collected on nine licensed operators in three-person crews completing ten scenarios with each incorporating two to four malfunction events; (2) individual operator performance is monitored using eye tracking technology and physiological recordings of skin conductance response and respiratory function. Expert-rated event management performance is the outcome to be modelled based on eye tracking and physiological data; and (3) the heterogeneous data sources are integrated using a support vector machine with bootstrap aggregation to develop a trained quantitative prediction model.

Chapter 6 focuses on the fourth objective. It investigates the effectiveness of a rerouting strategy in face of the shutdown of an airport due to extreme weather, along the following steps: (1) an aircraft re-routing optimization model is formulated to make periodic rerouting decisions with the objective of minimizing the overall distance travelled by all the aircraft; (2) the performance of this aircraft re-routing system is analyzed using system failure time as the metric, considering multiple sources of uncertainties; and (3) a Support Vector Regression (SVR) surrogate model is developed to efficiently construct the system failure time distribution to measure the performance of re-routing strategy.

Chapter 7 focuses on the fifth objective. It investigates a pre-disaster resilience-based design optimization approach for logistics service centers configuration, along the following steps: (1) a bi-level program is formulated, and the impact of potential disruptive events is accounted for by the upper-level decision maker. Two decision variables are involved: location of the service center and its capacity; (2) the objective of the formulated bi-level program is to maximize the resilience of the service center configuration, thereby increasing the ability of the system to withstand unexpected events, and (3) a multi-level cross-entropy method is leveraged to generate samples that gradually concentrates all its mass in the proximity of the optimal solution in an iterative way.

Chapter 8 focuses on the sixth objective. It conducts investigation on the optimization of system reconfiguration strategies to mitigate the congestion caused by emergency evacuation out of disaster-prone zones. The following steps are pursued: (1) the traffic system performance is restored through two reconfiguration schemes: contraflow (also referred to as lane reversal), and crossing elimination at intersections; (2) a bi-level mathematical model is developed to represent the two reconfiguration schemes and characterize the interactions between traffic operators and passengers; and (3) a probabilistic solution discovery algorithm is used to obtain the near-optimal reconfiguration solution that maximizes the system resilience.

Chapter 9 provides a summary of contributions made in this dissertation and the research directions worthy of investigation in the future.

Chapter 2

Background

This chapter first introduces system resilience modeling, then describes several state-of-the-art machine learning algorithms that are extensively used in the literature. Afterwards, we briefly review uncertainty analysis, system optimization, and a big data analytics framework. Following this structure, we define system resilience in a quantitative manner in Section 2.1. Next, two major machine learning algorithms, namely support vector machine and deep learning, are reviewed. The basic concept of support vector machine is firstly introduced in Section 2.2.1. In parallel, two popular deep learning algorithms: deep feedforward neural network and recurrent neural network, are introduced in Section 2.2.2. Besides, a Bayesian neural network, as a generic means to characterize the prediction uncertainty of neural networks, is introduced following Section 2.2.2. In Section 2.3, a bi-level optimization framework is introduced to model the interactions between multiple decision makers at different levels. In Section 2.4, we describe the categorization of uncertainties arising at various stages, and introduce global sensitivity analysis to measure the contribution of random variable to the system-level variability. Finally, Section 2.5 introduces the concept of a big data engine – Apache Spark – to process large volumes of raw data.

2.1 System Resilience

System resilience is a complex term, and it is a time-dependent function of many factors, e.g., the type of the disaster (flood, hurricane, earthquake, or others), characteristics of the disaster (i.e., location and temporal evolution of the disaster), the impact of the extreme event on the system, the property of the original system (i.e., redundancy, vulnerability), and operational flexibility (what options are available to restore the system in response to the extreme event). As a widely acknowledged concept, resilience has received extensive attentions from the risk analysis community following Holland's seminal study [8]. During the past ten years, numerous efforts have been dedicated to the development of quantitative measures/metrics to evaluate system resilience in response to different types of natural disasters or intentional attacks with applications to telecommunication systems [9], waterway network [10], electrical power system [11], and others [12, 13, 14, 15]. For example, Bruneau et al. [16] proposed a quantitative metric to measure the community seismic resilience as the extent to which the social communities are able to carry out recovery activities to mitigate the social disruption of future earthquakes. Henry and Ramirez-Marquez [2] defined system resilience as a time-dependent function, which is the ratio of the delivery function of the system that recovers over time and the initial performance loss caused by disruptive event. Baroud et al. [17] measured the importance of network components according to their contribution to the network resilience in inland waterway networks. In a recent study, Fotouhi et al. [18] formulated a bi-level, mixed-integer, stochastic program to quantify the resilience of an interdependent transportation-power network. Hosseini et al. [19] provided a comprehensive review on the recent advancements along the definition and quantification of system resilience in a variety of disciplines.

Even through there is no universally accepted resilience metric, all the aforementioned metrics share several significant characteristics: (I) resilience is regarded as a time-dependent metric. Obviously, the resilience of a system varies over time and is pertinent to the type of disruption; (II) realistic models need to be constructed to model the disturbance caused by the disruptive event and its impact on the system (absorptive ability, restoration ability); (III) an appropriate performance metric needs to be defined to characterize the system behavior before, during and after the disruption; (IV) reasonable functions need to be developed to associate the preventive (or pre-disaster activities) and corrective actions (or post-disaster activities) to the system performance. These key features substantially differentiate resilience from other measures of system performance, such as, reliability, sustainability, fault-tolerance, and flexibility.

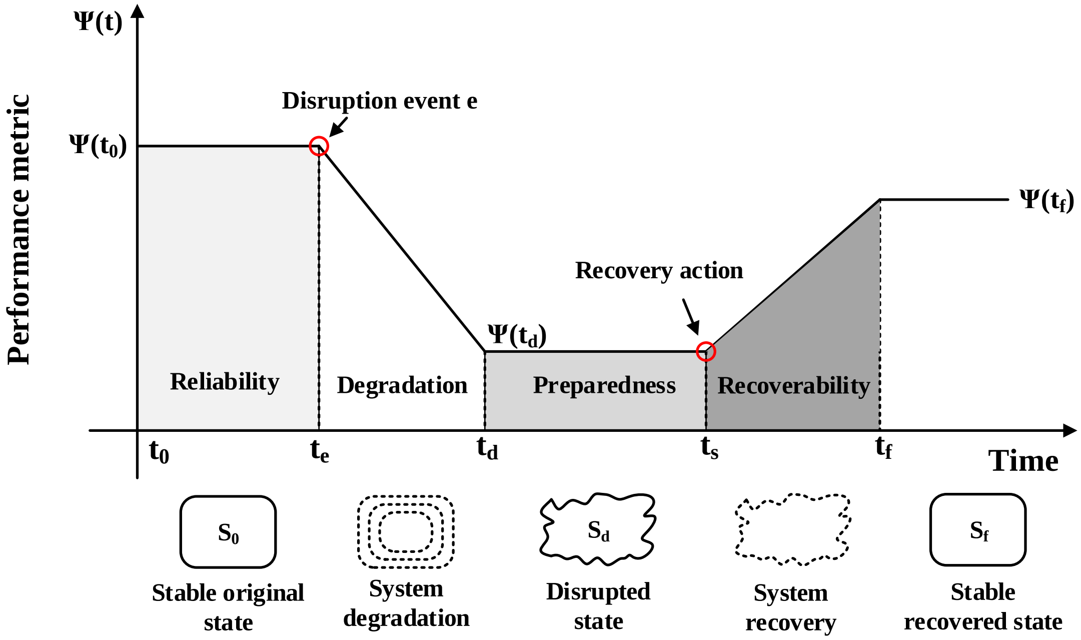

Figure 2.1: Concept of system resilience [2]

Consider an infrastructure system, such as a power network system, transportation system, inland waterway network etc. If unexpected disruptions occur, its state transitions can be modelled using Fig. 2.1. To quantify the system resilience R, we introduce a system performance function $\psi(t)$ to describe the system behavior at time t. Commonly used representations of this function can be network capacity, travel time, traffic flow, system throughput, or network connectivity depending on the specific system under consideration. As can be observed in Fig. 2.1, there are several distinct stages to characterize the transition of the system over time:

- Before the occurrence of the disruption, the original system is operated at the as-designed state S_0;

- Once the disruption event e happens at time t_e, the system performance starts to degrade over time due to the failure of system components or the loss of partial functionality. The system performance continues to degrade until it reaches a maximum disrupted state $\psi(S_d)$ at time t_d.

– In response to the disturbance, certain measures are carried out to recover the system functionality. At this stage, two different activities get involved: repair and system recovery. Preparation refers to the time required for identifying the system malfunction and repairing or replacing the impaired components. When all the preparation work is completed, the system performance begins to recover from the disrupted state S_d at time t_s. With time, the system performance restores to a new stable state S_f, and is maintained thereafter.

Let $R(t)$ denote the resilience of a system at time t, since resilience describes the ratio of system recovery at time t to the loss suffered by the system at some previous point in time t_d, then $R(t)$ can be expressed by the following equation [20]:

$$R(t) = \frac{\text{Recovery}(t)}{\text{Loss}(t_d)},\ t \geqslant t_d. \tag{2.1}$$

As shown in Fig. 2.1, $\psi(t_0)$ describes the value of the system service function corresponding to the stable state S_0. The system performance remains at this level until the occurrence of the disruptive event e at time t_e, upon which the system resilience is exhibited. Once the disruptive event e occurs, the system performance degrades gradually until it converges to a stable disrupted state S_d at time t_d, and the system delivery function value corresponding to this disrupted state is $\psi(t_d)$, which is lower than its original value $\psi(t_0)$. After a duration $t_s - t_d$, the recovery action is taken at time t_s, which restores the system from the disrupted state S_d to a new stable state S_f with system performance function value $\psi\left(t_f\right)$ at time t_f. Based on the above definitions, the system resilience given the disruptive event e can be defined as [20]:

$$R\left(t_f \middle| e\right) = \frac{\psi\left(t_f \middle| e\right) - \psi\left(t_d \middle| e\right)}{\psi(t_0) - \psi\left(t_d \middle| e\right)} \tag{2.2}$$

The above system resilience metric helps to quantify the impact of different restoration actions and operations on the recovery of system performance. In general, the higher the resilience value, the stronger the system's ability to recover. Along this direction, one study worthy of mention is that Zhang et al. [21] developed a nonlinear function to model the characteristics of each system component in the presence of the disruptive event e:

$$u_{ij}^{*}(t) = u_{ij}\left[a_{ij} + \lambda_{ij} \cdot \left(1 - a_{ij}\right) \cdot \left(1 - e^{-b_{ij}t}\right)\right] \tag{2.3}$$

where u_{ij} denotes the original performance of a component (i, j), t represents the duration after the disruption, $u_{ij}^{*}(t)$ represents the restored component capacity at time t, a_{ij} denotes the disrupted capacity retained in link (i, j) after the disruption, b_{ij} characterizes the restoration speed of link (i, j), and λ_{ij} is the ratio used to denote the degree to which the link is able to recover compared to its original performance.

This nonlinear function incorporates core resilience concepts (i.e., absorptive capacity and restorative ability) and the time to recovery in modelling the component resilience. In addition, the non-linear function defined in Eq. (2.3) is also equipped with the ability to characterize the variability of component performance restoration speed over time. Often, when we restore a complex component, the part that takes the least amount of time or resources will be repaired first, whereas the part which consumes the largest amount of resources or time will be repaired last. From this point of view, the speed of component performance restoration gets slower and slower over time [22]. This feature has been captured by the nonlinear function defined in Eq. (2.3).

In addition, the extra parameters, a, b, and λ introduced in this function increase the flexibility of this function, which enables us to handle the component recovery process in multiple different applications. Fig. 2.2a illustrates these concepts. Specifically, we fix the parameters b and λ at 2 and 0.8, respectively, and increase the value of a from 0 to 1 in a step size of 0.1. As can be observed, when $a = 0$, the component loses all of its capacity. With the increase of parameter a, more capacity along the component is retained. Especially when $a = 1$, the component is immune to this disruptive event, and no capacity

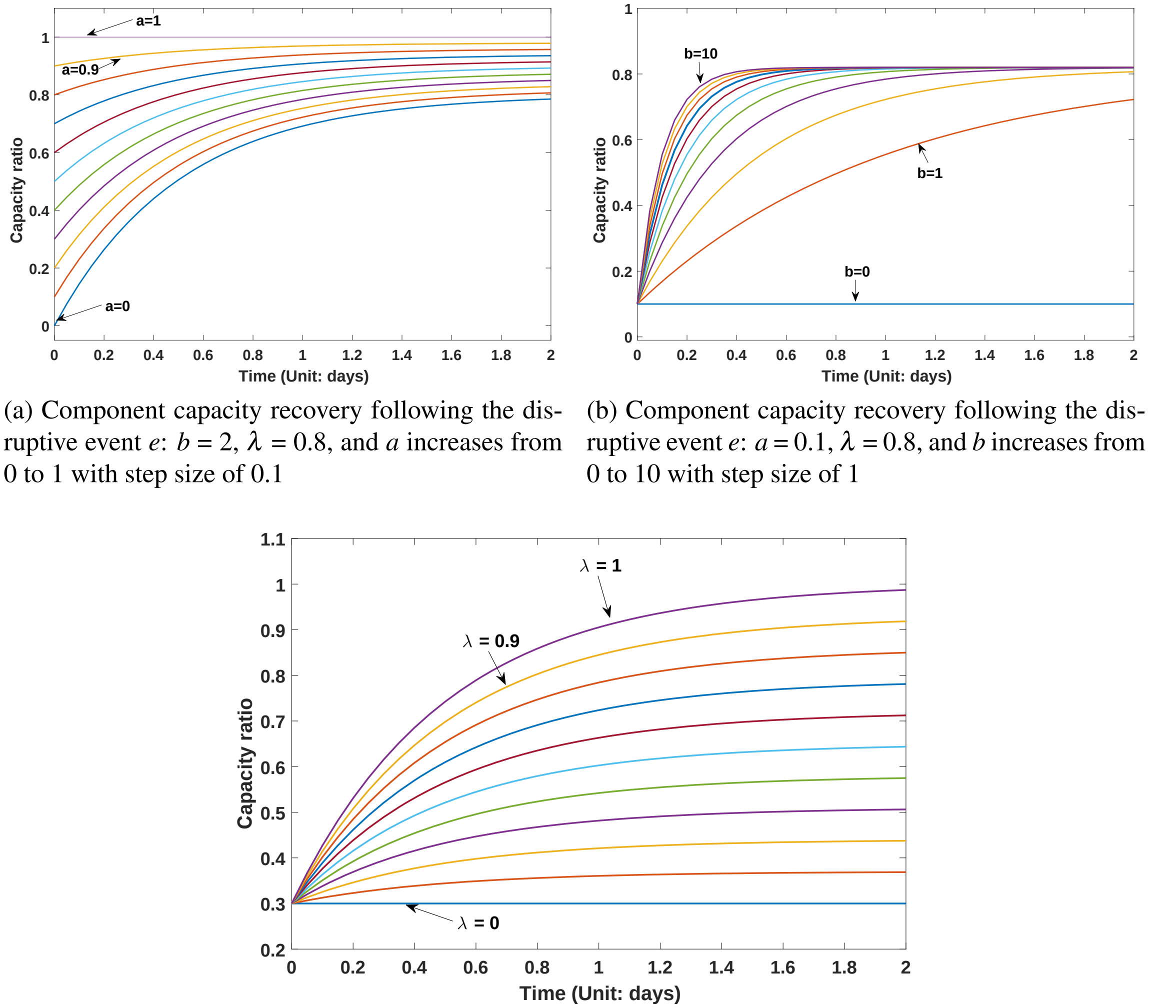

(a) Component capacity recovery following the disruptive event e: $b = 2$, $\lambda = 0.8$, and a increases from 0 to 1 with step size of 0.1

(b) Component capacity recovery following the disruptive event e: $a = 0.1$, $\lambda = 0.8$, and b increases from 0 to 10 with step size of 1

(c) Component capacity recovery following the disruptive event e: $a = 0.3$, $b = 2$, and λ increases from 0 to 1 with step size of 0.1

Figure 2.2: Component restoration behavior following a disruptive event e

is lost. The interpretation of parameter a is simple: the more functionality retained relative to original capacity, the higher the absorptive capacity. Similarly, the parameter b enables us to handle different restoration speeds (see Fig. 2.2b), and the parameter λ enables us to control the degree to which the component could recover relative to its original capacity (see Fig. 2.2c) after the disruptive event e.

In Chapters 7 and 8, the system resilience defined in this chapter will be used to maximize system performance through the implementation of different strategies to mitigate the impact of extreme events.

2.2 Machine Learning

In practice, physical-based models, such as, closed-form equations and physical laws, are widely used to describe many engineering systems. However, a number of physics-based models use parameterized form of approximations to represent the actual complex physical processes that are not fully understood. The calibration of parameters in physics-based models are computationally expensive due to the combinatorial nature of the search space. More importantly, it is impossible to describe many engineering systems through mathematical and physical equations, e.g., email filtering, computer vision. In face of these challenges, since the data pertaining to these systems can be collected easily in the big data era, researchers have switched to develop data-driven models to learn explainable relationships between system input variables and the quantities of interest with state-of-the-art machine learning algorithms. In this section, we introduce two classes of commonly used machine learning algorithms, namely support vector machine and deep learning models.

2.2.1 Support Vector Machine

Support vector machine (SVM) is a powerful tool for classification and function estimation problems since its introduction by Vapnic within the context of statistical learning theory and risk minimization [23]. Over the past decades, SVM has been successfully applied in pattern classification [24], image segmentation [25], object detection [26], and other problems [27].

Fig. 2.3 demonstrates the fundamental idea of classification using SVM in a 2-D space. A number of data points $(\boldsymbol{x_1}, y_1), \ldots, (\boldsymbol{x_i}, y_i)$, $i = 1, \ldots, N$ are distributed in the 2-D space, where $\boldsymbol{x_i} \in \mathbb{R}^d$ is a vector containing multiple features, and $y_i \in \{\pm 1\}$ is a class indicator with value either -1 or +1, which are denoted as circles and squares in Fig. 2.3, respectively. Suppose we have some hyperplane to separate the positive from the negative classes; there

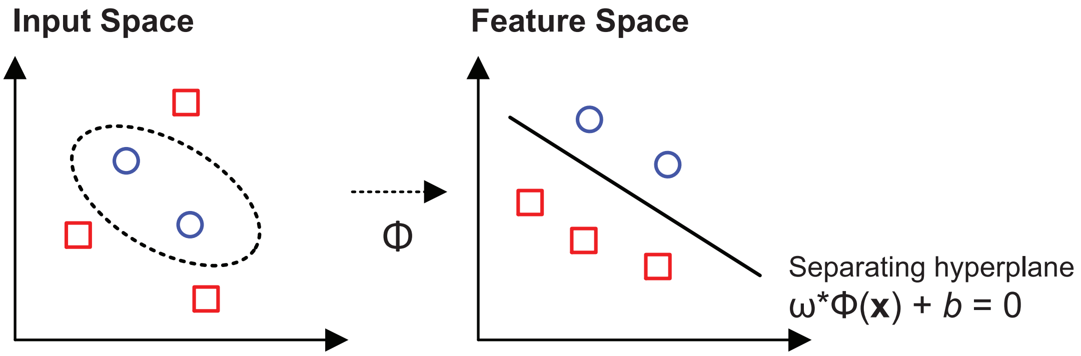

Figure 2.3: SVM to solve the binary classification problem separating circular balls from square tiles

exists a linear function in the following form:

$$f(\boldsymbol{x}) = \boldsymbol{\omega}\Phi(\boldsymbol{x}) + b \tag{2.4}$$

where Φ is a kernel function in the form of $\Phi(\boldsymbol{x_i})^{\mathrm{T}}\Phi\left(\boldsymbol{x_j}\right)$ that maps the training data from the input space into a higher dimensional feature space, such that for each training example $\boldsymbol{x_i}$, the mapped hyperplane satisfies the following constraints:

$$\begin{aligned} \boldsymbol{w}\cdot\Phi(\boldsymbol{x_i}) + b \geq 1, \quad \text{for } y_i = +1, \\ \boldsymbol{w}\cdot\Phi(\boldsymbol{x_i}) + b \leq -1, \quad \text{for } y_i = -1. \end{aligned} \tag{2.5}$$

The two constraints can be combined into one equation:

$$y_i(\boldsymbol{w}\cdot\Phi(\boldsymbol{x_i}) + b) - 1 \geq 0, \quad \forall i \tag{2.6}$$

Our objective is to find a hyperplane to separate the two classes, where $\boldsymbol{w}$ is normal to the hyperplane. Since there are many hyperplanes to separate the two classes, the SVM classifier is based on the hyperplane that maximizes the separation margin between the two classes if the mapped data is linearly separable in the projected high dimensional space. If the mapped data is not linearly separable, a positive penalty parameter C is usually introduced to penalize the misclassified samples. The introduction of the penalty parameter allows some data to be unclassified or on the wrong side of the decision boundary. By varying the value of C, we can decide the width of the margin between the separating hyperplane and the closest data point. Mathematically, the parameters of the nonlinear function are determined by the following minimization problem:

$$\min \quad \frac{1}{2}\|\boldsymbol{w}\|^2 + C\sum_{i=1}^{N}\xi_i \tag{2.7}$$

subject to:

$$y_i\left(\boldsymbol{w}\cdot\Phi\left(\boldsymbol{x_i}\right)+b\right) \geq 1-\xi_i, \quad \xi_i \geq 0;\ i=1,2,\ldots,N \tag{2.8}$$

where ξ_i is a slack variable introduced to relax the separability constraint formulated in Eq. (2.6).

As a variant of SVM, support vector regression (SVR) also reveals promising capabilities for regression problems. Since SVR has greater generalization ability and guarantees global minima for given training data, it has drawn the attention of researchers and has been applied in many practical applications, e.g., financial time series forecasting [28], and travel time prediction [29]. Different from neural networks, SVR formulates the learning process as a quadratic programming optimization problem with linear constraints.

Consider a typical regression problem with a set of data $(\boldsymbol{x_i}, y_i)$, $i = 1, \ldots, N$, where $\boldsymbol{x_i}$ is a vector of the model inputs, y_i is the actual value. The objective of regression analysis is to determine a function $f(\boldsymbol{x})$ so as to predict the desired targets accurately. To address the regression problem, we define a cost function to measure the degree of discrepancy between the predicted value and the actual value. A commonly used cost function in SVR is the robust ε-insensitive loss function L_ε, which is defined as [23]:

$$L_\varepsilon\left(f\left(\boldsymbol{x}\right),y\right) = \begin{cases} |f\left(\boldsymbol{x}\right)-y|-\varepsilon, & if\ |f\left(\boldsymbol{x}\right)-y| > \varepsilon, \\ 0 \quad \text{otherwise}. \end{cases} \tag{2.9}$$

where ε is a user-prescribed parameter to measure the approximation accuracy placed on the training data points.

Fig. 2.4 illustrates the concept of ε-insensitive SVR. As long as the deviation between prediction $f(\boldsymbol{x_i})$ and actual value y_i is less than ε, then L_ε takes the value of 0. Otherwise, $L_\varepsilon = |f(\boldsymbol{x_i}) - y_i| - \varepsilon$. By minimizing the regularized risk function, we estimate the unknown parameters $\boldsymbol{w}$ and b by solving the following optimization problem:

$$\min \quad C\sum_{i=1}^{N} L_\varepsilon\left(f\left(\boldsymbol{x_i}\right), y_i\right) + \frac{1}{2}\|\boldsymbol{w}\|^2 \tag{2.10}$$

where C is a user-determined parameter to control the trade-off between the prediction error and the complexity of the regression model.

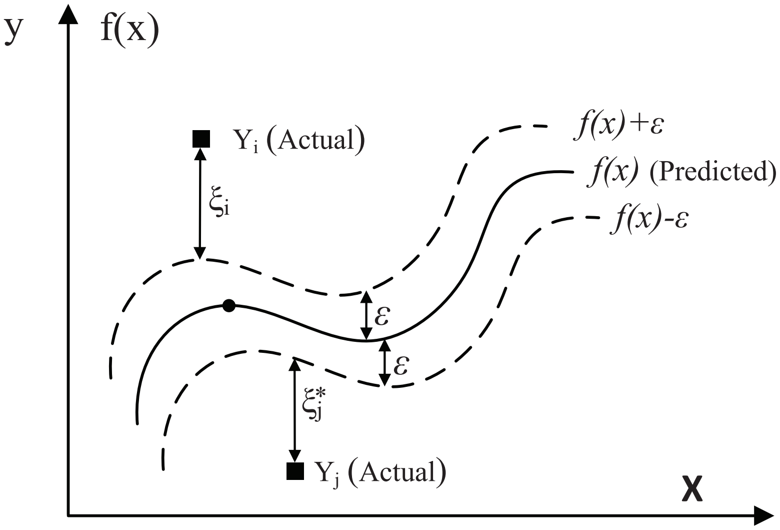

Figure 2.4: ε-insensitive SVR

Two positive slack variables, ξ_i, ξ_i^*, are introduced to quantify the derivation $(|f(\boldsymbol{x}) - y|)$ from the boundaries of the ε-insensitive zone. With the slack variables, we update Eq. (2.10) as follows:

$$\min \quad C\sum_{i=1}^{N} (\xi_i + \xi_i^*) + \frac{1}{2}\|\boldsymbol{w}\|^2, \tag{2.11}$$

subject to

$$\begin{cases} y_i - (\boldsymbol{w} \cdot \Phi(\boldsymbol{x_i}) + b) \leq \varepsilon + \xi_i, \\ \boldsymbol{w} \cdot \Phi(\boldsymbol{x_i}) + b - y_i \leq \varepsilon + \xi_i^*, \\ \xi_i, \xi_i^* \geq 0, \quad i = 1, \ldots, N. \end{cases}$$

With the help of Lagrange multipliers and KKT conditions, Eq. (2.11) yields the following dual Lagrangian form [23]:

$$\max \quad -\varepsilon \sum_{i=1}^{N} (\alpha_i + \alpha_i^*) + \sum_{i=1}^{N} (\alpha_i^* - \alpha_i) y_i - \frac{1}{2} \sum_{i,j=1}^{N} (\alpha_i^* - \alpha_i) \left(\alpha_j^* - \alpha_j\right) \boldsymbol{K}\left(\boldsymbol{x_i}, \boldsymbol{x_j}\right), \tag{2.12}$$

subject to

$$\begin{cases} \sum\limits_{i=1}^{N} (\alpha_i - \alpha_i^*) = 0, \\ 0 \leq \alpha_i, \alpha_i^* \leq C, \quad i = 1, \ldots, N. \end{cases} \tag{2.13}$$

where α_i, α_i^* are the optimum Lagrange multipliers, and $\boldsymbol{K}$ is the kernel function defined as:

$$\boldsymbol{K}(\boldsymbol{x_1}, \boldsymbol{x_2}) = \Phi(\boldsymbol{x_1}) \Phi(\boldsymbol{x_2}). \tag{2.14}$$

The optimal weight vector of the regression hyperplane is $\boldsymbol{w}^* = \sum\limits_{i=1}^{N} (\alpha_i - \alpha_i^*) \boldsymbol{x_i}$. Hence, the general form of the SVR-based regression function can be written as:

$$f(\boldsymbol{x}, \boldsymbol{w}) = f(\boldsymbol{x}, \alpha, \alpha^*) = \sum_{i=1}^{N} (\alpha_i - \alpha_i^*) \boldsymbol{K}(\boldsymbol{x}, \boldsymbol{x_i}) + b. \tag{2.15}$$

2.2.2 Deep Learning

In the past decade, deep learning has gained increasing attentions due to its promising features in automatic feature extraction and end-to-end modeling [30, 31]. The key advantage of deep learning over the classical machine learning algorithms is that it is able to learn appropriate representations from the raw data with multiple levels of abstraction in an automatic manner that are needed for detection or classification. Typically, conventional machine learning algorithms require manually designed rigorous feature extractor to elicit informative features from raw data (e.g., image) that usually needs careful engineering and a considerable amount of domain expertise, from which the classifier is able to learn and differentiate patterns revealed in the extracted features. Whereas, deep learning is able to extract features embodied in massive raw data with multiple levels of representation (e.g., orientation, location, motifs, and their combinations in images) from the training data automatically. As a result, it frees us from the design of a hand-engineered feature extractor to transform the raw data into a suitable representation or feature vector. In this section, we briefly introduce the underlying mechanisms for two neural networks, namely feedforward neural network, and recurrent neural network. In addition, a framework is introduced to characterize model prediction uncertainty following a Bayesian approach.

2.2.2.1 Feedforward Neural Network

The feedforward neural network was the first and simplest type of artificial neural network devised [31]. As revealed by its name, feedforward neural network is a computer system consisting of a number of feedforward, highly-connected neurons. These connected neurons represent the knowledge through a continuing process of stimulation by the environment in which the network is embedded. In general, there are four key components in a feedforward neural network: neuron, activation function, cost function, and optimization. Fig. 2.5 illustrates a feedforward neural network with two hidden layers and each hidden layer having four neurons. As can be observed, the neural network has one input layer to receive input variables, two hidden layers, and an output layer.

Inside each hidden neuron (e.g., the blue solid cells in Fig. 2.5) is a module composed of four parts: input links, input function, activation function, and output link. Fig. 2.6 shows the detailed structure of a hidden unit in the neural network. The input links represent the values of input variables received from preceding layer. Next, the input function performs a weighted sum operation on the values of input links, then pass the summed value to an

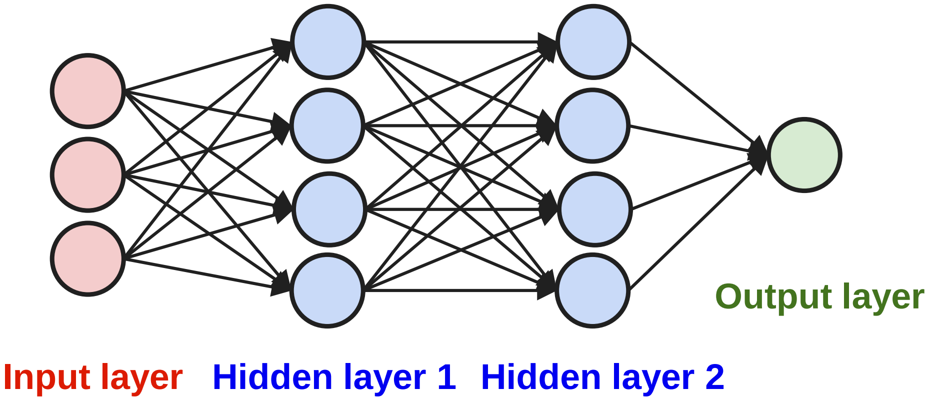

Figure 2.5: A feedforward neural network with two hidden layers [3]

activation function. The activation function squashes the weighted sum value to a fixed range, and pass it to the next layer. Mathematically, the aforementioned operations within each hidden unit can be represented as:

$$a_i = g\left(in_i\right) = g\left(\sum_{j=0}^{m} a_j W_{j,i}\right) \tag{2.16}$$

where i denotes the i-th hidden layer, $W_{0,i}$ is the bias, $W_{j,i}$ $(j \neq 0)$ represents the weight along each input link, g is an activation function, and m is the number of input links.

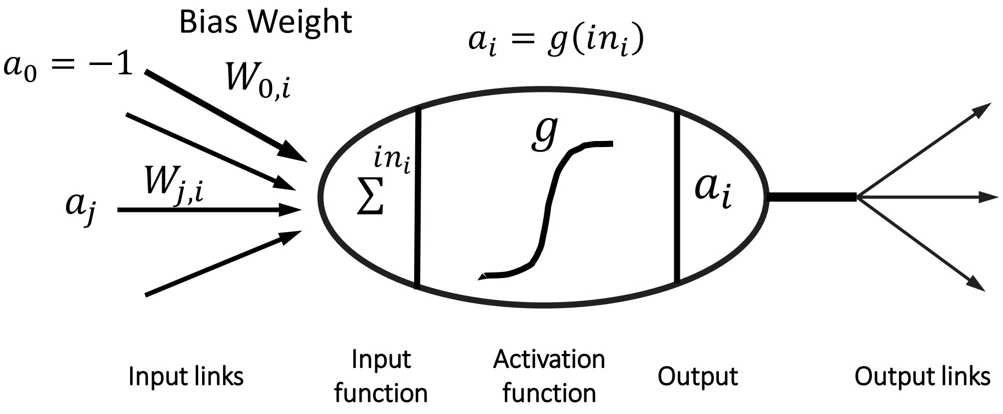

Figure 2.6: Detailed structure of a hidden unit in neural networks [3]

The activation function can take many different forms, such as sigmoid function ($g(z) =$

$\frac{1}{1+e^{-z}}$), rectified linear unit function ($g(z) = \max(0, z)$), and hyperbolic tangent function ($g(z) = \frac{2}{1+e^{-2z}} - 1$), etc. As mentioned earlier, all the activation functions have similar purpose to squash the input value within a fixed range.

In a similar way, the input variable can be passed through a stack of hidden layers. Finally, we obtain the value at the output layer in the neural network and use it as the model prediction. Similar to other machine learning algorithms, a cost function is defined to measure how far off our predictions are away from the actual values. A variety of cost functions (e.g., mean squared error loss, binary cross-entropy, hinge loss) are available depending on the purpose of the learning task (e.g., classification, regression). With the computed loss value at each iteration, backpropagation algorithms calculate the error at the output and then distribute it back through the network layers using chain rule to compute gradients for each layer. Next, adjustments are applied to the weights in each layer of the feedforward network so as to minimize the loss value in the next iteration. The same procedures continue until the loss function converges to a stable value.

2.2.2.2 Recurrent Neural Network

Different from the feedforward neural network, recurrent neural network contains a feedback loop that is connected to the past decisions (e.g., the information contained in the hidden cell) and ingests their own outputs moment after moment as input, which enables the network to learn the temporal dependencies in time series (or sequence) data. By preserving the sequential information and passing information from one step to the next through the hidden state variables, the RNN manages to maintain a memory of the temporal correlation between events separated by many moments. This feature makes it ideal to handle time series data. Among RNNs, the long short-term memory (LSTM) RNN as proposed by Hochreiter and Schmidhuber [32] has received increasing attention because it overcomes the vanishing and exploding gradients problem by enabling the network to learn when to forget the previous hidden states and when to update the hidden states by integrating with new memory in an adaptive manner [32].

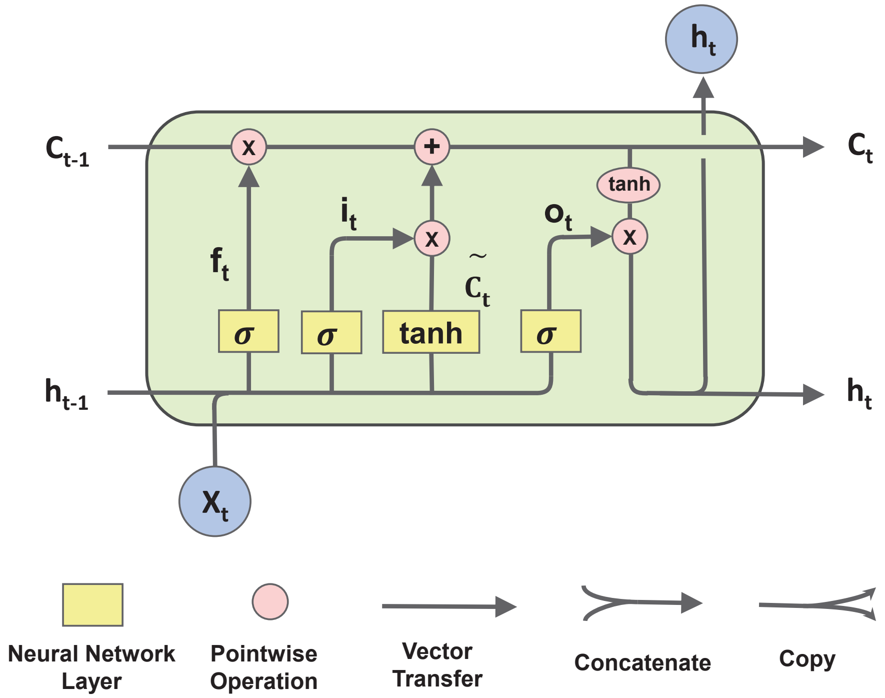

Figure 2.7: The structure of a LSTM block

To briefly introduce the concept of LSTM recurrent neural network, Fig. 2.7 shows the graphical representation of all the mathematical operations going on within a LSTM block. Let $\{\boldsymbol{x}_1, \cdots, \boldsymbol{x}_T\}$ denote a general input sequence for a LSTM, where $\boldsymbol{x}_t$ represents a k-dimensional input vector at the t-th time step. The most important element in a LSTM block is the cell state as represented by the horizontal line running through the top of the diagram in Fig. 2.7. The first step in the LSTM block is to decide what information to forget, which is determined by a sigmoid layer called "forget gate layer" as denoted in Eq. (2.17). The output of the forget gate layer is a value varying from 0 to 1, where 0 indicates the information in the previous cell state $\boldsymbol{C}_{t-1}$ is completely thrown away, and 1 reveals that the information in the previous cell state is completely retained. In the next step, decision is made regarding what new information to store in the cell state. In this case, a sigmoid "input gate layer" is firstly used to determine what values to update (see. Eq. (2.18)), then a tanh layer creates a set of candidate values $\widetilde{\boldsymbol{C}}_t$ to be added to the new cell state (see. Eq. (2.19)). Next, the new cell state is updated by combining the information retained in the previous cell state $\boldsymbol{C}_{t-1}$ with the new candidate information $\widetilde{\boldsymbol{C}}_t$ to be added (see. Eq. (2.20)). Finally, the output of the LSTM cell is to decided. To achieve this goal, a sigmoid layer is firstly used to determine which part to output (see Eq. (2.21)), then the new cell state $\boldsymbol{C}_t$ is pushed through a tanh layer such that the value is squashed into the range $[-1,1]$. The product of $\boldsymbol{o}_t$ and $\tanh(\boldsymbol{C}_t)$ composes the output value (see Eq. (2.22)).

$$\boldsymbol{f}_t = \sigma\left(\boldsymbol{W}_f\left[\boldsymbol{h}_{t-1}, \boldsymbol{x}_t\right] + \boldsymbol{b}_f\right) \tag{2.17}$$

$$\boldsymbol{i}_t = \sigma\left(\boldsymbol{W}_i\left[\boldsymbol{h}_{t-1}, \boldsymbol{x}_t\right] + \boldsymbol{b}_i\right) \tag{2.18}$$

$$\widetilde{\boldsymbol{C}}_t = \tanh\left(\boldsymbol{W}_C\left[\boldsymbol{h}_{t-1}, x_t\right] + \boldsymbol{b}_C\right) \tag{2.19}$$

$$\boldsymbol{C}_t = \boldsymbol{f}_t * \boldsymbol{C}_{t-1} + \boldsymbol{i}_t * \widetilde{\boldsymbol{C}}_t \tag{2.20}$$

$$\boldsymbol{o}_t = \sigma\left(\boldsymbol{W}_o\left[\boldsymbol{h}_{t-1}, \boldsymbol{x}_t\right] + \boldsymbol{b}_o\right) \tag{2.21}$$

$$\boldsymbol{h}_t = \boldsymbol{o}_t * \tanh\left(\boldsymbol{C}_t\right) \tag{2.22}$$

where $\boldsymbol{W}_f$, $\boldsymbol{W}_i$, $\boldsymbol{W}_C$, and $\boldsymbol{W}_o$ represent the weight matrices associated with each unit, and $\boldsymbol{b}_f$, $\boldsymbol{b}_i$, $\boldsymbol{b}_C$, $\boldsymbol{b}_o$ is the bias term corresponding to each unit, respectively.

The above short description introduces the underlying mechanism behind a single LSTM block. In practice, a number of LSTM blocks can be concatenated together in a hidden layer, and several hidden layers can be stacked together to learn the complex patterns in time series data. The same cost function and backpropagation algorithm as used in feed-forward neural networks can be leveraged to update the values of the weights.

2.2.2.3 Bayesian Neural Network

Consider a series of training inputs X $= \{X_1, X_2, \cdots, X_N\}$ and their corresponding outputs Y $= \{Y_1, Y_2, \cdots, Y_N\}$. Suppose we have a neural network denoted as $f^{\omega}(\cdot)$, where f represents the structure of the neural network (e.g., number of layers and hidden units, choice of activation functions), and $\boldsymbol{\omega}$ is the collection of model parameters to be estimated.

Since there are so many model parameters to estimate, one crucial question is to assess how much to trust the prediction of the trained model for new input value. With model prediction uncertainty beforehand, the prediction with high uncertainty and extreme cases can be handled in an explicit manner, thereby informing decision making with confidence. In the Bayesian context, we aim to infer the posterior distribution of model parameters $\boldsymbol{\omega}$ that are most likely to generate the observed data X and Y. To achieve this, in the Bayesian approach, we assign a prior distribution over the space of model parameters $p(\boldsymbol{\omega})$ to represent our prior belief on each candidate model parameter in generating the observed data, then a likelihood function $p(y|x,\omega)$ $(\omega \in \boldsymbol{\omega})$ is constructed to characterize the probability of generating the observed data given model parameter ω. The Bayesian inference aims at identifying a posterior distribution $p(\boldsymbol{\omega}|\mathrm{X},\mathrm{Y})$ over model parameters $\boldsymbol{\omega}$. Given the data X and Y, the posterior distribution exactly models how likely a variety of model parameters $\boldsymbol{\omega}$ are in generating them. With the posterior distribution, given a new data point x^*, the predictive distribution of x^* can be obtained by marginalizing out the posterior distribution:

$$p(y^*|x^*,\mathrm{X},\mathrm{Y}) = \int p(y^*|x^*,\boldsymbol{\omega})p(\boldsymbol{\omega}|\mathrm{X},\mathrm{Y})\,d\boldsymbol{\omega} \tag{2.23}$$

In neural networks, a popular way to define the prior distributions is to place a Gaussian distribution $p(\boldsymbol{\omega}) = \mathscr{N}(0,\mathscr{I})$ over a neural network's weights while the bias vectors are often assumed to be point estimates for the sake of simplicity [33]. The aforementioned procedures are often referred to as posterior inference. Unfortunately, it is computationally prohibitive to perform exact Bayesian inference with the classical algorithms (e.g., MCMC methods such as Gibbs sampling, Metropolis-Hastings) due to the non-linearity and non-conjugacy in deep neural networks, while most traditional algorithms for approximate Bayesian inference are not scalable in many deep neural networks with thousands of parameters. Furthermore, to characterize prediction uncertainty, the number of parameters to be estimated in these models is typically doubled for the same network size as mentioned earlier, which further increases the difficulty to make these algorithms scalable.

Gal and Ghahramani [34, 35], Gal [36] have developed a novel easy-to-implement alternative to MCMC, which is referred to as Monte Carlo dropout (MC dropout). As shown in Ref. [34], a deep neural network (NN) with arbitrary depth and non-linearities, with dropout applied before every weight layer, is mathematically equivalent to an approximation to the deep Gaussian process model [37]. To be specific, in a feedforward deep neural network, with dropout, we generate random samples using a Bernoulli distribution for each unit in the input layer and the hidden layers. Each sample takes the value of 1 with a probability of p_i. If the value of the binary variable is zero, then the corresponding unit is dropped accordingly. The implementation of dropout to a neural network amounts to sampling a thinner network from it with some units temporarily being removed. In back propagation, the value of each binary variable is used in updating the value of neural network weights. The dropout neural networks are trained in a way similar to standard neural nets with stochastic gradient descent. By doing this, we obtain a number of trained thinner neural network.

More importantly, the same Monte Carlo dropout strategy can also be leveraged to approximate model prediction uncertainty following a Bayesian approach in other types of neural networks, such as recurrent neural networks [35]. The key idea in the Monte Carlo dropout method is to approximate Bayesian inference with variational inference by defining a variational parametric distribution $q(\boldsymbol{\omega})$. Next, we minimize the Kullback–Leibler divergence between the approximating distribution and full posterior with Eq. (2.24), which is a measure of similarity between the two distributions.

$$\begin{aligned} KL(q(\omega)\|\, p(\omega|X,Y)) &\propto -\int q(\omega)\log p(Y|X,\omega)\,d\omega + KL(q(\omega)\|\, p(\omega)) \\ &= -\sum_{i=1}^{N}\int q(\omega)\log p(Y_i|\, f^{\omega}(X_i))\,d\omega + KL(q(\omega)\|\, p(\omega)) \end{aligned} \tag{2.24}$$

The MC dropout strategy has several promising features in comparison with other state-of-the-art approaches. First of all, it does not require any change of the existing model structure or optimization objective function. Instead, it is very straightforward to be implemented. Specifically, MC dropout is applied before each hidden layer, then the model output can be seen as random samples generated from the posterior prediction distributions [36]. Secondly, without loss of generality, MC dropout can be used to characterize prediction uncertainty in a variety of neural networks, such as feed-forward deep neural networks, recurrent neural networks, and convolutional neural networks.

2.3 System Optimization

In this section, we introduce a bi-level optimization program to characterize the interactions between decision makers at different levels. In the subsequent chapters, the bi-level program will be used to model the effect of different actions and strategies in mitigating the traffic congestion caused by extreme events.

2.3.1 Bi-level Program

In many engineering systems, multiple decisions makers are usually involved while each player has their own objectives and constraints. To characterize the interactions among the multiple decision makers at different levels, we form a hierarchical structure to nest each optimization task within the other. In the most simplest case, if there are only two decision makers in the system, the problem is usually formulated as a bi-level program. The outer optimization problem (upper level) is commonly referred to as leader's optimization problem, while the inner optimization problem (lower level) is typically known as the follower's optimization problem. Take the traffic system as an example, in the upper-level, traffic planners act as leaders and make changes (e.g., build new road, introduce new signal pattern) to the traffic system, while passengers act as followers to choose any path that minimizes their travel time from origin to destination freely. Even though traffic planners can influence the travelers' path-choosing behavior by the decisions/policies they make related to the traffic system, but have no control over travelers' behavior in choosing the path. Hence, when traffic planners make any changes to the traffic system, it is important to account for the dynamics of travelers' behavior. From a mathematical point of view, this problem can be formulated as:

$$\begin{aligned} (\underline{\text{U0}}) \quad & \min_{\boldsymbol{u}} \quad F(\boldsymbol{x},\boldsymbol{u}) \\ & s.t. \quad \boldsymbol{G}(\boldsymbol{x},\boldsymbol{u}) \leq \mathbf{0} \end{aligned} \tag{2.25}$$

where the vector $\boldsymbol{x} = \boldsymbol{x}(\boldsymbol{u})$ is determined via optimizing the following problem:

$$\begin{aligned} (\underline{\text{L0}}) \quad & \min_{\boldsymbol{x}} \quad f(\boldsymbol{x},\boldsymbol{u}) \\ & s.t. \quad \boldsymbol{g}(\boldsymbol{x},\boldsymbol{u}) \leq \mathbf{0} \end{aligned} \tag{2.26}$$

where the vector $\boldsymbol{u}$ in the upper level problem (U0) represents the system planers' decisions, e.g., building new roads, link capacity expansion, and traffic signal configurations. The vector $\boldsymbol{x}$ represents the equilibrium state of travelers' path-choosing behavior, which will be introduced in detail in the next section.

From the above bi-level program, it can be observed that the goal of the upper level problem (U0) is to minimize the value of objective function F through optimizing the decision variable $\boldsymbol{u}$ subject to the constraints $\boldsymbol{G}$ while the lower level decision vector $\boldsymbol{x}$ acts as parameters. Likewise, the lower level problem (L0) aims at minimizing the value of objective function f via optimizing the decision variable $\boldsymbol{x}$ under the constraint $\boldsymbol{g}$, while the upper level decision vector $\boldsymbol{u}$ acts as parameters. The bi-level optimization problem can also be regarded as a Stackelberg game [38], where the decision maker in the upper level has the leadership in playing the game first and carry out a set of operations/changes to the system, and the system users in the lower level react optimally to the decision makers' choice. The two players are connected by the response function $\boldsymbol{x} = \boldsymbol{x}(\boldsymbol{u})$. In other words, the two players are influenced by each other's decision through this function. For example, when traffic planners make any changes to the traffic network, they need to account for users' path-choosing behavior, which is represented by the vector $\boldsymbol{x}$ in the lower level problem. Once any changes are made to the network, the network users' path-choosing behavior changes accordingly given the updated state $\boldsymbol{u}$ of the traffic network.

2.3.2 User Equilibrium Traffic Assignment

In a traffic network, each network user non-cooperatively seeks to minimize his/her own total travel cost by taking the shortest path from the origin to the destination. Since the link cost is a monotonically increasing function of traffic flow, the travel time gets increased accordingly when the number of travelers along the shortest path increases. As a result, travelers switch to other alternate paths with shorter travel times. The same process continues until nobody can decrease their travel time by shifting to any other route. Under the resulting state, the traffic flow assignment in the network converges to an equilibrium state, and this state is also referred to as the Wardrop user equilibrium traffic assignment [39], where nobody can reduce the travel time by unilaterally changing their routes. Past studies have shown that traffic network enhancements (e.g., addition of a new road, road capacity expansion) without the consideration of users' path-choosing behavior might increase the network-wide congestion [40], which is also referred to as Braess's paradox [41]. Hence, it is essential to account for network users' path-choosing behavior when we make any changes to a traffic network.

Consider a connected network $G(V,E)$, where V denotes the set of nodes, and E represents the set of links. Let $\mathbb{OD}$ denote the set of origin-destination pairs in the network, (s,t) be one of the origin-destination pairs, where $(s,t) \in \mathbb{OD}$, and $d^{s,t}$ be the amount of traffic demand from the origin s to the destination t. Suppose $q_p^{s,t}$ represents the flow along the path p that originates at node s and destines at node t, then we have:

$$\sum_{p \in P^{s,t}} q_p^{s,t} = d^{s,t}, \quad \forall (s,t) \in \mathbb{OD}. \tag{2.27}$$

where $P^{s,t}$ denotes a set of cycle-free paths connecting the origin node s with the destination node t. The constraint imposed by Eq. (2.27) indicates that the total amount of flow along all the paths connecting the origin node s with the destination node t must be equal to the demand between the origin-destination pair (s,t). Obviously, all the traffic flows must be non-negative, thus we have:

$$q_p^{s,t} \geq 0, \quad \forall p \in P^{s,t}, \, \forall (s,t) \in \mathbb{OD}. \tag{2.28}$$

Let a $(a \in E)$ be one link in the network G, and x_a denotes the traffic flow along link a, then we have:

$$x_a = \sum_{(s,t) \in \mathbb{OD}} \sum_{p \in P^{s,t}} q_p^{s,t} \delta_{a,p}^{s,t}, \quad \forall a \in E. \tag{2.29}$$

where $\delta_{a,p}^{s,t}$ is a binary variable. When $\delta_{a,p}^{s,t} = 1$, it means that link a is a segment constituting the path p $(p \in P^{s,t})$. Otherwise, $\delta_{a,p}^{s,t} = 0$.

Given the above notations and constraints, the user equilibrium traffic assignment with fixed demand can be mathematically formulated as the following nonlinear optimization program:

$$\begin{aligned} (\underline{\text{L1}}) \quad \text{Min} \quad & f = \sum_{a \in E} \int_0^{x_a} t_a(x)\, dx \\ s.t. \quad & x_a = \sum_{(s,t) \in \mathbb{OD}} \sum_{p \in P^{s,t}} q_p^{s,t} \delta_{a,p}^{s,t}, \quad \forall a \in E, \\ & \sum_{p \in P^{s,t}} q_p^{s,t} = d^{s,t}, \quad \forall (s,t) \in \mathbb{OD}, \\ & q_p^{s,t} \geq 0, \quad \forall p \in P^{s,t}, \, \forall (s,t) \in \mathbb{OD}. \end{aligned} \tag{2.30}$$

where f is the objective function, $t_a(x)$ is a monotonically increasing function denoting the relationship between the travel time and the traffic flow along link a, x_a is the total traffic flow on link a, $\mathbb{OD}$ is the set of origin-destination traffic demand pairs, $d^{s,t}$ is the traffic demand among the origin-destination pair (s,t) $((s,t) \in \mathbb{OD})$, and $q_p^{s,t}$ denotes the traffic flow along the path p $(p \in P^{s,t})$ that connects origin node s with destination node t.

2.3.3 System-level Optimization

Although user equilibrium characterizes the path-choosing behavior of the traffic network users, it does not model the system-level decision maker's goal. Different from user equilibrium, system optimization models the problem from the perspective of the traffic planner, and it aims at coordinating all the travelers to choose the paths in such a way that the total travel time in the entire network is minimized. Mathematically, the system optimum assignment model with fixed demand can be expressed as follows:

$$
\begin{aligned}
(\underline{\text{U1}})\quad \text{Min}\quad & F = \sum_{a\in E} x_a t_a\left(x_a\right) \\
s.t.\quad & x_a = \sum_{(s,t)\in OD} \sum_{p\in P^{s,t}} q_p^{s,t} \delta_{a,p}^{s,t}, \quad \forall a \in E, \\
& \sum_{p\in P^{s,t}} q_p^{s,t} = d^{s,t}, \quad \forall (s,t) \in \mathbb{OD}, \\
& q_p^{s,t} \geq 0, \quad \forall p \in P^{s,t}, \forall (s,t) \in \mathbb{OD}.
\end{aligned}
\tag{2.31}
$$

Obviously, from the objective function formulated in U1, it can be seen that system optimum assignment has a different goal from the user equilibrium traffic assignment, and it aims at minimizing the total system travel time by coordinating the drivers' behavior in choosing the routes. In this case, the system congestion is minimised as drivers are told which routes to use.

2.4 Uncertainty Analysis

The uncertainty emerging in the design, analysis, and operation of engineering systems play a significant role in affecting their performance. In this section, we introduce the principal sources of uncertainty arising in engineering systems, and review global sensitivity analysis method to measure the contribution of each random variable to system variability.

2.4.1 Uncertainty Quantification

While many sources of uncertainty may exist, they are generally categorized into two classes: aleatory (natural variability) and epistemic uncertainty (lack of knowledge) [42]. The aleatory uncertainty refers to the inherent physical variability and randomness in a quantity. For example, when you roll a dice, you get a random experimental outcome each time when you run the experiment, then this is an example of aleatory uncertainty. To characterize aleatory uncertainty, we usually represent the random quantity as a probability distribution. On the contrary, epistemic uncertainty denotes the uncertainty that is caused by lack of knowledge. For example, due to insufficient experimental data, we cannot have an exact estimate on model parameters. While the aleatory uncertainty is irreducible, the epistemic uncertainty can be reduced by gathering more data or by refining the mathematical models.

Since aleatory uncertainty is irreducible, researchers have devoted more efforts on the modeling and quantification of epistemic uncertainty in recent years. The epistemic uncertainty is typically divided into two subcategories: statistical uncertainty and model uncertainty [43, 44]. Due to the inadequacies in the available data (e.g., sparse data, ambiguity in data, erroneous data), statistical uncertainty might arise on the deterministic quantity or the distribution characteristics of random variables. Several theories have been developed to address this challenge, such as Dempster-Shafer evidence theory [45], fuzzy sets [46, 47], and possibility theory [48]. Model uncertainty arises due to the uncertainty in model parameters, solution approximation, model discretization error, and model form assumption, etc.

In this dissertation, we focus on the quantification of one of the model uncertainty – model parameter uncertainty. Specifically, model parameter uncertainty denotes the uncertainty in the model parameters due to natural variability or limited data or both. As mentioned in Chapter 2.2.2.3, the uncertainty of the parameters in the deep neural networks is characterized following a Bayesian manner. Instead of having a deterministic point estimate for each weight variable in neural networks, a prior distribution $p(\boldsymbol{\omega})$ is used to denote our belief on the values of weight variables in deep neural networks. Next, the prior distribution $p(\boldsymbol{\omega})$ is combined with a likelihood function $p(y|x,\omega)$ $(\omega \in \boldsymbol{\omega})$ that denotes the probability of generating the observed data to infer the posterior distribution $p(\boldsymbol{\omega}|\mathrm{X},\mathrm{Y})$ on model parameters. By doing this, for a new data point x^*, we have a predictive distribution $p(y^*|x^*,\mathrm{X},\mathrm{Y})$ and the posterior distribution characterizes the uncertainty in the model prediction as a distribution, from which we measure the uncertainty in model prediction explicitly.

2.4.2 Global Sensitivity Analysis

Global sensitivity analysis is used to quantify the influence of stochastic model inputs on the output variability of a physical or mathematical model [49]. Among the abundant literature on sensitivity measures, Sobol' indices based on variance decomposition have received much attention. Consider the model:

$$y = f(\boldsymbol{x}) \tag{2.32}$$

where y is the output, $\boldsymbol{x} = (x_1, \cdots, x_p)$ are p independent input variables, f is the model function. These contributions of the variance of a single model input or a group of model inputs to the output variance of f are quantified using the following sensitivity indices:

$$S_i = \frac{V_{x_i}\left(\mathbb{E}_{x_{-i}}(y|x_i)\right)}{V(y)},\ S_{ij} = \frac{V_{x_i x_j}\left(\mathbb{E}_{x_{-i}x_{-j}}\left(y|x_i x_j\right)\right)}{V(y)} - S_i - S_j \tag{2.33}$$

where x_{-i} denotes all of the variables in $\boldsymbol{x}$ except x_i. Here, S_i is the first order Sobol' index quantifying the sensitivity of output variance to an individual variable x_i by itself (individual effect). The second order index S_{ij} quantifies the sensitivity to the interaction between variable x_i and x_j. The larger an index value is, the greater is the importance of the corresponding variable or group of variables.

According to the theorem of variance decomposition, we have:

$$V\left(y\right)=\mathbb{E}_{x_i}\left(V_{x_{-i}}\left(y|x_i\right)\right)+V_{x_i}\left(\mathbb{E}_{x_{-i}}\left(y|x_i\right)\right) \tag{2.34}$$

which implies that:

$$S_i=1-\frac{\mathbb{E}_{x_i}\left(V_{x_{-i}}\left(y|x_i\right)\right)}{V\left(y\right)} \tag{2.35}$$

The methods used for global sensitivity analysis can be broadly classified into two groups: analytical methods and sampling-based approaches. In the analytical methods, the key idea is to approximate the original model $y=f(\boldsymbol{x})$ with cheap algebraic surrogate models, such as Polynomial Chaos Expansion (PCE) model [50], or Kriging models [51]. Once the surrogate model is trained, the Sobol' indices are calculated analytically. For example, Sudret [50] constructed surrogate models with generalized polynomial chaos expansions (PCE), and derived analytical solution that computes the Sobol indices as a post-processing of the PCE coefficients. Wang et al. [51] built Kriging-based surrogate model to estimate the variance of conditional expectation for each random variable. Likewise, Ciuffo et al. [52] developed a robust Kriging emulator based on the recursive use of the DACE tool [53], and demonstrated that the variance-based sensitivity indices estimated based on the Kriging emulator were approximately identical to those derived by the complete variance-based approach.

In sampling-based approaches, a double-loop Monte Carlo simulation is typically required to estimate Sobol' indices S_i. The inner loop $V_{x_{-i}}\left(y|x_i\right)$ in Eq. (2.35) requires fixing x_i and changing all the other variables x_{-i}. The outer loop $\mathbb{E}_{x_i}\left(\bullet\right)$ requires fixing x_i at different locations, and these selected locations are sampled from the distribution of x_i. In recent years, significant progress has been made along this direction: design of experiments [54] and spectral approaches have been used to reduce the number of samples needed for global sensitivity analysis [55, 56]. For example, Kucherenko et al. [57] developed quasi-Monte Carlo (QMC) method to speed up the convergence rate of sampling-based approaches on sensitivity estimates. Tissot and Prieur [58] utilized randomized orthogonal arrays to estimate first-order Sobol' indices. As a typical spectral approach, Fourier amplitude sensitivity test (FAST) [55] is used to perform sensitivity analysis. For more details, Ref. [59] provides a detailed review on sampling-based sensitivity analysis.

2.5 Big Data - Apache Spark

With the advent of big data era, a large volume of data is readily available, which poses tremendous computational challenges. Since data sizes have outpaced the computational capability of single machine, new systems need to be developed to scale out computations to multiple nodes. To fulfill the computational need of massive data analysis, Apache Spark has emerged as a unified engine for large-scale data analysis across a wide range of fields because it can handle a large body of processing workloads that need to be processed by separate engines before, including SQL, streaming, machine learning, and graph processing [60, 61, 62]. Different from the rigid map-then-reduce disk-based model, Apache Spark performs all the data transformation and actions in memory. By doing this, Apache Spark achieves 100 times faster speed than the classical open-source framework Hadoop which is designed for distributed storage and processing of very large data sets across clusters of computers on disk in performance.

Fig. 2.8 shows the architecture of the Apache Spark computing platform. As can be observed, Spark core is the foundation of the Apache Spark computing platform. With the resilient distributed dataset (RDD) application program interface (API), Apache Spark provides a unified interface for processing large-scale data in various formats, such as, JSON, XML, Hbase, MySQL, etc. Moreover, Spark supports a variety of advanced programming languages, like Scala, Java, Python to name a few. The extensive APIs support of data transformations and actions in these high-level programming languages is essential for data analysis and machine learning algorithms in the upper-level libraries. In addition to support large-scale data management, Spark core also offers major functionalities for in-

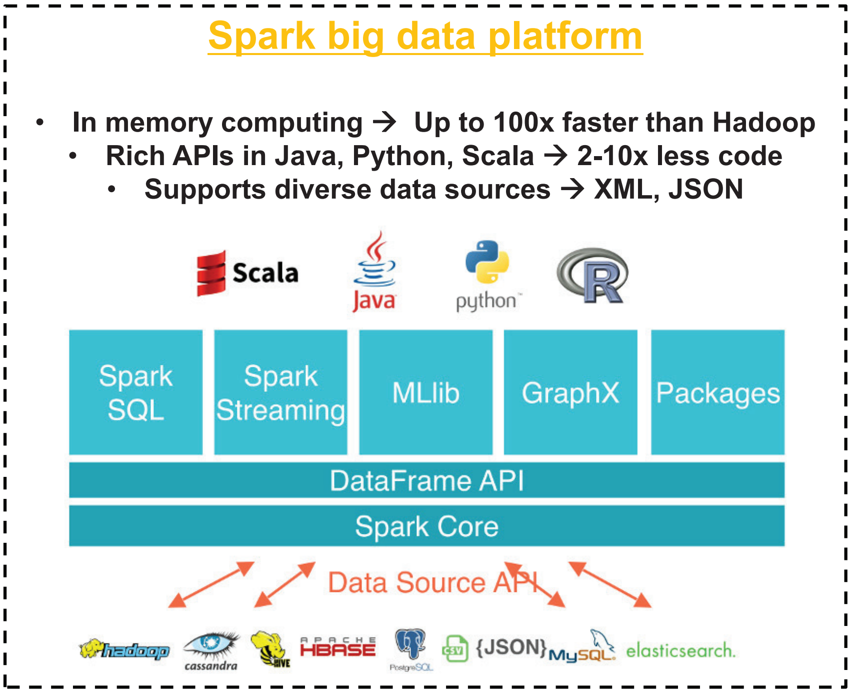

Figure 2.8: Architecture of Apache Spark [4]

memory cluster computing management, including job scheduling, memory management, data shuffling, and fault recovery. Such functionalities makes it easy to develop applications with Spark, where cluster memory, storage disk, and CPU will be utilized to their maximum level.

As shown in Fig. 2.8, above the DataFrame API is several upper-level libraries for performing various SQL queries [60], constructing machine learning algorithms [63], GraphX for graph processing [64], Spark Streaming for analyzing streaming data [62], as well as third-party packages for handling other tasks. The inclusion of these versatile functionalities reduces the workload significantly for developing large-scale data analytics and machine learning algorithms.

2.6 Summary

In this chapter, we review two commonly used machine learning algorithms: support vector machine and deep neural networks including deep feedforward neural network and recurrent neural network. In parallel, a Bayesian neural network is introduced as a generic framework to characterize model prediction uncertainty. Next, a quantitative metric has been defined to measure system resilience, and a bi-level optimization framework is formulated to model the interactions among multiple decision makers at different levels. The basic concepts of uncertainty quantification techniques are reviewed in Section 2.4, and global sensitivity analysis is introduced to measure the contribution of each random variable on the system-level variability. Finally, a big data engine Apache Spark is described to process large volume of data with scalable performance.

In Chapter 3, the big data engine Apache Spark is used to process massive raw data in an effective manner, then deep neural networks are trained to forecast the flight trajectories. In Chapter 4, the support vector machine and deep feedforward neural network are trained to predict the risk levels of abnormal event. In Chapters 5 and 6, support vector machine models are trained to measure operator performance and the effectiveness of rerouting strategy in handling off-nominal events, respectively. The bi-level program and system resilience concept are used in Chapters 7 and 8 to optimize transportation system performance. The quantification of model prediction uncertainty is illustrated for the flight trajectory prediction and aircraft rerouting problems in Chapters 3 and 5, respectively.

Chapter 3

Deep Learning Models for Early Warning of the Occurrences of Hazardous Events[1]

3.1 Introduction

Prior to the occurrence of hazardous events, an effective way to increase operators' situation awareness is to build a predictive model to forecast system behavior in advance and provide early warning to relevant stakeholders on the occurrence of potential hazardous events. In this chapter, we work along this direction to develop deep learning-based predictive models, and illustrate the approach in forecasting the behavior of flight trajectory in the air transportation system.

Air transportation has witnessed tremendous growth over the past decades. As forecast by the International Air Transport Association (IATA), the worldwide air travel demand will be nearly doubled over the next two decades compared to the 3.8 billion air travellers in 2016 [66]. One straightforward way to meet the need of the fast-growing air travel demand is to increase the aircraft density within the same airspace by reducing the allowed horizontal and vertical separation distance between two adjacent airplanes. By doing this, the same airspace could afford more number of airplanes than before, but of course this increases congestion in the airspace. Since safety is of the greatest importance in the domain of civil aviation, it is critical to investigate whether we are able to maintain the safety of the air transportation system at an acceptable level before implementing the strategy of separation distance reduction. To accomplish this objective, we need to develop accurate and robust predictive models to assess the flight safety variation over time, with the consideration of uncertainties arising from heterogeneous sources, e.g., Automatic Dependent Surveillance Broadcast (ADS-B) transponder precision, weather forecast uncertainty, and model predictive uncertainty. As part of the European Air Traffic Control Harmoni-

[1] An archival paper related to this chapter has been submitted for publication in the journal Decision Support Systems. For more details, see Ref. [65]

sation and Integration Programme (EATCHIP) managed by the European Organisation for the Safety of Air Navigation (EUROCONTROL), trajectory prediction is also highlighted as an essential operational requirement in the European Air Traffic Management (EATM) modernisation programme [67].

At the forefront of transformation to future National Airspace System (NAS), an important upgrade in the Next Generation Air Transportation System (NextGen) is the transition from radar-based operations to satellite-based navigation and surveillance. Together with Automatic Dependent Surveillance–Broadcast (ADS-B) system, satellite-based operations provide enhanced accuracy for aircraft navigation, surveillance, and position tracking [68, 69]. With the centralized NAS data sharing backbone – System Wide Information Management (SWIM), real-time, accurate flight, surveillance, weather, and aeronautical information is broadcast to related stakeholders on a regular basis. As mentioned in the Federal Aviation Administration (FAA) report on the future of the NAS [70], one significant need in NextGen is to develop predictable and efficient services across tower, terminal, and en route domains, which can then be used to assist controllers to handle off-nominal events or demand-capacity imbalances in a more strategic and efficient manner. Along this direction, flight trajectory prediction is an important constituent need, and accurate prediction of flight trajectory is vital to avoid accidents and reduce errors while ensuring safety and efficiency.

In brief, flight trajectory is the core information that is used by the system as a basis for distributing flight information to relevant airlines and air traffic control (ATC) units, facilitating the timely coordination between sectors and units, correlating flight data with tracks, monitoring the adherence of an aircraft with its assigned route, and detecting and resolving conflicts. In this respect, trajectory prediction algorithms are a crucial component of decision support tools (DST) for conflict detection and resolution, arrival metering, and other applications in air traffic management automation. Considering its paramount importance in assuring the safety of the air transportation system, a large number of studies have emphasized the development of models and algorithms for flight trajectory prediction (TP) over the past decades [71]. For example, Prats et al. [72] used an iterative quasi-Newton method to find depature flight trajectory for the purpose of minimizing the noise annoyance. de Leege et al. [73] trained a machine learning model to predict flight arrival time over points along the fixed arrival route based on generalized linear models (GLM), where aircraft state parameters (i.e., aircraft type, aircraft ground speed, aircraft altitude) and meteorological conditions (i.e., surface wind, altitude wind) were used as model inputs. Gong and McNally [74] developed a versatile methodology for automated trajectory prediction analysis such that the error measurements were sensitive to small trajectory prediction algorithm changes. Franco et al. [75] developed a probabilistic approach to predict aircraft flight time and fuel consumption during the cruise phase, in which they accounted for wind prediction uncertainty (both along-track winds and crosswinds) provided by Ensemble Weather Forecasting.

The above literature review reveals that trajectory prediction has gained growing interest of researchers with different backgrounds from a variety of domains. The current state-of-the-art approaches for trajectory prediction can be categorized into two major classes: physics-based models and data-driven models. In physics-based models, the aircraft is represented as a point mass, and Newton's law is utilized to associate the force/thrust generated by the aircraft engine with the inertial acceleration of its mass [76]. Typically, physics-based models are represented as a set of differential equations. Given the initial state of an aircraft (i.e., mass, thrust, position, velocity, bank angle) and meteorological conditions (i.e., wind velocity and direction), we predict the successive points of future aircraft trajectory by integrating the differential equations over a time interval. Take the Base of Aircraft Data (BADA) as an example, it is an aircraft performance model designed with a mass-varying, kinetic approach as developed and maintained by EUROCONTROL [77], which is used for trajectory computation, simulation and prediction in Air Traffic Management (ATM). However, physics-based models typically require explicit modeling of aircraft performance procedures and the real-time aircraft state (i.e., thrust, speed intent), while the models and most of model inputs might not be always readily available to the ground-based systems due to commercial sensitivity. Considering such a significant deficiency in physics-based models, researchers have shifted to data-driven models for predicting flight trajectory by learning from the historical flight trajectory data with machine learning and data mining techniques [78, 79]. In particular, with the advent of the big data era, a large amount of flight trajectory data becomes available, which makes the mining of complex trajectory patterns and feature interactions from the massive historical flight trajectory data possible. For example, Alligier and Gianazza [80] applied a machine learning approach to predict aircraft mass and speed intent on the climb phase with the ADS-B data coming from the OpenSky network. Di Ciccio et al. [81] developed an automated prediction model to detect flight diversions based on the flight track updates (i.e., position, velocity, altitude, and intended destination) such that the receiving parties could respond in a timely way to unexpected events that occurred to the flight. Among machine learning models, deep learning (or deep neural networks) has gained popularity due to its promising features in automatic feature extraction and end-to-end modeling [30, 31]. In quite a few domains, recurrent neural network has demonstrated outstanding performance in predicting the trajectory evolution [82, 83, 84]. For example, Moradi Kordmahalleh et al. [85] developed a sparse recurrent neural network with flexible topology to make trajectory prediction 6 and 12 hours ahead of four catastrophic Atlantic hurricanes. Alahi et al. [86] proposed a Long Short Term Memory (LSTM)-based recurrent neural network to jointly reason across multiple individuals to predict human trajectories in a scene, in which one LSTM was trained for each trajectory and the information was shared between the LSTMs through the introduction of a new social pooling layer. Wu et al. [87] incorporated the constraint of topological structure on trajectory modeling, and developed two recurrent neural network-based models to make trajectory prediction.

Model prediction uncertainty is an important consideration in machine learning [88, 89]. In particular, in the aviation sector, it is extremely important to account for trajectory prediction uncertainty because it is closely related to risk assessment in decision making activities pertaining to maintaining flight safety, e.g., separation distance. In this study, we characterize model prediction uncertainty from a Bayesian perspective. Bayesian probability theory provides a mathematically well-grounded approach to reason about model prediction uncertainty. However, given the large number of parameters to be optimized in deep learning, the implementation of Bayesian inference in deep learning is usually unachievable due to several reasons. First of all, if we represent each parameter in deep learning as a parametric distribution (e.g., normal distribution), then the number of parameters in the neural network will be doubled (i.e., mean and variance), which will further increase the computational burden in training the neural network. Secondly, the non-linearity and non conjugacy in neural networks make closed-form Bayesian inference impossible. Thirdly, given the large number of layers and parameters in deep learning, the conventional inference algorithms (i.e., MCMC, Metropolis–Hastings algorithm) are computationally intractable in the context of deep learning. Recently, Gal and Ghahramani [90, 34, 35] proposed that dropout can be interpreted as a variational approximation to the posterior of a Bayesian neural network. More importantly, the variational approximation to Bayesian inference with dropout does not sacrifice either computational complexity or model prediction accuracy. From then on, dropout implementation to approximate Bayesian inference has drawn tremendous attention with applications to forecasting the number of trips at Uber [91, 92], camera relocalization [93].

In this study, we train two separate Bayesian neural networks to make predictions on flight trajectory behavior. With the massive flight and track data in Flight Information Exchange Model (FIXM) and custom XML format streamed from Federal Aviation Administration (FAA) System Wide Information Management (SWIM), a robust distributed computing platform – Apache Spark – is leveraged to parse the flight data from SWIM flight data publication service (SFDPS) [94, 95], from which the data pertaining to actual flight trajectory, target flight trajectory, aircraft states (e.g., velocity, altitude, and position), as well as historical flight trajectory is extracted. Next, we build two Bayesian neural network models: in the first model, a feed-forward Bayesian neural network (DNN) is trained for one-step-ahead prediction on the deviation between actual trajectory and target flight trajectory. In the second model, a long short-term memory (LSTM) recurrent neural network (RNN) is trained with historical flight trajectory data to make long-term predictions on the future state of an ongoing flight. Afterwards, the two models are blended through a discrepancy term to make accurate trajectory prediction for ongoing flights. A separation distance-based safety indicator is developed to measure flight safety in the air transportation system. The major contributions we have made in this chapter are multifold.

1. We develop an efficient program based on a high performance computing platform – Apache Spark – to parse the raw SFDPS data in FIXM format, which lays a firm foundation for the development of subsequent Bayesian deep learning models.

2. Two individual Bayesian neural networks are trained to make flight trajectory prediction from different angles. In the first model, a feed-forward deep neural network is trained to make single-step predictions on the deviation between actual flight trajectory and target flight trajectory. In the second model, a LSTM recurrent neural network is trained to make longer-term prediction of the future states (i.e., latitude, longitude, altitude, velocity) of an ongoing flight.

3. The two Bayesian neural networks are integrated together for making accurate long-term predictions for ongoing flights. By doing this, we leverage the advantages of both models: the high prediction accuracy of the DNN and long-term prediction capability of the LSTM RNN.

4. In both models, model prediction uncertainty is accounted using the dropout strategy, and propagated through the integrated models with Monte Carlo samples.

5. A probabilistic safety indicator is used to measure the horizontal and vertical separation distance between two flights.

3.2 SWIM SFDPS Data Overview

SWIM is a National Airspace System (NAS)-wide information system that supports Next Generation Air Transportation System (NextGen) goals. Acting as a digital data-sharing backbone, SWIM enables increased common situational awareness and improved NAS agility to deliver the right information to the right people at the right time [96]. This information-sharing platform offers a single point of access for aviation data ranging from flight data to weather information. Users with granted credentials from FAA have access to the SWIM database via subscription to particular channels (i.e., SWIM Terminal Data Distribution System – STDDS, Time Based Flow Management – TBFM, Traffic Flow Management System – TFMS, SWIM Flight Data Publication Service – SFDPS, Wx, and others). Over the past one year, we have focused on analyzing flight trajectory data by subscribing to the SWIM flight data publication service (SFDPS) stream. In brief, SFDPS provides real-time en route flight data via batched track messages and custom FIXM formats to NAS consumers.

Fig. 3.1 shows a specific SFDPS tracking message for a flight operated by the JetBlue airline that departs from the Logan International Airport (code: KBOS) and arrives at the Baltimore–Washington International Airport (code: KBWI) on October 16 in 2018 from SWIM. As can be observed, all the en-route flight tracking information is stored in the International Civil Aviation Organization (ICAO) Flight Information Exchange Model (FIXM) format. In each tracking message, there are five major types of information: flight origin and destination, timestamp, en route flight information (i.e., flight speed and velocity, altitude, position, target altitude and position), flight ID and supplemental data. In SFDPS, flight tracking information are broken out by flight with just one track update per flight in one message. The flight tracking messages are updated on a regular basis of 12 seconds

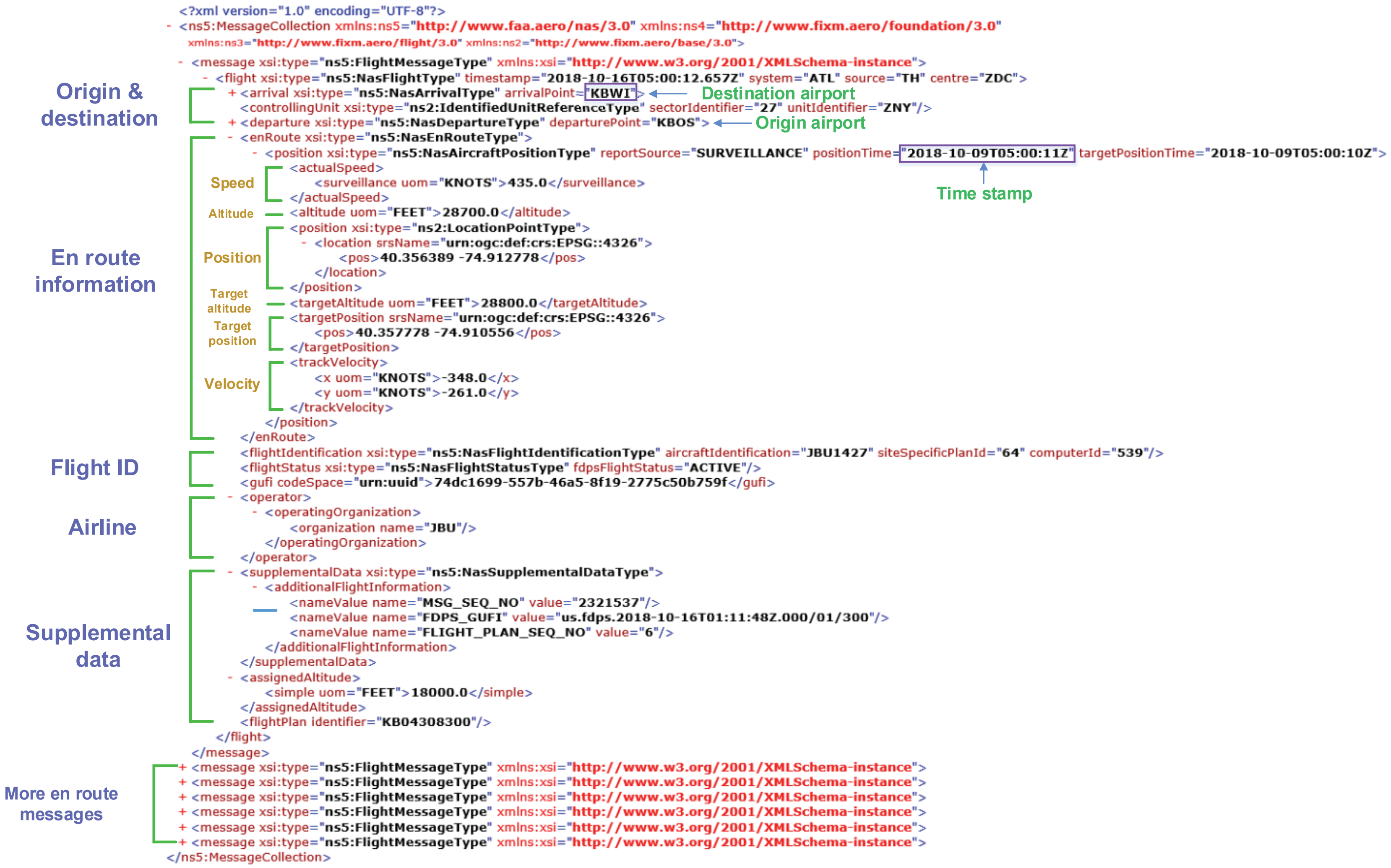

```
  <?xml version="1.0" encoding="UTF-8"?>
- <ns5:MessageCollection xmlns:ns5="http://www.faa.aero/nas/3.0" xmlns:ns4="http://www.fixm.aero/foundation/3.0"
    xmlns:ns3="http://www.fixm.aero/flight/3.0" xmlns:ns2="http://www.fixm.aero/base/3.0">
  - <message xsi:type="ns5:FlightMessageType" xmlns:xsi="http://www.w3.org/2001/XMLSchema-instance">
    - <flight xsi:type="ns5:NasFlightType" timestamp="2018-10-16T05:00:12.657Z" system="ATL" source="TH" centre="ZDC">
      + <arrival xsi:type="ns5:NasArrivalType" arrivalPoint="KBWI">
        <controllingUnit xsi:type="ns2:IdentifiedUnitReferenceType" sectorIdentifier="27" unitIdentifier="ZNY"/>
      + <departure xsi:type="ns5:NasDepartureType" departurePoint="KBOS">
      - <enRoute xsi:type="ns5:NasEnRouteType">
        - <position xsi:type="ns5:NasAircraftPositionType" reportSource="SURVEILLANCE" positionTime="2018-10-09T05:00:11Z" targetPositionTime="2018-10-09T05:00:10Z">
            <actualSpeed>
              <surveillance uom="KNOTS">435.0</surveillance>
            </actualSpeed>
            <altitude uom="FEET">28700.0</altitude>
            <position xsi:type="ns2:LocationPointType">
            - <location srsName="urn:ogc:def:crs:EPSG::4326">
                <pos>40.356389 -74.912778</pos>
              </location>
            </position>
            <targetAltitude uom="FEET">28800.0</targetAltitude>
            <targetPosition srsName="urn:ogc:def:crs:EPSG::4326">
              <pos>40.357778 -74.910556</pos>
            </targetPosition>
            <trackVelocity>
              <x uom="KNOTS">-348.0</x>
              <y uom="KNOTS">-261.0</y>
            </trackVelocity>
          </position>
        </enRoute>
        <flightIdentification xsi:type="ns5:NasFlightIdentificationType" aircraftIdentification="JBU1427" siteSpecificPlanId="64" computerId="539"/>
        <flightStatus xsi:type="ns5:NasFlightStatusType" fdpsFlightStatus="ACTIVE"/>
        <gufi codeSpace="urn:uuid">74dc1699-557b-46a5-8f19-2775c50b759f</gufi>
      - <operator>
        - <operatingOrganization>
            <organization name="JBU"/>
          </operatingOrganization>
        </operator>
      - <supplementalData xsi:type="ns5:NasSupplementalDataType">
        - <additionalFlightInformation>
            <nameValue name="MSG_SEQ_NO" value="2321537"/>
            <nameValue name="FDPS_GUFI" value="us.fdps.2018-10-16T01:11:48Z.000/01/300"/>
            <nameValue name="FLIGHT_PLAN_SEQ_NO" value="6"/>
          </additionalFlightInformation>
        </supplementalData>
      - <assignedAltitude>
          <simple uom="FEET">18000.0</simple>
        </assignedAltitude>
        <flightPlan identifier="KB04308300"/>
      </flight>
    </message>
  + <message xsi:type="ns5:FlightMessageType" xmlns:xsi="http://www.w3.org/2001/XMLSchema-instance">
  + <message xsi:type="ns5:FlightMessageType" xmlns:xsi="http://www.w3.org/2001/XMLSchema-instance">
  + <message xsi:type="ns5:FlightMessageType" xmlns:xsi="http://www.w3.org/2001/XMLSchema-instance">
  + <message xsi:type="ns5:FlightMessageType" xmlns:xsi="http://www.w3.org/2001/XMLSchema-instance">
  + <message xsi:type="ns5:FlightMessageType" xmlns:xsi="http://www.w3.org/2001/XMLSchema-instance">
  + <message xsi:type="ns5:FlightMessageType" xmlns:xsi="http://www.w3.org/2001/XMLSchema-instance">
  </ns5:MessageCollection>
```

Figure 3.1: An illustration of the SFDPS en-route flight message

for an active flight while the flight is in an Air Route Traffic Control Center's (ARTCC) airspace. Since there are more than 20,000 commercial flights within the airspace of USA every day, we stream nearly 100 GB of SFDPS messages from SWIM per day. Given such big data, an efficient method is needed to parse the flight trajectory data from the massive FIXM files.

3.3 Proposed Method

In this section, a four-step approach is developed to train two individual Bayesian deep learning models from the massive historical flight trajectory data to support the assessment of flight safety. The overall framework of the proposed methodology is illustrated in Fig. 3.2. In the first step, we develop a scalable program with a unified distributed high-performance computing framework – Apache Spark – to process a large volume of raw flight tracking messages in FIXM format. After the information pertaining to flight trajectory is extracted from the raw data, two individual Bayesian deep learning models are trained to make predictions on the future state of ongoing flights from different perspectives. Next, the predictions from the two deep learning models are fused together to enhance the model prediction accuracy as well as to reduce the model prediction uncertainty. Finally, the fused models are then utilized to make trajectory predictions on multiple flights and evaluate the safety of two given flights, where separation distance is used as a quantitative safety metric.

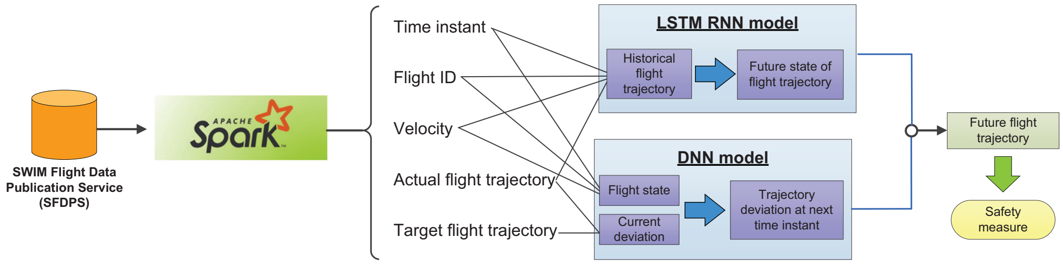

Figure 3.2: Flowchart of proposed methodology for flight trajectory prediction

3.3.1 SFDPS Message Processing

As mentioned before, SFDPS publishes a wide variety of en route messages, such as en route flight data messages, en route airspace data messages, en route operational data messages, and en route general messages. Among all the published messages, we are most interested in the information relevant to flight trajectory including flight ID, origin and destination, and en-route position surveillance data (e.g., latitude, longitude, and altitude). Within the US airspace, there are more than 20,000 commercial flights every day. In terms of data volume, more than 100 GB of SFDPS messages is broadcast by SWIM and streamed to the local storage disk. As shown in Fig. 3.1, all the significant content is batched in FIXM format. To meet the intensive computational requirements of massive data analysis, we leverage a general-purpose scalable high-performance computing framework – Apache Spark – to parse the large volume of SFDPS messages in FIXM format. As a unified engine for big data analytics, Apache Spark combines a core engine for distributed computing with an advanced programming model for in-memory data processing through a data sharing schema – resilient distributed dataset (RDD). The Spark framework's in memory programming model results in up-to 100 times faster than Hadoop in big data analytics [97]. Besides, Apache Spark offers rich APIs in high-level languages (e.g., Python, Java, Scala) for performing complex data operations, such as data transformation, SQL query [4]. Last but not the least, Apache Spark supports operating on a rich set of data sources through the DataFrame interface, such as JSON, CSV, database connection, and XML etc.

In this study, we utilize the spark-xml library for parsing and querying FIXM data within Apache Spark [98]. After the raw FIXM data is parsed, we designate the row tag as 'flight', then spark-xml library transforms the content within this row tag into a row consisting of all the attribute names and their values. Next, we filter out flight tracking information that contains track updates for individual flights from all the SFDPS messages by specifying the source of tracking messages as 'TH' (see Fig. 3.1), then we group the trajectory data by flight date and flight ID, and rank them according to the position time (see Fig. 3.1 for more details). The sorted flight trajectory data is then outputted as a single CSV file per flight by Apache Spark in parallel. By adopting Apache Spark to process the raw SFDPS messages, the required time of performing all the aforementioned operations on SFDPS messages spanning a time duration of 24 hours decreases dramatically from nearly one week to approximately 10 hours on a Windows 10 desktop with an Inter Core i7-4790 CPU (3.60 GHz) and 16 GB memory. Table 3.1 shows a small portion of processed tracking information for an American Airline flight with Call Sign (or flight ID) AAL10 that departed from Los Angeles International Airport (ICAO code: KLAX) and destined at John F. Kennedy International Airport (ICAO code: KJFK) on January 11, 2019.

Significant flight trajectory information, such as timestamp, flight position, and flight state derived from the SFDPS messages, is illustrated in Table 3.1. To be more specific, the second column reveals the airline that operates this flight. The subsequent two columns show the departure and arrival airports of this flight as represented by four-letter ICAO airport codes, respectively. The next two columns (position time and target position time represent the time instant associated with the current position of an active flight and the time associated with the raw radar return, respectively. As can be seen from the column position time, flight position comprised of latitude, longitude, and altitude is periodically updated approximately at intervals of 12 seconds, except the shaded cells. The next three columns show the aircraft state at corresponding position time. Specifically, the column actual speed denotes the ground speed of the flight in the unit of knots per hour. The next two columns X and Y velocity describe the flight speed along the X and Y components tracked by radar surveillance. Similarly, the target altitude represents the assigned altitude or flight level in feet. For example, an assigned altitude of 1700 means that the aircraft is to fly at 1,700 feet. The preceding column actual altitude denotes the actual flight level at each time instant. The actual position indicates the actual location of an active flight in latitude/longitude format as reported by surveillance, and target position shows the target

ID	Airline	Arrival Point	Departure Point	Position Time	Target Position Time	Actual Speed	X velocity	Y velocity	Actual Altitude	Target Altitude	Actual Position	Target Position
1	AAL	KJFK	KLAX	2019-01-11T23:16:26.000-06:00	2019-01-12T05:16:26Z	210	-201	-61	2100	2100	33.930556 -118.457778	33.930556 -118.457778
2	AAL	KJFK	KLAX	2019-01-11T23:16:38.000-06:00	2019-01-12T05:16:38Z	210	-190	-89	2300	2300	33.924722 -118.470278	33.924722 -118.470000
3	AAL	KJFK	KLAX	2019-01-11T23:17:02.000-06:00	2019-01-12T05:17:02Z	218	-171	-135	2600	2600	33.908333 -118.492778	33.908333 -118.493333
4	AAL	KJFK	KLAX	2019-01-11T23:17:14.000-06:00	2019-01-12T05:17:14Z	238	-145	-188	3000	3000	33.896667 -118.503611	33.897778 -118.504167
5	AAL	KJFK	KLAX	2019-01-11T23:17:25.000-06:00	2019-01-12T05:17:25Z	248	-89	-232	3600	3600	33.883889 -118.508611	33.884722 -118.509167
6	AAL	KJFK	KLAX	2019-01-11T23:17:37.000-06:00	2019-01-12T05:17:37Z	246	-20	-245	4200	4200	33.870278 -118.509167	33.871389 -118.510278
7	AAL	KJFK	KLAX	2019-01-11T23:17:49.000-06:00	2019-01-12T05:17:49Z	242	-12	-242	4800	4800	33.857222 -118.510000	33.857500 -118.510556
8	AAL	KJFK	KLAX	2019-01-11T23:18:01.000-06:00	2019-01-12T05:18:01Z	242	-12	-241	5400	5400	33.843889 -118.510833	33.844722 -118.512222
9	AAL	KJFK	KLAX	2019-01-11T23:18:13.000-06:00	2019-01-12T05:18:13Z	242	-12	-241	5800	5800	33.830556 -118.511667	33.831389 -118.513333
10	AAL	KJFK	KLAX	2019-01-11T23:18:25.000-06:00	2019-01-12T05:18:25Z	242	-13	-241	6300	6300	33.816667 -118.512778	33.817222 -118.513611
11	AAL	KJFK	KLAX	2019-01-11T23:18:37.000-06:00	2019-01-12T05:18:37Z	243	-13	-242	6800	6800	33.803056 -118.513611	33.803333 -118.515000
12	AAL	KJFK	KLAX	...	...	...	...	...	...	...	...	...
13	AAL	KJFK	KLAX	2019-01-11T02:30:22.000-06:00	2019-01-11T08:30:22Z	528	528	16	35000	35000	37.926667 -87.807222	37.928056 -87.808056
14	AAL	KJFK	KLAX	2019-01-11T02:30:22.000-06:00	2019-01-11T08:30:22Z	532	532	15	35000	35000	37.928333 -87.806667	37.928889 -87.807222
15	AAL	KJFK	KLAX	2019-01-11T02:30:34.000-06:00	2019-01-11T08:30:34Z	528	528	16	35000	35000	37.927778 -87.770000	37.929444 -87.770556
16	AAL	KJFK	KLAX	2019-01-11T02:30:34.000-06:00	2019-01-11T08:30:34Z	532	532	15	35000	35000	37.929444 -87.769722	37.930278 -87.769722
17	AAL	KJFK	KLAX	2019-01-11T02:30:46.000-06:00	2019-01-11T08:30:46Z	528	528	17	35000	35000	37.928611 -87.733056	37.928889 -87.734167
18	AAL	KJFK	KLAX	2019-01-11T02:30:46.000-06:00	2019-01-11T08:30:46Z	532	531	15	35000	35000	37.930000 -87.732778	37.929722 -87.733333
19	AAL	KJFK	KLAX	...	...	...	...	...	...	...	...	...
20	AAL	KJFK	KLAX	2019-01-11T04:08:47.000-06:00	2019-01-11T10:08:47Z	126	-108	64	1300	1300	40.613611 -73.695278	40.613056 -73.695000
21	AAL	KJFK	KLAX	2019-01-11T04:08:54.000-06:00	2019-01-11T10:08:54Z	139	-116	76	1300	1300	40.617500 -73.700556	40.616667 -73.700278
22	AAL	KJFK	KLAX	2019-01-11T04:08:57.000-06:00	2019-01-11T10:08:57Z	126	-109	63	1200	1200	40.616667 -73.701389	40.617222 -73.700833
23	AAL	KJFK	KLAX	2019-01-11T04:09:11.000-06:00	2019-01-11T10:09:11Z	126	-109	63	1100	1100	40.620556 -73.710000	40.621111 -73.708056
24	AAL	KJFK	KLAX	2019-01-11T04:09:24.000-06:00	2019-01-11T10:09:24Z	125	-108	62	900	900	40.623889 -73.718611	40.623333 -73.718056
25	AAL	KJFK	KLAX	2019-01-11T04:09:34.000-06:00	2019-01-11T10:09:34Z	122	-105	62	800	800	40.626944 -73.723889	40.627500 -73.720833
26	AAL	KJFK	KLAX	2019-01-11T04:09:48.000-06:00	2019-01-11T10:09:48Z	122	-104	63	600	600	40.631111 -73.732222	40.631667 -73.729722
27	AAL	KJFK	KLAX	2019-01-11T04:10:02.000-06:00	2019-01-11T10:10:02Z	122	-104	64	500	500	40.634722 -73.740833	40.634167 -73.741111
28	AAL	KJFK	KLAX	2019-01-11T04:10:11.000-06:00	2019-01-11T10:10:11Z	121	-103	63	400	400	40.636944 -73.746389	40.636389 -73.747222
29	AAL	KJFK	KLAX	2019-01-11T04:10:15.000-06:00	2019-01-11T10:10:15Z	121	-103	63	300	300	40.638333 -73.749167	40.638611 -73.748611
30	AAL	KJFK	KLAX	2019-01-11T04:10:31.000-06:00	2019-01-11T10:10:15Z	121	-103	63	300	300	40.643056 -73.758889	40.638611 -73.748611

Table 3.1: Sample flight trajectory parsed from SFDPS messages on January 11st 2019

position of the flight at the given time instant.

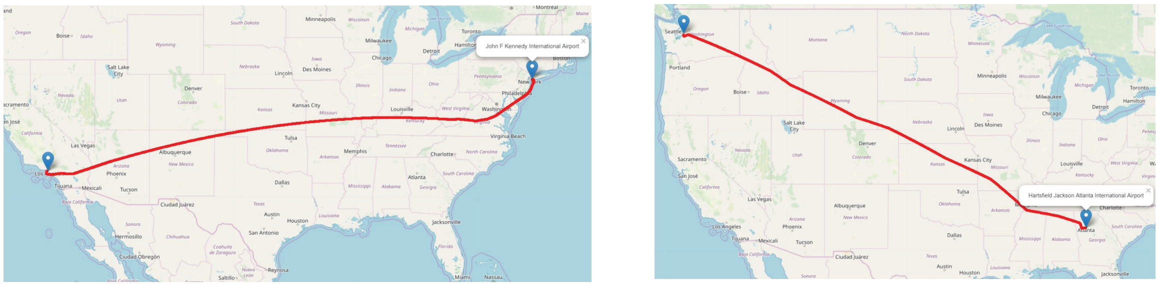

(a) American Airlines AAL10: Los Angeles International Airport (LAX) to John F. Kennedy International Airport (JFK)

(b) Delta Airlines DAL2775: Seattle Tacoma International Airport (SEA) to Hartsfield Jackson Atlanta International Airport (ATL)

Figure 3.3: Visualization of two sample flight trajectories: AAL10 and DAL2775 on January 11, 2019

As implied by the variation of actual flight altitude shown in Table 3.1, we observe that taking off and landing are also included in the derived flight trajectory. With respect to the flight speed, it gradually increases from 210 knots per hour to the maximum value 532 knots per hour during the cruise phase. During the landing phase, the actual flight speed significantly reduces in accordance with the decrease of altitude until touchdown. With the derived flight trajectory, we project the trajectory data on the map to check whether any large segment of flight trajectory is missing. Fig. 3.3 shows the visualization of the full trajectory of two sample flights, namely American Airline AAL10 from Los Angeles International Airport (LAX) to John F. Kennedy International Airport (JFK); and Delta Airline DAL2775 from Seattle Tacoma International Airport (SEA) to Hartsfield Jackson Atlanta International Airport (ATL) both on January 11st 2019. The map visualization helps to verify the integrity of each derived flight trajectory quickly. If any explicit gap exists in the visualized flight trajectory, we are able to locate the missing flight trajectory segments in an efficient manner.

3.3.2 Model Construction

3.3.2.1 Data Processing

Prior to model construction, flight trajectory data needs to be preprocessed such that all the reported flight positions have equal time intervals. In this regard, two specific issues need to be addressed. First of all, since an aircraft can be tracked by several radars simultaneously, the same flight position and state might be reported multiple times, as shown by the green shaded cells in Table 3.1. Besides, the time interval between two consecutively reported flight positions might be much less than the regular position tracking frequency of 12 seconds. For example, the duration between two timestamps shown in the 20th and 21st row is only 7 seconds, as shown by the blue shaded cells in Table 3.1. The rows with duplicated records can be dropped in a straightforward manner by retaining only one unique record in the dataset. While for the case of excessive records as indicated in the blue shaded cells in Table 3.1, we develop a method to maintain the correct records subject to the 12 seconds time interval constraint. As shown in Fig. 3.4, suppose the timestamp of the current record is '2019-01-11T**04:08:47**.000-06:00', then the expected timestamp of the next record should be '2019-01-11T**04:08:59**.000-06:00'. Next, we define a search region comprised of a fixed number of four rows following the current record, and identify the record that has the minimum distance away from the expected timestamp of next record within the search region, which is '2019-01-11T04:08:58.000-06:00' in this case. All the records between the current record and the identified next record are then eliminated accordingly. Afterwards, we treat the identified next record as the current record and start searching for the new next record. The same procedures are repeated until all the excessive records are eliminated from the dataset.

On the other hand, the red shaded cells in Table 3.1 indicate that the time interval between the two records is 24 seconds (other values like 36 seconds, 48 seconds etc. are also observed in the original dataset), which implies that one (or multiple) record(s) is(are) miss-

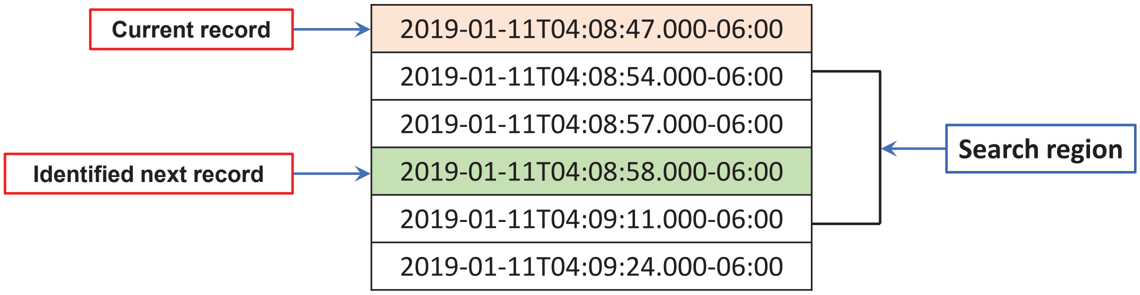
Current record
Identified next record
2019-01-11T04:08:47.000-06:00
2019-01-11T04:08:54.000-06:00
2019-01-11T04:08:57.000-06:00
2019-01-11T04:08:58.000-06:00
2019-01-11T04:09:11.000-06:00
2019-01-11T04:09:24.000-06:00
Search region

Figure 3.4: Illustration of developed method for filtering out excessive records

ing. To address this issue, we first determine how many records are missing in-between, then linear interpolation is used to make up the missing records for the sake of simplicity. With the aforementioned operations, we thereby guarantee that all the flight positions in the dataset have equal time intervals. The equal time intervals play a significant role for the subsequent model construction.

3.3.2.2 Trajectory Deviation Prediction by Feed-forward Deep Neural Network

Considering the information shown in Table 3.1, flight trajectory prediction can be carried out from several different perspectives. Since flight plan is already given, one straightforward approach is to forecast the deviation between the actual flight trajectory and the filed target trajectory over time. The critical question to be addressed here is that given the deviation from the filed flight plan at present and the current airplane state, we aim to predict the trajectory deviation in the next time instant. To accomplish this goal, we build a feed-forward neural network consisting of three hidden layers with each hidden layer having 32, 64, and 32 hidden units, respectively, and use rectified linear units (ReLU) as the activation functions across all the layers. Fig. 3.5 shows the distribution of trajectory deviation of a sample flight with flight ID AAL598. As can be observed, flight trajectory deviation primarily occurs along the dimension of latitude and longitude, while the altitude of the actual trajectory complies with the target altitude across the entire course of the flight. Such phenomenon is observed in almost all of the commercial flights we analyzed.

From this standpoint, since flight altitude almost never deviates from the target altitude, we only need to build two individual models to predict the trajectory deviation along the latitude and longitude.

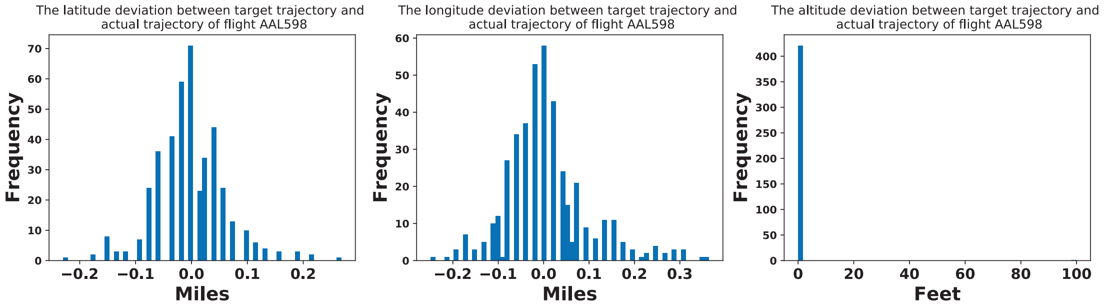

Figure 3.5: Trajectory deviation of a sample flight with call sign AAL598 departing from New York LaGuardia Airport (LGA) and landing at Charlotte Douglas International Airport (CLT)

In the deep feed-forward neural network for flight trajectory deviation prediction, we regard the latest flight state and trajectory deviation at the current time instant t as model inputs, and the model output is the deviation from the target trajectory in the next time instant $t+1$. Fig. 3.6 illustrates the framework of the constructed deep feed-forward neural network. As can be seen, there are five input variables, namely trajectory deviation at the current time instant t, aircraft velocity along X and Y, current altitude and aircraft speed. Our goal is to make trajectory deviation prediction at the next time instant $t+1$. As mentioned earlier, one important consideration is to account for model prediction uncertainty (e.g., parameter uncertainty and model structure uncertainty) given so many DNN parameters to be estimated in the model. To do this, we perform MC dropout with 10% of units randomly dropped before each hidden layer to approximate Bayesian posterior distribution, from which we obtain a predictive distribution for the latitude and longitude deviation for the next time instant.

By doing this, we forecast the trajectory deviation along latitude and longitude for the next time instant $t+1$. The trajectory deviation prediction enables us to estimate the future position of an ongoing flight, and to offer early warning to ground controllers if any

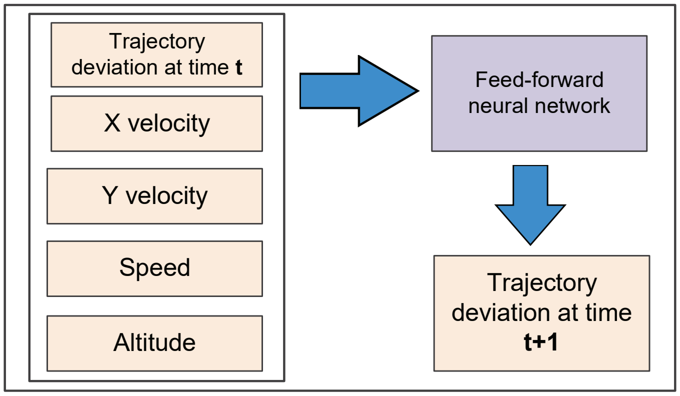
Trajectory deviation at time **t**
X velocity
Y velocity
Speed
Altitude
Feed-forward neural network
Trajectory deviation at time **t+1**

Figure 3.6: Framework of deep feed-forward neural network

anomalous trajectory deviation is forecast to happen in the future.

3.3.2.3 Flight State Prediction by Recurrent Neural Network

Since massive historical flight trajectories are readily available, another approach to trajectory prediction problem is to mine complex flight patterns from the historical data; then the patterns learned from the historical data can be further utilized to predict the trend of an ongoing flight with the same origin and destination. In this regard, recurrent neural networks (RNNs), as a powerful learning model, have demonstrated remarkable effectiveness in various domains, such as image recognition [99], speech recognition [100, 101], machine translation [102], and others [103, 104, 105].

In this study, we work along this direction and train two individual LSTM models (based on the categories mentioned below) to make prediction on the full state of flight trajectory. The detailed architecture of the LSTM model is shown in Fig. 3.7. As can be seen, two hidden LSTM layers are stacked together, in which each hidden layer consists of 20 LSTM blocks and each LSTM block has 50 dimensions. Every time, 20 time steps of past flight trajectory $(\boldsymbol{x}_{t-19}, \cdots, \boldsymbol{x}_t)$ comprised of latitude, longitude, altitude, flight velocity along X and Y, and speed, are fed into the constructed LSTM model, and the output of the last LSTM block at the top hidden layer is fed into a conventional feed-forward densely connected layer, which maps the intermediate LSTM output to the flight trajectory in the subsequent five time instants $(\hat{\boldsymbol{x}}_{t+1}, \cdots, \hat{\boldsymbol{x}}_{t+5})$. The predicted flight trajectory $(\hat{\boldsymbol{x}}_{t+1}, \cdots, \hat{\boldsymbol{x}}_{t+5})$ can be further used as new inputs to the LSTM model, then the trained model is used to make prediction on the future flight trajectory again $(\hat{\boldsymbol{x}}_{t+6}, \cdots, \hat{\boldsymbol{x}}_{t+10})$ as shown in the blue dashed boxes in Fig. 3.7.

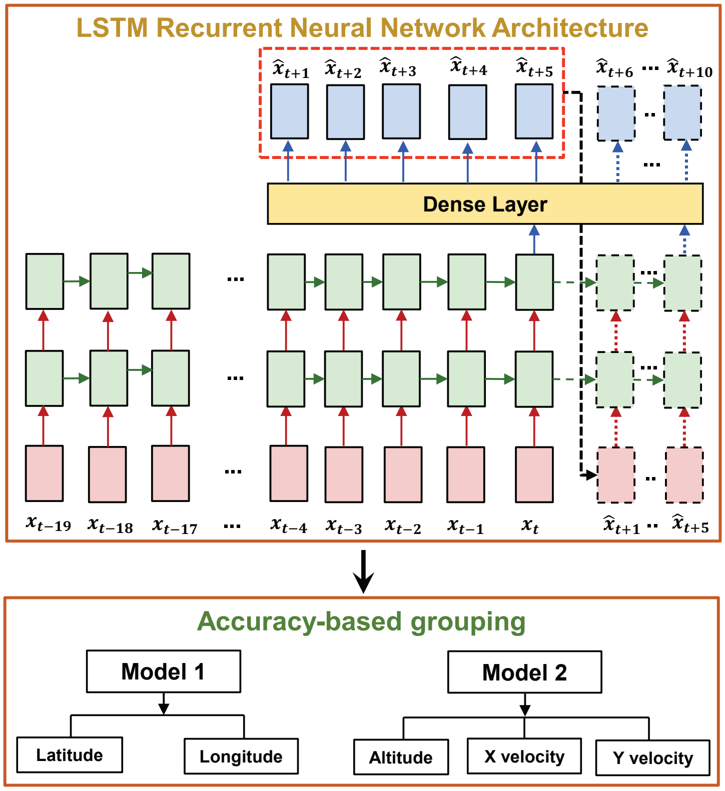
LSTM Recurrent Neural Network Architecture
$\hat{x}_{t+1}$ $\hat{x}_{t+2}$ $\hat{x}_{t+3}$ $\hat{x}_{t+4}$ $\hat{x}_{t+5}$
$\hat{x}_{t+6}$ ··· $\hat{x}_{t+10}$
Dense Layer
x_{t-19} x_{t-18} x_{t-17} ··· x_{t-4} x_{t-3} x_{t-2} x_{t-1} x_t $\hat{x}_{t+1}$ ·· $\hat{x}_{t+5}$
Accuracy-based grouping
Model 1
Model 2
Latitude
Longitude
Altitude
X velocity
Y velocity

Figure 3.7: Structure of proposed long short-term memory (LSTM) recurrent neural network

In the constructed LSTM model, since we make predictions on the full state of the flight trajectory, the number of the input features is the same as that of output variables. Since there are six variables in total, we group them into two categories: latitude and longitude, altitude and flight velocity along X and Y (since flight speed can be calculated from flight velocity along X and Y easily, thus it is ignored here). If we only build one model in which all the variables are used as outputs, then the model will be driven by the variable with the largest loss value in each iteration. Under this circumstance, the weights of the LSTM model will be optimized along the direction that minimizes the loss function of the variable with the largest loss value. Since the five response variables share many common parameters in the first two LSTM layers, the dominance of the variable with the largest loss value results in the ignorance of the optimization of the weights for the remaining variables. Therefore, we categorize the five response variables with similar loss values in the same group, and train two individual LSTM models to address the deficiency in building one single model. By grouping the variables with similar loss values together, we also maintain the different prediction precision demand specific to each variable. In particular, since a small prediction error in latitude and longitude is a large value in terms of distance in reality, there is an important need for high prediction precision for both variables. If the other variables (e.g., velocity) dominate the loss function, then the prediction precision for latitude and longitude will be compromised significantly.

To obtain the Bayesian posterior distribution for model prediction, we perform Monte Carlo dropout for both inputs, outputs, and recurrent layers with a dropout probability of 0.05 following the guidance in Gal and Ghahramani [35]. The MC dropout enables us to have an approximated Bayesian posterior distribution on the future state of flight trajectory of interest, in which the uncertainty on each aspect of flight trajectory is estimated properly.

3.3.3 Model Integration

As introduced before, two individual models are trained to make predictions on flight trajectory from different views. Specifically, the feed-forward deep neural network (DNN) makes a one-step-ahead prediction with high accuracy on the deviation of the actual flight trajectory away from the filed flight plan, while the LSTM model forecasts the full state of flight trajectory for a longer term (e.g., five steps or longer) but has a relatively low accuracy in comparison with the DNN model. Integration of the two models will have both high prediction accuracy and longer-term prediction capability.

Suppose we have observations on the actual flight trajectory up to the time instant t, DNN predicts flight trajectory deviation at the next time instant $t+1$ based on the degree of trajectory deviation at the previous time instant t. Given the predicted deviation at time instant $t+1$, the predicted flight position at time $t+1$ by DNN is readily available by combining the predicted deviation and the filed flight plan. Suppose the LSTM model utilizes the past 20 observed trajectory data to predict the state of flight along the subsequent five time instants $t+1,\cdots,t+5$. Let DNN's trajectory deviation prediction at time instant $t+1$ be denoted by $\boldsymbol{\tau}_{t+1}$; then we have:

$$E\left(\hat{\boldsymbol{y}}_{t+1}\right)=\boldsymbol{q}_{t+1}+E\left(\boldsymbol{\tau}_{t+1}\right) \tag{3.1}$$

where $\boldsymbol{q}_{t+1}$ denotes the planed flight position including latitude, longitude, and altitude at the time instant $t+1$, $E\left(\boldsymbol{\tau}_{t+1}\right)$ is the mean value of DNN's trajectory deviation prediction at time instant $t+1$, and $E\left(\hat{\boldsymbol{y}}_{t+1}\right)$ represents the mean value of DNN's prediction on the flight trajectory at time instant $t+1$.

Considering the two response variables (latitude and longitude) shared by the two models, one straightforward way to integrate the two models is to correct the low-accuracy model with the results from high-accuracy model through a discrepancy term as calculated following Eq. (3.2).

$$\boldsymbol{\Delta}_{t+1}=E\left(\hat{\boldsymbol{y}}_{t+1}\right)-E\left(\hat{\boldsymbol{x}}_{t+1}^{c}\right) \tag{3.2}$$

where $E\left(\hat{\boldsymbol{x}}_{t+1}^{c}\right)$ denotes the mean value of LSTM model's prediction on the two common quantities (latitude and longitude) at the time instant $t+1$, and $\boldsymbol{\Delta}_{t+1}$ represents the discrepancy between DNN's mean predictions and LSTM model's mean predictions.

Once the discrepancy between the two model predictions in latitude and longitude prediction at time $t+1$ is estimated, then the LSTM model's prediction on the two quantities for the subsequent time instants $t+1,\cdots,t+5$ can be updated accordingly by adding the discrepancy term to its predictions as shown in Eq. (3.3).

$$\overline{\boldsymbol{x}}_{i}^{c}=\hat{\boldsymbol{x}}_{i}^{c}+\boldsymbol{\Delta}_{t+1},\ \forall i\in[t+1,\cdots,t+5] \tag{3.3}$$

where $\overline{\boldsymbol{x}}_i^c$ denotes the updated LSTM model prediction on latitude, longitude, and altitude for the subsequent time instants $t+1,\cdots,t+5$.

Thus, by combining DNN prediction $\hat{\boldsymbol{y}}_{t+1}$ with the LSTM model prediction $\hat{\boldsymbol{x}}_{t+1}$, both high accuracy and longer-term prediction capability are achieved in the integrated model.

3.3.4 Safety Measure

The objective of trajectory prediction is to assess the en-route flight safety of the NAS. Separation distance, as a widely used safety metric during the en-route phase, is used as a quantitative metric in this study to measure the system safety. In the en-route airspace, the minimum horizontal separation distance is 5 nautical miles, while no aircraft should come vertically closer than 300 metres at an altitude of 29,000 feet [76]. With the probabilistic predictions on the trajectory of any two given flights, the safety metric used in this study is mathematically formulated in the following equation.

$$I\left[p\left(\boldsymbol{d}_i^h\left(\overline{\boldsymbol{x}}_i^c(A),\overline{\boldsymbol{x}}_i^c(B)\right)<\delta^h\right)>\lambda \textbf{ and } p\left(\boldsymbol{d}_i^v\left(\overline{\boldsymbol{x}}_i^c(A),\overline{\boldsymbol{x}}_i^c(B)\right)<\delta^v\right)>\lambda\right],\ \forall i\in[t+1,\cdots,t+5] \tag{3.4}$$

where $\overline{\boldsymbol{x}}_i^c(A)$ and $\overline{\boldsymbol{x}}_i^c(B)$ denote the integrated model's predictions on the trajectories of flight A and B, respectively; $\boldsymbol{d}_i^h\left(\overline{\boldsymbol{x}}_i^c(A),\overline{\boldsymbol{x}}_i^c(B)\right)$ and $\boldsymbol{d}_i^v\left(\overline{\boldsymbol{x}}_i^c(A),\overline{\boldsymbol{x}}_i^c(B)\right)$ represent the horizontal and vertical separation distance between the two flights A and B as forecast by the integrated model. Since the trajectory prediction of the integrated model is a probabilistic quantity, a probabilistic metric $p\left(\boldsymbol{d}_i^h\left(\overline{\boldsymbol{x}}_i^c(A),\overline{\boldsymbol{x}}_i^c(B)\right)<\delta^h\right)$ and $p\left(\boldsymbol{d}_i^v\left(\overline{\boldsymbol{x}}_i^c(A),\overline{\boldsymbol{x}}_i^c(B)\right)<\delta^v\right)$ are defined to measure the degree to which the horizontal and vertical separation distance is violated against the recommended threshold values δ_h and δ_v, respectively. Herein, $I[\cdot]$ is an indicator function; if both the horizontal are vertical separation distance are violated, then the indicator function takes a value of one, indicating that the safety of the two flights in terms of separation distance is compromised. Otherwise, its takes a value of zero to indicate the two flights are safe in terms of separation distance.

With the introduction of the probabilistic safety indicator, the trajectory prediction from the integrated model is related to the safety condition between any two given flights. In particular, since the LSTM model has a long-term prediction ability, if the probability of separation distance violation forecast by the integrated model is above some threshold probability value, then the ground controllers could be alerted to take appropriate actions to increase the separation distance between the two flights.

3.3.5 Summary

The methodology developed in this section tackles the problem of en-route flight trajectory prediction in the NAS following a four-step procedure (see Fig. 3.2).

1. Considering the large volume of raw SFDPS messages in FIXM format, Apache Spark is leveraged to extract important trajectory information (i.e., flight position, aircraft velocity) pertaining to each flight. SQL query is performed to group flight trajectory by flight ID and date, and to save flight trajectory as a single CSV file per flight with Apache Spark. Data pre-processing techniques are used to drop redundant data and impute missing data.

2. Two deep learning models are trained to predict flight trajectory from different angles: A deep feed-forward neural network is constructed for one-step-ahead prediction of the deviation of actual flight trajectory from its corresponding flight plan, and a LSTM recurrent neural network is developed to make longer-term prediction of the flight trajectory. The uncertainty in both models is quantified following a Bayesian approach and approximated with Monte Carlo dropout.

3. To fully exploit the advantages of both the deep learning models, we propose to integrate them through a discrepancy term calculated as the difference between the two models' mean predictions. By doing this, the integrated model retains both LSTM

model's longer-term prediction capability and DNN model's high prediction accuracy.

4. With the integrated model, trajectory prediction is executed for multiple adjacent flights in a probabilistic manner. A probabilistic separation distance-based safety metric is used to measure en-route flight safety in a quantitative manner. The real-time en-route safety assessment helps to monitor the system safety and prevent the occurrence of safety hazard in advance.

3.4 Computational Results

In this section, we illustrate the computational results of the developed deep learning models, and demonstrate the superior performance of the integrated model over the two individual deep learning models in trajectory prediction.

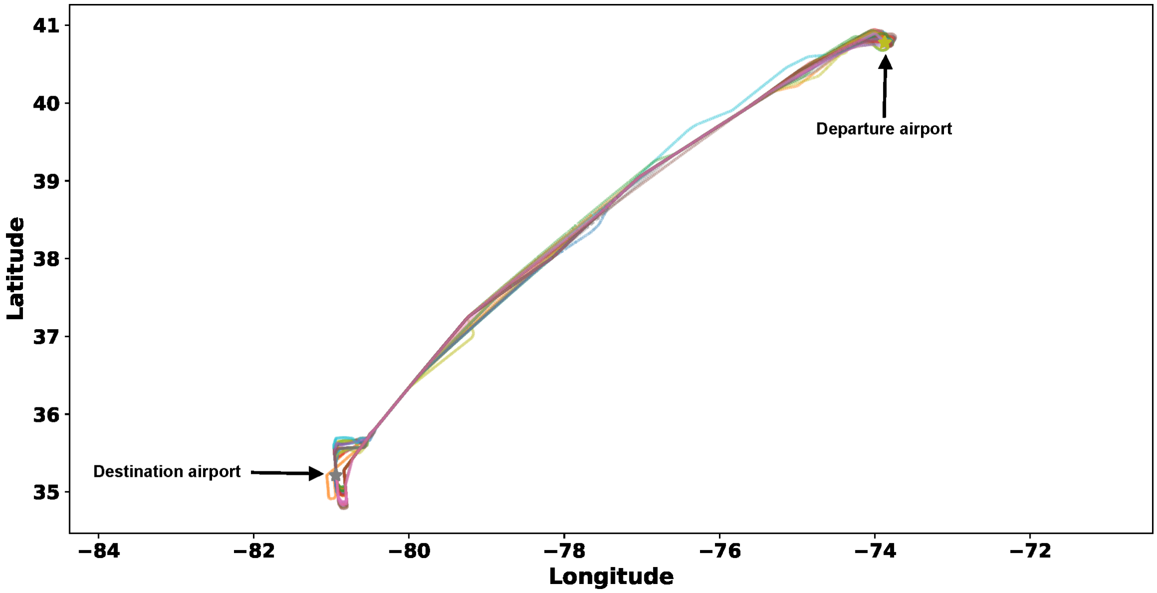

Figure 3.8: The historical trajectories of flight AA598 from 19th December 2018 to 8th February 2019

3.4.1 Data

We streamed SFDPS messages from 19th December 2018 to 8th February 2019. In terms of data volume, nearly 4.2 TB of SFDPS messages is processed with Apache Spark, from which we extract flight trajectories for 48 days. In order to demonstrate the trajectory prediction of an ongoing flight, we pick a flight trajectory on a randomly selected date and use it to test the prediction performance of the deep learning models, while the remaining flight trajectories are used to train the two deep learning models. We pick a specific flight AA598 for the sake of illustration. Fig. 3.8 shows the trajectories of flight AA598 from 19th December 2018 to 8th February 2019. The top right and bottom left corners indicate the departure airport (LaGuardia Airport) and destination airport (Charlotte Douglas International Airport), respectively. Obviously, the flight trajectory varies from day to day as impacted by traffic flow control, different weather conditions, and other factors.

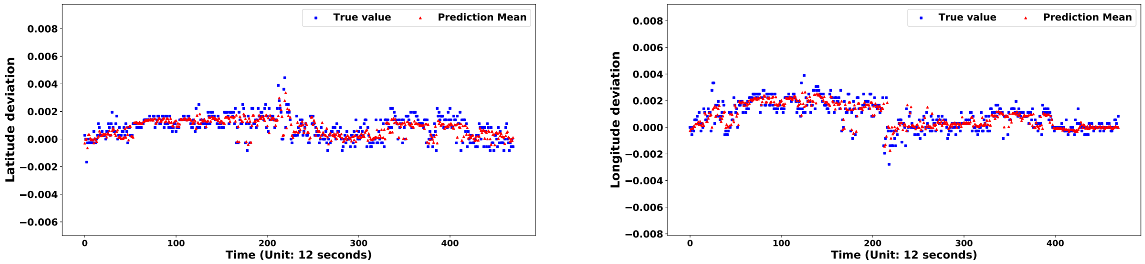

(a) Mean latitude deviation prediction vs actual values on sample flight AA598

(b) Mean longitude deviation prediction vs actual values on sample flight AA598

Figure 3.9: DNN prediction on trajectory deviation

3.4.2 Model Training and Assessment

Prior to the training of DNN model, the input and output data is normalized with the MinMaxScaler. When training the DNN model, we use the Adam optimizer with a learning rate of 0.001 to optimize the weights of deep neural networks for 15,000 iterations. Dropout with a probability of 0.1 is applied before each hidden layer to avoid overfitting during training. Two individual DNN models are trained for predicting the trajectory deviation along latitude and longitude, respectively. When making predictions, Monte Carlo dropout with the same probability is used to approximate Bayesian posterior distribution on the new data point. Fig. 3.9 shows the trajectory deviation prediction made by the DNN model on the test flight AA598. As can be observed from Fig. 3.9, the trained DNN model captures most of the variation on the trajectory deviation over time.

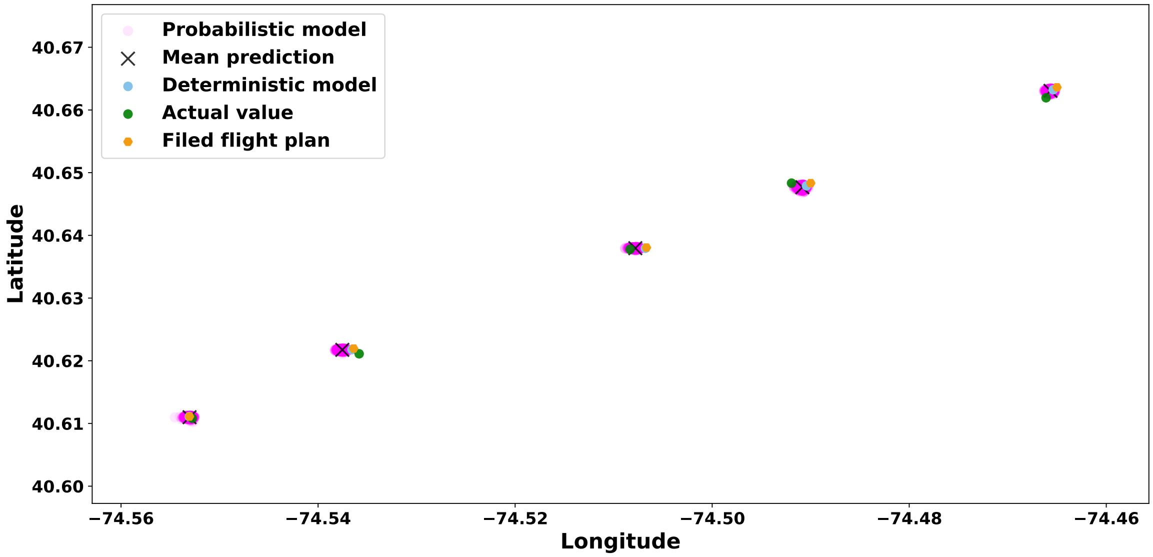

Figure 3.10: Comparisons on the trajectory predictions of flight AA598

To compare the computational results of deterministic model and probabilistic model, Fig. 3.10 illustrates the one step ahead prediction on the latitude and longitude in the trajectory of flight AA598. With the trajectory deviation forecast by the DNN model, the trajectory in terms of latitude and longitude in the next time instant can be calculated in a straightforward manner. As shown in Fig. 3.10, the actual position for the flight AA598 is denoted as solid green dots, the prediction of deterministic model on flight trajectory is represented as solid light blue dots, the solid pink dots are 1,000 samples drawn from the trained DNN model, the black crosses denote the mean prediction of the probabilistic model, and the solid yellow dots are the expected position where the flight should be in the flied flight plan. As can be observed, most of the actual values fall within the cluster formed by the samples of the probabilistic models, while they deviate relatively far away from the prediction of the deterministic model. Hence, the probabilistic model outperforms the deterministic model in the latitude and longitude prediction. The inclusion of model prediction uncertainty enables us to assess the level of uncertainty and risk involved when making decisions in a quantitative manner.

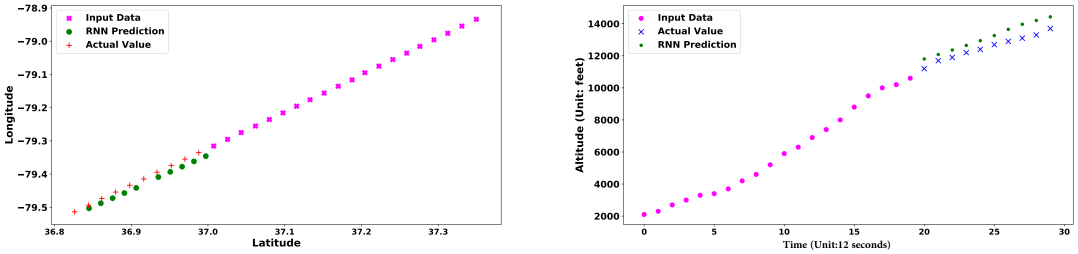

(a) Mean latitude and longitude prediction by LSTM model vs actual values on sample flight AA598

(b) Mean altitude prediction by LSTM model vs actual values on sample flight AA598

Figure 3.11: LSTM prediction of flight trajectory

We retain the same trajectory to verify the performance of the trained LSTM model. To avoid model overfitting, regularization is performed on layer parameters, and $L2$ regularization is applied to the recurrent connections. The LSTM model has two stacked layers with each layer having 20 LSTM blocks. The output of the last LSTM block at the top hidden layer is flattened and fed into a densely connected layer. Two individual models are trained with the same LSTM architecture. The first model predicts the flight latitude and longitude along the subsequent five time steps, while the second model forecasts the flight altitude, and velocities along X and Y in the subsequent five time steps. To make even longer prediction, we take the LSTM model's prediction as new inputs, and feed them into the trained LSTM model to make predictions again. Fig. 3.11 shows the predictions of LSTM model on the latitude, longitude, and altitude of the test flight AA598 for the next 10 time instants (2 minutes). From LSTM's predictions, we observe that it demonstrates promising performance in predicting the flight trajectory over time. There is slight discrepancy between LSTM model's prediction and the actual values. The powerful longer-term prediction ability in the LSTM model enables us to have a 2-minutes-ahead view on the possible behavior of each flight, and take preventive action to mitigate any safety hazard.

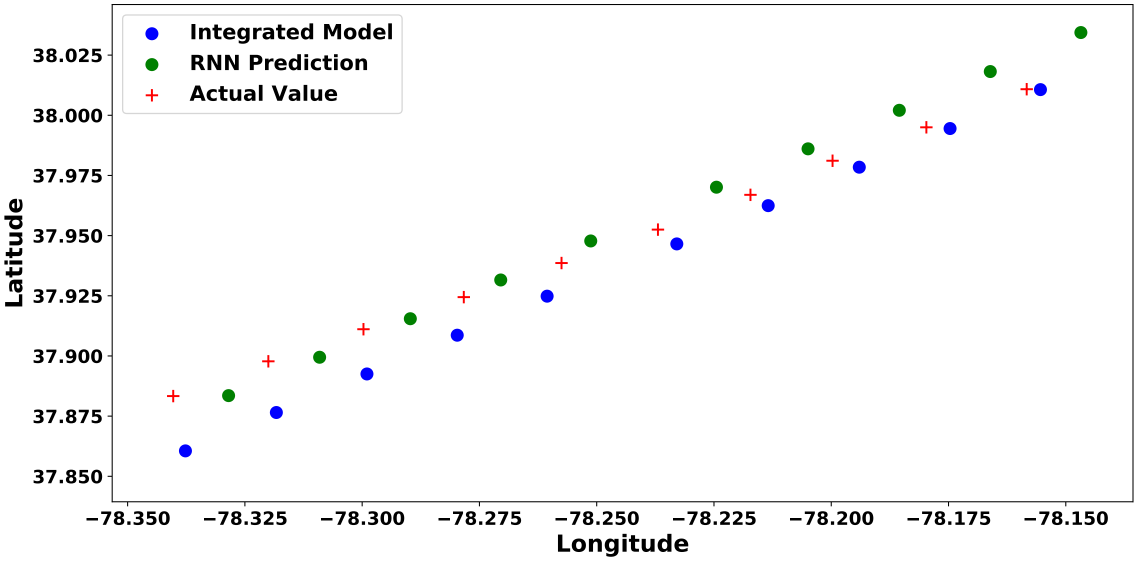

Figure 3.12: Comparison of LSTM model predictions before and after integration with the DNN model

Both the DNN and LSTM models make predictions on the same flight trajectory from different perspectives. As indicated in Fig. 3.5, since the deviation along latitude and longitude is small for DNN, the DNN prediction on flight trajectory can be utilized to correct the LSTM model's prediction on the common quantities of the two models. Fig. 3.12 compares the predictions of the LSTM model before and after the integration with the DNN model. It can be observed that the integrated model makes a much more accurate prediction on the flight trajectory than the predictions from the LSTM model only. By doing this, the high accuracy and longer-term prediction ability are achieved in the integrated model, thus supporting more robust decision making.

The above computational results only illustrate the performance of one trained DNN model and LSTM model on predicting flight trajectory. To make sure that the improvement in prediction performance is general, we repeat the same procedures with a double loop program. In the inner loop, we randomly pick the test flight trajectory and train the models with the remaining trajectories for ten times. In the outer loop, we run the program within the inner loop for five times. The root mean squared error (RMSE) between the model predictions and actual values is used as a metric to compare all the models. Since training deep learning models, especially LSTM models, is time-consuming, we accelerate the running speed of the program by executing it on a NVIDIA Pascal GPU. Table 3.2 compares the performance of the deterministic and probabilistic deep learning models on the trajectory deviation prediction. Here, we use the mean value of probabilistic model prediction to calculate the RMSE. As indicated in the comparison results, the RMSE of the probabilistic DNN model has reduced by 2% and 74% for the latitude and longitude deviation prediction, respectively. Similarly, we compare the performance of the LSTM model and the integrated model on flight state prediction. As shown in Table 3.3, the integrated model demonstrates a much better performance on the common quantities of the two models: latitude and longitude prediction. The value of RMSE is reduced by 47% and 53% compared to the LSTM model, respectively. These cross-validation results show that the integrated model achieves much higher accuracy in flight state prediction.

Table 3.2: Performance comparisons on trajectory deviation prediction

	Deterministic		**Probabilistic**	
	Latitude	Longitude	Latitude (μ)	Longitude (μ)
Root Mean Squared Error	3.36×10^{-2}	9.73×10^{-2}	3.29×10^{-2}	2.51×10^{-2}

Table 3.3: Performance comparisons on flight state prediction

	LSTM Model		**Integrated Model**		**LSTM Model**		
	Latitude	Longitude	Latitude	Longitude	Altitude	X Velocity	Y Velocity
Root Mean Squared Error	2.48×10^{-2}	2.96×10^{-2}	1.32×10^{-2}	1.38×10^{-2}	650	16.29	20.11

3.4.3 Safety Assessment

To measure the flight safety, we pick another flight UAL1767 that starts from Denver International Airport and ends at Ronald Reagan Washington National Airport on 23rd January, 2019. Once the deep learning models are trained, we calculate the horizontal and vertical separation distances between the two flights. Fig. 3.13 compares the model

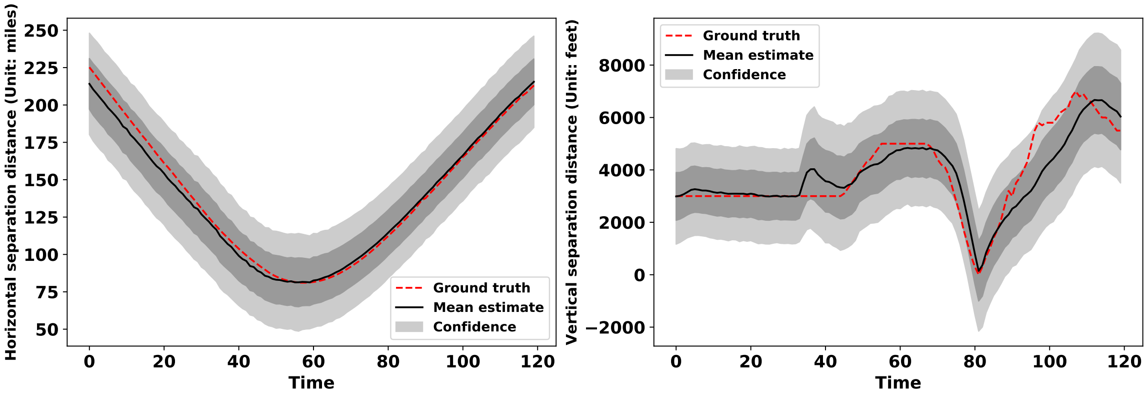

Figure 3.13: Performance comparison of separation distance

prediction and the ground truth of the separation distance between the two flights. In this figure, the red dashed lines indicate the actual horizontal and vertical separation distances between the two flights, the black solid lines denote the mean value of separation distance as estimated by the probabilistic models, and the shaded areas in dark grey and light grey demonstrate the confidence interval for one standard deviation and two standard deviations away from the mean value, respectively. As can be observed, the deep learning model captures both separation distances very well. The probabilistic metric formulated in Eq. (3.4) indicates that two flights did not violate the separation distance constraint.

3.5 Summary

In this chapter, we developed and combined deep learning-based models with the SFDPS messages streamed from FAA's SWIM Flight Data Publication Service for en-route flight safety prediction. To accomplish this goal, a four-step methodology is developed. In the first step, a unified distributed high-performance computing platform Apache Spark is leveraged to parse the massive SFDPS messages in FIXM format, from which key information pertaining to flight trajectory is extracted. Next, we develop two individual deep learning models for trajectory prediction from different views. The first feed-forward deep neural network is trained for one-step prediction of the deviation between actual trajectory and target flight trajectory. The second LSTM recurrent neural network is utilized for make longer-term prediction on the full state of the flight trajectory. In the third step, the two deep learning models are integrated via a discrepancy term, which is calculated as the discrepancy between DNN prediction and LSTM prediction on the common response variables (i.e., latitude and longitude). The integration of the two deep learning models preserves both the high accuracy of the DNN model and the longer-term prediction ability of LSTM model. Finally, the same approach is extended to multiple flights, and we are then able to predict the en-route flight safety, in which probabilistic separation distance is used as a quantitative safety metric.

The proposed methodology has made several significant contributions to the state-of-the-art studies towards flight trajectory prediction using machine learning from historical data. First of all, we utilize a distributed computing engine Apache Spark to process a large volume of raw data in FIXM format, and it demonstrates scalable and promising performance. The same strategy can be implemented to handle more complex aeronautical data in the future, such as weather data. Secondly, different from existing studies, we characterize the model prediction uncertainty following a Bayesian approach. The quantification of model prediction uncertainty allows us to make decisions with probabilistic information on the safety risk. Thirdly, the trained deep learning models offer new insights to view the trajectory prediction from different angles. By integrating the two models together, we not only improves the overall prediction accuracy, but also retain a longer-term prediction capability.

This chapter develops a multi-fidelity deep learning-based model for system behavior prediction, the idea of multi-fidelity approach can be generalized to many other applications. In particular, by blending two prediction models together, we achieve both long-term prediction capability and high prediction accuracy. The fast and accurate prediction of system behavior enabled by the multi-fidelity model greatly improves operators' preparedness for hazardous events, thereby increasing system resilience.

Chapter 4

Ensemble Machine Learning Models for Risk Prediction of the Consequences of Hazardous Events[1]

4.1 Introduction

In addition to predicting when a hazardous event is about to happen (as in the previous chapter), another perspective to strengthen the resilience of a system is that, given that an anomalous event has already occurred, we can increase the preparedness of relevant stakeholders for the consequences of the hazardous event. One means to achieve this goal is to equip the stakeholders with a tool to forecast the consequence of any abnormal event with the anomalous behavior of the system observed so far. In this chapter, we develop an ensemble machine learning approach to predict the outcomes of the abnormal events, and illustrate the approach using aviation incidents.

As mentioned earlier in Chapter 3, the air traffic is experiencing a steady and tremendous growth, and the rapid increase in air traffic demand poses a tremendous operational challenge on the air transportation system, which is already struggling to cope with the current demand. Over the past decades, numerous efforts have been dedicated to the development on comprehensive safety metrics as well as qualitative/quantitative approaches to detect anomalous behavior, assess the safety, and quantify the risk associated with one subsystem (i.e., airport ground operations, flight tracking, or taxiway and runway system) or a mixture of subsystems in the air transportation system [106]. In general, there are two principal strategies to enhance the air transportation system safety: (I) increase system/-subsystem reliability, i.e., reduce the probability of operators making mistakes or systems having malfunctions; and (II) improve the operators' preparedness. Although tremendous progress has been made over the past decades for enhancing the air transportation system

[1] An archival paper related to this chapter has been published in the journal Decision Support Systems. For more details, see Ref. [69]

safety, most of the studies emphasize identifying the accident precursors and initiating corrective actions to prevent future errors, which can be grouped into the first strategy. Among the existing studies, much of the effort has been devoted to investigating human factors induced accidents and constructing causal models [107, 108]. For example, Wiegmann and Shappell [109] described the Human Factors Analysis and Classification System (HFACS) and provided aviation case studies on human factor analysis with HFACS. However, air transportation is a complex system of systems involving many varied but yet interlinking distributed networks of human operators, technical/technological procedures and systems, and organizations/stakeholders. The scarcity in the operational data and the involvement of a variety of human operators are major challenges that severely affect the prediction of erroneous operation, and challenge the assessment and improvement of the system reliability.

As mentioned in Chapter 1, the first set of measures we take to enhance system resilience is to increase operators' situation awareness on the dynamic evolution of hazardous events. As indicated in chapter 3, we accomplish this goal by enhancing operators' situation awareness on the future state of en-route flight trajectory by learning from massive historical trajectory data. By doing this, we equip operators with a look-ahead ability, from which they gain a better sense on the moment when the loss of flight separation distance occurs (separation distance is the event we investigate in Chapter 3). On the other hand, if system malfunction already happens, one way to strengthen operators' preparedness is to get them ready for the consequence of anomalous events. By doing this, when a hazardous event occurs, the operator can take appropriate safety measures to reduce the cost of the consequence caused by the hazardous event with the minimum time [110, 111, 20].

In Chapter 4, we emphasize the "proactive safety" paradigm [112] and work along this direction with a focus on strengthening the capability and efficiency of the operators in response to the abnormal events with appropriate actions, thereby mitigating the consequence or severity of hazardous events. In this connection, a large number of incident/accident reports have been filed over the past half century together. A few machine learning studies have been carried out to analyze these reports. For example, Oza et al. [113] developed two algorithms – Mariana and nonnegative matrix factorization-based algorithm – to perform multi-label classification for the reports of Aviation Safety Reporting System (ASRS). Budalakoti et al. [114] presented a set of algorithms to detect and characterize anomalies in discrete symbol sequences arising from recordings of switch sensors in the cockpits of commercial airliners. These studies have not explored the intricate relationships between abnormal event characteristics and the induced consequences. This chapter aims to mine the complex associations between anomalous event behavior and the consequence of these events through the development of a hybrid machine learning model. This type of analysis will help to develop a decision support system that can learn the patterns in the data and help the analyst examine incidents/accidents quickly and systematically, thus assisting the risk manager in risk quantification, priority setting, resource allocation and decision making in support of the implementation of proactive safety paradigm.

While in Chapter 3, flight trajectory is represented as numerical values, the anomalous incidents in this chapter, their characteristics, and event consequences are primarily depicted in the categorical and text format. To develop the model for event consequence prediction, we have utilized the Aviation Safety Reporting System (ASRS), which is as a state-of-the-art aviation incident database that provides a plethora of incidents/accidents that occur over the course of the past several decades. The incident reports are submitted by pilots, air traffic controllers, dispatchers, cabin crew, maintenance technicians, and others, and describe both unsafe occurrences and hazardous situations [115]. ASRS covers almost all the domains of aircraft operations that could go wrong. However, it is a non-trivial task to build a model from the ASRS data for the prediction of risk associated with the consequence of hazardous events due to the following challenges:

1. High-dimensional data. Each incident record consists of more than 50 items ranging from the operational context (weather, visibility, flight phase, and flight condi-

tions) to the characteristics of the anomalous operation (aircraft equipment, malfunction type, and event synopsis). The url https://asrs.arc.nasa.gov/docs/dbol/ASRS_CodingTaxonomy.pdf gives a detailed description of each item. Besides, air traffic operation is a complex system composed of a number of programs and personnel. It is likely for the incident to occur at any phase and location due to a variety of factors (i.e., operation violation, visibility, human factors etc.), which makes it hard for the machine learning algorithm to predict the exact level of risk associated with each event outcome.

2. Primarily categorical data. Over 99% of the items in the ASRS database are categorical, and only one attribute (crew size) is numerical in each record. Although the categorical information offers a high-level description of the context of each incident, very limited information specific to each abnormal event can be derived from such categorical information, e.g., how did the incident happen, how did the incident evolve over time in the system, what operation the pilot took to resolve the issue, etc. Since the categorical features are not informative, how to blend the predictions of the model trained by the categorical features and the predictions from the model trained by other informative indicators (e.g., event synopsis) without compromising the model performance is an issue worthy of investigation.

3. Unstructured data. One important unstructured attribute is event synopsis, which is a concise summary of the incident/accident in the form of text. Mining causal relationships from the unstructured text data is a daunting task [116]. A common characteristic in handling text data is to transform it into numerical data in the representation of term frequency of each individual document. Along this direction, researchers have developed numerous techniques to elicit useful knowledge from the text data, e.g., support vector machine [117], latent Dirichlet allocation-based topic mining [118, 119, 120], Naïve Bayes-based document classification [121], k-

nearest-neighbor (k-NN) classification [122], and others [123, 124]. Among them, support vector machine [125] has demonstrated good performance in text categorization because it overcomes over-fitting and local minima, thereby achieving good generalization to applications [126, 127].

4. Imbalanced class distribution. In the ASRS, the number of records in one class (i.e., possible outcome) is significantly larger than that of the others. The distribution of the outcomes for all the hazardous events reported between January 2006 and December 2017 is illustrated in Fig. 4.1. As can be observed, the number of records across different classes is highly imbalanced. Such imbalanced class distribution has posed a serious challenge to machine learning algorithms which assume a relatively well-balanced distribution [128].

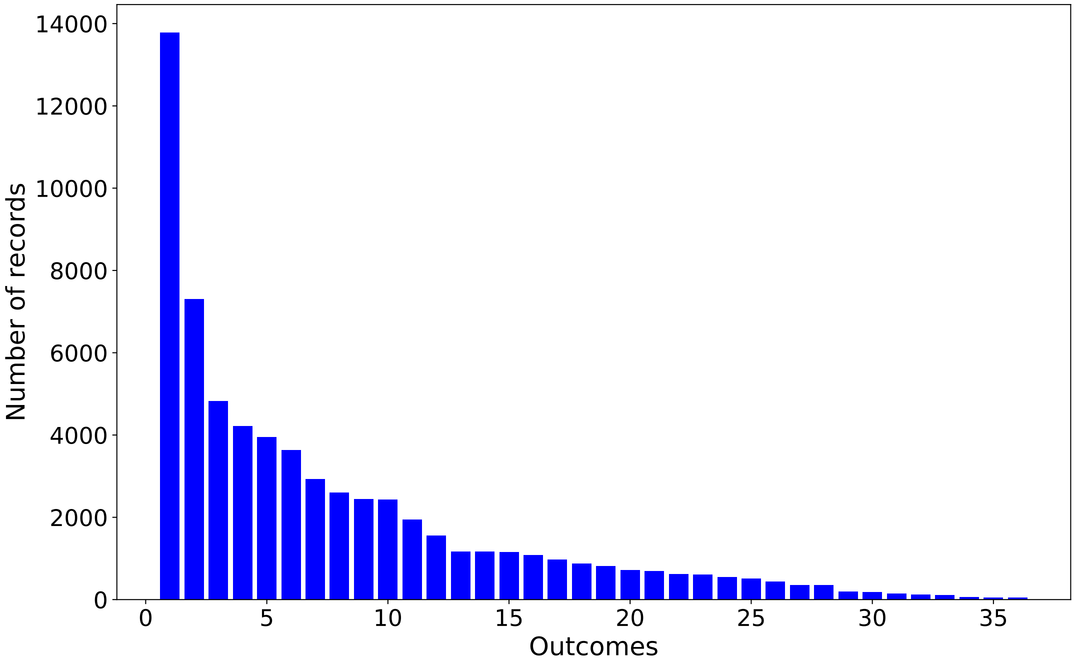

Figure 4.1: Distribution of outcomes for all incidents/accidents between January 2006 and December 2017

Since ASRS consists of a variety of heterogeneous data (e.g., text data, categorical data, and numerical data), it is challenging to develop one single model to learn from the entire dataset for predicting the risk associated with the consequence of hazardous events. In this chapter, we adopt the "divide and conquer" strategy to split the data into two parts: structured and unstructured, and develop a hybrid model to handle the two types of data, respectively. By doing this, we are able to leverage the strengths of each model in processing certain type of data. Compared with building a single model, the dimension of the problem is reduced significantly. With respect to categorical data, considering its high-dimensional feature space, deep learning might be a good candidate to discover the highly intricate relationship between event contextual characteristics and event consequence due to its powerful ability in establishing a dense representation of the feature space, which makes it effective in learning high-order features from the raw data [129, 130]. As a result, a deep learning model is developed to process the categorical data for the purpose of learning the associations between event contextual features and event outcomes. In parallel, a support vector machine model is trained to identify the relationships between text-based event synopsis and the risk level associated with the consequence of each incident. Afterwards, the predictions from the two machine learning models are fused together for quantifying the risk associated with the consequence of each incident. Finally, the prediction on risk level categorization is extended to event-level outcomes through a probabilistic decision tree. Compared to the current state of the art in machine learning for aviation safety, we make the following contributions:

1. We have developed a machine learning methodology to learn the relationships between abnormal event characteristics and their consequences. We focus on the data set that has a large number of outcomes and imbalance of available data regarding these outcomes. This challenge is overcome by grouping the event outcomes into five risk categories and by up-sampling the minority classes.

2. A probabilistic fusion rule is developed to blend the predictions of multiple machine learning models that are built on different segments of the available data. Specifi-

cally, a hybrid model blending SVM prediction on unstructured data and deep neural network ensemble on structured data is developed to quantify the risk of the consequence of hazardous events, in which the record-level prediction probabilities, class-level prediction accuracy in each respective model, and the proportion of each class in the records with disagreeing predictions are considered in model fusion.

4.2 Aviation Safety Reporting System

The Aviation Safety Reporting System (ASRS) is a program operated by the National Aeronautics and Space Administration (NASA) with the ultimate goal of increasing aviation system safety by discovering system safety hazards hidden in the multitude of air traffic operations. Over the past few decades, ASRS has become one of the world's largest sources of information on aviation safety and human factors [115]. As one of its primary tasks, ASRS collects, processes, and analyzes voluntarily submitted aviation incident/situation reports from pilots, flight attendants, air traffic controllers, dispatchers, cabin crew, ground workers, maintenance technicians, and others involved in aviation operations.

Reports submitted to ASRS include both unsafe occurrences and hazardous situations. Each submitted report is first screened by two analysts to provide the initial categorization and to determine the triage of processing. During this process, ASRS analysts identify hazardous situations from the reports, and issue an alert message to persons in a position to correct them. Based on the initial categorization, ASRS analysts might aggregate multiple reports on the same event to form one database "record". If any information needs to be further clarified, ASRS analysts might choose to call a reporter over the telephone to gather more information. After all the necessary information is collected, the reports are codified using the ASRS taxonomy and recorded in the database. Next, some critical information in each record is de-identified; then ASRS distributes the incident/accident records gathered from these reports to all the stakeholders in positions of authority for future evaluation and potential corrective action development.

Table 4.1: A sample incident/accident record extracted from ASRS

Attribute	**Content**
Time / Day	Date : 201702 Local Time Of Day : 0601-1200
Place	Locale Reference.Airport : BUR.Airport State Reference : CA Altitude.MSL.Single Value : 2500
Environment	Flight Conditions : VMC Weather Elements / Visibility.Visibility : 10 Light: Daylight Ceiling.Single Value : 12000
Aircraft	Reference : X ATC / Advisory.Center : BUR Aircraft Operator : Personal Make Model Name : PA-28R Cherokee Arrow All Series **Crew Size.Number Of Crew** : 1 Operating Under FAR Part : Part 91 Flight Plan : VFR Mission : Personal Flight Phase : Initial Approach Route In Use : Visual Approach Airspace.Class D : VNY
Component	Aircraft Component : Engine Air Problem : Malfunctioning
Person	Reference : 1 Location Of Person : X Location In Aircraft : Flight Deck Reporter Organization : Personal Function.Flight Crew : Single Pilot Qualification.Flight Crew : Private Experience.Flight Crew.Total : 175 Experience.Flight Crew.Last 90 Days : 30 Experience.Flight Crew.Type : 175 ASRS Report Number.Accession Number : 1428684 Human Factors : Confusion
Events	Anomaly.Deviation - Altitude : Excursion From Assigned Altitude Anomaly.Deviation - Track / Heading : All Types Anomaly.Deviation - Procedural : Clearance Anomaly.Inflight Event / Encounter : Unstabilized Approach Detector.Person : Air Traffic Control When Detected : In-flight Result.Flight Crew : Returned To Clearance Result.Flight Crew : Became Reoriented Result.Air Traffic Control : Issued New Clearance Result.Air Traffic Control : Issued Advisory / Alert
Assessments	Contributing Factors / Situations : Airspace Structure Contributing Factors / Situations : Human Factors Primary Problem : Human Factors
Synopsis	PA28R pilot reported becoming confused during a VFR flight to BUR and lined up on VNY. BUR Tower detected the error and issued a new heading and climb back to assigned altitude.

Table 4.1 presents a sample situation record extracted from the ASRS database. As can be observed, each record has more than 20 fields ranging from event occurrence location to event characteristics. Here, we briefly introduce several primary attributes in each record:

1. Time and location of the abnormal event: The incident in Table 4.1 occurred on February 2017 at the BUR airport in USA. Here, BUR is the International Air Transport Association (IATA) code of the airport, and it refers to the Hollywood Burbank Airport located in Los Angeles County, California. Besides, the record also provides the basic altitude above Mean Sea Level (MSL). In this case, the hazardous event occurred when the flight was at an altitude of 2500 feet.

2. Environment: This describes the surrounding conditions encompassing the aircraft operations. Examples are: flight conditions (VMC, IMC, marginal, or mixed), and weather elements such as visibility, light, and ceiling. Here, VMC refers to visual meteorological condition (VMC) under visual flight rules (VFR) flight. In VMC, pilots have sufficient visibility to fly the aircraft maintaining visual separation from the terrain and other aircraft. Different from VMC, instrument meteorological condition (IMC) represents the category that describes weather conditions that require pilots to fly primarily by reference to instruments under instrument flight rules (IFR). Visibility and cloud ceiling are two key factors in determining whether the weather condition is VMC or IMC, and the boundary between IMC and VMC is known as VMC minima. “Marginal VMC” refers to conditions above but close to one VMC minima or more.

3. Aircraft: This attribute reports the basic aircraft and flight information, including the aircraft make and model, flight type (personal or commercial), the number of crew onboard, flight plan, flight mission, flight phase, and the airspace class the flight is in. Such information details the specific flight phase in which the hazardous event occurs. The basic aircraft information also enables us to have an understanding of

the scale of the possible event consequence.

4. Component: If there is any mechanical failure in the aircraft, the record will have the component field, and it describes which aircraft component is faulty (i.e., engine, nosewheel, transponder etc.) and the type of the problem as well (i.e., malfunctioning, improperly operated, or others). This field might be empty if there is no component malfunction.

5. Person: Person describes the fundamental information of the personnel that reports the problem. For example, the location of the person, his/her location in the aircraft, the reporter organization, the qualification of the reporter, and the contributing human factor (e.g., fatigue, distraction, confusion, and time pressure).

6. Events: This attribute provides the basic characteristics of anomalous behavior and its consequence. In this record, BUR Tower detected the excursion of the flight from the assigned altitude and issued course correction to avoid the traffic. After taking course correction to avoid traffic, the pilot did not maintain the same course heading to Burbank while ATC assumed that the pilot was on correct heading. As a result, the BUR Tower recognized the error and issued a new heading and commanded the pilot to climb back to the assigned altitude to perform landing from the very start.

7. Assessments: Assessments provide evaluation of the root cause and other factors that contribute to the occurrence of the abnormal event.

Table 4.2: Two examples of event synopsis in ASRS

Date	**Event Synopsis**
February, 2017	A319 Flight Attendant reported smoke in the cabin near the overwing exits during climb.
January, 2017	A319 flight crew reported fumes in the flight deck. After a short time they began to experience problems concentrating and the onset of incapacitation.

8. Synopsis: All the above fields are categorical except the crew size. The last row of Table 4.1 and Table 4.2 provide several sample event synopses elicited from the ASRS database. As can be observed, event synopses gives a brief summary of the cause of the problem, and how the abnormal event evolves over time. Such information is helpful for us to assess the severity of the hazardous event and analyze possible consequences.

The above descriptions provide a brief introduction to the physical meanings of some important fields in each record. In ASRS, other records might differ from the above sample records in certain fields or they might have additional fields which are absent in the sample record due to the difference in the type and characteristics of the abnormal event.

4.3 Proposed Methodology

We develop a hybrid method to estimate the risk of the event consequence with the consideration of operational conditions and event characteristics. To build the hybrid model, we investigate the incidents/accidents that occurred from January 2006 to December 2017. The detailed proposed framework is outlined in Fig. 4.2, which shows a four-step procedure. In the first step, we perform a risk-based event outcome categorization. That is we employ the level of risk as a quantitative metric to measure the severity of the event outcome and collapse all the possible event outcomes into five categories: high risk, moderately high risk, medium risk, moderately medium risk, and low risk. Given the restructured categories, two models are developed in the second step to process the unstructured data (text data) and structured data (categorical and numerical information). Specifically, a support vector machine (SVM) model is developed to represent the relationship between event synopsis and the risk pertaining to the event outcome, and an ensemble of deep neural networks (DNN) is trained to predict the level of risk based on contextual features of each abnormal event. In the third step, we develop an innovative fusion rule to blend the prediction results from the SVM and DNN models. Finally, the risk-level prediction is further expanded to event-level outcome analysis in through a probabilistic tree.

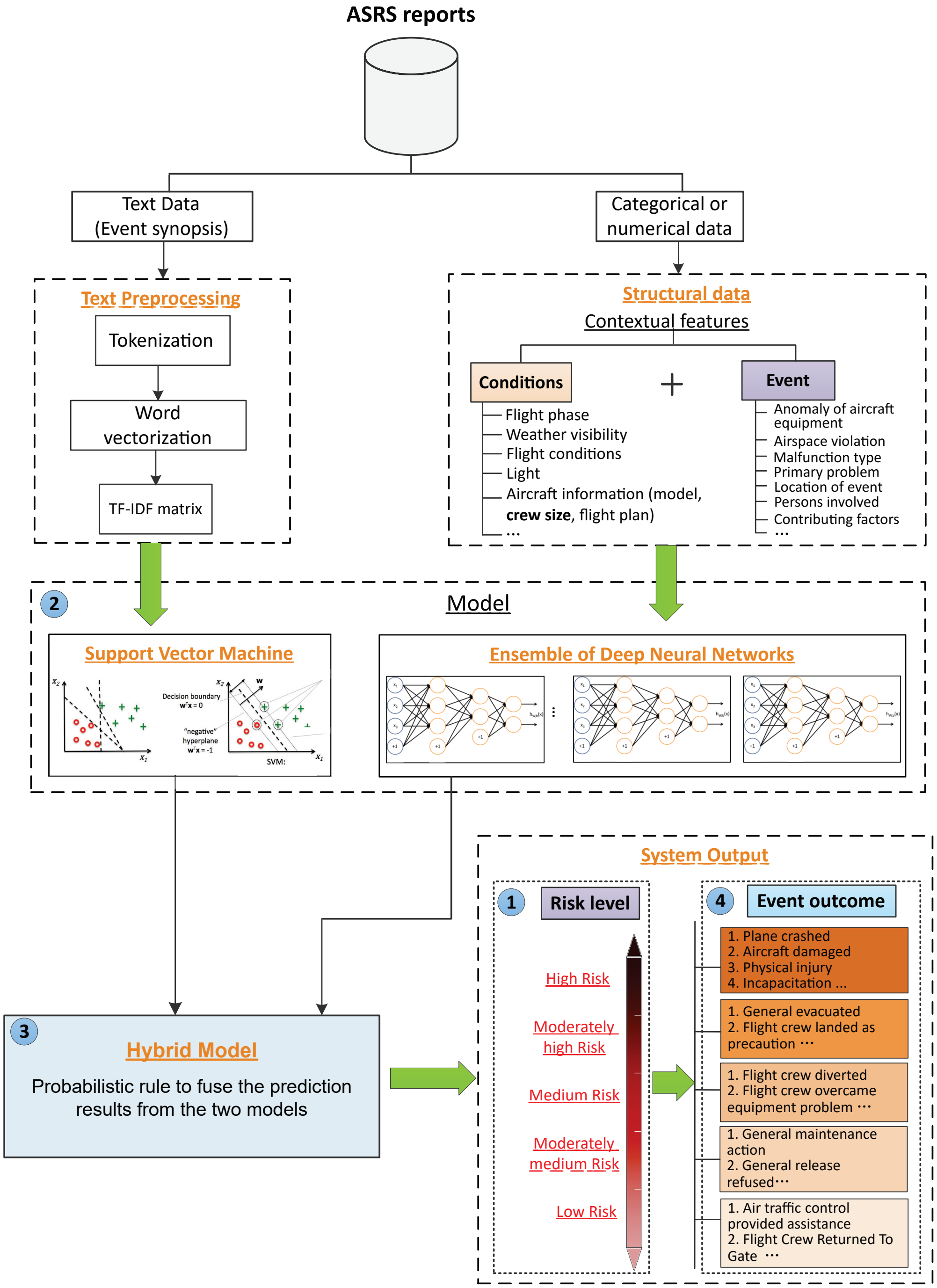

Figure 4.2: Hybrid machine learning framework for risk prediction

4.3.1 Risk-based Event Outcome Categorization

As shown in Fig. 4.1, there are 36 unique event outcomes among the incident reports. Because almost all of the contextual features are categorical, they are uninformative indicators of the event outcome considering that one contextual condition might correspond to a large number of event outcomes that belong to different risk levels. For example, if we are only given the weather visibility, it is challenging to predict what might happen because the information is too limited. In other words, there exist too many possible scenarios given the weather visibility. From this perspective, event synopsis is the only attribute left that can help us to differentiate the event outcome. Since the event synopsis embodies the complex event evolution process, it is difficult to use the current state-of-the-art text mining techniques to understand the semantics, discover the causal relationships, mine the event sequences, and associate with the event consequence from such a short and condensed report. Considering that there are 36 unique event outcomes, the machine learning algorithm is challenged by the lack of significant predictors in the ASRS records that can be used to distinguish the event outcomes.

Another challenge is that the class distribution is severely imbalanced. In such circumstances, the standard classification algorithms are often biased toward the majority class, leading to a high misclassification rate for the minority class [131, 132, 133]. To overcome this problem, one popular way is to generate additional samples by randomly duplicating observations from the existing records in the minority class with replacement (referred to as up-sampling in the rest of the chapter) so as to balance the number of records for the majority and minority classes. Since the ratio between the majority class 1 and minority class 36 is larger than 1000, a large number of samples needs to be generated to increase the number of records for the minority class. As can be observed from Fig. 4.1, this is also true for many other minority classes. Therefore, some additional operations need to be considered to reduce the number of samples that need to be generated. Also, the prediction model built with the upsampled data needs to account for the upsampling.

The last issue is that one abnormal event might result in multiple outcomes. For example, as shown in the eighth row of Table 4.1, there are four different types of outcomes (as underlined in Table 4.1) for this sample record. It is impossible to train four individual machine learning models with each model being used to predict a particular event outcome. Besides, accident/incident records with multiple consequences are not rare in the ASRS database, and occupy almost 50% of the entire data.

To address the above three challenges, we develop a risk-based event outcome categorization, where each event outcome is associated with a specific risk indicator out of five categories: high risk, moderately high risk, medium risk, moderately medium risk, and low risk. According to the severity of event consequence, each event is assigned to a particular risk group based on expert opinion. Table 4.3 reports the five risk categories and the set of outcomes belonging to that risk category. By doing this, we collapse the original 36 unique event outcomes into five groups, and project the event outcome to one of the five risk groups. Now, even if an event has multiple consequences, we can identify the highest risk group corresponding to the outcomes of that event, and use it to indicate the amount of risk related to that abnormal event. Another benefit is that the number of samples that need to be generated to balance the majority and minority classes is reduced by a large factor. Fig. 4.3 illustrates the class distribution after the collapse operation. It can be noticed that the class distribution is in better shape compared to the distribution of the original 36 classes. The ratio between the class with the most number of records and the class with the least number of records is reduced from 1000 to 2.1. The decrease in the number of samples that need to be generated also mitigates the computational effort for the machine learning models constructed in the next section.

4.3.2 Model Construction

The ASRS data can be classified into two groups: structured data and unstructured data. In particular, structured data include numerical data (e.g., crew size) and categorical data

Table 4.3: Mapping between risk levels and event outcomes

Risk Level	**Event Outcome**
High risk	General Declared Emergency General Physical Injury / Incapacitation Flight Crew Inflight Shutdown Air Traffic Control Separated Traffic Aircraft Damaged
Moderately high risk	General Evacuated Flight Crew Regained Aircraft Control Air Traffic Control Issued Advisory / Alert Flight Crew Landed in Emergency Condition
Medium risk	General Work Refused Flight Crew Became Reoriented Flight Crew Diverted Flight Crew Executed Go Around Missed Approach Flight Crew Overcame Equipment Problem Flight Crew Rejected Takeoff Flight Crew Took Evasive Action Air Traffic Control Issued New Clearance
Moderately medium risk	General Maintenance Action General Flight Cancelled Delayed General Release Refused Aircraft Not Accepted Flight Crew Overrode Automation Flight Crew FLC Overrode Automation Flight Crew Exited Penetrated Airspace Flight Crew Requested ATC Assistance Clarification Flight Crew Landed As Precaution Flight Crew Returned To Clearance Flight Crew Returned To Departure Airport Aircraft Automation Overrode Flight Crew
Low risk	General Police Security Involved Flight Crew Returned To Gate Aircraft Equipment Problem Dissipated Air Traffic Control Provided Assistance General None Reported Taken Flight Crew FLC complied w Automation Advisory

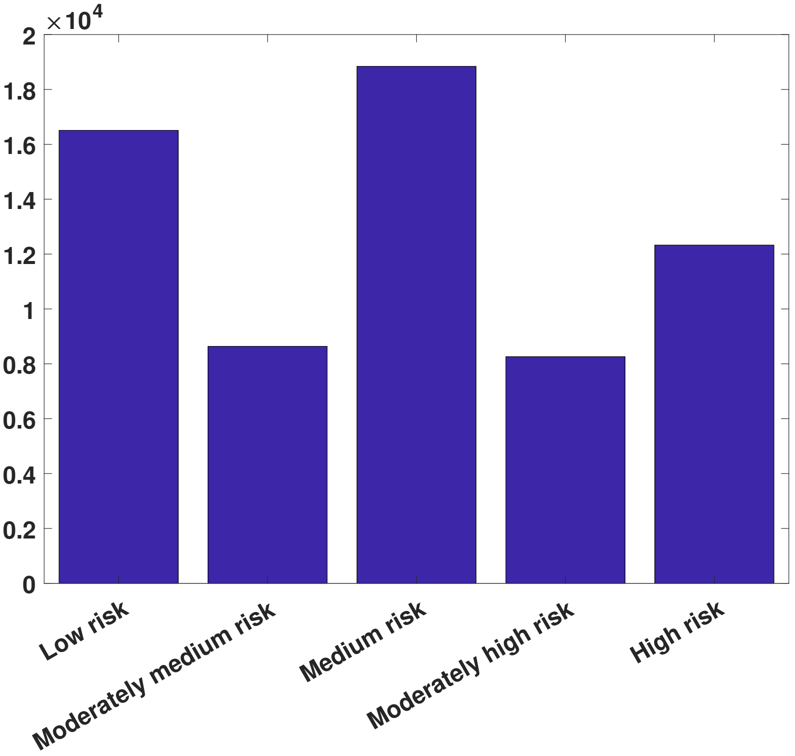

Figure 4.3: Distribution of risk outcomes after recategorization of incidents/accidents from January 2006 to December 2017

(e.g., flight phase, weather visibility, flight conditions etc.). In ASRS, event synopsis is the only unstructured data, and it is used to describe how the accident/incident occurred.

Before developing the two machine learning approaches, we up-sample the minority classes in the restructured risk domain. Basically, up-sampling is the process of randomly duplicating observations from the minority class to reinforce its signal. With respect to the reorganized risk categories, we perform resampling with replacement for the three minority classes, namely: high risk, moderately high risk and moderately medium risk, so that the number of records for them matches with the majority class (medium risk). After the up-sampling operation, we develop two individual models to handle the structured and unstructured data, separately. The flowchart of the developed method is illustrated in Algorithm 1. In Algorithm 1, the five risk categories varying from high risk to low risk are represented by five numerical values 5, 4, 3, 2, and 1, respectively.

Algorithm 1 : Hybrid model development

```
Input: Two already trained models: support vector machine $M_1$ and ensemble deep neural networks $M_2$, and test dataset $D = \{(\mathbf{x}_1, y_1), (\mathbf{x}_2, y_2), \ldots, (\mathbf{x}_m, y_m)\}$
Process:
for $t = 1$ to $m$ do
    if $M_1(\mathbf{x}_t) = M_2(\mathbf{x}_t)$ then
        Output the prediction
    else if $M_1(\mathbf{x}_t) \neq M_2(\mathbf{x}_t)$ then
        Calculate the proportion of each class in the records with disagreeing predictions
        $p(j) = \frac{N_j - \lambda_j \times N_j^c}{\sum_{k=1}^{5} (N_k - \lambda_k \times N_k^c)}, \quad \text{for } j = 1, 2, \ldots, 5$
        Compute record-level prediction probabilities for $\mathbf{x}_t$ in the two trained models $M_1$ and $M_2$
        Compute the model predictions for record $\mathbf{x}_i$
        $p(Y_{\mathbf{x}_t}^s = i) \propto \sum_{j=1}^{5} \left[ p\left(\boldsymbol{Y} = \boldsymbol{i} | \widetilde{\boldsymbol{Y}}^s = \boldsymbol{j}\right) \times p\left(\widetilde{Y}_{\mathbf{x}_t}^s = j\right) \times \frac{N_j - \lambda_j \times N_j^c}{\sum_{k=1}^{5} (N_k - \lambda_k \times N_k^c)} \right]$
        $p\left(Y_{\mathbf{x}_t}^d = i\right) \propto \sum_{j=1}^{5} \left[ p\left(\boldsymbol{Y} = \boldsymbol{i} | \widetilde{Y}^{\boldsymbol{d}} = \boldsymbol{j}\right) \times p\left(\widetilde{Y}_{\mathbf{x}_t}^d = j\right) \times \frac{N_j - \lambda_j \times N_j^c}{\sum_{k=1}^{5} (N_k - \lambda_k \times N_k^c)} \right]$
        Return the label with the highest prediction probability from $p\left(\mathbf{Y}_{\mathbf{x}_t}^s\right)$ and $p\left(\mathbf{Y}_{\mathbf{x}_t}^d\right)$
    end if
end for
Output: hybrid model prediction
```

4.3.2.1 Support Vector Machine for Text-based Classification

Regarding the text data, our objective is to automatically categorize the abnormal event into the correct risk category based on the content of the event synopsis. In the past decades, a large number of statistical and computational methods have been developed for classification based on text data [124, 134], for example, Naïve Bayes [135, 6], support vector machine [136], maximum entropy [137], and others [138]. As described in Section 2.2.1, support vector machine (SVM) has been found to provide a higher prediction accuracy than most other techniques [139] due to the introduction of a structural risk minimization function, which entails finding an optimal hyperplane to separate the different classes with the maximum margin. The structural risk minimization (regularization term) function enables SVM to have a good generalization characteristic, thereby guaranteeing the lower classification error on unseen instances.

The first essential step in applying SVM for text classification is to transform the text data into numerical feature vectors; this is referred to as text representation. Since the text descriptions of the incidents/accidents appear in the form of long sentences in different records, we employ the bag-of-words (BoW) representation to transform the text data into numerical features. Specifically, we utilize the tokenizer in the natural language processing toolbox to split raw text into sentences, words and punctuation [140]. Afterwards, all the stop words and punctuation are eliminated from the BoW representation, and we extract distinct words from all the event synopsis records, assign a fixed integer id to each term present in any event synopsis, and represent the content of a document as a vector in the term space, which is also referred to as a vector space model. However, in many cases, term frequency alone might not be adequate in differentiating the documents. For example, since the word ‘the’ is a very common term that appears in every document, the term frequency method will tend to incorrectly emphasize documents with the usage of frequent terms (such as, ‘the’, ‘a’) but carrying very little information about the contents of the document, while more meaningful terms might be shadowed. As developed by Spärck Jones [141], the term frequency-inverse document frequency (TF-IDF) method overcomes this drawback by determining the relative frequency of a word in a document compared to the inverse proportion of that word across all the documents, which is defined as:

$$\text{tf-idf}(t,d) = \text{tf}(t,d) \times \left(1 + \log \frac{1+n_d}{1+\text{df}(d,t)}\right) \tag{4.1}$$

where $\mathrm{tf}(\mathrm{t},\mathrm{d})$ is the number of occurrences of term t in document d, n_d is the total number of documents, and $\mathrm{df}(\mathrm{d},\mathrm{t})$ is the number of documents that contain the term t.

By performing this operation, we can increase the term's discriminating ability and make the weight of terms suitable to be used by the classifier. Given the TF-IDF vector representation of each event synopsis, we feed it into a support vector machine model in order to identify a hyperplane that separates the different classes with the maximum margin. In the next section, we will discuss the details on how to tune the model parameters in the support vector machine model.

4.3.2.2 Ensemble of Deep Neural Networks

With respect to the structured data, there are 29 different data items after removing the attributes which are empty in 80% of the records. As shown in Fig. 4.2, the structured data can be further classified into three groups: flight conditions, event characteristics, and operations. The flight conditions primarily depict the basic operational condition for each flight, including the weather condition, airport visibility, aircraft characteristics (i.e., model, flight mission, and flight plan), the persons involved (i.e., location of person, reporter organization), and other contributing factors (i.e., ATC equipment, human factors, and communication ambiguity). The flight conditions specify the context in which the accident/incident occurs. Next, the event characteristics describe the important features pertaining to the accident/incident, including the severity of the aircraft equipment problem (less severe or critical), the type of the event (illness, smoke, fire, procedural deviation, or airspace violation), whether passengers were involved in the event, the detecting person, as well as the time when event is detected (routine inspection, maintenance, or in-flight). The event characteristics enable us to have a better resolution in understanding a variety of aspects of the incident, for example, what is the cause of the event, when it happened, and the severity of the problem. Third, when the pilot or other operator is faced with the problem, they take certain measures to resolve the issue (e.g., flight crew took evasive action, or flight crew executed an emergency landing as precaution). All the event outcomes are displayed in the dashed box in the diagram at the bottom right of Fig. 4.2.

Considering the dimension of the input variables, we leverage the deep neural network (DNN, also referred to as deep learning) to learn the associations between the contextual features and event outcomes. Over the last five years, DNN has been proven to be very good at discovering intricate structures in high-dimensional data [30, 103], and has dramatically improved the performance of the state-of-the-art in image classification [142], speech recognition [143], and natural language understanding [144]. Since deep learning requires very little engineering by hand, it can be updated by additional collection of abnormal event records in the ASRS database. Leveraging the powerful capabilities of deep learning, we have developed an ensemble of feedforward deep neural networks in which each network consists of two hidden layers with each hidden layer having 24 and 12 neurons. The construction and performance of the ensemble of deep neural networks will be discussed in the next section.

4.3.3 Model Fusion

As described above, we develop two models: one for the unstructured data, and the other one for the structured data. How to fuse the prediction results of the two trained models is the next challenge. Many approaches have been developed to address this issue, including majority voting schemes (unanimous voting, simple majority, and majority voting), weighted sum, and support function fusion based on the ranking of each predicted class in terms of the estimated likelihood in each individual classifier [145]. Several challenges arise when we attempt to fuse the predictions from the two models by using these strategies. First of all, since there are only two models here, majority voting is not possible when the two models have different predictions. Secondly, as there are five classes in the risk-based event outcome categorization, weighted sum is inappropriate to be implemented in this circumstance. For example, suppose the support vector machine and the deep neural network ensemble have 60% and 80% overall prediction accuracy, respectively. Now they are given a new test record (not used in training), and suppose the predictions from the SVM and DNN models are classes 1 and 5, respectively. In this case, the model prediction after we perform a simple weighted sum operation will be $\frac{0.6}{0.6+0.8} \times 1 + \frac{0.8}{0.6+0.8} \times 5 = 3.28$, which does not make any sense. Note also that the fused prediction result needs to be an integer. Even if we take certain operations (e.g., rounding, flooring) to transform the decimal into an integer, the model prediction (3) after the transformation might be the least probable prediction in the two models. Consequently, the weighted sum operation is inappropriate to be implemented in this problem.

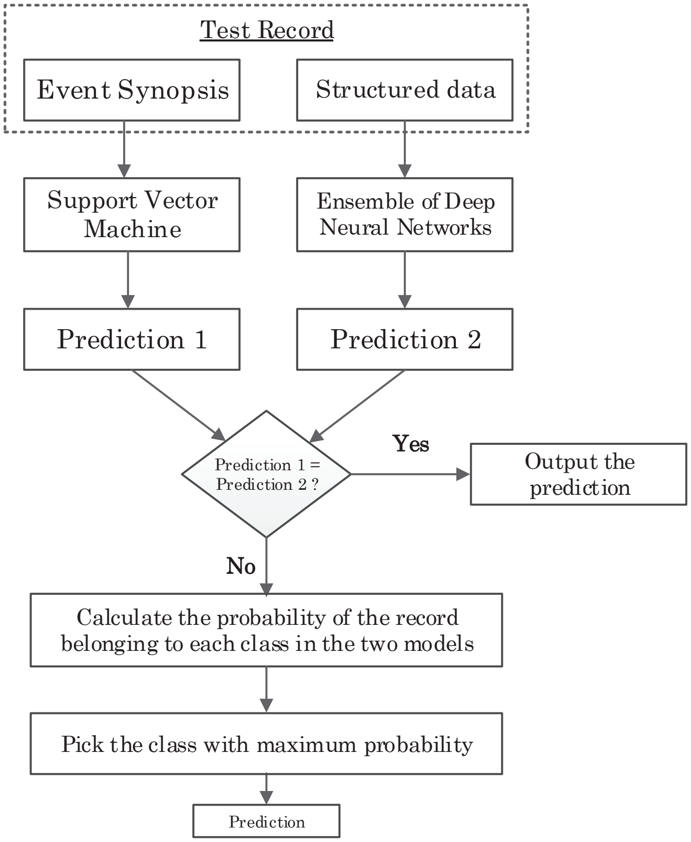
Test Record
Event Synopsis
Structured data
Support Vector Machine
Ensemble of Deep Neural Networks
Prediction 1
Prediction 2
Prediction 1 = Prediction 2 ?
Yes
Output the prediction
No
Calculate the probability of the record belonging to each class in the two models
Pick the class with maximum probability
Prediction

Figure 4.4: Proposed fusion rule to integrate the two models

We develop a probabilistic fusion rule to blend the predictions from the two models. The framework of the proposed fusion rule is demonstrated in Fig. 4.4. In the first place, if the two models have the same prediction (prediction 1 = prediction 2), then the prediction result is easy to be determined. If the two models have different predictions, then we calculate the probability of the test record belonging to each class among the five risk categories in each model. To illustrate the proposed method, Table 4.4 reports the performance metrics of the two models on a validation dataset. The validation dataset consists of N_1, N_2, N_3, N_4, and N_5 records in the five respective classes, where $A^s_{i,j}$ and $A^d_{i,j}$ represents the number of records that actually belong to class i but are labelled as class j in the support vector machine and DNN ensemble, respectively. The third to the seventh columns present the confusion matrix of the trained support vector machine on the validation dataset, while the confusion matrix of the deep learning ensemble is reported in the thirteenth to seventeenth column. The ninth column of Table 4.4 reports the number of consistent predictions between the two trained models on the validation dataset, while the tenth column reports the accuracy of the correctly labeled records among the consistent predictions of the two models in the validation dataset.

When the two models have disagreeing predictions, one important underlying mechanism when developing the fusion strategy is: since no model is perfect, each model is expected to have misclassifications or make erroneous predictions. However, the valuable information embodied in the misclassifications should be further utilized to correct the model predictions on the subsequent unseen test dataset in a way that makes up the class that the observation should belong to if we know how often the model mislabels the class as other classes. Considering the various types of misclassifications that the trained model is prone to make, one way to achieve this objective is to increase the probability of labeling the observation as the correct class, while reducing the probability of labeling the record as the predicted class given by the model. Fortunately, such information can be derived from the confusion matrix. In fact, a confusion matrix not only provides class-level model prediction accuracy, but also the probability of mislabeling a record as other classes. Next, we will utilize the model misclassification probability to correct the model prediction on new test records. Suppose the two models have different predictions on a new test record *a*; there are three important considerations in determining the probability of the new test record *a* belonging to each of the five classes *i* in the two models:

1. Record-level prediction probabilities: As mentioned earlier, two models have been trained: support vector machine and a deep neural network ensemble. The record-level probability $p(\widetilde{Y}_a = i)$ measures the probability that the trained model assigns the test record *a* to a given class *i*. To be specific, with respect to the DNN ensemble, the record-level prediction probabilities can be measured as the ratio of the most frequent prediction to the total number of model predictions (which is 10, in this case). For example, if the most frequent prediction of the ten models is class 5, and it appears six times out of the ten model predictions, then the model prediction probability for this particular record belonging to class 5 is $6/10$ (0.6). Regarding the support vector machine, since samples far away from the separating hyperplane are presumably more likely to be classified correctly, we can use the distance from the hyperplane as a measure of record-level prediction probability following the method introduced in Ref. [146].

2. Proportion of each class in the records with disagreeing predictions: When the two models are trained, there are the same number of records belonging to each class in the training dataset. In other words, the data is balanced for each class in the training dataset. However, when we use the trained models to make predictions on test records, we only need decisions when the two trained models have inconsistent predictions. With respect to the set of disagreeing predictions, the actual proportion of records belonging to each class might be different (imbalanced) from the training dataset (balanced). The use of the model trained by the balanced class distribution will result in a biased estimator if it is directly utilized for making predictions on the set of records with inconsistent model predictions.

   To address this issue, we introduce a weight factor to correct the trained model to fit the class distribution in the set of records with disagreeing model predictions, thereby ensuring that the updated estimator is unbiased. The number of records with consistent model predictions in each class is complementary to the amount of records with inconsistent model predictions in that class. In general, the more records the two classifiers agree on, the less the number of records the two classifiers disagree on. As a result, we formulate the following equation to represent the total number of records with inconsistent model predictions across all the classes considered:

$$T = \sum_{i=1}^{5} \left(N_i - \lambda_i \times N_i^c\right) \tag{4.2}$$

where i is the class label, N_i denotes the actual number of records that should have been labeled as class i, N_i^c represents the number of consistent predictions between the two models on all the records, and λ_i is the model accuracy with respect to the consistent predictions.

Considering the total number of disagreeing predictions across all the classes, the proportion w.r.t. class j is:

$$p(j) = \frac{N_j - \lambda_j \times N_j^c}{T} \tag{4.3}$$

Given the already correctly labeled samples by the two trained models, the probability of a new test record a that results in disagreeing predictions between the two models belonging to class j is $p(j)$.

3. Class-level accuracy: This measures the degree of consistency between model predictions and actual observations. Mathematically, it can be represented as: $p\left(\boldsymbol{Y} = \boldsymbol{i} | \widetilde{\boldsymbol{Y}} = \boldsymbol{j}\right)$, where $\widetilde{\boldsymbol{Y}} = \boldsymbol{j}$ represents the samples with model predictions being class j, and p $\left(\boldsymbol{Y} = \boldsymbol{i} | \widetilde{\boldsymbol{Y}} = \boldsymbol{j}\right)$ $(\boldsymbol{j} \neq \boldsymbol{i})$ quantifies the proportion of samples with model predictions being class j that should have been labeled as class i. In particular, when $\boldsymbol{j} = \boldsymbol{i}$, then $p\left(\boldsymbol{Y} = \boldsymbol{i} | \widetilde{\boldsymbol{Y}} = \boldsymbol{i}\right)$ measures the ratio of samples actually belonging to class i to the number of samples with model predictions being class i, which can also be

referred to as a likelihood function. In other words, the likelihood function measures the probability of observing the data given the prediction. Such a quantitative metric $p\left(\boldsymbol{Y} = \boldsymbol{i} | \widetilde{\boldsymbol{Y}} = \boldsymbol{i}\right)$ measures the accuracy of the trained model in making predictions with respect to class i.

If we only consider the special case $(\boldsymbol{i} = \boldsymbol{j})$, then the Bayes factor (or likelihood ratio) can be used to help decide which model supports our observation better from the two trained models, thereby assisting the model selection [147]. However, the Bayes factor does not consider the information embodied in the model misclassifications. Therefore, we propose an equation below to handle all the possible situations existing in the five-class classification problem by utilizing the information contained in the term $p\left(\boldsymbol{Y} = \boldsymbol{i} | \widetilde{\boldsymbol{Y}} = \boldsymbol{j}\right)$. The quantitative metric $p\left(\boldsymbol{Y} = \boldsymbol{i} | \widetilde{\boldsymbol{Y}} = \boldsymbol{j}\right)$ is equivalent to the confusion matrix used in the performance evaluation on the validation dataset. By utilizing the metric $p\left(\boldsymbol{Y} = \boldsymbol{i} | \widetilde{\boldsymbol{Y}} = \boldsymbol{j}\right)$, we relate the model predictions to the actual observations, from which we compute the probability of a test record a actually belonging to a given class i in the subsequent sections.

For a given new test record a, the proposed fusion rule based on the above three considerations is:

$$p\left(Y_a = i\right) = \sum_{j=1}^{5} \left[p\left(\boldsymbol{Y} = \boldsymbol{i} | \widetilde{\boldsymbol{Y}} = \boldsymbol{j}\right) p\left(\widetilde{Y}_a = j\right) \times \frac{p\left(j\right)}{\widetilde{p}\left(j\right)} \right] \tag{4.4}$$

where $p\left(\boldsymbol{Y} = \boldsymbol{i} | \widetilde{\boldsymbol{Y}} = \boldsymbol{j}\right) (\boldsymbol{j} \neq \boldsymbol{i})$ is the model misclassification rate, in which the model prediction is class j while the actual observation is class i; when $\boldsymbol{j} = \boldsymbol{i}$, then $p\left(\boldsymbol{Y} = \boldsymbol{i} | \widetilde{\boldsymbol{Y}} = \boldsymbol{i}\right)$ denotes the model prediction precision with respect to class i, $p\left(j\right)$ is the proportion of class j in the set of inconsistent model predictions, $\widetilde{p}\left(j\right)$ represents the proportion of class j in the training dataset, and $p\left(\widetilde{Y}_a = j\right)$ represents the confidence of the model in classifying the test record a as class j.

Table 4.4: Performance metrics for the two trained models. Here, the support column denotes the number of occurrences of each class in the actual observation, the consistent prediction column represents the number of consistent predictions between the two models for each class, and consistent prediction accuracy denotes the proportion of records in the consistent model predictions that are correctly labeled. The five numerical values 1, 2, 3, 4, and 5 denote the five risk categories from low risk to high risk

Support Vector Machine							**Shared Attributes**			**Deep Learning Ensemble**						
		Predicted Label					Support	Consistent Prediction	Consistent Prediction Accuracy			**Predicted Label**				
		1	2	3	4	5						1	2	3	4	5
True Label	1	$A^s_{1,1}$	$A^s_{1,2}$	$A^s_{1,3}$	$A^s_{1,4}$	$A^s_{1,5}$	N_1	N^c_1	λ_1	**True Label**	1	$A^d_{1,1}$	$A^d_{1,2}$	$A^d_{1,3}$	$A^d_{1,4}$	$A^d_{1,5}$
	2	$A^s_{2,1}$	$A^s_{2,2}$	$A^s_{2,3}$	$A^s_{2,4}$	$A^s_{2,5}$	N_2	N^c_2	λ_2		2	$A^d_{2,1}$	$A^d_{2,2}$	$A^d_{2,3}$	$A^d_{2,4}$	$A^d_{2,5}$
	3	$A^s_{3,1}$	$A^s_{3,2}$	$A^s_{3,3}$	$A^s_{3,4}$	$A^s_{3,5}$	N_3	N^c_3	λ_3		3	$A^d_{3,1}$	$A^d_{3,2}$	$A^d_{3,3}$	$A^d_{3,4}$	$A^d_{3,5}$
	4	$A^s_{4,1}$	$A^s_{4,2}$	$A^s_{4,3}$	$A^s_{4,4}$	$A^s_{4,5}$	N_4	N^c_4	λ_4		4	$A^d_{4,1}$	$A^d_{4,2}$	$A^d_{4,3}$	$A^d_{4,4}$	$A^d_{4,5}$
	5	$A^s_{5,1}$	$A^s_{5,2}$	$A^s_{5,3}$	$A^s_{5,4}$	$A^s_{5,5}$	N_5	N^c_5	λ_5		5	$A^d_{5,1}$	$A^d_{5,2}$	$A^d_{5,3}$	$A^d_{5,4}$	$A^d_{5,5}$

By substituting Eq. (4.3) into Eq. (4.4), we have:

$$p\left(Y_a = i\right) = \sum_{j=1}^{5}\left[p\left(\boldsymbol{Y} = \boldsymbol{i}|\widetilde{\boldsymbol{Y}} = \boldsymbol{j}\right)p\left(\widetilde{Y}_a = j\right)\times\frac{1}{\widetilde{p}\left(j\right)}\times\frac{N_j - \lambda_j \times N_j^c}{T}\right] \tag{4.5}$$

Since all the five classes are evenly distributed in the training dataset, $\widetilde{p}\left(j\right)$ is a constant, which can be ignored, then we have:

$$p\left(Y_a = i\right) \propto \sum_{j=1}^{5}\left[p\left(\boldsymbol{Y} = \boldsymbol{i}|\widetilde{\boldsymbol{Y}} = \boldsymbol{j}\right)p\left(\widetilde{Y}_a = j\right)\times\frac{N_j - \lambda_j \times N_j^c}{T}\right] \tag{4.6}$$

Next, we perform the normalization operation following Eq. (4.7) such that the sum of the probability over the five classes in each model is 1.

$$p\left(Y_a = i\right) = \frac{\sum\limits_{j=1}^{5}\left[p\left(\boldsymbol{Y} = i|\widetilde{\boldsymbol{Y}} = \boldsymbol{j}\right)p\left(\widetilde{Y}_a = j\right)\times\frac{N_j - \lambda_j \times N_j^c}{T}\right]}{\sum\limits_{i=1}^{5}\sum\limits_{j=1}^{5}\left[p\left(\boldsymbol{Y} = \boldsymbol{i}|\widetilde{\boldsymbol{Y}} = \boldsymbol{j}\right)p\left(\widetilde{Y}_a = j\right)\times\frac{N_j - \lambda_j \times N_j^c}{T}\right]} \tag{4.7}$$

With respect to the support vector machine, the likelihood function $p\left(\boldsymbol{Y} = \boldsymbol{i}|\widetilde{\boldsymbol{Y}} = \boldsymbol{j}\right)$ is calculated as:

$$p\left(\boldsymbol{Y} = \boldsymbol{i}|\widetilde{\boldsymbol{Y}}^{\boldsymbol{s}} = \boldsymbol{j}\right) = \frac{A_{i,j}^s}{\sum\limits_{i=1}^{5} A_{i,j}^s} \tag{4.8}$$

where $A_{i,j}^s$ denotes the number of samples with model predictions being class j, but actually belonging to class i in the validation dataset.

In a similar way, the metric $p\left(\boldsymbol{Y} = \boldsymbol{i}|\widetilde{\boldsymbol{Y}} = \boldsymbol{j}\right)$ in the DNN ensemble is computed accordingly. Given the model classification performance $p\left(\boldsymbol{Y} = \boldsymbol{i}|\widetilde{\boldsymbol{Y}} = \boldsymbol{j}\right)$, the probability of test record *a* belonging to each class in each model is computed as below:

$$\begin{aligned}
p\left(Y_a^s=i\right) &\propto \sum_{j=1}^{5}\left[p\left(\boldsymbol{Y}=\boldsymbol{i}|\widetilde{\boldsymbol{Y}}^{s}=\boldsymbol{j}\right)\times p\left(\widetilde{Y}_a^s=j\right)\times\frac{N_j-\lambda_j\times N_j^c}{\sum_{k=1}^{5}\left(N_k-\lambda_k\times N_k^c\right)}\right]\\
&\propto \sum_{j=1}^{5}\left[\frac{A_{i,j}^s}{\sum_{i=1}^{5}A_{i,j}^s}\times p\left(\widetilde{Y}_a^s=j\right)\times\frac{N_j-\lambda_j\times N_j^c}{\sum_{k=1}^{5}\left(N_k-\lambda_k\times N_k^c\right)}\right]\\
p\left(Y_a^d=i\right) &\propto \sum_{j=1}^{5}\left[p\left(\boldsymbol{Y}=\boldsymbol{i}|\widetilde{Y}^{\boldsymbol{d}}=\boldsymbol{j}\right)\times p\left(\widetilde{Y}_a^d=j\right)\times\frac{N_j-\lambda_j\times N_j^c}{\sum_{k=1}^{5}\left(N_k-\lambda_k\times N_k^c\right)}\right]\\
&\propto \sum_{j=1}^{5}\left[\frac{A_{i,j}^d}{\sum_{i=1}^{5}A_{i,j}^d}\times p\left(\widetilde{Y}_a^d=j\right)\times\frac{N_j-\lambda_j\times N_j^c}{\sum_{k=1}^{5}\left(N_k-\lambda_k\times N_k^c\right)}\right]\\
&\cdots\cdots
\end{aligned} \tag{4.9}$$

where $p\left(Y_a^s=i\right)$ and $p\left(Y_a^d=i\right)$ represent the probability of support vector machine and deep learning models in labeling the test record as class *i*, the term $\frac{N_j-\lambda_j\times N_j^c}{\sum_{k=1}^{5}N_k-\lambda_k\times N_k^c}$ in Eq. (4.9) denotes the proportion of records belonging to class *j* in the set of inconsistent model predictions; the terms $A_{i,j}^s$ and $A_{i,j}^d$ represent the samples belonging to class *i* but labeled as class *j* in the two respective models, and $p\left(\widetilde{Y}_a^s=j\right)$ and $p\left(\widetilde{Y}_a^d=j\right)$ are the prediction confidence of the two respective models to classify the test record *a* as class *j*.

After normalizing the probability of the test record *a* belonging to each class in each model, we select the predicted class with the maximum probability from the two models as the hybrid model prediction. By considering the three factors, the proposed method successfully adjusts the trained model to suit the classification with respect to the records within the inconsistent model predictions. After we obtain the probability of the test record belonging to each class in each model, then we assign the test record to the class with the maximum probability.

4.3.4 Event-level Outcome Analysis

After the risk-level category that the test record should belong to is probabilistically determined, then event-level outcome can be derived by measuring the event synopsis similarity between the test record a and other records belonging to the same risk category. One popular way to measure document similarity is based on the content overlap between two documents [148] as represented in Eq. (4.10).

$$\text{sim}\left(d_i, d_j\right) = \frac{\sum\limits_{m=1}^{k} w_{m,i} \times w_{m,j}}{\sqrt{\sum\limits_{m=1}^{k} \left(w_{m,i}\right)^2} \times \sqrt{\sum\limits_{m=1}^{k} \left(w_{m,j}\right)^2}} \tag{4.10}$$

where d_i and d_j denote two documents, $w_{m,i}$ ($w_{m,j}$) is the frequency of object (words, or terms) o_m present in document d_i (d_j), and k is the number of unique objects across all the documents.

The similarity metric defined in Eq. (4.10) measures the cosine of the angle between vector-based representations of the two documents. Since there are multiple documents belonging to the same risk category as the test record a, we formulate the following equation to address such issues:

$$p\left(e = k \,|\, Y_a = j\right) = \frac{1}{c_k} \sum_{v=1}^{c_k} \text{sim}\left(d_a, d_{I(v)}\right) \tag{4.11}$$

where c_k denotes the number of records having event outcome k in the training dataset, and $I(v)$ denotes the index of the v-th record having event outcome k in the training dataset.

Afterwards, a normalization operation can be performed by taking into account all the possible event outcomes in the j-th risk category.

$$p\left(e = k \,|\, Y_a = j\right) = \frac{p\left(e = k \,|\, Y_a = j\right)}{\sum\limits_{k=1}^{K} p\left(e = k \,|\, Y_a = j\right)} \tag{4.12}$$

where K represents the number of possible event consequences in the j-th risk category.

By considering the event outcomes in the corresponding risk category, a decision tree can be constructed to demonstrate the probability of each event to occur. In this way, the risk-level category can be mapped to event-level outcome.

4.3.5 Summary

The methodology developed in this section tackles the problem of risk quantification regarding the consequences of abnormal events in the national airspace system with a four-step procedure (see Fig. 4.2):

1. We reorganize all the incidents/accidents based on the risk associated with the consequence of each hazardous event. The risk-based event outcome categorization enables us to collapse the original 36 unique event outcomes into five groups, and project the event outcome to the dimension of risk quantification in the representation of five risk groups: high risk, moderately high risk, medium risk, moderately medium risk, and low risk. Considering the five risk groups, up-sampling is performed to balance the number of records between minority classes and majority classes.

2. Two models are developed to process the structured data and unstructured data, respectively. To handle the structured data in high dimension, an ensemble of deep neural networks are trained to associate the event contextual features with the event outcomes. A support vector machine model is used to discover the relationships between event synopsis and event consequence.

3. A probabilistic fusion decision rule is developed to blend the predictions by the two machine learning models. When the prediction results are inconsistent, a quantitative metric is proposed to compute the likelihood that the test record belongs to each predicted class, from which we can determine the class the test record should be assigned to.

4. Once the test record is assigned to a specific risk category, we map the risk-level category to event-level outcomes through a probabilistic tree, in which all the possible event outcomes in the corresponding risk category are considered.

4.4 Computational Results

4.4.1 Data Description

We collected 12 years of incident reports (from January 2006 to December 2017) from ASRS, thus obtaining 64,573 records. The number of records belonging to each risk class is shown in Table 4.5. To address the imbalance, we up-sample the three minority classes (high, moderately high, and moderately medium) with replacement to get the same amount of data as in the majority class to form a balanced dataset. After up-sampling, the dataset contains 18,841 records for the high, moderately high, medium, and moderately medium risk classes respectively, and 16,508 number of records in the low risk category. After the up-sampling operation, there are 91,872 number of records in total.

Table 4.5: The number of records belonging to each risk category

Class	High	Moderately high	Medium	Moderately medium	Low
Number of records	12327	8261	18841	8636	16508

All the input variables are summarized in Fig. 4.5, and they are grouped into two categories: unstructured data and structured data. The structured data includes 29 different variables ranging from aircraft information to event characteristics, while the unstructured (text) data only includes event synopsis. With the 29 structured variables and one unstructured variable, we train the SVM and DNN models.

Table 4.6: Confusion matrix

	Predicted as positive	Predicted as negative
Actually positive	True Positives (TP)	False Negative (FN)
Actually negative	False Positives (FP)	True Negative (TN)

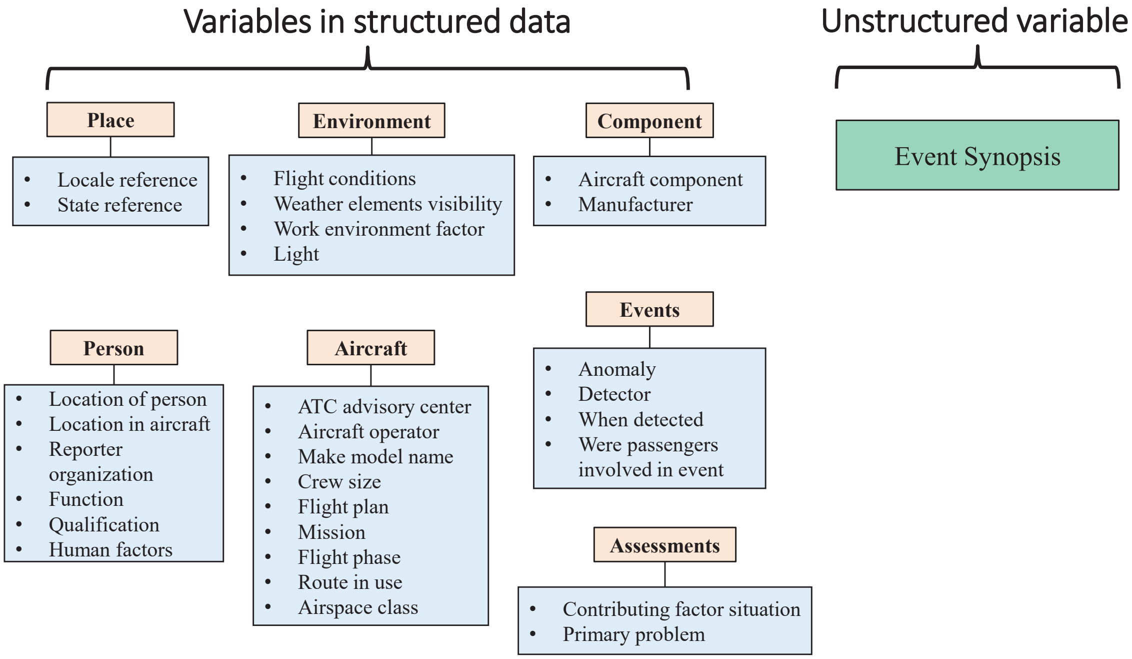

Figure 4.5: Datasets and model inputs

Given a trained classifier and a test dataset, the relationship between model predictions and true observations can be represented as a confusion matrix, as illustrated in Table 4.6. To assess the performance of every machine learning model, we adopt three most commonly used performance metrics.

1. Precision: Mathematically, Precision ($\frac{\text{TP}}{\text{TP} + \text{FP}}$) is the ratio of correctly predicted positive observations to the total predicted positive observations, and high precision typically corresponds to low false positive predictions.

2. Recall: Recall is defined as Recall ($\frac{\text{TP}}{\text{TP} + \text{FN}}$) quantifies the ratio of correctly labeled positive observations to all the positive observations in the actual class. It measures the ability of the trained model in identifying positive observations from all the samples that should have been labeled as positive.

3. The F1 score is the weighted average of precision and recall, which is mathematically described as $\text{F1} = 2 \times \frac{\text{precision} * \text{recall}}{\text{precision} + \text{recall}}$. In the F1 score, the relative contribution of

precision and recall is the same. In other words, the F1-measure is the harmonic mean of precision and recall.

4.4.2 Experimental Analysis

We split the 91,872 records into three parts: training set (85%), validation set (5%), and test set (10%). The training set is used to guide the machine learning algorithms to optimize the relevant parameters so as to minimize prediction error; the validation set is utilized to develop the performance metrics for an unseen dataset (i.e., prediction accuracy). With the performance metrics obtained from the validation dataset, we then blend the predictions from the two trained models for the test dataset.

Regarding the SVM estimator for text classification, we leverage grid search to optimize the relevant hyperparameters. Specifically, we optimize the loss function (hinge, log, perceptron, squared loss, etc.), the regularization function ($l1, l2$, or elasticnet), the coefficient of regularization function ($\left[10^{-2}, 10^{-5}\right]$), and the range of N-gram (N-gram is a contiguous sequence of n items from a given sample of text). The grid search exhaustively generates candidates from the set of parameter values, and evaluates all the possible combinations of parameter values on the training dataset and selects the best combination. After the optimal hyperparameters are identified, we run the trained support vector machine algorithm on the validation data to obtain its performance metrics. The left part of Table 4.7 reports the performance metrics of the trained support vector machine model on the validation dataset.

In the DNN model, all the categorical features are encoded using one hot encoding. We randomly select 85% records from the training dataset to train a deep neural network, then we repeat the same procedure ten times to obtain an ensemble of deep neural networks. Every DNN has the same structure – 8 hidden layers and 40 neurons per layer. We choose an Adam Optimizer [149] with a learning rate of 0.001 to perform backward propagation in adjusting the weight variables with the objective of minimizing the categorical cross

Table 4.7: Performance metrics for the two trained models. Here, the support column denotes the number of occurrences of each class in the actual observation, the consistent prediction column represents the number of consistent predictions between the two models for each class, and consistent prediction accuracy denotes the proportion of records in the consistent model predictions that are correctly labeled. The five numerical values 1, 2, 3, 4, and 5 denote the five risk categories from low risk to high risk

Support Vector Machine							**Shared Attributes**			**Deep Neural Networks**						
		Predicted Label					Support	Consistent Prediction	Consistent Prediction Accuracy			**Predicted Label**				
		1	2	3	4	5						1	2	3	4	5
True Label	1	550	82	205	69	41	947	491	0.82	**True Label**	1	567	74	204	46	56
	2	14	951	27	13	12	1017	988	0.93		2	25	931	28	5	28
	3	153	65	592	119	59	988	448	0.76		3	208	72	495	97	116
	4	16	7	43	943	25	1034	936	0.96		4	19	11	48	927	29
	5	20	17	34	22	883	976	861	0.93		5	38	27	45	28	838

entropy as defined in Eq. (4.13).

$$L\left(\boldsymbol{Y}, \widetilde{\boldsymbol{Y}}^{d}\right) = -\frac{1}{n}\sum_{i=1}^{n}\left[Y_i \log \widetilde{Y}_i^{d}\right] \tag{4.13}$$

where n is the number of training samples, Y_i is a one-hot-encoding representation of the actual observation with the corresponding class label being 1 and the values of other classes being zero, and $\widetilde{Y}_i^{d}$ is the probabilistic estimation of ensemble deep learning models on the record i.

After the ten deep neural networks are trained, we use them to make predictions on the validation dataset, and the results are reported in Table 4.7. It is observed that the DNN ensemble does not perform as well as the SVM model in terms of precision and recall for classes 2, 3, and 5 due to the low level of information contained in the categorical features. As shown in the ninth column of Table 4.7, the two trained models agree on 491, 988, 448, 936, and 961 predictions with respect to the five classes. Among the consistent predictions of the two models, 401, 922, 339, 897, and 804 predictions with respect to the five classes are correctly classified, from which we can compute the ratio of consistent predictions that are correctly labeled in the validation dataset. Next, we utilize the two trained models to make predictions on the test dataset. With the performance metrics acquired on the validation dataset, we blend the predictions of the two models. Suppose the two models have probabilistic classifications on the test record a as shown in Table 4.8; each cell represents the probability that the test example a is a member of the class. Regarding the test record a, the SVM model supports class 5 the most, whereas the DNN ensemble assigns the highest probability to class 2.

Table 4.8: Model predictions with respect to test record a

Model	1	2	3	4	5
SVM	0.10	0.20	0.20	0.20	0.30
DNN	0.20	0.40	0.10	0.02	0.28

Following the method introduced before, the total number of inconsistent model predictions is $T = (947-401)+(1017-922)+(988-339)+(1034-897)+(976-804) = 1599$. Then the proportion of each class in the disagreeing records is calculated as:

$$\boldsymbol{p} = \begin{bmatrix} 0.34 & 0.06 & 0.40 & 0.09 & 0.11 \end{bmatrix}$$

Then the probability of assigning the test record a to class 1 in the SVM model is computed as:

$$\begin{aligned}
&p\left(Y_a^s = 1\right) \propto \sum_{j=1}^{5} \left[p\left(Y = 1|\widetilde{Y}^s = j\right) \times p\left(\widetilde{Y}^s = j\right) \times p\left(j\right)\right] \\
&= \tfrac{550}{550+14+153+16+20} \times 0.1 \times 0.34 + \tfrac{82}{82+951+65+7+17} \times 0.2 \times 0.06 \\
&+ \tfrac{205}{205+27+592+43+34} \times 0.2 \times 0.4 + \tfrac{69}{69+13+119+943+22} \times 0.2 \times 0.09 \\
&+ \tfrac{41}{41+12+59+25+883} \times 0.3 \times 0.11 \\
&= \mathbf{0.0468}
\end{aligned}$$

In a similar way, the probabilities of labeling the test record a as other classes in the SVM model is calculated:

$$\begin{aligned}
&p\left(Y_a^s = 2\right) \propto 0.0137, p\left(Y_a^s = 3\right) \propto 0.0646 \\
&p\left(Y_a^s = 4\right) \propto 0.0193, p\left(Y_a^s = 5\right) \propto 0.0324
\end{aligned}$$

After normalization, the probability of the test record belonging to each class in the SVM model is:

$$\begin{aligned}
&p\left(Y_a^s = 1\right) = 0.26, p\left(Y_a^s = 2\right) = 0.08, p\left(Y_a^s = 3\right) = 0.37, \\
&p\left(Y_a^s = 4\right) = 0.11, p\left(Y_a^s = 5\right) = 0.18.
\end{aligned}$$

Likewise, with the DNN ensemble, the probabilities of the test record a belonging to class 1 to 5 are calculated as:

$$\begin{aligned}
&p\left(Y_a^d = 1\right) = 0.35, p\left(Y_a^d = 2\right) = 0.15, p\left(Y_a^d = 3\right) = 0.28, \\
&p\left(Y_a^d = 4\right) = 0.04, p\left(Y_a^d = 5\right) = 0.18.
\end{aligned}$$

From the above computational results, test record a has the highest probability (0.37) of being labeled as class 3 in the SVM model. As a result, this test record a is assigned to class 3 in the hybrid model. For the remaining test records, we blend the two model predictions in a similar manner.

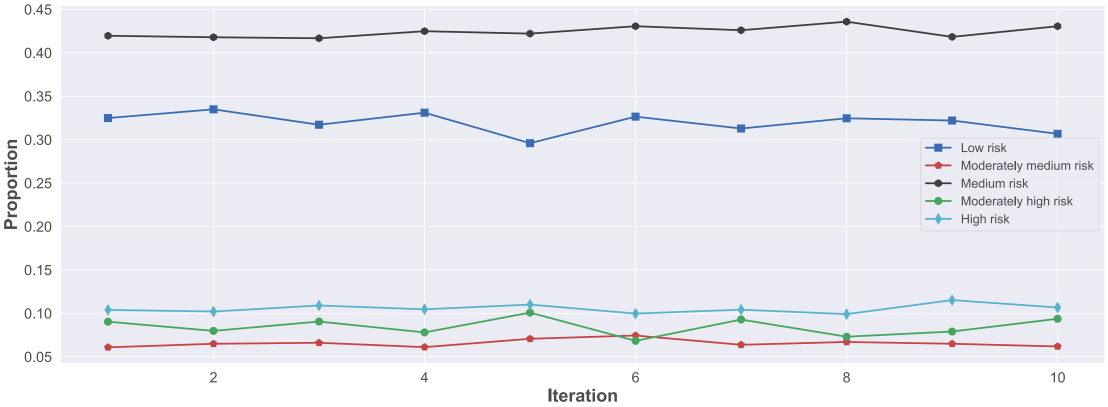

Figure 4.6: Proportion of each class in the records with disagreeing predictions

To compare the performance of all the investigated models, we randomly split the original dataset into ten equal sized groups to perform ten-fold cross-validation. The procedure presented in Algorithm 1 is repeated over the ten equal sized groups. Fig. 4.6 shows the proportions of five risk categories in the records with disagreeing predictions. Among the five risk categories, the medium risk class has the largest proportion of records with disagreeing predictions, followed by low risk and high risk classes. The proportion of each class with disagreeing prediction is relatively stable with a small variability. Due to the imbalanced class distribution in the records with disagreeing predictions, the adjustment factor introduced in Eq. (4.4) plays an essential role in embodying such information in the subsequent hybrid model predictions.

In addition, we implement ordinal logistic regression (OLR) for the purpose of comparing its performance with the DNN ensemble on the structured data [150, 151]. The computational result of ten-fold cross-validation for the four models is demonstrated as a boxplot in Fig. 4.7. It is worth noting that we shift the values of the three performance indicators of ordinal logistic regression by +0.4 for the sake of demonstrating the four models' performance deviation clearly. As can be observed, the hybrid model outperforms SVM, DNN ensemble, and OLR in terms of precision, recall and F1 score. More importantly, the hybrid model has a much smaller deviation for all the performance metrics when compared to all the other three models. In other words, it has the most stable prediction capability, thereby making it the best candidate for quantifying the risk of abnormal events. Since OLR is inferior to the other three models, we do not analyze its performance any further. From a quantitative viewpoint, based on the cross-validation results, the proposed hybrid model yields a better performance in precision, with an average score of 0.81, 3% higher than the scores of SVM and 6% higher than DNN ensemble models. The proposed hybrid model also outperforms the other two models regarding the recall rate. In other words, the hybrid model has a better performance in correctly identifying the records that actually belong to each class. Besides, the F1 score of the hybrid model is 3% higher than the support vector machine and 6% higher than deep neural networks on average. Regarding the predictions on the structured data, ordinal logistic regression performs much worse than deep learning ensemble. In summary, the proposed decision rule to fuse the predictions from the two models is effective in enhancing the hybrid model performance.

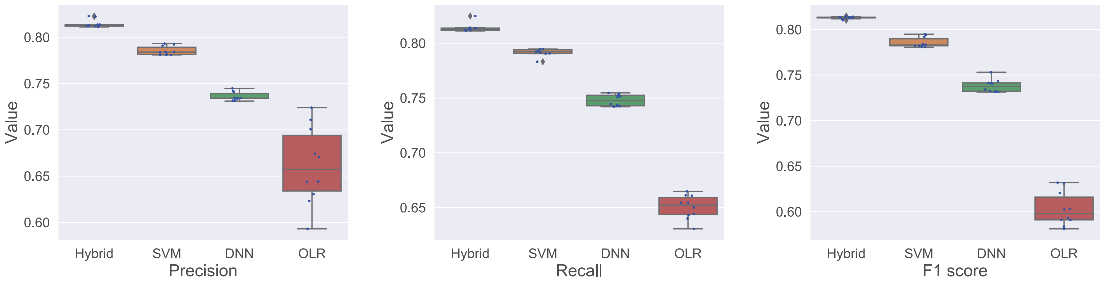

Figure 4.7: The performance of hybrid model versus support vector machine (SVM), ensemble of deep neural networks (DNN), and ordinal logistic regression (OLR)

In addition to the boxplot illustrated in Fig 4.7, statistical t-test is also used to check whether there is a significant difference in the prediction performance of the four models [152]. Specifically, we make a null hypothesis that the means of population from hybrid model and any other individual model are the same, and rejection of this hypothesis indicates that there is sufficient evidence that the means of the populations are significantly different, while failing to reject this hypothesis reveals that the distributions are identical. The t-test rejected the null hypothesis for all three aforementioned performance indicators, thus implying that there is a statistically significant improvement in the performance of the hybrid model compared to the SVM, DNN ensemble and OLR models.

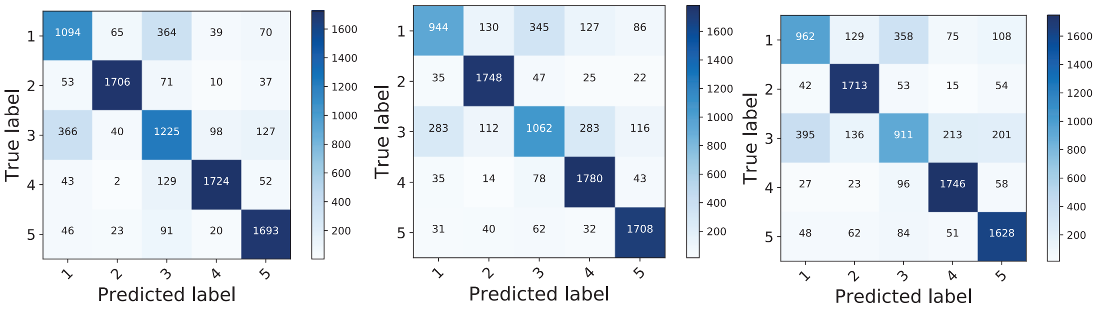

Figure 4.8: Confusion matrix. (a) the hybrid method, (b) support vector machine, (c) deep neural networks. The entry in the *i*-th row and *j*-th column corresponds to the percentage of samples from class *i* that were classified as class *j*. 1: low, 2: moderately medium, 3: medium, 4: moderately high, 5: high

Fig. 4.8 shows the confusion matrices of the three trained models for the five considered classes in one test case. It can be observed that the hybrid method significantly increases the number of correct predictions for class 1 and class 3, while maintaining the prediction accuracy for the remaining three classes almost at the same level as the other two algorithms. The confusion matrices in Fig. 4.8 provide comprehensive information in terms of the number of correctly identified observations in each class. Across the five risk groups, the hybrid model correctly identifies 200 more observations than the SVM model. Besides, confusion matrices also embody the misclassification information. As illustrated in Fig. 4.8, it is most probable for all the three models to misclassify the records in class 1 as class 3, and vice versa. Such information can be utilized to guide the further refinement of the hybrid model.

Table 4.9: Event synopsis of test record *a*

Date	**Event Synopsis**
March, 2017	After initiating descent on a visual approach with glideslope out of service; an A319 Flight Crew initiated a go-around when flight director caused airspeed increase and climb to intercept altitude set for ILS to previously assigned runway.

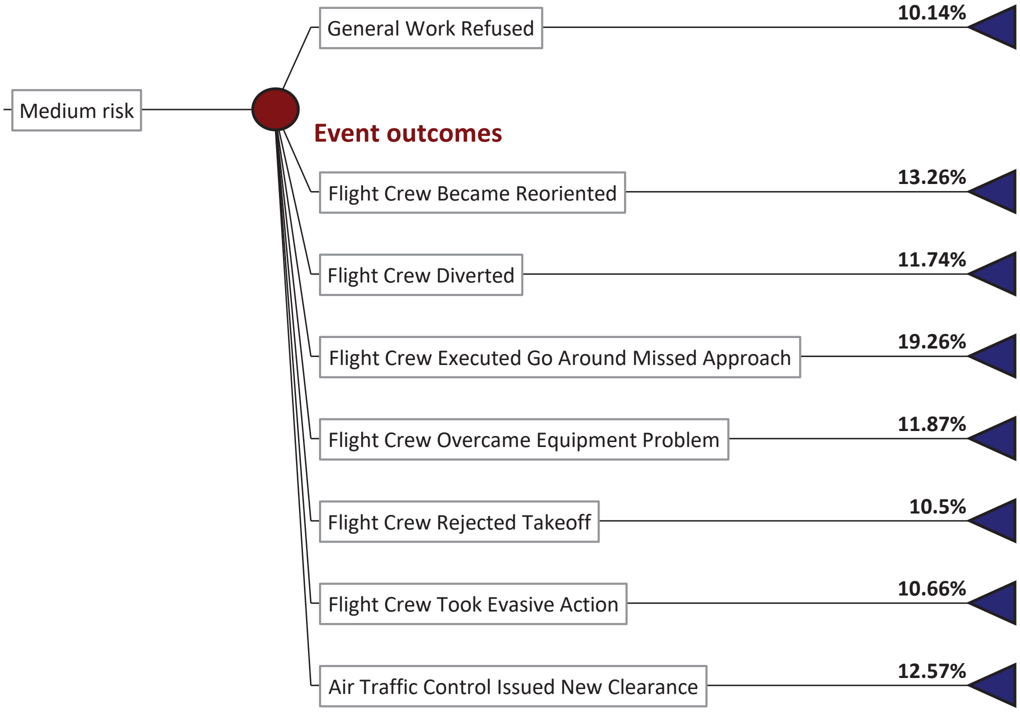
Medium risk
Event outcomes
General Work Refused
10.14%
Flight Crew Became Reoriented
13.26%
Flight Crew Diverted
11.74%
Flight Crew Executed Go Around Missed Approach
19.26%
Flight Crew Overcame Equipment Problem
11.87%
Flight Crew Rejected Takeoff
10.5%
Flight Crew Took Evasive Action
10.66%
Air Traffic Control Issued New Clearance
12.57%

Figure 4.9: The probabilistic event outcomes for test record *a*

Considering that the test record *a* is labeled as class 3 (medium risk), and the event synopsis of the test record *a* is shown in Table 4.9, then a tree is built to demonstrate the likelihood of the occurrence of every event outcome in the medium risk category. By measuring the similarity between the event synopsis of test record *a* and that of other records in the medium risk category, the probability for test record *a* having each outcome is obtained, and the result is illustrated in Fig. 4.9. The red filled node is a chance node used to identify the event in a decision tree where a degree of uncertainty exists. In this case, since the hybrid model does not have the capability to make event-level outcome prediction, we expand the risk-level prediction to event-level outcome prediction by considering all the possible event outcomes under the corresponding risk category. Along each line is shown the probability of each event to occur. As can be seen, it is most probable for the test record *a* to have event outcome “Flight Crew Executed Go Around Missed Approach”, followed by “Flight Crew Became Reoriented” and “Air Traffic Control Issued New Clearance”. With respect to other risk categories, similar diagrams can be constructed to represent event-level outcomes. Such event-level outcomes enable to connect the root cause (i.e., malfunction) and the consequence of the incident at the event outcome level.

4.5 Summary

This chapter developed a hybrid machine learning model by blending support vector machine and an ensemble of deep neural networks, in order to quantify the risk pertaining to the consequence of hazardous events in the air transportation system. The SVM model is trained using the event synopsis text, while the DNN ensemble is trained using categorical and numerical data. By merging the predictions from the two models, we formulate a hybrid model to assess the severity of abnormal event outcomes in terms of their risk levels using 64,573 reports on incidents/accidents that were reported between January 2006 and December 2017.

Several contributions have been made in the developed approach. First, we develop a risk-based event outcome categorization strategy to project the event outcomes in the space of risk quantification by collapsing the original 36 unique event outcomes into five risk groups. Secondly, we propose a support vector machine and deep learning-based hybrid model to make prediction on the risk level associated with the event outcome by analyzing the event contextual features and event description in an integrated way. Thirdly, an innovative fusion rule is developed to blend the predictions from the two trained machine learning algorithms. Finally, a probabilistic tree is constructed to map the risk-level prediction to event-level outcomes. The results demonstrate that the developed hybrid model outperforms the individual models in terms of precision, recall and F1 score.

The development of predictive model in this chapter enhances operators' situation awareness on the evolution of hazardous events and prepare them for the consequence of system malfunction events in advance. With the prediction on malfunction event consequence, operators have more time to prepare necessary resources and take appropriate measures and actions to prevent the escalation of anomalous events in the system. Even though the predictive models developed in Chapters 3 and 4 increase operators' situation awareness on abnormal events significantly, what matters more is that how human operators respond in the presence of system malfunction events and how reliable their responses are, which will be investigated in Chapter 5.

Chapter 5

Human Reliability Analysis in Diagnosing and Correcting System Malfunctions[1]

5.1 Introduction

There are numerous malfunction events that could happen in a system and each off-nominal event has its own characteristics w.r.t. event detection, diagnosis, and correction. Even if the operators (i.e., pilots, controllers) are well-trained, it is not certain that they will take appropriate actions to eliminate system malfunctions effectively in emergency situations. Hence, this chapter is motivated to investigate the reliability of the human operators in diagnosing and correcting system malfunctions, and we illustrate the approach with control room operator assessment in a nuclear power plant.

In handling anomalous events, operators' prior experience and training play an essential role in affecting their effectiveness in responding to the malfunction events. To measure the reliability of operators in eliminating malfunction events, we analyze the results of an experimental study to characterize the performance of operators in responding to system disturbances. Such research is important to support ongoing efforts to modernize the nuclear power plant (NPP) control rooms with fully digital instrumentation and control (I&C) design. Researchers and practitioners are investigating new technologies to modernize the user interfaces in NPP control rooms (e.g., design and layout of the graphics, informativeness of the alarm system, and ecological interfaces) so that important information regarding situations can be displayed with appropriate level of salience and effort to access, thereby enhancing the situation awareness of the operators [154, 155, 156]. Thus innovative human reliability analysis (HRA) methods are needed to verify the expected improvements in ensuring safe, reliable, cost-competitive production of electricity [157]. It is essential to assess the performance of each crew team in maintaining the plant safety margin when the

[1] An archival paper related to this chapter has been published in the journal Reliability Engineering & System Safety. For more details, see Ref. [153]

new I&C technologies are introduced.

To support such assessment, quantitative methods need to be developed to predict the operator performance based on his/her responses in different contexts and scenarios [154]. As indicated by Mosleh et al. [158], the improvement of human reliability models requires the inclusion of cognitive theories and measurable human responses. Recent research is making noticeable advancement in using physiological data for HRA [159], in which fifteen graduate students were employed to participate a reactor shutdown scenario in the control room in a mid-fidelity simulation environment. In transportation, Healey and Picard [160] tracked a number of physiological indicators, including electrocardiogram, electromyogram, skin conductance, and respiration, while drivers followed a set route through open roads in the greater Boston area. This study demonstrated that physiological signals were good indicators of the driver stress. Liang and Lee [161] developed a layered algorithm that integrates a Dynamic Bayesian Network (DBN) with supervised clustering to detect the cognitive distraction using eye movement data (i.e., blink frequency, fixation duration, pursuit duration, and pursuit direction) and driving performance measures.

Adopting a similar direction, we develop an information fusion approach that leverages physiological and eye tracking data for predicting operator performance in responding to the malfunction events. A significant difference between our investigation and other HRA models is that the approach developed in this chapter aims at predicting the operator performance while other HRA models aim at producing failure probability values of human operators in different scenarios through human-in-the-loop experiments. The difference in research objective has resulted in a distinct data collection and model structure in our study. Specifically, we innovate an information fusion approach built on data from a full-scope, human-in-the-loop simulation experiment that was performed at the Center for Advanced Engineering and Research (CAER), Forest, Virginia [162, 163]. The experiment employed a full-scale Generic Pressurized Water Reactor (GPWR) simulator in the CAER control room research facility and recruited nine previously licensed operators to form three crews. Each crew included the positions of unit supervisor (US), reactor-side operator (RO) and balance-of-plant-side operator (BOP). Ten scenarios were developed to test the performance of each group. Each experimental scenario consists of two to four malfunction events. The experimental data include: scenario characteristics, eye tracking data, physiological data (i.e., skin conductance response and respiration), expert-rated task performance (i.e., Operator Performance Assessment System – OPAS [164]), self-rated task performance, subjective workload ratings (the Halden Task Complexity Scale [165]), situation awareness (SA) (the Process Overview Measure [166]), and subjective SA confidence ratings. Our information fusion extracted and fused numerous features from these heterogeneous sources of information by a support vector machine model to predict the operator performance.

The methodology pursued in this chapter has the following components:

1. Quantitative modeling: A novel quantitative model based on empirical data is developed to predict the control room operator performance, based on physiological and eye tracking data collected in simulator experiments as well as task workload, operators' situation awareness (SA) and SA confidence level.

2. Information fusion: We innovate a framework to integrate multiple, heterogeneous sources of information. By utilizing various data analytic techniques, we elicit numerous features from the different types of data. These features are incorporated in the empirical data model for predicting the operator performance.

3. Expert rating: We develop an approach to transform linguistic (categorical) ratings by experts on the items belonging to each malfunction into numerical counts.

4. Dimension reduction: Correlation analysis is performed among the extracted physiological features. If the correlation coefficient between any two physiological features is larger than a threshold, the two variables are assumed to carry similar information.

In this case, only one of them is selected as input to the model, thereby reducing the problem dimension.

5. Ensemble modeling: We integrate the support vector machine technique with bootstrap aggregating to build ensembles of models to leverage the complete dataset and improve the prediction accuracy given 22 input variables but only 107 records. The trained quantitative models are then used to predict the performance of the crew team in other scenarios, and the ensemble model outperforms the individual models in prediction accuracy.

5.2 Experimental study

This section briefly describes the role of each participant, experimental environment, scenario development process, experimental procedures, and measures of operator performance.

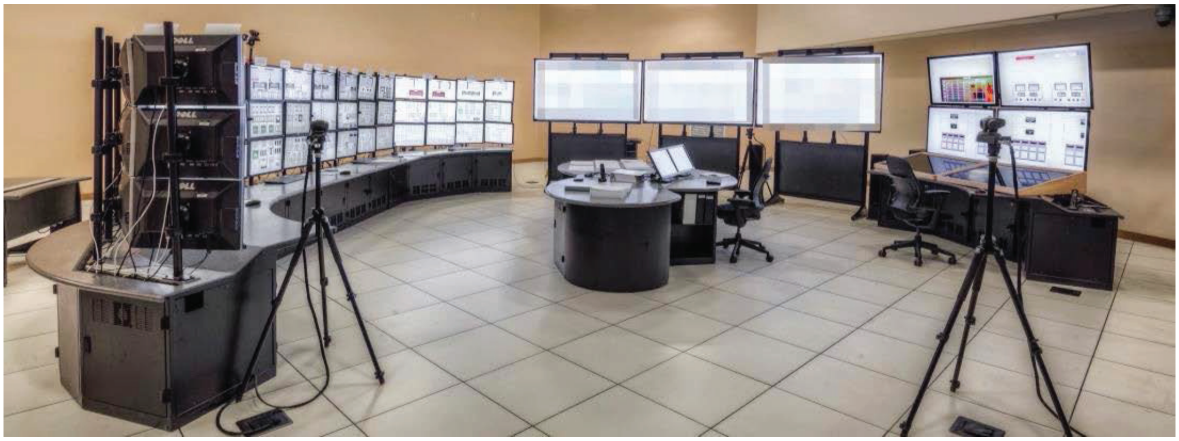

Figure 5.1: Simulated control room configuration. Left: reactor operator workstations; Center: large screen display; Right: turbine operator workstation

5.2.1 Participants

Nine previously licensed operators ($n = 9$) were recruited to form three crews of three members each. Each crew was composed of one reactor operator (RO), one unit supervisor (US), and one balance-of-plant (BOP) operator. The three operators have different roles and responsibilities in maintaining the normal operations of NPP. Specifically, the reactor operator is primarily concerned with managing the nuclear reactor, monitoring the power-generating equipment, and controlling the amounts of nuclear reactivity through the control panel; the unit supervisor is mainly responsible for supervising and coordinating the activities of the control room staff to guarantee the nominal operations of NPP; and the balance-of-plant operator's principal responsibility is to ensure that the generated power flow is equivalent to the amount of energy that is consumed by the market. Each participant maintained the assigned position for the entire week.

5.2.2 Experimental Environment

A full-scale Generic Pressurized Water Reactor (GPWR) simulator [167] in the CAER control room was used as the experimental platform. The GPWR simulator provides real-time simulation of actual nuclear plant operations, and is therefore an effective tool for evaluating control room design and operator performance. Fig. 5.1 shows the reactor and turbine operator in the CAER control room, and the hard-wired panels of the GPWR simulator are displayed across forty eight 24-inch computer monitors. The paper-based and digital NPP operation procedure manuals are located at the supervisor workstation in the center of the control room.

On one side of the control room is an observation gallery enclosed by one-way mirrors for the experimenters to observe the responses and actions of crew members interacting with the simulator. All the equipment used to collect the physiological data are installed in this room. As illustrated in Fig. 5.2, the observation gallery is divided into three parts. The middle of the observation gallery is equipped for the simulator operator (SO) to initialize the simulator conditions and inject the malfunction during the simulation trial. The left and right of the observation gallery are equipped for experimenters whose primary tasks are to rate the operator's performance according to their observations of the plant parameters

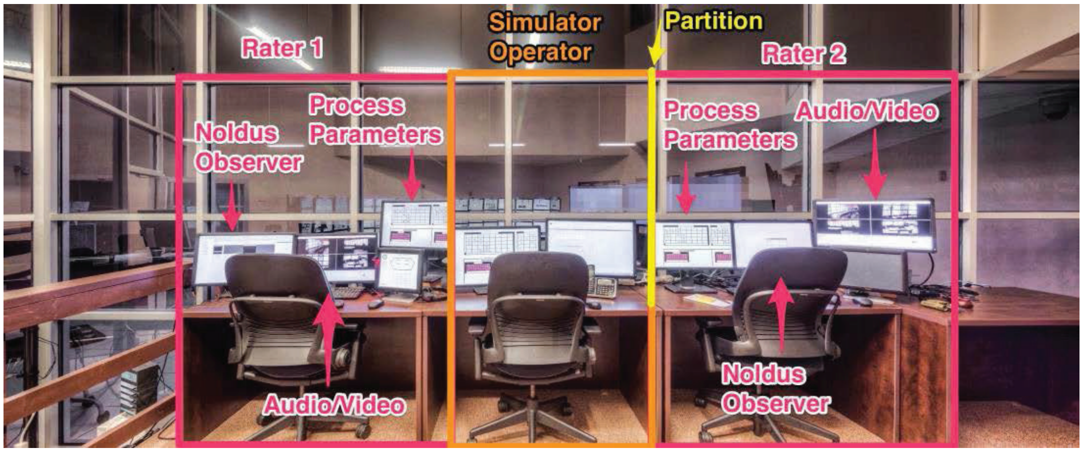

Figure 5.2: Configuration of experimental team members in the observation gallery

and participant behaviours. To support experimenter observation and ratings, the Noldus Observer XT [168] is used to provide or integrate multi-channel audio, multi-angle video, annotations of operator behavior, physiological data, and plant simulator logs.

5.2.3 Scenario Development

A process expert, recently retired as the simulation trainer at an NPP facility, developed the initial set of non-site specific process events for all the scenarios to test participants, who were previously licensed operators. The initial set of process events in each scenario were then tested and refined at the CAER facility with the support of a second simulation trainer, who was recently retired from the NPP simulated by the GPWR. This assistant scenario developer helped fine-tune the individual events to achieve the desired nuclear and thermo-hydraulic process behaviors in the simulator.

The refined scenarios were further evaluated with two additional pilot operators, who were also retired NPP operators (these pilot operators subsequently served as the human performance raters in this study). The pilot operators were not previously exposed to the scenarios in any way. They commented (i.e., think aloud) on the plant process behaviors as they acted as operators monitoring, diagnosing, and controlling the GPWR for the 10 refined scenarios. The scenario developer refined the scenarios to final specification after addressing the pilot operators' concerns raised from the perspective of the participants. In addition, two process experts independently rated each event in each scenario on four different dimensions of difficulty: detection, diagnosis, intervention, and restoration. Each dimension was rated on a five-point Likert scale [169].

5.2.4 Experimental Procedures

Before the data collection, a retired NPP operator trainer familiarized the participating operators with the GPWR power plant systems, and guided the practice on operating the GPWR for one day and a half. After the training, the operators took part in a practice scenario to get accustomed to all the items in the experimental trial, i.e., wearing the physiological gear, calibration of the devices, and completing the questionnaires.

All the operators wore several data collection instruments: wireless microphones (BOP, RO, US), Tobii$^{\text{TM}}$ eye tracking glasses (BOP, US) [170], BIOPAC BN-PPGED electrodermal activity transmitters [171] (RO, US), and BIOPAC BN-RESP-XDCR thoracic expansion (i.e., breathing) transducers [172] (RO, US). The selection of the data collection instruments was based on practicality in terms of comfort and setup time, availability to the research team, and relevance of the measurements according to the literature.

During the experiment, the participants completed ten different scenarios, and each scenario consisted of two to four malfunction events of varying difficulty levels. Each crew acted as if they were on duty to eliminate the malfunction events to maintain the plant safety as well as to bring the plant back to steady state. Each scenario lasted for nearly 1.5 hours, and was subdivided into two periods. A "scenario-freeze" (lasting around 20 minutes) was defined to signal the termination of each period. During this freeze period, the operators responded to human performance questionnaires at workstations away from the control room area. The entire experiment protocol takes one week to test the performance of each crew on the ten scenarios.

5.2.5 Operator Performance Measures

Data was collected on a variety of factors: plant performance (based on simulator logs including alarms, and trend graphs), task performance (both expert- and self-ratings), workload, situation awareness (SA), SA confidence, and physiological measures (electrodermal activity, thoracic expansion, and eye tracking). The selection of these performance measures was based on the key human factors engineering design goals prescribed by the NRC in NUREG 0711 [173]. In the subsections, we briefly describe these human performance measures.

5.2.5.1 Workload

Table 5.1: Modified Halden Task Complexity Scale (HTCS) questionnaire used in the experiment

Workload items	**How difficult was this scenario with respect to:**
Item 1	Ambiguous, misleading or missing information on the displays
Item 2	Ambiguous, misleading or missing feedback on control actions
Item 3	Time for planning and responding to the plant event/disturbance
Item 4	Execution of every single task complicated by many simultaneous tasks
Item 5	Collection and utilization of information to handle the plant disturbance

A modified Halden Task Complexity Scale (HTCS) [174] was used to measure the operator workload. The HTCS, originally developed by the Halden Reactor Project in Norway, is a subjective task-complexity scale that measures the degree of difficulty encountered by the control room operators. In this experiment, all the operators rated the five items shown in Table 5.1 on a seven-point Likert scale [169] varying from ‘very difficult’ (1) to ‘very easy’ (7).

5.2.5.2 Situation Awareness

Situation awareness (SA) was assessed through the Process Overview Measure (POM) [175, 176], in which a series of queries were employed to elicit the operator’s awareness on the

Table 5.2: Sample process overview measure items

Compared to its value when the "charging pumps discharge header high-low flow" alarm (ALB 06-1-1) was received?			
1. Median Tavg Recorder indication is now:	Lower	Same	Higher
What is your confidence in your answer?	Not Conf	Neutral	Conf
2. Pressurizer Level indication (LI-461) is now:	Lower	Same	Higher
What is your confidence in your answer?	Not Conf	Neutral	Conf
3. Main Generator Gross Electrical Output is now:	Lower	Same	Higher
What is your confidence in your answer?	Not Conf	Neutral	Conf
4. VCT Level indication (LI-115) is now:	Lower	Same	Higher
What is your confidence in your answer?	Not Conf	Neutral	Conf
5. Charging Flow indication (FI-122) is now:	Lower	Same	Higher
What is your confidence in your answer?	Not Conf	Neutral	Conf
6. RHX Letdown Temperature indication (TI-140) is now:	Lower	Same	Higher
What is your confidence in your answer?	Not Conf	Neutral	Conf

changes in relevant plant parameters pertaining to the malfunction event. Table 5.2 presents six process overview queries that were administered during one scenario-freeze. Each question elicited the operator's awareness on the parameter change: whether the parameter had "increased", "decreased", or "remained the same" after the introduction of the abnormal event. In addition to the situation awareness on the parameter change, the operators were instructed to provide a confidence rating specific to their response to each query, i.e., "confident", "neutral", or "not confident". During each simulator freeze, the operators completed the six process overview queries and corresponding confidence ratings. These queries are used to measure each operator's understanding of the plant state change, and are closely related to the operator's performance in resolving the malfunction. The confidence ratings are used to indicate the operator meta-awareness (i.e., limitation of their own knowledge) that would be relevant to direct their monitoring behavior.

5.2.5.3 Expert-rated Task Performance

The task performance of each team was rated independently by the two process experts using the rating sheet developed according to the Operator Performance Assessment System (OPAS) [164]. The performance rating items were developed by the scenario designer, and included the expected stepwise operator reactions to eliminate the corresponding malfunctions. Table 5.3 shows a sample of OPAS rating items for the first scenario (note: there

Table 5.3: Sample malfunction and OPAS rating items in the first scenario

Malfunction & Expected Operator Actions	**Range of Performance**	**Score**
Malfunction: LT-459 failure **DETECTION** * Responds to alarms for decreasing PZR level and increasing CHG flow * Team compares channels of PZR level identifying the failed channel	Expert use of available diverse indications.	3
	Minor delays in checking diverse indications.	2
	Significant lapses in use of available indications delay response to failure.	1
	Diverse indications not used effectively.	0
DIAGNOSIS * When LT-459 $<$ 17% Team IDs: * Letdown has isolated * PZR heaters OFF	Timely ID Letdown isolated and heaters off.	3
	Minor delay in ID.	2
	IDs but does not recognize significance.	1
	Does not identify letdown isolation & heaters off.	0
RESPONSE Takes action to limit PZR Level increase: * Reduces CHG to minimum (0gpm) * Reduces seal injection within limits	CHG to 0 gpm and Seal Injection to minimum.	3
	CHG to 0gpm but no Seal Injection adjustment.	2
	CHG reduced but not to 0 gpm.	1
	CHG not reduced.	0
RESPONSE Monitors parameters: * PZR Level * RCS Pressure * Blender AUTO makeup	Broad awareness and verification of operation.	3
	Occasional monitoring – generally aware.	2
	Few checks not aware of some AUTO Makeups.	1
	No monitoring.	0
RESPONSE Utilizes ALB 9-4-3 to: * Deselect LT-459 (control & RCDR) * Initiate OWP-RP * Resets & energizes PZR Heaters	All aspects of ARP properly implemented.	3
	Deselects but a few other aspects not addressed.	2
	Slow to deselect – several aspects not addressed.	1
	Fails utilize ARP.	0
RESPONSE OP-107, Sect. 1.4 (L/D): * Proper sequence for valve operation * Proper PCV operation (no RV lift) * Proper CHG flow for Letdown Flow	All aspects of Letdown rest properly performed.	3
	Minor challenges to RV or Letdown cooling.	2
	Lifts RV, inadequate CHG flow	1
	Not performed.	0
RESPONSE Restore PZR level to program: * Adequate CHG for letdown * Steady trend toward program * Restores control system to AUTO	Level toward program – control back to AUTO.	3
	Level toward program – maintains MAN control.	2
	Slow to restore level – few T alarms	1
	No attempt to restore level, inadequate cooling.	0

are four malfunction events in the first scenario, Table 5.3 only describes the first malfunction event and the correct procedures to resolve the malfunction), in which the malfunction and expected operator actions are clearly demonstrated. The sample illustrates that each item included predefined performance criteria associated with a score between zero and three. The score zero implies failing to complete the step and three represents an ideal response.

Two process experts (retired, formerly licensed NPP operators) rated the participants on the corresponding OPAS items from the observation gallery based on the observed behavior of the participants as well as the process parameter values from the simulator, and the integrated audio/video information from the Noldus Observer XT. Rater 1 was present for all three weeks of the experiment, while Rater 2 was only present for weeks 1 and 3. The two raters were separated by a partition in the gallery and refrained from discussion to minimize mutual rating influence.

5.3 Data Analysis

This section presents the analysis performed on the different types of experimental data, and introduces the analytic techniques used to derive significant features from these heterogeneous data. These features subsequently serve as inputs to the quantitative model for predicting the operator performance.

The developed methodology consists of four parts, as illustrated in Fig. 5.3. First, we extract the context characteristics of each scenario from the relevant documents, e.g., scenario reports. These data provide scenario-wide features, including scenario difficulty, task complexity, and workload. The linguistic ratings on participants' situation awareness are converted into numerical scores by comparing the responses of the operators to those provided by the simulator operator and incorporating the operator confidence ratings. Second, the physiological data, e.g., skin conductivity (also known as electrodermal activity or EDA) and respiration data, are subjected to event-related analysis to identify

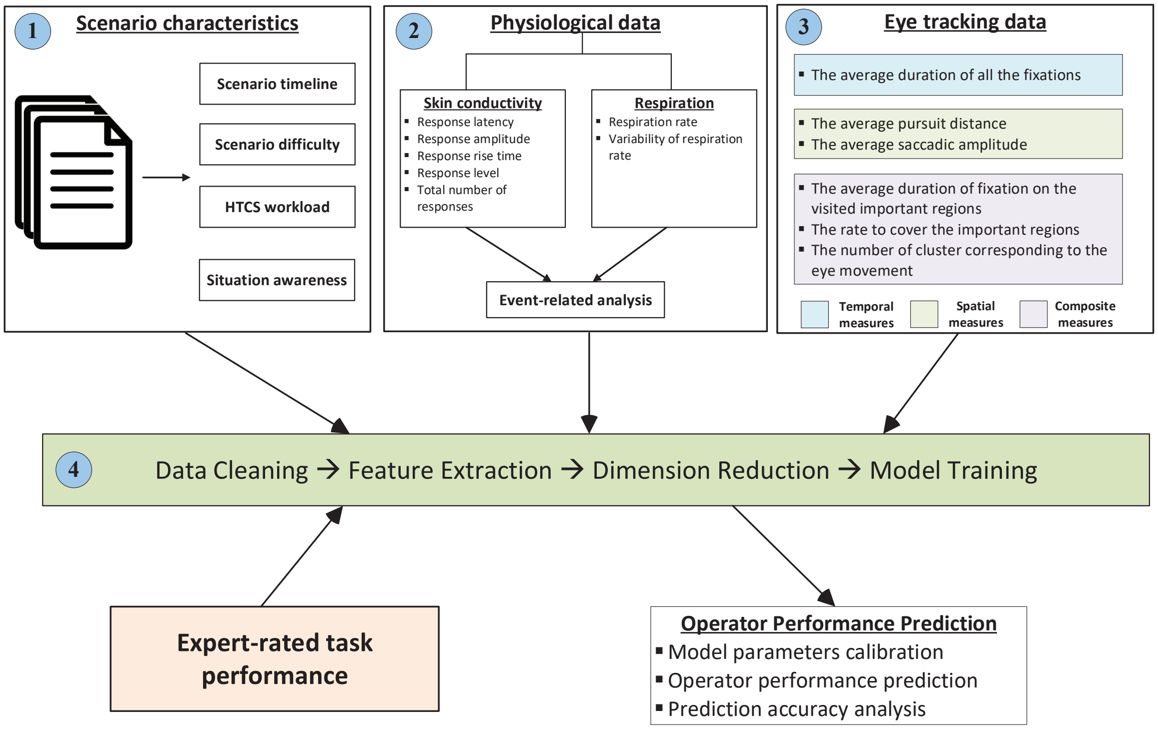
1
Scenario characteristics
Scenario timeline
Scenario difficulty
HTCS workload
Situation awareness
2
Physiological data
Skin conductivity
Response latency
Response amplitude
Response rise time
Response level
Total number of responses
Respiration
Respiration rate
Variability of respiration rate
Event-related analysis
3
Eye tracking data
The average duration of all the fixations
The average pursuit distance
The average saccadic amplitude
The average duration of fixation on the visited important regions
The rate to cover the important regions
The number of cluster corresponding to the eye movement
Temporal measures
Spatial measures
Composite measures
4
Data Cleaning → Feature Extraction → Dimension Reduction → Model Training
Expert-rated task performance
Operator Performance Prediction
Model parameters calibration
Operator performance prediction
Prediction accuracy analysis

Figure 5.3: Proposed methodology

each operator's physiological response to the injected malfunction event, thereby extracting physiological features corresponding to each event. The physiological features include skin conductance response level, response latency, skin conductance response rise time, and the mean of respiration effort, etc (see Section 3.2 and 3.3). Third, we elicit the eye-gaze based temporal (i.e., average fixation duration), spatial (i.e., the pursuit distance, the saccadic amplitude), and composite features (i.e., average duration of fixation on the visited important regions, the ratio that the important regions are covered, and the number of clusters corresponding to the eye movement). Finally, correlation analysis is conducted to reduce the problem dimensions and form the final set of input variables. All the remaining features are combined with the expert-rated task performance to train a quantitative model, and the performance of the trained model is validated by comparing its predictions against the actual observations on some other malfunction events.

5.3.1 Scenario Characteristics Extraction

Table 5.4: Difficulty ratings for Scenario 1

Scenario	Malfunction event	Rater	Detection	Diagnosis	Intervention	Restoration
1	1	1	2	2	3	2
1	1	2	2	2	3	2

Table 5.5: HTCS workload ratings on the first scenario

Scenario	Week	Day	Rater	Workload item	Score
1	3	2	RO	1	2
1	3	2	RO	2	2
1	3	2	RO	3	3
1	3	2	RO	4	2
1	3	2	RO	5	3
1	3	2	BOP	1	3
1	3	2	BOP	2	3
1	3	2	BOP	3	3
1	3	2	BOP	4	3
1	3	2	BOP	5	3
1	3	2	US	1	1
1	3	2	US	2	2
1	3	2	US	3	3
1	3	2	US	4	2
1	3	2	US	5	2

As indicated in Fig. 5.3, the scenario-wide characteristics are embodied in several data sources, including the scenario difficulty, HTCS workload, and situation awareness of each operator on each scenario. In the remainder of the chapter, we take one scenario as an example to illustrate the data available to us. Table 5.4 presents the two process experts' difficulty ratings on four dimensions (detection, diagnosis, intervention, and restoration) for the first malfunction event in the first scenario. Many existing studies have demonstrated that the difficulty of the scenario is closely correlated with performance. For example, Healey & Picard [160] showed that the driver's stress was heavily influenced by the driving conditions (highway driving, or city driving) because the roads with higher traffic flow increase the driver's cognitive workload, thus decreasing his performance accordingly. The scenario difficulty plays a similar role in this study. The scenario with higher overall difficulty rating are hypothesized to decrease the situation awareness and task performance.

Another important factor is workload measured through the HTCS. The participated operators rated five items shown in Table 5.1 on a 7-point Likert scale. Table 5.5 shows the specific HTCS workload ratings on the first scenario by the three operators in the first crew. The workload ratings are useful indicators on the operators' perceived challenges in monitoring abnormal plant states, the possible causes of such states, as well as the number and type of tasks that need to be accomplished to eliminate such abnormal events. If too many tasks are assigned to one operator, then the operator is overloaded with the assigned tasks, his performance will be impacted.

Table 5.6: Operators' situation awareness on the malfunction events in the first scenario (SO: simulator operator, RO: reactor operator, BOP: balance-of-plant-side operator, US: unit supervisor)

Scenario	Week	Day	Rater	Item	Score	Confidence	Converted numerical values
1	3	2	SO	1	same	confident	-
1	3	2	SO	2	lower	confident	-
1	3	2	SO	3	same	confident	-
1	3	2	SO	4	higher	confident	-
1	3	2	SO	5	lower	confident	-
1	3	2	SO	6	higher	confident	-
1	3	2	RO	1	same	confident	-3
1	3	2	RO	2	same	confident	3
1	3	2	RO	3	same	neutral	-2
1	3	2	RO	4	higher	confident	-3
1	3	2	RO	5	lower	confident	-3
1	3	2	RO	6	higher	not confident	-1
1	3	2	BOP	1	same	neutral	-2
1	3	2	BOP	2	same	neutral	2
1	3	2	BOP	3	higher	confident	3
1	3	2	BOP	4	higher	confident	-3
1	3	2	BOP	5	lower	neutral	-2
1	3	2	BOP	6	higher	neutral	-2
1	3	2	US	1	higher	neutral	2
1	3	2	US	2	same	confident	3
1	3	2	US	3	higher	confident	3
1	3	2	US	4	higher	confident	-3
1	3	2	US	5	same	confident	3
1	3	2	US	6	same	neutral	2

Situation awareness indicates the operator's mental awareness on the system states and the mechanisms causing abnormal events. In an NPP, when an abnormal situation occurs in an NPP, operators perform situation assessment by monitoring the relevant plant parameters, then process the information to establish appropriate situation models to explain the plant's state. If the situation model precisely reflects the plant's state, the operator is considered to have good situation awareness. As the plant state evolves, the operators must periodically re-sample or monitor the relevant process parameters based on their confidence of whether the parameters might have deviated from the knowledge generated from prior sampling of process information. In this study, the items listed in Table 5.2 are utilized to measure each operator's perceived understanding and confidence on the changes of the relevant system parameters of the nuclear power plant. The correct responses to the parameter changes provided an indication of their situation awareness on the entire process; whereas, the confidence ratings provided an indication of operator meta-awareness or meta-SA on their own understanding on the plant process. Operators who were confident and accurate in their awareness of parameter changes most likely engaged in appropriate sampling of process information, whereas, operators who were less confident in their accurate awareness of parameter changes would more likely sample the wrong process information.

Table 5.6 illustrates each operator's specific responses to the questions listed in Table 5.2. The sixth and seventh column represents the operator response and confidence on the parameter changes in linguistic terms, respectively. In addition to the three operators' (BOP, US, and RO) responses, we have responses from the Simulator Operator (SO). It is worth noting that prior to the data collection, the scenario developer acted as the simulator operator for all the scenarios to evaluate the actual parameter changes. Thus, the ratings from the simulation operator can be considered as true states of the system.

One challenge here is how to convert the linguistic terms into numerical values. Here, we replace the linguistic ratings "higher", "same", and "lower" using +1, 0, and -1 respectively, then compare the responses of the operators to those provided by the simulator operator to obtain the deviation between their situation awareness. As shown in Fig. 5.4,

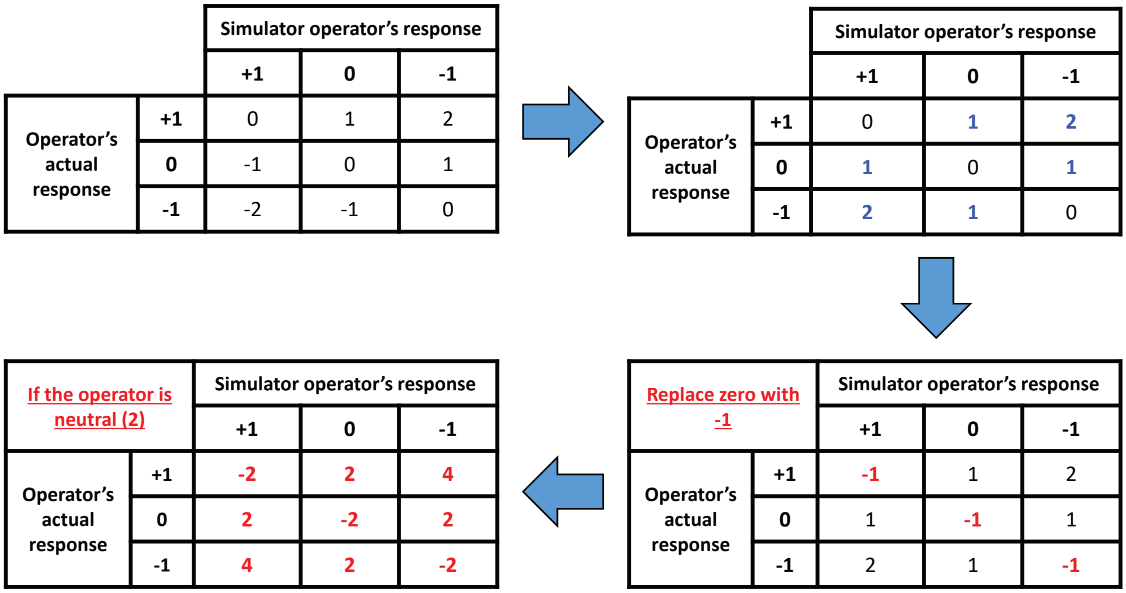

		Simulator operator’s response		
		+1	0	-1
Operator’s actual response	+1	0	1	2
	0	-1	0	1
	-1	-2	-1	0

		Simulator operator’s response		
		+1	0	-1
Operator’s actual response	+1	0	1	2
	0	1	0	1
	-1	2	1	0

Replace zero with -1		Simulator operator’s response		
		+1	0	-1
Operator’s actual response	+1	-1	1	2
	0	1	-1	1
	-1	2	1	-1

If the operator is neutral (2)		Simulator operator’s response		
		+1	0	-1
Operator’s actual response	+1	-2	2	4
	0	2	-2	2
	-1	4	2	-2

Figure 5.4: Conversion process for situation awareness ratings

the table in the top left shows the difference among the two raters after we subtract the simulator operator’s rating from the operator’s actual rating. The values of all the diagonal elements are zero because the operator’s situation awareness conforms with the simulator operator’s. Afterwards, we take their absolute values to measure the relative distance between the two operators’ ratings, which is shown in the table at the top right of Fig. 5.4. Next, we substitute the different confidence ratings “confident”, “neutral”, and “not confident” with +3, +2, and +1 respectively. The product of the confidence rating and the relative distance of the operators’ response from the simulator operator’s response is used as an indicator of situation awareness for each operator in understanding the impact of the abnormal events on the plant states. As can be observed from the table at the top right, if the ratings between the simulator and the plant operator are the same, we cannot distinguish the different confidence levels because the product of the two factors is always zero whether the operator is confident ($0 \times 3 = 0$), neutral ($0 \times 2 = 0$), or not confident ($0 \times 1 = 0$).

To address this issue, we substitute the zeros in this table with ‘-1’ if the responses of the simulator operator and the participant operator are the same, as shown in the table at the bottom right. Afterwards, we multiply the relative distance with the corresponding confidence level to acquire the situation awareness of each operator. From the table at the bottom left of Fig. 5.4, we can differentiate the different confidence levels of the plant operator if his/her response conforms with the simulator operator's response. Another consideration is that the lower the numerical values, the better the situation awareness, therefore this justifies replacing zero with -1. The last column in Table 5.6 displays the converted numerical values for the three participating operators, and these values will be utilized in the quantitative model in the following sections.

Another problem is that some of the data on confidence ratings related to the situation awareness are missing (about 16% of the values in the seventh column in Table 5.6). In this case, since we do not know the degree of operator's confidence on the plant parameter change, the lack of such knowledge forces us to provide a value that reveals no preference on the operator's confidence. Hence, we replace the missing values with the confidence rating "neutral".

5.3.2 Physiological Data Analysis

5.3.2.1 Skin Conductance Response Data Analysis

Electrodermal activity is an umbrella term for autonomic changes in the electrical properties of the skin. A widely used measure is skin conductance response (SCR). The fundamental mechanism of the skin conductance response is to apply electrical potential and then measure the current flow between two points of skin contact. The skin conductance response is the most useful indicator on the dynamic changes of the participating operator's emotional and cognitive states. In fact, this metric has been proposed for detecting vehicle driver's stress [160], assessing aircrew workload [177], and evaluating the cognitive workload [178] because they can be collected continuously without interfering with the operator's task performance.

In this study, we used the Electrodermal Activity (EDA) BioNomadix module from the BIOPAC Systems to collect the skin conductance response for the unit supervisor and the

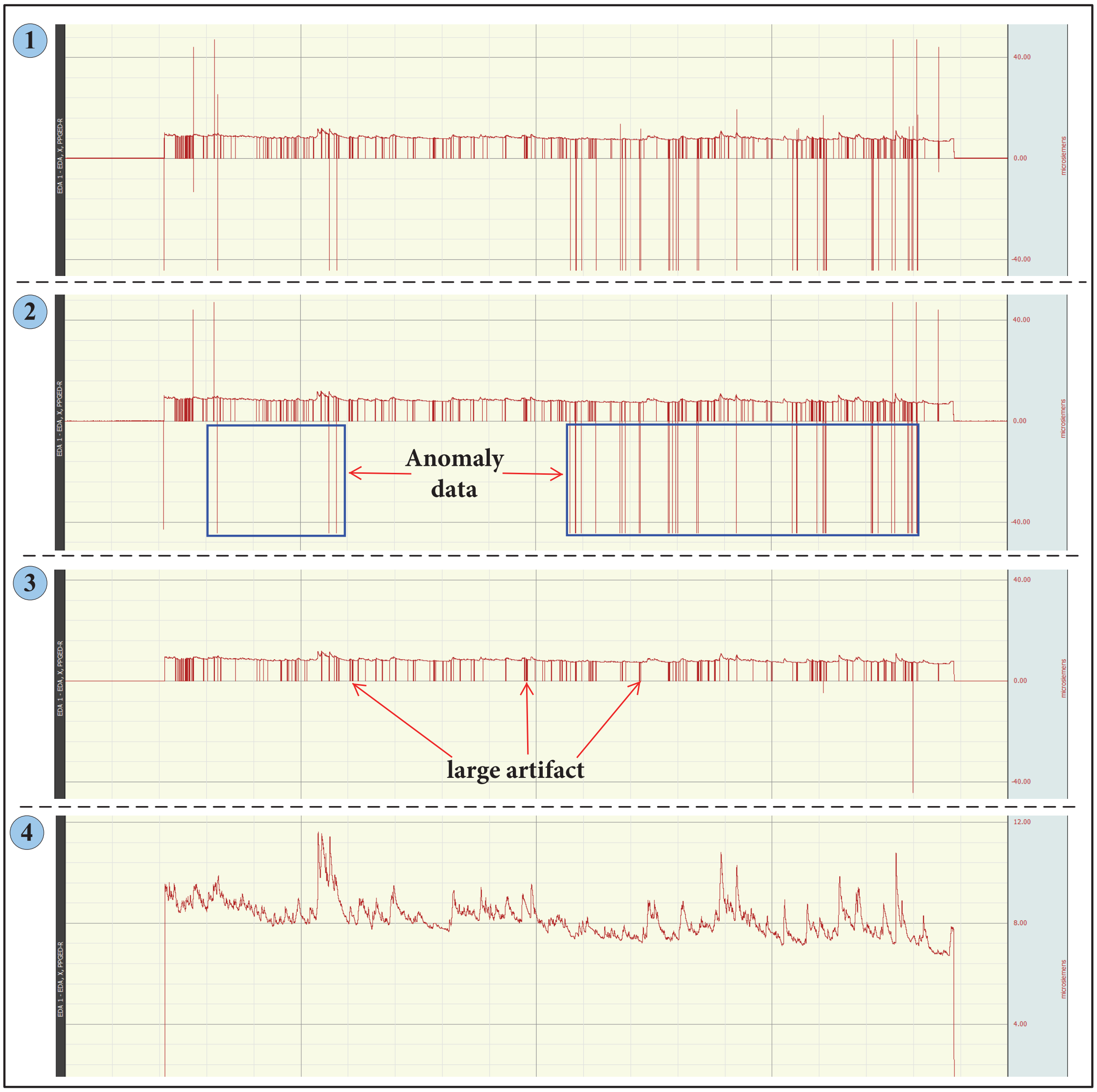

Figure 5.5: Cleaning of the skin conductance response signal

reactor operator. Here, we pick a particular waveform of the skin conductance response from the unit supervisor in one scenario to illustrate the data analysis procedures using the software AcqKnowledge 5.0.1. Fig. 5.5 shows four steps of the data cleaning operations. Initially, we load the raw data into the software and the original tonic skin conductance signal is shown at the very top of Fig. 5.5. Tonic skin conductance, also known as Skin Conductance Level (SCL), is generally considered as the level of skin conductance in the absence of any particular discrete environmental event or external stimuli. In our study, 1,000 samples are collected per second to characterize the tonic skin conductance. To reduce the computational burden and speed up the analysis, we resample the waveform at a rate of 62.5 samples per second, and the resampled waveform is displayed in the second row of Fig. 5.5. The multiple square-wave spikes in the resampled waveform are the artifacts of the signals because the skin conductance cannot change in such a huge magnitude within such a short time. Hence, we apply a median-based smoothing with a factor of 63 samples, from which about 20% of artifacts in the original EDA signal are removed. The third row of Fig. 5.5 shows a processed waveform, in which many higher transient spikes have disappeared while some lower transient spikes remain. Since these lower transient spikes cover a spectrum of wide area, the median smoothing operation fails to eliminate these large artifacts. To remove these mild spikes, we zoom into the signal and manually connect the endpoints of each spike using a straight line. The most bottom graph in Fig. 5.5 shows the final waveform after cleaning the data.

Afterwards, we conduct event-related data analysis to identify the consequent skin conductance responses driven by each injected malfunction event. The three-step procedure is demonstrated in Fig. 5.6. First, we construct a new phasic EDA signal by subtracting the (median value smoothing) filtered waveform from the original. Since median value smoothing discards the areas of rapid change, subtracting this smoothed waveform from the original enables us to focus on sections where the data are changing rapidly. The phasic skin conductance, also referred to as skin conductance response (SCR), is a common reaction to short-term events that occur in the presence of discrete environmental stimuli, and the stimuli usually cause an abrupt increase in the skin conductance, or "peaks" in the skin conductance. The phasic skin conductance facilitates the quantification on the magnitude and duration of each operator in physiological response to the abnormal event. The top two graphs of Fig. 5.6 represent the original waveforms of the phasic skin conductance and the skin conductance response, respectively. The blue markers in the waveform represent the SCR, but they are not related to any stimuli yet.

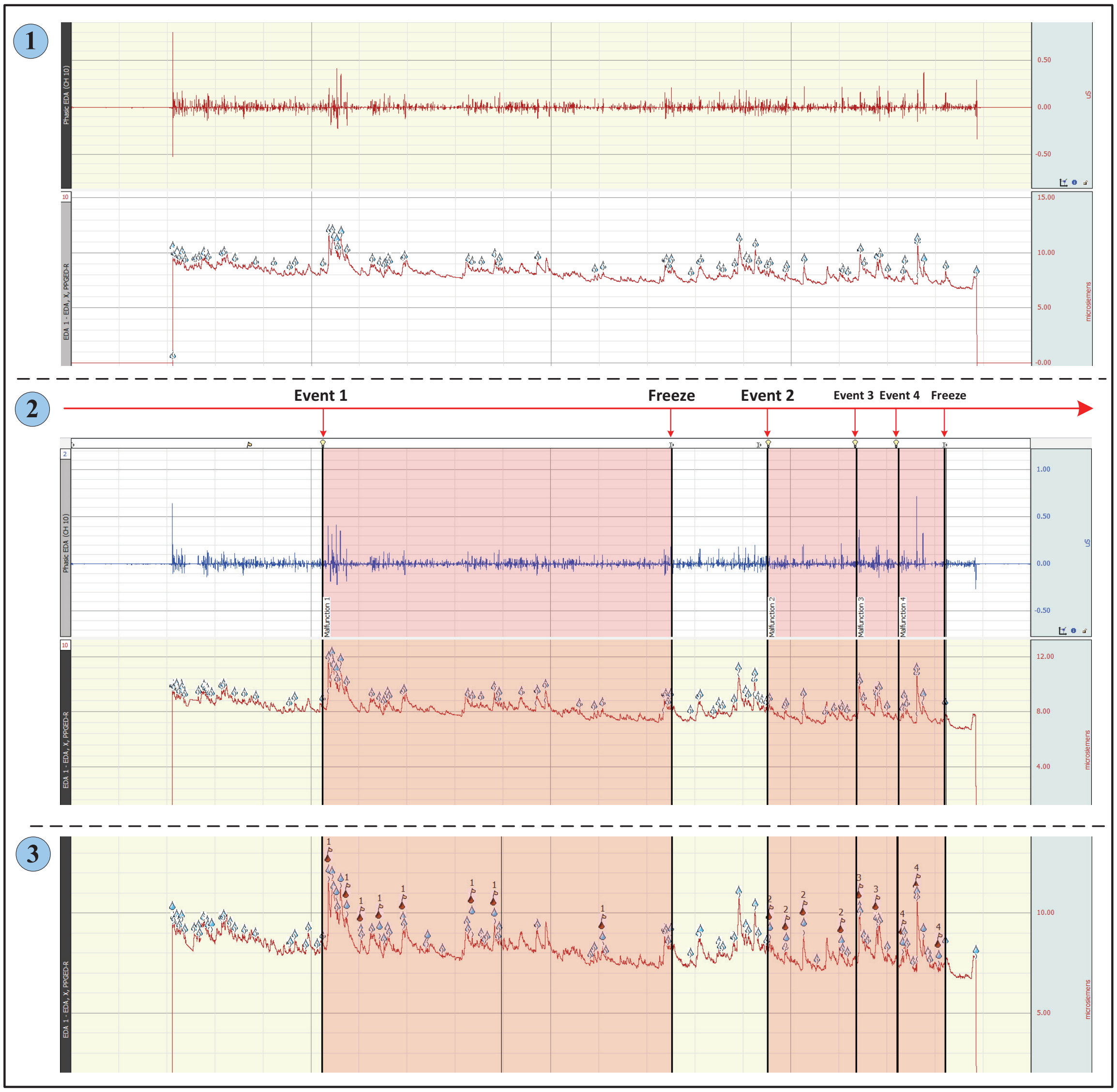

Figure 5.6: Event-related data analysis on the skin conductance response

To relate the SCR to malfunctions, we load the scenario timeline by importing markers from Observer XT. The middle graph of Fig. 5.6 illustrates four different malfunction events for this scenario. The scenario timeline specifies the important time stamps when each malfunction starts or ends, and the "scenario-freeze". The integration of the timeline and the phasic skin conductance signal provides the foundation for the subsequent event-related data analysis. Finally, event-related data analysis is performed, resulting in the bottom graph of Fig. 5.6. The red water drops represent the response related to that

Table 5.7: Event-related data analysis results for the skin conductance response

Stimuli Time	SCL	SCL Latency	SCR Amplitude	SCR Rise Time	SCR Size	SCR Onset	Stimuli Label	SCR Area
1675	8.3759	32.7970	0.1844	1.6640	11.6007	11.4162	1	0.1534
1800	10.2278	29.5200	0.1291	0.6240	9.8032	9.6741	1	0.0403
1920	8.1650	3.7440	0.1037	0.8160	8.6426	8.5389	1	0.0423
2040	8.3533	7.0240	0.0672	0.4000	8.6361	8.5689	1	0.0134
2160	8.1276	42.0640	0.0628	1.0720	9.1032	9.0404	1	0.0336
2640	8.6290	21.4720	0.0668	0.9440	8.7232	8.6564	1	0.0315
2760	8.4522	49.0720	0.0970	0.9600	9.4163	9.3193	1	0.0466
3480	7.7527	47.5520	0.0762	1.0080	8.2521	8.1760	1	0.0384
4629	8.0997	5.9510	0.0656	1.2640	8.5859	8.5203	2	0.0415
4740	7.8968	5.0560	0.0893	0.9280	8.2071	8.1178	2	0.0414
4860	8.6609	1.2160	0.1964	0.8160	8.9353	8.7388	2	0.0801
5100	8.2027	12.4480	0.1870	0.7040	8.0695	7.8825	2	0.0658
5206	7.6931	24.5180	0.2190	0.5600	9.9280	9.7091	3	0.0613
5322	7.7521	22.7520	0.1521	1.4880	9.2145	9.0624	3	0.1132
5480	7.6537	36.9890	0.0804	0.3360	7.8558	7.7754	4	0.0135
5598	7.2007	14.2880	3.1407	0.8960	10.5426	7.4020	4	1.4070
5718	7.3414	37.5840	0.1424	1.1360	7.3202	7.1779	4	0.0809

particular event, and the labels above them specify the event causes the skin conductance response.

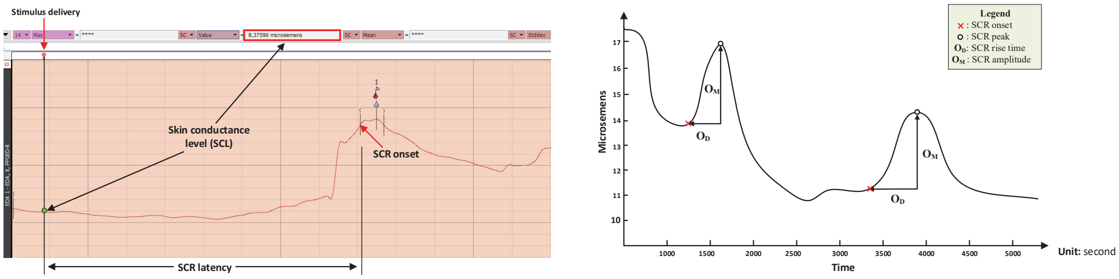

(a) Skin conductance level and skin conductance response latency

(b) Skin conductance response related notations

Figure 5.7: Quantitative metrics related to skin conductance response

Table 5.7 shows the statistical features extracted from the electrodermal activity to characterize the orienting skin conductance response. The first column in Table 5.7 indicates the time within the recording where the stimulus delivery event is located (here the stimulus delivery event refers to the system malfunction event and its associated consequence, e.g., emergency alarm in NPP control room and nuclear siren), the second column denotes the skin conductance level at the moment that the malfunction event is injected, and the third column represents the duration between the injection of malfunction event and the first skin conductance response. Fig. 5.7a clarifies the corresponding notations. In Fig. 5.7a, each skin conductance response is denoted as a red water droplet with an open bracket indicating the response onset and a closed bracket indicating the response offset. The skin conductance latency measures the duration between stimulus presentation and the onset of the first skin conductance response.

Fig. 5.7b shows a series of two orienting skin conductance responses, along with the marks indicating the onset and peak of each response, and labels of the response amplitude O_M and the duration O_D that each orienting response takes to rise to the peak value. These peaks and onsets are detected by identifying the slopes exceeding a critical threshold value and then finding the local minimum preceding that point (onset) and the local maximum following that point (peak). This algorithm is available in AcqKnowledge, which extracted the following features: SCR amplitude, SCR rise time, SCR onset, SCR size and SCR area, where the SCR onset refers to the startle skin conductance response magnitude, SCR size denotes the maximum skin conductance level in the response triplet, and SCR area denotes the area under the response triplet (approximately equal to $1/2 * O_D * O_M$). The numerical values of these features are displayed in the third column to the last column in Table 5.7, respectively. The eighth column in Table 5.7 are labels of the event that causes the skin conductance response.

Using the quantitative characteristics extracted for each skin conductance response, we propose seven SCR-related features for the quantitative model to predict the operator performance: sum of the areas under the response triplet ($\sum \frac{1}{2} O_D \times O_M$), sum of SCR response latency, sum of the response amplitude ($\sum O_M$), sum of the response durations ($\sum O_D$), sum of the response level at the peak, sum of SCR onset level, and total number of such responses for each malfunction. Table 5.8 presents the computational results.

The above procedures constitute the process to extract features from the electrodermal activity of one operator in a scenario. The same procedures are carried out on individual operators over the remaining nine scenarios. For each malfunction, we extract 14 features

Table 5.8: Skin conductance response-derived features

Malfunction	Total SCR Area	Total SCR Latency	Total SCR Amplitude	Total SCR Rise Time	Total SCR Size	Total SCR Onset	Number of Responses
1	0.3996	233.2450	0.7872	7.4880	74.1773	73.3901	8
2	0.2289	24.6710	0.5383	3.7120	33.7978	33.2595	4
3	0.1745	47.2700	0.3711	2.0480	19.1426	18.7715	2
4	1.5014	88.8610	3.3634	2.3680	25.7187	22.3552	3

(7 features * 2 operators) to characterize the skin conductance response.

5.3.2.2 Respiration Data Analysis

In this experiment, the participants wore a respiration belt around the abdomen/chest, and their thoracic expansion and contraction while breathing was measured continuously through the BioNomadix Respiration Transducer at 2000 Hz, providing high resolution signal waveforms. Past studies have showed that the respiration data might be a useful metric in quantifying the operator's stress level [160]. Thus, we include the respiration data in the quantitative model. Fig. 5.8 presents the respiration signal of the unit supervisor in one scenario.

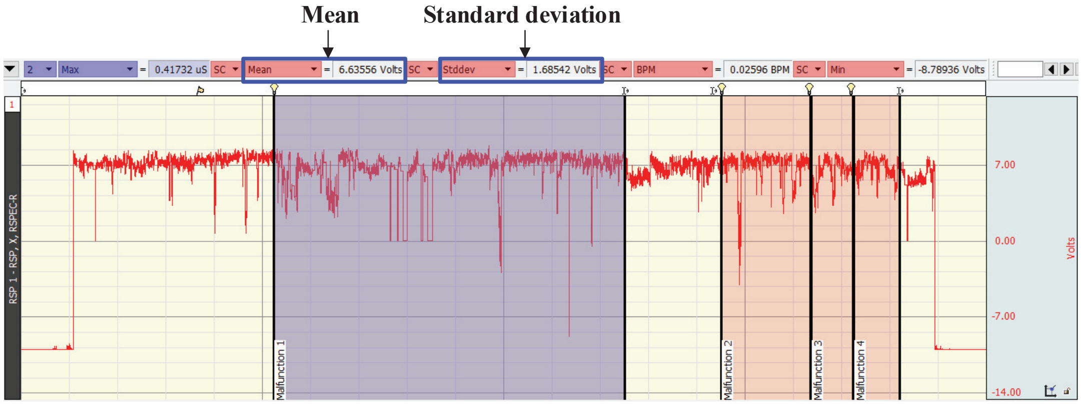

Max = 0.41732 uS SC | Mean = 6.63556 Volts SC | Stddev = 1.68542 Volts SC | BPM = 0.02596 BPM SC | Min = -8.78936 Volts

Figure 5.8: The respiration data of the unit supervisor in the first scenario

Two statistical features are extracted from the respiration data on unit supervisor and reactor operator for each malfunction: the mean of the thoracic expansion, and the standard deviation of the expansion. Fig. 5.8 shows that the numerical values for the unit supervisor and scenario are 6.63556 and 1.68542 volts, respectively. Similarly, we follow the same method to derive the features for the reactor operator, which are 6.6369 and 1.6855 volts, respectively. Hence, for each malfunction, we acquire four different features (2 features * 2 operators) from the respiration data for each malfunction. In a similar way, we process all the other respiration data to elicit these features.

5.3.3 Eye Tracking Data Analysis

The eye movement data were collected at 50 Hz using the Tobii eye tracking glasses. In the experiment, the unit supervisor (US) and balance-of-plant-side operator (BOP) were equipped with Tobii eye tracking glasses. The eye tracking system consists of one high-definition camera used to capture what is in front of the participant, eye tracking sensors to record the eye gaze, and infraRed (IR) sensors to detect IR markers and thus determine the direction of the operator's gaze. The IR markers are small devices attached at the edges or corners of the displays in the control room for broadcasting their exact locations to Tobii Glasses. A snapshot of the experimental set up and IR markers is shown in Fig. 5.9. There are 29 IR markers distributed over different locations of the control room to cover the entire display. Each IR marker has a unique ID number, and they can be combined together to define different areas of interest. Next, a recording unit is connected to the eye tracker via HDMI cable to store the data on an SD memory card. Finally, the videos captured by the eye tracking glasses are analyzed by the software Tobii Studio to identify the horizontal and vertical coordinates of eye fixations, the duration of each fixation, and eye movement traces.

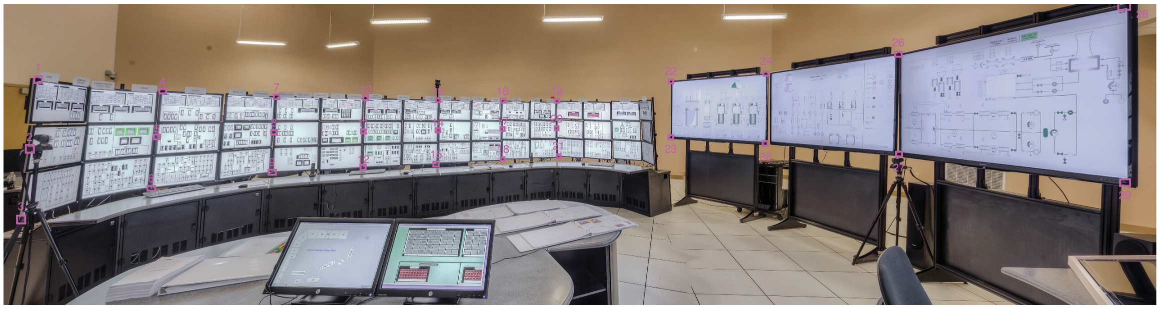

Figure 5.9: Snapshot of the experimental set up with IR markers and their IDs

Tobii Studio can map the eye gaze videos of Tobii glasses on to an imported static image (see Fig. 5.9) indicated with placement and ID of the IR markers. After importing the recorded eye-gaze video data into the software, we extract the starting and ending time from the system logs and drag the timeline marker to the corresponding locations to set the start and the end of the malfunction, from which we create a video segment for that malfunction. Then, we import the static image with placement and ID of the IR markers identified, the coordinates of eye movement from the eye tracking glasses are mapped onto the control room displays. Fig. 5.10 presents an example of the analysis results, that correspond to one operator's eye movement activities in resolving one of the scenario malfunctions. In Fig. 5.10, the size of the dots indicates the fixation duration, the numbers within the dots represent the order of gaze fixations, and the lines connecting the dots denote the eye movement trails. These quantitative values enable us to elicit the temporal and spatial features described in Fig. 5.3 (e.g., fixation duration and pursuit distance).

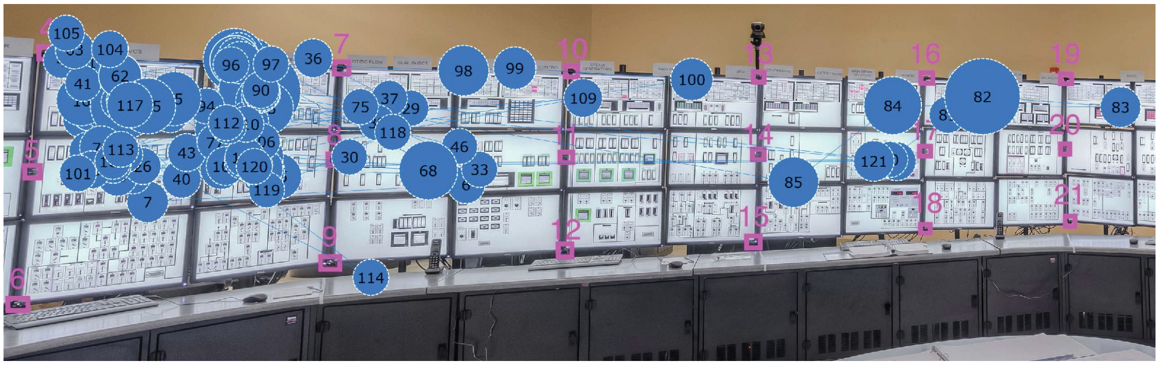

Figure 5.10: Mapped eye tracking data

The scenario reports provide the expected (or correct) operator response that enable another process expert to derive the important regions in the displays. Fig. 5.11 illustrates the important regions that are related to the diagnosis and elimination of the first malfunction in the first scenario. Fig. 5.11 shows nine important regions representing different information sources must be monitored to achieve accurate the diagnosis and elimination of the malfunction. These important regions are known as Areas of Interest (AOIs), i.e., a field of view that hold significant meaning or indicate a specific source of information.

With respect to the nuclear power plant, AOIs represent critical system parameters and components, such as pressurizer, steam generator, reactor, etc.

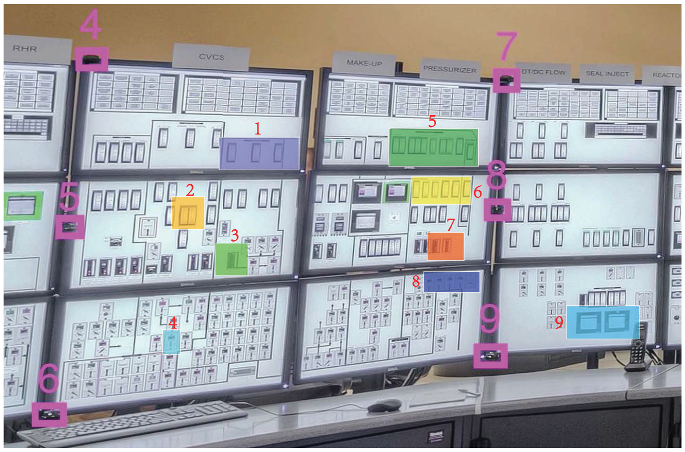

Figure 5.11: Areas of interest in the first malfunction of the first scenario. Larger fonts indicate the IR marker IDs, while smaller fonts are the labels for the important regions

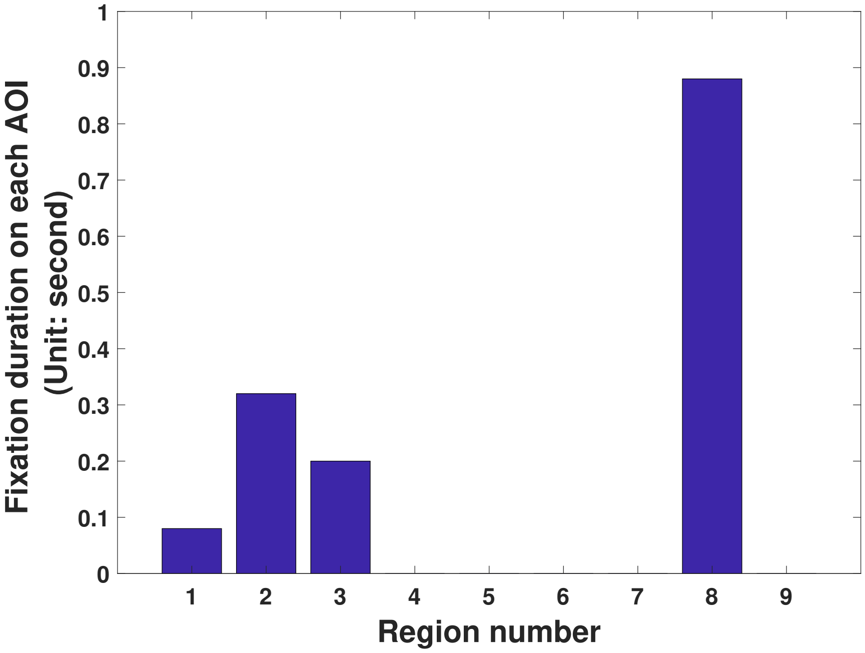

Figure 5.12: The fixation duration on the important regions

We map the eye tracking data onto the AOIs to calculate the amount of time that the operators stared at the designated areas, and thereby derive the amount of attentional resources that each operator allocated to different valuable information sources. As indicated in Ref. [179], the attention-resource effectiveness measure is a promising metric for quantifying the human performance. One composite metric developed in Ref. [179] is the fixation-to-importance (FIR) ratio, and it is defined as the relative attentional resources spent on the information source divided by the relative importance of that source. Herein, we assume all the regions are equally important. Thus, the amount of time that each operator spent on the important AOIs (relevant to each malfunction) is used as a metric to measure the attentional resource allocation. Fig. 5.12 shows fixation duration on each AOI for one malfunction in the first scenario, illustrating that the operator allocated most of his attention to the 8th region and the 2nd region, but missed five other important regions. From such quantitative information, we derive two composite features: the average fixation duration on the visited important regions, and the ratio of the important regions that are visited by the operator. According to Fig. 5.12, we calculate the coverage ratio as 4/9 (4 out of 9), and the average fixation duration on the visited important regions is 0.37 seconds. In addition, we utilize the Tobii Studio to calculate the number of clusters for the eye movement in response to this malfunction, and the result is shown in Fig. 5.13. We assume that the number of clusters reflects the operator's perceived understanding of the malfunction event and his consequent actions in distributing the attentional resources. The three composite features mentioned above (fixation duration in important regions, coverage ratio, and number of clusters) provide quantitative connections to the performance of each crew team in resolving the system malfunction and allocating valuable attentional resources.

With respect to the temporal characteristics of eye movement, we use the average duration of all the gaze fixations as a measure to represent the fixation duration. By using such a metric, we can identify where the operator allocates more attentional resources. Regarding the spatial features of eye movement, numerous studies have shown the link between saccade, cognitive workload, and distraction [180, 181]. For example, Rantanen and Goldberg [182] found that the visual field shrank 7.8% in a moderate-workload counting

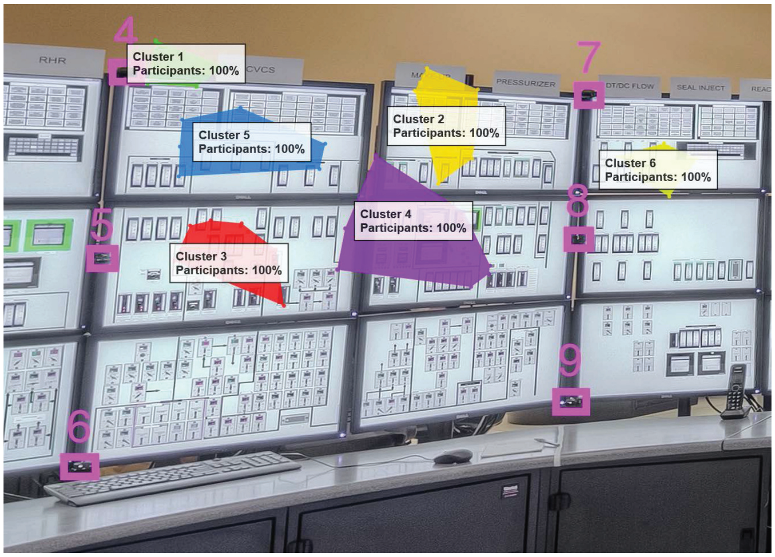

Figure 5.13: Number of clusters corresponding to the eye movement of the first malfunction in the first scenario

task and 13.6% during a cognitively demanding counting task. Thus, the measurements on saccade are good candidates to predict the cognitive workload. In general, saccades are extremely fast jumps from one fixation to the other, and the saccade pattern is an indicator on the operator's problem understanding and confusion. In this study, we employ two different metrics – average pursuit distance and average saccadic amplitude – to represent the spatial features of eye movement. For the sake of completeness, we clarify the meanings of all the six features in Table 5.9 and their significance in assisting the prediction of operator performance.

- Fixation duration measures the average duration for all the fixations, and is an indication of information processing and cognitive activities. This metric indicates how much attentional resources are allocated to specific regions, and whether the specific regions are closely related to the malfunction. The longer fixation duration indicates more difficulty in extracting information and more effort, from which we can further analyze their performance.

- Pursuit distance is the spatial distance between two consecutive fixation locations and represents the operator's effort when locating the root cause of the malfunction, diagnosing the system states, and searching for possible solutions.

- Saccadic amplitude measures the distance in visual degrees between the previous fixation location to the current fixation location. The pattern in the saccadic amplitude reflects the operator's perceived problem understanding and the confusion in diagnosing the system malfunction. Any saccade larger than 90 degrees from the preceding saccade indicates a rapid change in the search direction.

- The number of clusters reveals the operator's attentional resource distribution across the displays, and indicates the viewer's region-of-interest, from which we can measure the operator's perceived complexity in understanding the situation.

- Duration in important regions indicates the average duration of operators' eye fixation on the visited important regions and reflects the degree to which each operator correctly understands and diagnoses the system malfunction. In general, the longer the operators fixate on the important regions, the more likely that they will eliminate the malfunction successfully.

- Coverage ratio indicates how many important regions are visited by the operators and whether the operators fully grasp the situation. If all the important regions are visited by the operators, they may have a higher chance to identify the root cause to the malfunction.

The above six features enable quantitative analysis of the operator's eye movement from three different perspectives: temporal, spatial, and composite. Table 5.9 summarizes the six different features elicited from the eye tracking data for the four malfunctions in the first scenario. We repeat the same procedures to derive the same features for all the other malfunctions and scenarios.

Table 5.9: Eye tracking data-derived features

Malfunction	**Fixation Duration**	**Pursuit Distance**	**Saccadic Amplitude**	**Number of Clusters**	**Duration in Important Regions**	**Coverage Ratio**
1	1.9481	2.7268	2.2374	6	0.3700	0.4400
2	2.2778	4.1321	2.6285	6	1.1440	0.7100
3	1.7876	3.5518	2.3329	3	0.5025	0.6700
4	0.4680	0	6.7900	1	0	0

5.3.4 Expert-rated Task Performance

The team performance was rated by two process experts independently according to the OPAS items. Table 5.10 lists a small number of the OPAS items that the scenario developer specified for the first two malfunctions in one scenario. These items cover a wide spectrum of operator tasks, from simple identification of the problem to a ready-made solution to eliminate the malfunction. The last two columns of Table 5.10 show the specific ratings of the two process experts on the team performance in the detection, diagnosis, response and coordination in resolving the abnormal events. The last two rows of Table 5.10, the expert ratings are missing as some crews failed to reach the last malfunction event in some scenarios or pursued some unexpected control actions that rendered some performance items irrelevant. Thus, about 11% data on the expert-rated task performance is missing. We propose dealing with the missing values by replacing them with an average value of 2 for the rating because we do not have the knowledge regarding the operator's specific performance in accomplishing the task.

Since the team performance is reflected in the expert ratings, the goal of our quantitative model is to predict these numerical values listed in the last two columns of 5.10. As each malfunction has numerous rating items, it is difficult to establish a model to accommodate so many factors and associate the specific operations in each item to the team performance. Further, each malfunction event has a different number of rating items, the content of each rating item and the number of rating items in each malfunction event are only same for the same scenario. As such, we will not have enough data to train the model to predict ratings

Table 5.10: Expert-rated task performance

Scenario	Item number	Event	Item type	Description	R1 Score	R2 Score
1	1	1	detection	LT-459 failure *Responds to alarms for decreasing PZR level and increasing CHG flow. *Team compares channels of PZR level identifying the failed channel.	3	3
1	2	1	diagnosis	When LT-459 < 17% Team IDs: *Letdown has isolated *PZR heaters OFF	3	3
1	3	1	response	Takes action to limit PZR Level increase: *Reduces CHG to minimum (0gpm) *Reduces Seal Injection within limits.	2	2
1	4	1	response	Monitors parameters: *PZR Level *RCS Pressure *Blender AUTO makeup	3	3
1	5	1	response	Utilizes ALB 9-4-3 to: *Deselect LT-459 (control & RCDR) *Initiate OWP-RP *Resets & energizes PZR Heaters	3	3
1	6	1	response	OP-107, Sect. 1.4 (L/D): *Proper sequence for valve operation *Proper PCV operation (no RV lift) *Proper CHG flow for Letdown Flow	3	2
1	7	1	response	Restore PZR level to program: *Adequate CHG for Letdown *Steady trend toward program *Restores control system to AUTO	3	3
1	8	2	detection	Detects transient - reduced steam demand: *Rods inserting *Tavg increases (Tavg/Tref deviation) *Steam & Feed flow decreases	3	2
1	9	2	diagnosis	Checks cause for reduced steam demand *Turbine Load decrease? *Valve closure?	2	2
1	10	2	diagnosis	Identifies #3 GV closed *Light indication on Turbine section *Position indication available	2	3
1	11	2	response	Stabilizes plant at reduced power *Rods above insertion limit *Verifies/restores Delta Flux *Evaluates Turbine load adjustment *Considers Boration.	3	3
1	12	2	coordination	Coordinates recovery *Dispatch operator to check *Contact MAINT *Notify OMOC *Determines continued ops allowed	3	3
1	13	2	detection	Detects transient - reduced steam demand: *Rods inserting *Tavg increases (Tavg/Tref deviation) *Steam & Feed flow decreases	-	-
1	14	2	diagnosis	Checks cause for reduced steam demand *Turbine Load decrease? *Valve closure?	-	-

Table 5.11: Transformation of expert ratings into numerical counts (for one malfunction in one scenario)

Expert rating	**0**	**1**	**2**	**3**
Numerical counts	0	0	1	6

for specific performance items because only three crews take part in the same scenario. To address this issue, we aggregate the expert ratings and transform them into numerical counts to compress the number of items that the surrogate model needs to predict. Specifically, instead of predicting the rating value for each item, we predict the frequencies of different rating values in the expert rating. For example, for the first event in the first scenario, we have converted the first expert's (R1) ratings into a frequency table (Table 5.11). Table 5.11 shows rating values 2 and 3 appear once and six times in the expert-rated team performance for this particular malfunction, respectively. This avoids predicting the rating values for the seven items in the first malfunction. The dimension of system response is fixed to four individual variables across all the scenarios.

Compared with aggregating the expert-rated team performance into one value, the four-variable representation provides relatively higher resolution to examine the expert-rated team performance for each malfunction, from which team performance under different NPP control room designs can be better characterized and compared. In contrast, with an aggregated value that is averaged over the rating items within a malfunction, it is difficult to compare team performance across teams, for example, when they have the same aggregated performance scores.

5.4 Quantitative Model Development

In this section, we develop a quantitative model to predict the operator performance in resolving the malfunction events. The input and output variables are summarized in Fig. 5.14. The input variables include the HTCS workload and situation awareness ratings from the three operators (BOP, US, and RO), the scenario difficulty rated by the two process experts, the features extracted from the physiological data on the two operators (BOP and US), and the features from the eye tracking data. The model output is a vector of four values denoting the numerical counts that each rating value of task performance assigned by the process experts to individual operator.

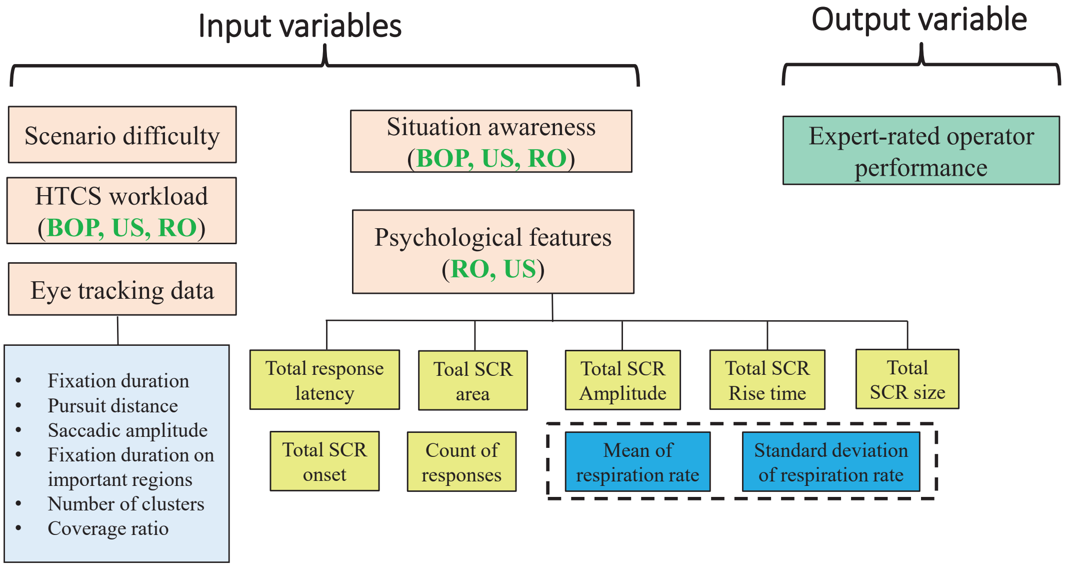

Figure 5.14: Model inputs and outputs

Regarding the input variables, we have 15 (5 items * 3 operators) variables for the HTCS workload, 18 (6 * 3) variables representing the three operators' situation awareness, 8 (4 * 2) variables denoting the scenario difficulty, 14 (7 * 2) features derived from the skin conductance response, 4 (2 * 2) variables extracted from the respiration data, and 6 variables from the eye tracking data. In total, there are 65 (15 + 18 + 8 + 14 + 4 + 6 = 65) different input variables. To reduce the dimension of the input variables in the model, we perform the following operations:

1. We average the difficulty ratings of the two process experts over four criteria (detection, diagnosis, intervention, and restoration) on each scenario to acquire an aggregated indicator of the scenario difficulty. As a result, the eight variables that are used to represent the scenario difficulty are represented by one summarized variable.

2. The HTCS workload is averaged over the five workload items and three operators, by which we obtain a comprehensive evaluation on the workload for each scenario. In this way, we reduce the number of variables from 15 to 1.

3. The situation awareness of each operator is averaged over the six items listed in the questionnaire. Thus, we reduced the number of variables used to denote the situation awareness from 18 to 3.

4. We conduct correlation analysis among the elicited physiological features. If the correlation coefficient between any two physiological features is larger than a threshold (We ranked the correlations among the physiological variables from the highest to the lowest and then chose the average value (0.85) of the correlations ranked in top 10%.), the two variables likely carry similar information. In this case, we only retain one of the variables because one of them will suffice to feed the model. This procedure eliminates seven variables extracted from the physiological data: total amplitude, total size, total onset, count of response from the reactor operator, total rise time, total onset, and count of response from the unit supervisor.

Through the above operations, the number of model inputs is reduced from 65 to 22. The 22 variables retained in the final model are: scenario difficulty (1 feature), HTCS workload (1 feature), situation awareness of BOP, US, and RO (3 features), physiological features (11 features: total response latency, total SCR area, total SCR rise time, mean of respiration rate, and standard deviation of respiration rate of **RO**; total response latency, total SCR area, total SCR amplitude, total SCR size, mean of respiration rate, and standard deviation of respiration rate of **US**), and eye tracking features (6 features: fixation duration, pursuit distance, saccadic amplitude, fixation duration on important regions, number of clusters, and coverage ratio). Fig. 5.15 illustrates the correlation matrix among the 22 input variables. As can be observed, all the considered input variables do not exhibit high correlations after the removal of highly correlated variables.

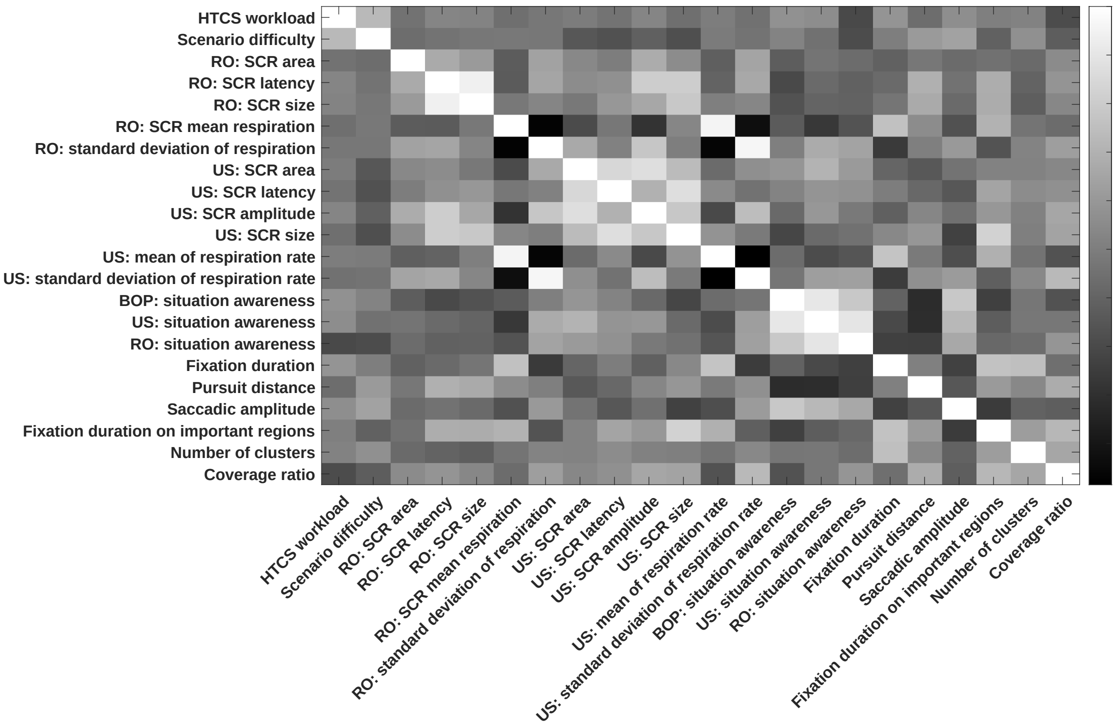

Figure 5.15: Correlations among the 22 input variables

This study yields a total of 107 data points. Considering that there are 22 input variables, it is challenging to build a regression model to predict operator performance with high precision. Moreover, as illustrated in Table 5.11, the quantity of interest – numerical counts of expert ratings – is discrete while the output variables usually take continuous values in regression problems. Using regression, the fit is quite poor, (R^2 is almost zero) after the relevant parameters are tuned. In contrast, if we model this as a classification problem, the prediction accuracy is much higher. Thus, we treated this as a classification problem and utilized the support vector machine (SVM) technique to predict the numerical counts of performance ratings for each expert for the performance of each operator when resolving the malfunction.

For the team performance analysis, the SVM model was trained to the team operation performance measured by the numerical counts (as indicated in Table 5.11) of each performance rating value across all the rating items in some scenarios, Model inputs were collected from heterogeneous sources, including the HTCS workload, situation awareness ratings from the three operators (BOP, US, and RO), the scenario difficulty, the features extracted from the physiological data on the two operators (BOP and US), and features extracted from the eye tracking data. The ultimate classification results provide the team performance level in the representation of numerical counts of each rating value over all the rating items when handling the malfunction events under the particular control room design.

5.4.1 Model Construction

It is a challenging task to build a quantitative model to predict operator performance for several reasons:

- The nuclear power plant is a complex system. The operators respond to the unexpected malfunctions through a series of cognitive activities. The physiological data on the operators might not fully characterize their cognitive activities and situational awareness.
- Although the problem dimension is reduced to 22, it is challenging to build a model to make predictions with high accuracy with only 107 records.
- The correlations among the input variables and outputs are found to be weak (the correlations vary within the range $[-0.3217, 0.3826]$). Thus, none of the inputs to the model is particularly dominant.
- As mentioned earlier, the data set contains missing values. For example, of 16% data are missing for the confidence level in the situation awareness, and 11% of the expert-rated task performance data are missing.

As mentioned previously, we model it as a classification problem rather than a regression problem for better performance. Specifically, we use the "LIBSVM" Matlab toolbox developed by Chang and Lin [183] to build SVM classification models, in which the polynomial kernel function is used as the kernel function:

$$K\left(\boldsymbol{x}_i, \boldsymbol{x}_j\right) = \left(\boldsymbol{x}_i^T \boldsymbol{x}_j + c\right)^d \tag{5.1}$$

where $\boldsymbol{x}_i$ and $\boldsymbol{x}_j$ are the vectors denoting the features of two samples i and j, d is the degree of kernel function, and $c \geq 0$ is a parameter used to control the impact of the order of the kernel function.

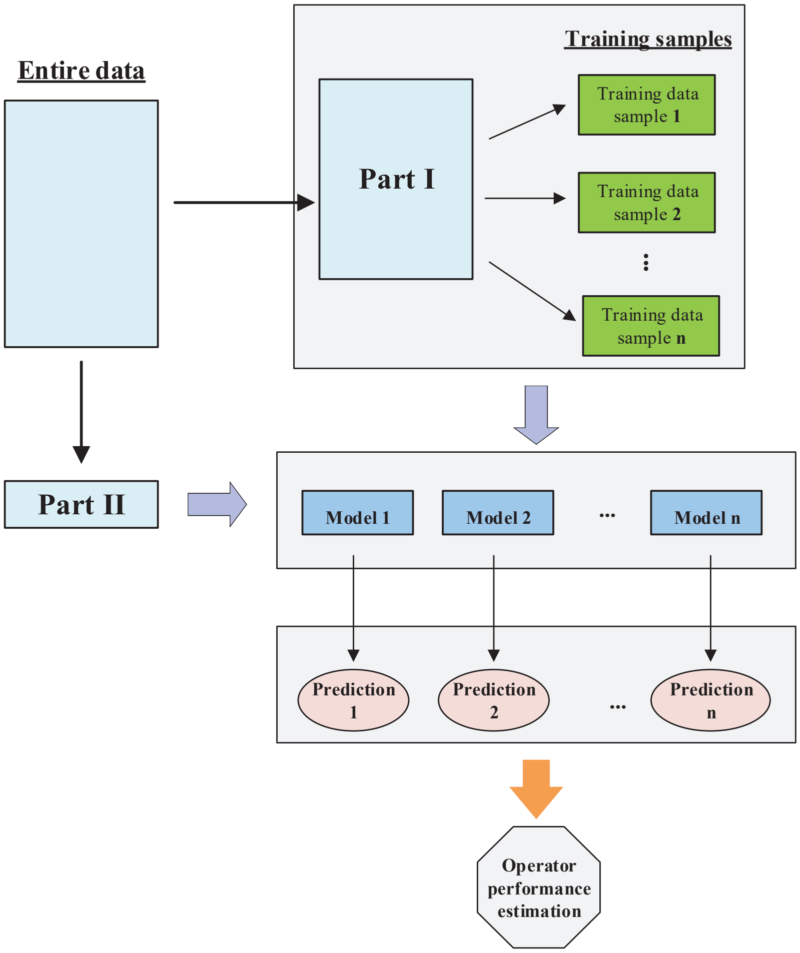

Figure 5.16: Framework of the quantitative model

Next, we build four individual models to predict the numerical counts corresponding to each rating value as indicated in Table 5.11. For all the four models, we set the value of parameter d the same: $d = 3$. With respect to the value of parameter C for each class,

Table 5.12: Prediction accuracy of the four individual models

Rating value	**0**	**1**	**2**	**3**
Classes	[0, 1, 2, 3, 6]	[0, 1, 2, 3, 4]	[0, 1, 2, 3, 4]	[0, 1, 2, 3, 4, 5, 6, 7, 8]
Prediction accuracy	83.33%	75.50%	82.28%	75.13% ([mode-1, mode + 1])

we make its value inversely proportional to the number of data belonging to each class in the training dataset, thereby overcoming the imbalanced class distribution. As mentioned earlier, since the size of the problem dimension is relatively large compared to the number of data records, any single model might not be adequate to capture different patterns equally well. Different from an individual model, ensembles of models build their outcome from a combination of the outcomes of individual models, and they have been shown to be effective in addressing many practical problems because of their prediction accuracy and stability as well as the advantage in avoiding overfitting [184, 185]. Herein, we integrate the support vector machine with bootstrap aggregating to improve the prediction accuracy by combining the classification results from numerous models trained by randomly selected samples.

The framework of the proposed methodology is illustrated in Fig. 5.16. The entire data is split into two parts: Part I is used for training the model, and Part II is used for verifying the performance of the trained model. We randomly select 10 records to validate the performance of the trained model. Then we randomly choose 85% data of Part I data for 100 times and each combination of the randomly chosen samples is used to train one model. Thus, we have 100 trained models. Then all the trained models are used to predict the system response for the verification data. To measure the prediction accuracy, for the first three models, we use majority voting to determine the class because the majority voting represents the class predicted most often by the 100 base classifiers and it also helps to cancel out the impact of random variation. Then we compare the results against the actual numerical counts. For the fourth model, we count the times the actual numerical count falls within the interval [mode - 1, mode + 1] and divide it by the number of validation data points to compute the prediction accuracy because there are 9 classes in this model. We repeat the same process twenty times to acquire an average prediction accuracy of the four individual models, and the results are shown in Table 5.12. As can be observed, the prediction accuracy for the third model is the highest among the four models.

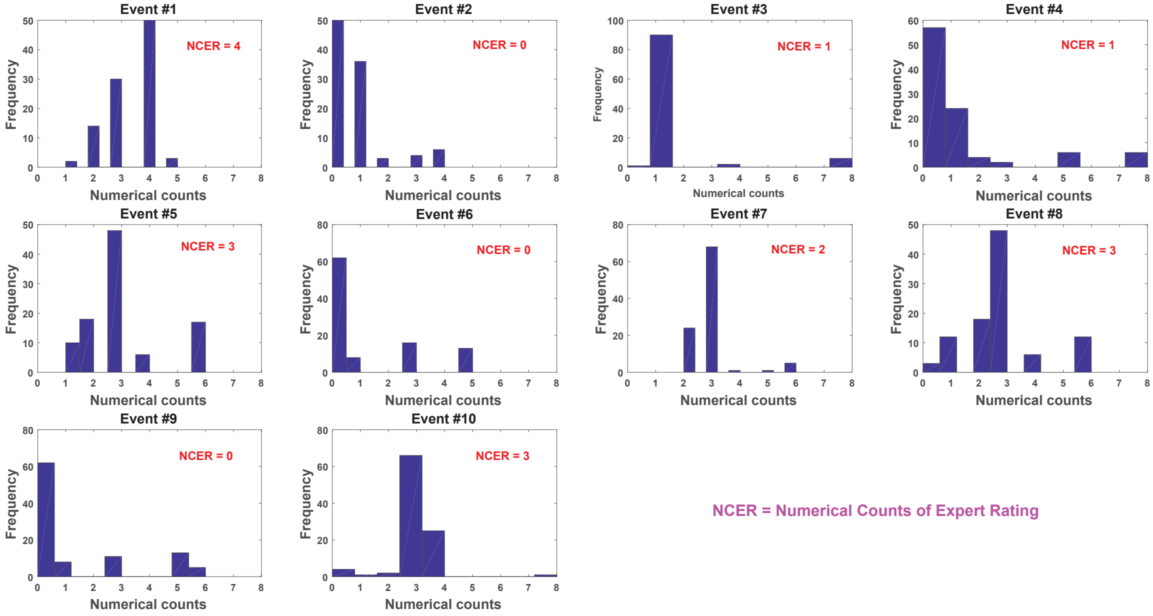

Figure 5.17: Predicted numerical counts for ten validation malfunctions (rating value is 2: minor delays in response to malfunction events)

Fig. 5.17 shows the predicted numerical counts for the ten malfunctions in the verification dataset when the rating value is 2 (minor delays in response to malfunction events). The blue bars demonstrate the predictions from the 100 trained models, and NCER indicates the actual numerical counts calculated from the expert ratings. It is seen that the modes of the predictions from the ensemble models agree with the expert ratings. Out of ten malfunction events, prediction frequencies of eight are consistent with the numerical counts of expert ratings. Regarding the remaining two malfunction events, although the predictions are different from the expert ratings, they are only one unit away.

Similarly, the trained model also demonstrates a significantly higher prediction accuracy when the rating values are 1, 2, or 4. As shown in Table 5.12, the model has a prediction accuracy of 83% and 76% for the rating value 0 (i.e., failing to eliminate the malfunction) and 1 (significant lapse in performing the task), respectively. Since there are nine unique numerical counts for the rating value 3 (timely response to malfunction events), we checked whether the actual numerical count fell within the prediction interval [mode - 1, mode + 1], and the model had an accuracy of 75.1%. The performance analysis across the four rating values illustrates that the proposed methodology can significantly predict the team performance through fusing the heterogeneous sources of data. In addition, to assess the relative contribution to prediction accuracy of physiological data versus eye tracking data, we created SVM models that used each of these sources individually. Neither model outperformed the model containing both data sources the fused model outperformed the two alternative models by 1% to 7%, respectively, in predicting the team performance.

5.5 Summary

This chapter presents an application of information fusion to develop a data-driven model to assess the operator performance in restoring system performance by eliminating abnormal events in NPP control rooms. Based on a dataset from a full-scope nuclear power plant simulator experiment recruiting previously licensed operators, we have developed a method that combines support vector machine with bootstrap aggregating to build a data-driven model for predicting crew performance. Our method first extracts numerous features from a heterogeneous dataset and then fuses the quantitative information derived from the diverse sources, thereby learning the relations between the elicited features and crew performance. Despite the limited amount of data (107 records), the best trained ensemble model, which contains 22 input variables/features, has an 82.28% accuracy in predicting crew performance in terms of the numerical counts of expert ratings (on an ordinal scale between zero and three). This ensemble model of the full heterogeneous dataset is superior to SVM models built with either physiological or eye-tracking data, and substantially better than simple correlation between performance outcome (i.e., OPAS) and any individual input features. Further, we can expect additional data are expected to improve the prediction accuracy of operator performance. The overall results of this study thus illustrate that the proposed information fusion approach is promising for estimating performance of NPP operators.

The principal merit of the proposed information fusion methodology is in combining diverse data sources for model prediction. First, the 22 input features are highly heterogeneous, deriving from scenario characteristics, subjective ratings of workload, situation awareness of process parameters, eye-tracking data, respiration rate, and skin conductance response. Second, the Pearson-product moment correlation analysis indicates that the strength of correlation between all the 22 input features and performance outcome of interest is at best moderate (between -0.32 and 0.38), suggesting that none of the features is dominantly predictive. Yet, the trained ensemble model is able to predict the operator performance outcome at a reasonable accuracy (prediction accuracy of 75%-83%), indicating that information fusion can capitalize on diverse measurement types, each of which improves performance prediction incrementally.

Our results also suggest the merit of employing physiological measurements in estimating operator performance. Physiological measurements, besides eye-tracking, in high fidelity NPP control room simulator experiments are virtually non-existent in the literature [186]. Our empirical data-driven model shows a reasonable predictive relationship between operator physiological indicators and visual activity and crew performance. The proposed approach can be used to provide a means for comparing crew performances under different operating conditions through the various physiological indicators and eye movement activity. The results of this study is encouraging for further research in physiological measures for assessing crew performance.

A method for building human performance data models could be invaluable to assess operator qualification and control room design given many on-going modernization and new construction projects. While the literature contains a few quantitative assessments of nuclear power plant operators [187, 188, 189], most studies rely on either subjective discussion or rudimentary quantitative methods (e.g., simple correlation statistics) of integrating results of multiple measurement dimensions (e.g., SA, workload, eye-gaze). In contrast, we describe a quantitative data-driven approach to fuse different performance dimensions that could provide a more holistic and precise assessment of operator qualification and control room design than the current state-of-research or practice [179, 190].

The proposed empirical approach has several features that maybe useful to the next generation human reliability models. The proposed framework may reduce demand on experts to rate task performance, which has been identified as one of the major needs in the next generation models [186]. In addition, the physiological responses and eye-gaze behaviors may provide additional objective measures of operator performance [191]. As indicated in Ref. [186], the next generation human reliability methods need to be detailed enough to support data collection and experimental validation. We specify a set of input features and corresponding extraction methods for diverse types of experimental data, providing guidance to researchers and practitioners for carrying out operator assessment with an information fusion approach. The direct measurable factors on each operator (i.e., skin conductance response, respiration data, and eye movements) might also enhance the model's capability to predict individual and crew performance. Finally, the results of this study indicates that our methodology, or the information fusion approach in general, can yield meaningful prediction of operator performance with a reasonable amount of data that individual NPPs can feasibly generate more than the data available in our study through the mandatory simulation training of professional operators.

The reliability analysis of nuclear power plant control room operator in dealing with system malfunctions deepens our understanding on the response effectiveness of human operators. By assessing the response effectiveness of human operators, it might enable us to pinpoint the directions (e.g., upgrading to ecological interface, developing diagnosis decision aiding tools) to move towards for the sake of enhancing operators' responsiveness. For example, the interface can be improved to include more salient features, which will enable operators to diagnose anomalous system behavior quickly; visualization decision support systems can be integrated in the NPP control room to support and speed up operators' diagnosis process. Such operations in improving human response effectiveness will significantly strengthen the resilience of the human-in-the-loop system against disturbances, and accelerate the speed of restoring system performance to normal level.

In addition to human response, the algorithms/strategies taken to handle emergency situation also plays an essential role in system performance recovery. In Chapter 6, we focus on characterizing the effectiveness of algorithmic response in handling extreme events.

Chapter 6

Performance Assessment of Algorithmic Response to Hazardous Events[1]

6.1 Introduction

In addition to human operators, the strategies that are used to manage hazardous events also have an explicit impact on the degree to which system performance could be restored. In this chapter, we develop a simulation-based approach to investigate the effectiveness of an algorithmic response in mitigating the impact of extreme event. In particular, we analyze how long the system survives under a given algorithmic strategy with the consideration of uncertainties arising from multiple sources, and the proposed method is illustrated with a rerouting algorithm that is used to respond to the closure of a destination airport.

Consider a disruptive event caused by an abnormal weather condition that results in the closure of an airport. Under this circumstance, we need to seek feasible alternate routes for all the aircraft that are flying towards this airport based on the characteristics of each aircraft and available space at nearby airports. In the literature, many measures, such as delaying flights already en route by restricting miles-in-trail or other means, and Ground Delay Programs (GDPs) [192], have been investigated to alleviate the congestion caused by the closure of an airport. Compared with other possible measures, aircraft re-routing is one of the most commonly used strategies because it imposes less controller workload, and the risk is very low. Currently, many ATFM operators, such as the Air Traffic Command Center (ATCC) coordinating flow management in US, are called upon to reschedule and re-route the aircraft so as to minimize the delay costs caused by congestion. Specifically, in the context of airline operations, prior to the disruption, the aircraft are scheduled to fly a set of routes as planned. Upon the occurrence of a disruption, the initial routes become infeasible, which calls for aircraft re-routing, that is to identify a new feasible route for

[1] An archival paper related to this chapter has been published in the journal Decision Support Systems. For more details, see Ref. [27]

each aircraft.

There is extensive literature on flight re-routing to minimize congestion cost [193, 194, 195, 196, 197]. In particular, Odoni presented seminal work [198] to model the flow management problem (FMP) as a discretized representation of flows, which is fundamental to the approaches developed subsequently. Bertsimas and Patterson [199] extended the Air Traffic Flow Management (ATFM) model to account for the re-routing of soon-to-depart or airborne flights. Subsequently, they developed a dynamic network flow approach to address the problem of determining how to reroute aircraft when faced with dynamically changing weather conditions [200]. Matos and Ormerod [201] discussed the issues in European ATFM and identified the needs in terms of Decision Support Systems (DSS) for re-routing flights. In response to Matos and Ormerod, Leal and Powell [202] attempted to build a re-routing decision support system in Europe by identifying participants and investigating the requirements for re-routing systems. To respond to aircraft grounding and delays experienced over the course of the day, Bard and Arguello [203] proposed a time-band optimization model for reconstructing aircraft routing, in which the time horizon transformed from the routing problem is discretized. Balen and Bil [204] analyzed an optimal aircraft re-routing plan in a free flight environment in the case of airspace closure and developed a software to re-route the aircraft around the closed airspace. Recently, an integer programming model has been proposed in [205] for large-scale instances of the ATFM problem covering all the stages of each flight, i.e., take off, cruise, and landing. Subsequently, a method is proposed in [206] based on [205], which accounts for the airspace volume. Seminal work is presented in [207] on ATFM rerouting *under uncertainty* in airport arrival and departure capacity, air sector capacity and flight demand. Rosenberger *et al.* [208] developed an optimization model for aircraft recovery (ARO) that reschedules legs and reroutes aircraft by minimizing an objective function involving rerouting and cancellation costs.

Some of the above studies have considered uncertainty, but mostly related to the external environment, e.g., uncertainty in weather prediction [201, 209, 210]. Even when some studies focus on the inherent uncertainty in the air traffic control (ATC) system, only one or two system components are taken into consideration, such as ground and departure delays [211]. Aircraft re-routing is a complicated process, in which several subsystems are involved, such as radar performance, message communication, airport resource management, etc. Visit https://www.faa.gov/air_traffic/flight_across_america/ for details on the process of a flight across the USA. At each phase, several sources of variability and uncertainty emerge in different subsystems. These uncertainty sources have a significant effect on the air traffic, which challenges the management techniques and decision support systems classically used by the researchers.

In the past years, several studies have made significant effort in the development of management policy or decision support systems in the presence of uncertainty because the problem under uncertainty is completely different from the deterministic case. For example, to cope with the uncertainty in the travel demands and traffic conditions, Balbo et al. [212] developed an adaptive solution to the bus network management problem by utilizing multi-agent approach to model the various bus network activities. To design the optimal policy for the transportation networks, Pathak et al. [213] proposed an agent-based model, in which they accounted for both aleatory uncertainties (e.g., random demand, randomness in speed) and epistemic uncertainty (e.g., the incomplete information of user behavior). Yoon et al. [214] developed a computer-based training prototype to improve the emergency response and recovery effectiveness under the pressures of incomplete and erroneous information. As mentioned earlier, due to the uncertainty arisen in the ATC system, there is also an increasing demand for developing a decision support system with the consideration of the multiple sources of uncertainties emerging in the re-routing process [215]. Prior to developing the decision support system, we need to answer several questions: where the uncertainties come from, how to characterize these uncertainties, how to propagate the uncertainties through the system, and how to quantify their influence on the system performance. Answering these questions will lay a firm foundation for the development of ATC decision support system under uncertainty.

In this chapter, we consider re-routing aircraft given the occurrence of an abnormal weather condition. Thus, the weather condition is given and there is no uncertainty, especially considering the short duration of the re-routing simulation. As indicated in the chapter later, there are 10 simulation cycles in our analysis, and each simulation cycle lasts for 5 minutes, which means the total simulation duration is only 50 minutes. We assume that there is no uncertainty in forecasting the weather condition for the 50 minutes; this is reasonable given the current technology for monitoring and forecasting the weather. On the other hand, our focus is on the inherent uncertainty sources within the re-routing system, e.g., message communication, radar, aircraft, and airport. By investigating their effect on the system performance, we aim to establish the foundation for the design optimization of the re-routing system. Obviously, weather is an external condition and is not a design variable.

Since aircraft re-routing is a complicated process, there are many interactions among the components, e.g. radar and decision maker, decision maker and airport, airport and aircraft. Moreover, the status of the aircraft (e.g., detected or not, registered or not, assigned or not) and radar (e.g., beam orientation) are varying over time. Simulation methods [213, 216] are capable of capturing the time-varying updates and the information exchange between the multiple components of such systems. As a result, we construct a simulation-based approach to mimic the aircraft re-routing process and account for the aforementioned multiple sources of uncertainties. Compared to the current state of the art, we have made the following contributions :

1. We develop a simulation framework to model the aircraft re-routing process and incorporate a formulation for optimal re-routing assignments. Our simulation framework considers the aircraft re-routing process as a system of systems, and enables us to have a comprehensive understanding of the system work flow and the interactions among various systems. Such a simulation-based approach facilitates quantitative

evaluation of the re-routing methodology.

2. We analyze various uncertainty sources in the systems involved in the re-routing process (aircraft, radars, communication systems, and neighboring airports), and perform the simulation and re-routing optimization by incorporating the uncertain sources. Incorporation of uncertainty sources is essential in ensuring a robust and reliable re-routing system.

3. We develop a methodology to quantitatively evaluate the performance of the re-routing system by considering the effect of the various uncertainty sources on the system performance, and incorporate reliability analysis techniques for this purpose.

4. We incorporate novel stochastic sensitivity analysis techniques to quantify the relative contributions of the different uncertainty sources on the system performance; this facilitates a quantitative basis for optimal allocation of limited resources to improve the system performance.

5. We incorporate surrogate modeling to improve the computational efficiency and enable fast analysis of system performance. This helps to quantitatively evaluate and compare several different competing strategies for re-routing optimization and system improvement.

In our simulation system, there are three core modules: radar system, communication system, and the assignment algorithm, which will be introduced in Section 2. The following uncertainty sources have been considered in this chapter:

- Radar performance: Radar performance depends on three parameters, namely: initial orientation, detection radius, and beam rotation speed. All three parameters are stochastic and follow different distributions.

- Neighboring airports: Space availability (gate, runway, and airspace) at each airport is uncertain, and is varying with time.

- Message communication system: Delay is commonly encountered in the communication system, and the amount of delay is stochastic.
- Aircraft: Aircraft have four attributes: speed, size, entry time and location. All of them are stochastic variables when analyzing or designing the overall system.

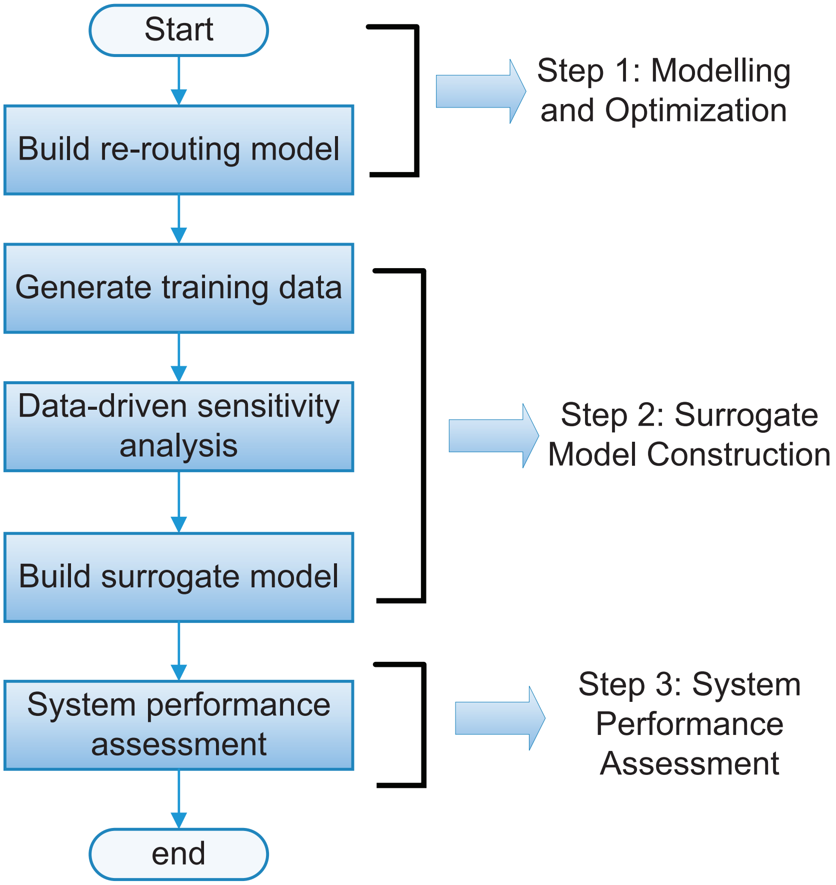
Start
Build re-routing model
Generate training data
Data-driven sensitivity analysis
Build surrogate model
System performance assessment
end
Step 1: Modelling and Optimization
Step 2: Surrogate Model Construction
Step 3: System Performance Assessment

Figure 6.1: Framework of aircraft re-routing optimization and performance assessment

In the presence of the aforementioned uncertainty sources, some challenges emerge: (1) How to propagate the uncertainty through the re-routing system, (2) how to evaluate the system performance with the consideration of the aforementioned uncertainties, and (3) how to quantify the effect of each uncertain variable on the overall system performance.

In this study, we address these challenges by developing a dynamic simulation-based approach that accounts for multiple uncertainty sources and their impact on the aircraft re-routing decision. We do not consider the uncertainty from the external environment, such as the uncertainty in weather prediction; that is, we consider re-routing for a given weather condition. We focus on the aleatory uncertainty in the re-routing system related to message transmission, radar performance, demand from incoming aircraft, and space availability at nearby airports.

An optimization model is constructed to make periodic assignments of the registered aircraft with the objective of minimizing the overall travel distance. We use the system failure time, which is defined as the time instant that at least one aircraft in the simulation runs out of fuel, as a metric to measure the re-routing system performance. Since the duration of each simulation is limited, the system performance is not available in all simulations. An effective strategy is developed to extract the lower bound of the system failure time from right-censored data. The above procedures are represented as Step 1 in Fig. 6.1.

As stated previously, we are interested in evaluating the re-routing system performance in terms of the system failure time. To achieve this objective, a large number of simulations is required to build the probability distribution of system failure time. However, each simulation is very time consuming. Hence, we build a surrogate model to replace the original simulation. Since there are too many random input variables, we implement a data-driven sensitivity analysis method to identify the dominant variables, then build the surrogate model using support vector regression with the identified dominant variables. Then we construct the system failure time distribution using the surrogate model. The aforementioned processes are denoted as Steps 2 and 3 in Fig. 6.1.

6.2 Proposed Methodology for Aircraft Re-routing

In this section, we introduce the components of the proposed re-routing methodology – problem description, airspace system model, uncertainties considered and the assignment algorithm.

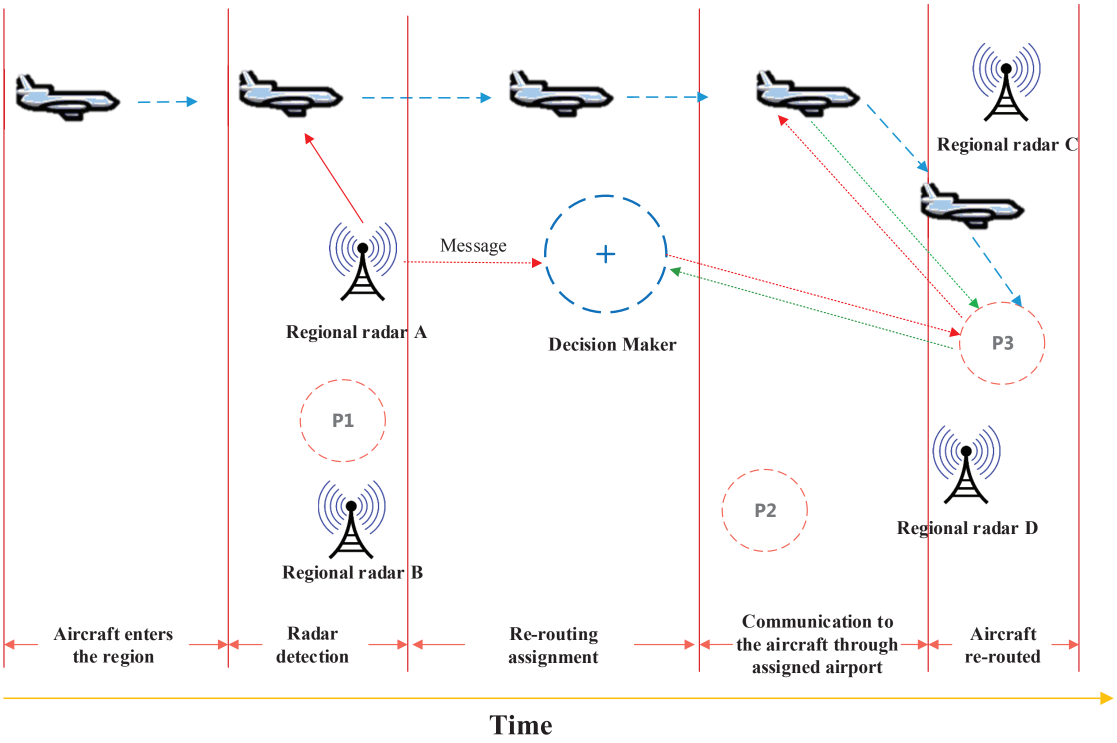

Figure 6.2: Aircraft re-routing process

6.2.1 Problem Description

In the United States, the control of air traffic is carried out at 22 regional centers that receive information from aircraft and ground-based radars on location, altitude, and speed of the aircraft. The Air Traffic Command Center (ATCC) aggregates all the information collected by the 22 regional centers to reschedule and reroute flights when a hazardous event (e.g., bad weather) occurs [200]. In this study, as shown in Fig. 6.2, we characterize this process in a simplified manner using a five-step procedure:

(1) In the first phase, the aircraft enters the region at a randomly generated location and time instant, and flies towards its destination airport at a constant speed. We assume that the flight path follows a straight line in a 2-D space that connects the entry location and the destination airport.

(2) The time when the aircraft enters the region of interest is Entry Time. Once the aircraft

enters the region, it is detected after some time by either a regional radar or a local radar. The detection time is uncertain depending on the radar's orientation, detection angle, and detection radius. The time instant the aircraft is detected by the radar is Detection Time. Once a radar detects an incoming aircraft, it sends a message to the decision maker (DM). This message might be delayed. When DM receives the message from the radar, the aircraft is registered in the system. The time instant when the aircraft is registered in the system is called Registration Time.

(3) The DM periodically makes re-routing assignments for all the aircraft that are registered in the system and waiting to be re-routed. The re-routing decision for a particular aircraft requires the corresponding resources to be available and compatible, i.e., the aircraft of a particular size can only land at the airport with available airspace, runway, and gate that are suitable for that aircraft size. The specific assignment algorithm will be developed in Section 6.2.4. The time instant when the aircraft is re-assigned is called Assignment Time.

(4) After the assignment decision is made, DM sends a message to the assigned airport. When the assigned airport receives the message, it sends an acknowledgement message to DM. It also sends a message to the assigned aircraft to establish further communication for landing. All three messages can be delayed.

(5) When the aircraft receives the message from the assigned airport, it sends an acknowledgement message to the assigned airport and starts flying towards the assigned airport. After the aircraft arrives at the assigned airport, the corresponding resources, e.g., gate, runway, and airspace, are released for future assignment. We name the time when the aircraft lands safely as Leaving System Time.

Obviously, aircraft re-routing is a complicated process, where multiple subsystems and components are involved, and the uncertainty related to each component further intensifies the complexity of this problem. In this study, the system performance we are interested in is measured by the system failure time metric, defined as below:

Definition 6.2.1 ***System failure time****: When at least one aircraft runs out of fuel, the re-routing system fails at that time instant. This time instant is defined as the system failure time.*

Since several uncertain variables contribute to the variability of system performance, we are motivated to quantify the contribution of each uncertain variable, thus facilitating our decision making process for the purpose of enhancing system performance. To achieve these objectives, a simulation-based approach is used to characterize the re-routing process, by which we are able to capture the complex interactions among various subsystems. In the following sections, we introduce the modelling of each component and subsystem in the re-routing process.

6.2.2 System Model

In this section, we introduce the simulation model we built to account for the various uncertainties in the process, related to airports, aircraft, radar, and communication. Before formulating the problem, we need to introduce the fundamental assumptions with respect to each component, in order to facilitate the discussion.

6.2.2.1 Region

Region refers to the specific area where we perform the simulation; all the components (e.g. radar, aircraft, airport), are operated within the region. For the sake of illustration, in the numerical example, we use a 500×500 square area as shown in Fig. 6.3 as our simulation space. In reality, the region can be any shape, e.g., polygons, triangle, or any other shape.

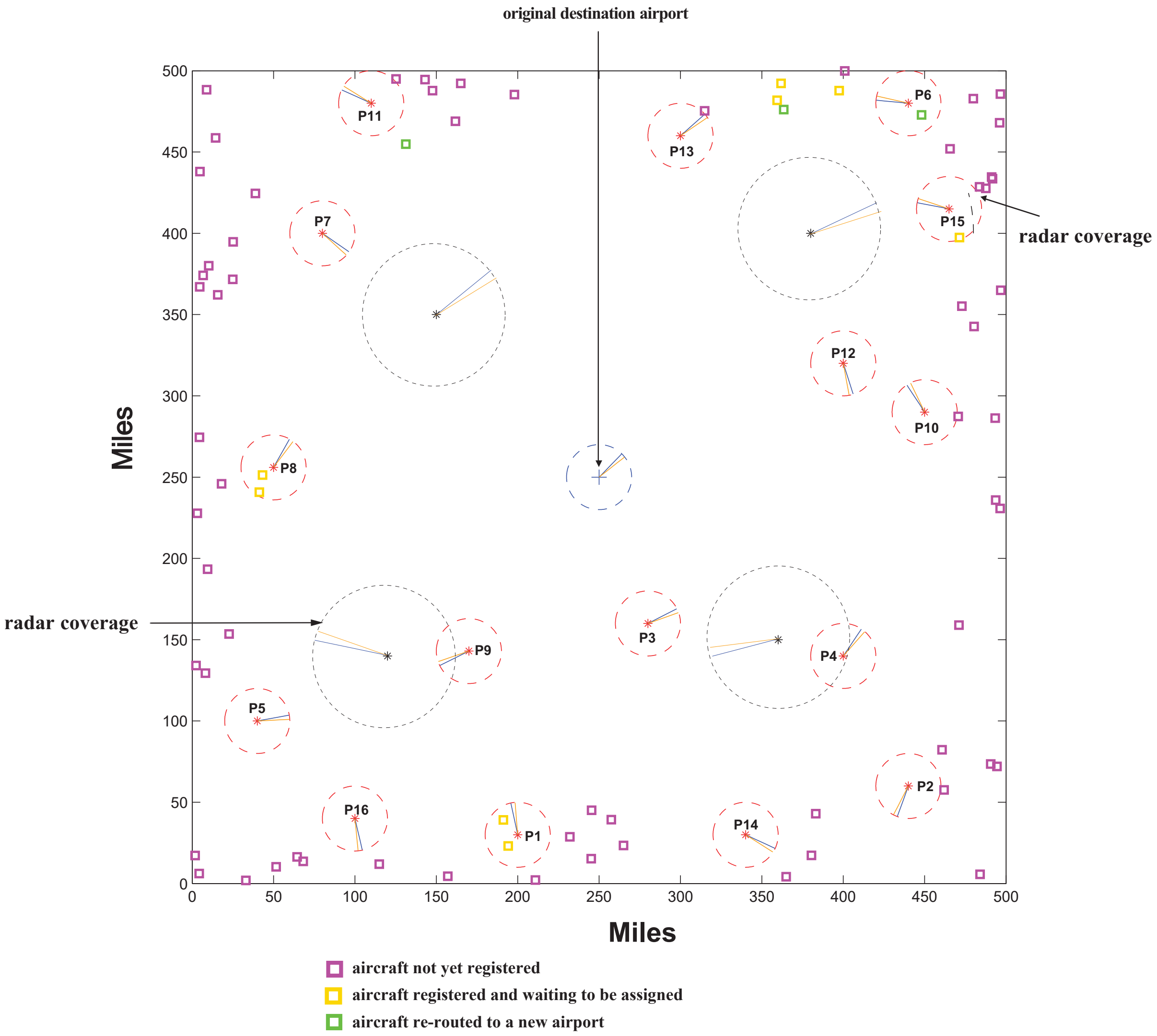

Figure 6.3: A snapshot of the simulation system

6.2.2.2 Aircraft

In the re-routing problem considered, the aircraft are assumed to be flying towards a single destination airport at a constant speed. For each aircraft, we need to generate its entry time, entry location, aircraft size, speed, and remaining miles. Each of these variables is associated with uncertainty; we will discuss these uncertainties in Section 6.2.3. For the sake of simplicity, in the re-routing simulation, we only consider the aircraft flying into the region and heading towards the closed airport. As shown in Fig. 6.3, the airport indicated by a dashed circle in the center of the square is closed due to extreme weather, hence all the aircraft heading towards this airport will be re-routed to other alternate airports.

6.2.2.3 Nearby Airports

A very important component in the re-routing decision is space availability at the nearby airports. In this study, we choose 16 airports for the sake of illustration as shown in Fig. 6.3, but our simulation can handle any number of available airports for re-routing the aircraft. The availability of runways, gates, and airspace in each airport is considered by the assignment algorithm. In order to guarantee the safe landing of the aircraft, all the necessary facilities need to be available. There are several uncertain variables related to the space availability, and these will be introduced in Section 6.2.3.

6.2.2.4 Radars

Once an aircraft enters the region of interest, it might be detected by the radars in the system. Two different types of radar are considered: regional radars and airport (local) radars. The only difference between them is the detection radius. Regional radars have larger detection radius than local ones. The locations of all the radars are fixed. In this study, we consider three uncertain variables related to radar: radar's initial orientation, radar beam rotation speed, and radar range, which will be described in Section 6.2.3 in detail. In this study, we use a sparse cluster of radars for the sake of illustration, but the simulation is general to account for the case with a high density of radars within the region.

6.2.2.5 Communication

There are many communications among the various components, for example, radar needs to send message to the decision maker to inform the newly detected aircraft. Currently, controller-pilot data link communication (CPDLC) is a commonly used means of communication between controller and pilot [217]. There is a sequence of messages between the pilot and the controller, which is referred to as dialogue. The duration of the dialogue is variable, depending on several factors, such as clarity of the vocal phraseology, controller workload, and the deviation of the revised route from the original one. All these factors increase our uncertainty in estimating the time of the communication.

Such delay has significant influence on the controller-pilot communication, manifested in increased number of “step-ons” (instances when a pilot or a controller begins his/her transmission before the previous transmission is over, resulting in interference blocking both transmissions), increased controller and pilot workload, and increased risk of violating aircraft separation [218]. Typically, controllers control traffic by issuing specific instructions and commands to pilots, then the pilots, after an unavoidable delay, execute the instructed maneuvers. If the time delays are long or have significant variability, accurate prediction of their consequences becomes difficult, thus substantially increasing controllers mental workload and the probability of errors [219]. Therefore, understanding the effects of communication delay on system performance is important. In Ref. [218], several sources of uncertainty: audio delay (AD), pilot delay (PD), and controller delay (CD), were identified, and two experiments were performed to examine the impact of systemic delay in the pilot-controller communication loop. The cumulative effect of communication delays may be of significance depending on the specific context. In particular, in congested airspaces, the controller often has a limited number of alternatives to choose from, and the success of his or her control actions will depend on the appropriate timing of the issued command and the pilot’s response.

6.2.3 Stochastic Variables Considered

Note that in our case, initially, we do not know the relative contribution of each stochastic variable (aircraft, nearby airports, radar performance, and communication delays) on the system performance. Therefore, it is reasonable to first include all of them in our model; later, sensitivity analysis is used to identify the significant variables to be included in the model. In the following sections, we introduce the modeling of the uncertainty associated with each variable one by one.

6.2.3.1 Aircraft

With respect to the aircraft, we consider four different stochastic variables:

- **Entry Time**: Entry time determines when the aircraft enters the simulation region. Since the Poisson distribution is frequently used to express the probability of a given number of events occurring in a given amount of time if these events occur with a known average rate [220], we use it to generate the sequence of aircraft to enter the region in each simulation cycle. Thus, the inter-arrival time is modeled by an exponential distribution.

- **Entry Location**: The exact entry location of each aircraft could be anywhere on the boundary of the region. Since we use a square to represent the region of interest, two uniform random variables are used to characterize this uncertainty. The first variable determines one of four edges indicating the approach direction, while the other one specifies the location on the randomly selected edge. Using two independent random variables allows us to adjust the proportion of aircraft entries from different directions; for example, more aircraft could enter the region from the bottom edge if we assign a larger weight to it.

- **Size**: Aircraft of similar size have approximately the same passenger capacities, ranges, and velocities. Once an aircraft's arrival time and location are simulated, its size is randomly selected in the simulation. In this study, aircraft are assumed to have three different sizes: large, medium, and small. We assume aircraft size is randomly selected among three options – large, medium, and small – with equal probabilities.

- **Speed**: Aircraft speed is related to its size. Typically, aircraft of larger size have higher cruise speed. In addition, even among the aircraft of the same size, the speed might vary from aircraft to aircraft. In this study, we assume three different lognormal distributions to represent the speed for aircraft of large, medium, and small sizes, respectively.

- **Remaining Miles**: The number of remaining miles depends on the amount of fuel remaining in the aircraft. It is difficult to know the exact number of remaining miles of each aircraft. Thus, we use a lognormal distribution to characterize this uncertainty. The standard deviation is assumed to be 10 miles, and the mean value is assumed to be the product of a factor β and the distance from the aircraft entry location to the farthest airport in the region. This is only for the sake of illustration; the uncertainty regarding remaining miles can be represented in different ways. For example, the mean value could also be the distance from the entry location to the destination airport, multiplied by a factor greater than unity.

6.2.3.2 Nearby Airports

In reality, each nearby airport might have different numbers of runways, gates, and airspace. To characterize the variability across the airports, we represent their mean values using variables κ, ξ, and η, which follow three different uniform distributions. In addition to that, for a given airport, there are aircraft arrivals and departures over time, which will occupy or release the resources over time. Two types of sampling are implemented in this chapter to represent this variability: at the beginning of each simulation, the mean values κ, ξ, and η are randomly generated; in each assignment cycle, we make specific realizations with respect to the available runways, gates, and airspace, by which we account for the dynamic change of available space at each nearby airport. The above three types of spaces are classified by three different sizes of aircraft: large, medium, and small. In order to guarantee the safe landing of an aircraft in an airport, all three types of spaces should be available and suitable for that aircraft size. Then we account for the physical relationship between aircraft size and airport availability. For example, if the airport cannot accommodate large size aircraft, the variables κ, ξ, η corresponding to large size aircraft will be zero.

6.2.3.3 Radar Performance Uncertainty

In reality, the radar performance is affected by many factors, such as the power density at the target position, reflected power, radar cross section, antenna gain etc. The target detection not only depends on the power density at the target position, but also on how much power is reflected in the direction of the radar. A commonly used equation to compute the maximum radar detection range is [221]:

$$R = \sqrt[4]{\frac{P_S \cdot G^2 \cdot \lambda^2 \cdot \rho}{P_E \cdot (4\pi)^3}} \tag{6.1}$$

where P_S is the transmit power, G is the antenna gain, λ is the transmit wavelength, ρ is the radar cross section, and P_E is the power received by radar antenna, expressed as

$$P_E = \frac{P_S \cdot G \cdot \rho}{(4\pi)^2 \cdot R^4} \tag{6.2}$$

As shown in Eq. (6.2), the power received by the radar P_E is inversely proportional to R^4, while the strength of the received power will influence whether the target can be detected accurately or not. Suppose $P_{E_{min}}$ is the smallest power that can be detected by the radar; if the power is less than $P_{E_{min}}$, then it is not usable because it is lost in the noise of the receiver. In other words, the probability of detecting a given target is associated with the strength of the received power, while the received power varies with the distance between the target and the center of the antenna beam. In addition to distance, when electromagnetic waves cross airlayers at different density, the occurrence of refraction results in the dispersion of the transmitter energy, which affects the energy received by the receiving antenna. Except refraction and dispersion, some other phenomena also have significant effect on radar's performance, e.g., interference with other signals, noise in the radar signal. Another important factor is the radar cross section ρ, and it is related to the angle formed by the aircraft flight path and the beam orientation.

These uncertainties are important for safety in aircraft operations. As indicated in

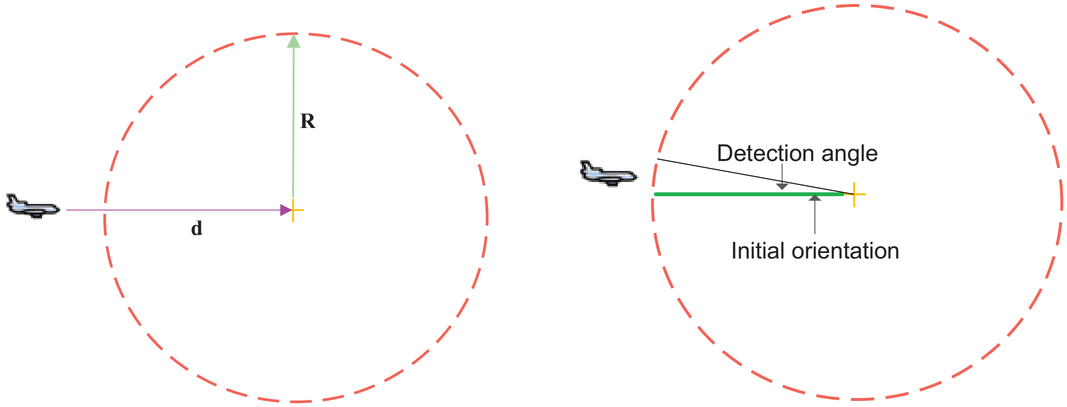

(a) Radar detection event (b) Radar detection angle

Figure 6.4: Radar performance uncertainty

Ref. [222], airborne radar can be utilized to sense the surrounding environment, e.g., wind speed, meteorological condition, thus aiding the aircraft Inertial Navigation System (INS). In this process, the uncertainty inherent in radar antenna and radar pointing angles, if not corrected, will seriously degrade the dual-Doppler winds. Besides, radar is also used to monitor aircraft location and aid aircraft navigation [223, 224]. If the uncertainty associated with the radar is too large, it increases the difficulty in estimating the aircraft location. In this case, to maintain the safety of each aircraft, we must make the separation distance larger. On the contrary, if we know the precise location of each aircraft, we can make the separation distance smaller, thus enabling us to accommodate more aircraft in the same airspace. This argument has been reflected in the development of NextGen technologies. One proposal to overcome radar uncertainty is the transition from radar surveillance to ADS-B (Automatic Dependent Surveillance-Broadcast) to track airplanes in flight and on the ground more accurately and reliably [225]. Such a proposal clearly demonstrates the significance of radar uncertainty in air traffic system. See Ref. [226] for the description of ADS-B.

To account for the above uncertainties related to radar, we model it in a simplified manner by characterizing its detection radius as a lognormal distribution. Specifically speaking, we consider the following uncertainties related to the radar:

- The detection radius varies from radar to radar. In the numerical example, regional radars are assumed to have a detection radius following a lognormal distribution $LN(R_r, 10)$ whereas local radars have a detection radius of $LN(R_l, 5)$. In the simulation, we implement different realizations for each radar. When the distance d is less than the specific radar range realization R, where d is the distance from the aircraft to the center of the radar (see Fig. 6.4a), then the detection event occurs.

- The exact time when the aircraft is detected also depends on the initial orientation and radar beam rotation speed. The initial orientation of the radar beam varies from radar to radar. In this study, the initial orientation is assumed to follow a uniform distribution $U(0, 2\pi)$. The beam rotation speed determines the sector that a radar can cross in a second. Suppose the radar antenna has 2 revolutions per minute (RPM), then it covers a 12^0 sector in one second. The beam rotation speed also varies from radar to radar. A lognormal distribution is used to characterize the variability of the beam rotation speed. As shown in Fig. 6.4b, an aircraft can be detected only when it is within the detection sector.

6.2.3.4 Communication Delays

When disruption or inclement weather happens, the Air Traffic Command Center (ATCC) contacts each airline's Airline Operations Center (AOC) to inform about the necessity of re-routing. In this process, the regional radar and associated operators need to send messages to ATCC on the aircraft status, e.g., its altitude, location, and original landing airport. Based on the information collected from the ground-based radars, ATCC re-routes the corresponding flight to the available airport [200]. Multiple communications emerge in this process. Once the flight plan is filed, the communication starts between aircraft (pilot) and assigned airport (controller). Prior to landing, all Instrument Flight Rule (IFR) flights are conducted with controller-pilot communication regarding the status of runway clearance,

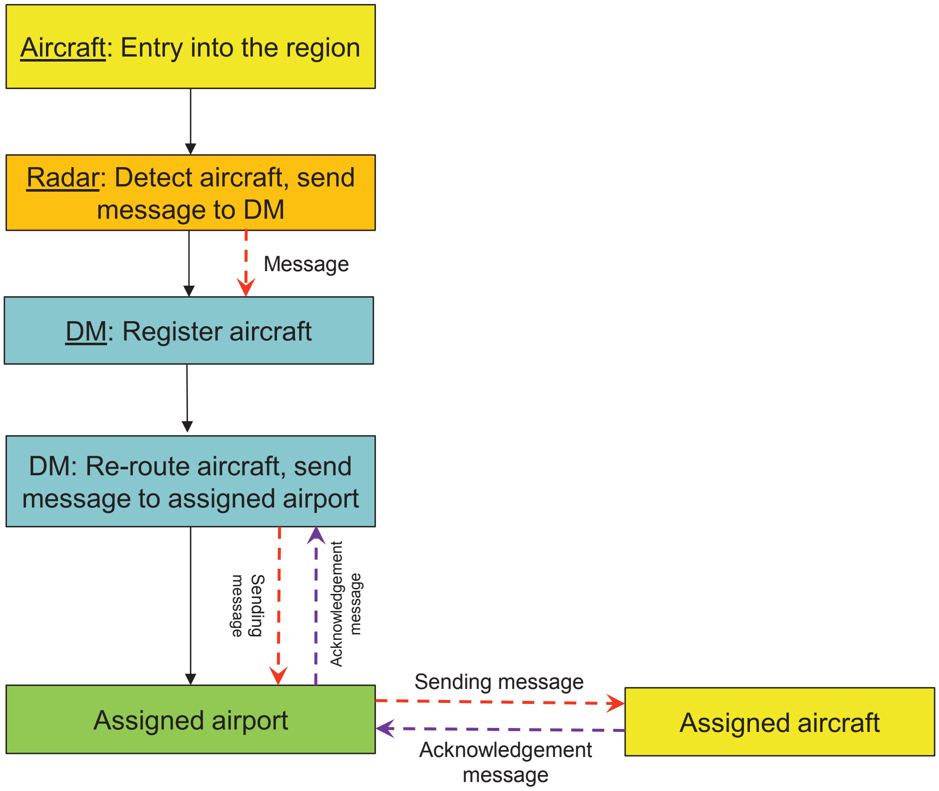

Figure 6.5: System workflow

gate availability, and taxiways [227]. Each time the communication occurs, message delay or loss arises with a given probability.

In this chapter, we simulate the above process in a simplified manner, in which the DM plays the role of ATCC. Fig. 6.5 illustrates the specific system work flow. There are three types of communication: registration, message communication between DM and assigned airport, and communication between assigned airport and assigned aircraft. Message delay can happen in any of three communications shown in Fig. 6.5. For the sake of simplicity, all delays are simulated using independent but identical lognormal distributions $LN(m_d, 4)$ seconds. If the message delay exceeds a predefined threshold, the message is treated as lost. To avoid message loss, each message sender periodically checks for acknowledgement (every 40 secs for the sake of illustration), and sends a repeat message if acknowledgement is not received.

List of Symbols

α_{ij} A variable used to denote the size of aircraft i. If $j = 1$, the size is large; if $j = 2$, the aircraft's size is medium; if $j = 3$, its size is small

AS_i Speed of aircraft i.

$d_t(i,k)$ Distance between the i_{th} aircraft and the k_{th} airport at time t

LF_{it} The remaining miles for i_{th} airplane at time t

M The number of airports in the system

P_t The number of aircraft at time t

SG^k_{jt} The number of available gates for airplanes of size j in the k_{th} airport at time t

SR^k_{jt} The number of available runways for airplanes of size j in the k_{th} airport at time t

SS^k_{jt} The number of available airspace for airplanes of size j in the k_{th} airport at time t

δ_{ikt} A binary variable. $\delta_{ikt} = 1$, if i_{th} aircraft is assigned to the k_{th} airport at time t. Otherwise, $\delta_{ikt} = 0$

6.2.4 Mathematical Model of Aircraft Re-routing Optimization

In the aircraft re-routing problem, suppose we have P_t aircraft in the region at time t and M airports. The DM makes periodic re-routing assignments. The objective is to the total distance travelled by all the airplanes, for safety and economic reasons [228, 229], subject to system resources. The optimization problem can be formulated as:

$$Minimize \sum_{i=1}^{P_t}\sum_{k=1}^{M} d_t\,(i,k)\delta_{ikt} \tag{6.3}$$

$s.t.$

$$\delta_{ikt} = 0 \;\; or \;\; 1, \tag{6.4}$$

$$\sum_{k=1}^{M} \delta_{ikt} = 1, \quad i = 1, \ldots, P_t \tag{6.5}$$

$$\sum_{j=1}^{3} \alpha_{ij} = 1, \quad i = 1, \ldots, P_t \tag{6.6}$$

$$\sum_{k=1}^{M} \sum_{i=1}^{P_t} \delta_{ikt} = P_t, \tag{6.7}$$

$$P\left(LF_{it} - d_t\left(i,k\right) \geq 0\right) \geq 0.9\delta_{ikt}, \quad i = 1, \ldots, P_t,\ k = 1, \ldots, M \tag{6.8}$$

$$\sum_{i=1}^{P_t} \alpha_{ij}\delta_{ikt} \leq min(SR^k_{jt}, SG^k_{jt}, SS^k_{jt}) \quad j = 1, \ldots, 3,\ k = 1, \ldots, M \tag{6.9}$$

$$LF_{it} = LF_{i0} - AS_i \times t, \quad i = 1, \ldots, P_t \tag{6.10}$$

where the decision variable δ_{ikt} is binary, defined as:

$$\delta_{ikt} = \begin{cases} 1, & \text{if the } i_{th} \text{ aircraft is assigned to the } k_{th} \text{ airport at time } t \\ 0, & \text{otherwise.} \end{cases}$$

The constraint in Eq. (6.5) requires that each aircraft registered in the system in the current cycle must be assigned to one of the available airports. Eq. (6.6) imposes aircraft size restrictions. Eq. (6.7) requires that all the aircraft registered before time t should be assigned at time t. Eq. (6.8) is a reliability constraint. Both LF_{it} and $d_t(i,k)$ are random variables. This constraint requires that the remaining miles in any aircraft is larger than the distance between the aircraft and the assigned airport with a probability of 0.9. Eq. (6.9) imposes the constraint that the number of aircraft of size j assigned to airport k should be less than the number of available resources in size j in airport k (runways, gates, and airspace). Constraint (6.10) denotes the relationship between the remaining miles and time, where LF_{i0} indicates the initial remaining miles for i_{th} aircraft.

This is an integer linear programming problem, in which only δ_{ikt} is the decision variable. In this study, we use the built-in algorithm – **intlinprog** – in Matlab to approach the solution of this problem.

When the assignment model formulated in Eq. (6.3) cannot make feasible assignment of all the registered aircraft, i.e., space is not available at any of the nearby airports for some of the registered aircraft, we do not consider the system to have failed immediately. Instead, we build a waiting queue for the registered but yet unassigned aircraft. According to the available space, e.g., runways, gates, and airspaces, at all the airports, we select the same number of aircraft from the waiting queue to make the assignment. There are many ways to rank the aircraft in the waiting queue, e.g., by registration time, or by remaining miles. For the sake of illustration, we carry out a "first-come first-served" (FCFS) strategy to order the aircraft in the waiting queue according to their registration time.

The optimization objective formulated in Eq. (6.3) is only for the sake of illustration, there are many other alternatives in real-world applications. In some programs, the airline company or ATCC aims to minimize the delay costs, e.g., passengers' delay, by re-routing certain flights. When some unexpected disruptions occur, passengers are inconvenienced and various costs are incurred. From the airline's perspective, their goal is to minimize the influence caused by disruption, e.g., minimizing deviations from the original schedule. In this study, we focus more on the uncertainty involved in the re-routing process rather than the optimization objective. Hence, for the sake of illustration, we minimize the total distance travelled by all the assigned aircraft to ensure safe landing within available remaining miles for as many aircraft as possible.

6.3 Proposed Methodology for Performance Assessment

In this section, we describe the extraction of the system failure time from the re-routing simulation, conduct variance-based sensitivity analysis to identify significant variables, and construct an SVR surrogate model with precise and imprecise data in order to construct the probability distribution of system failure time.

6.3.1 System Failure Time

As mentioned in Section 2, system failure time (see definition 2.1) is the metric of interest in analyzing the re-routing system performance. To build the system failure time distribution efficiently, the following analyses need to be performed:

- Given a specific input variable setting, how to efficiently predict the system failure time distribution without running the entire simulation?
- How to quantify the contribution of each uncertain input variable towards the variance of the output of interest, i.e. system failure time?

In each simulation, we have a fixed duration T to run the simulation to see if the system survives or fails. However, in some cases, the system survives longer than time T, which results in right-censored data defined as below.

Definition 6.3.1 ***Type 1 Censored Data***: *Consider reliability testing of n (non-repairable) units taken randomly from a population. During T hours, we observe r* ($0 \leq r \leq n$) *failures. The exact failure times are* $t_1, t_2, \ldots, t_r$, *and the other* $n - r$ *units survive the entire* T*-hour test without failing. This type of censoring is named "right censored" data since the times of failure to the right (i.e., larger than T) are not available.*

Since the times of failure to the right (i.e., larger than T) are missing for some simulations, the challenge is how to estimate the system failure time. But when the system fails, we have the information of all the aircraft waiting to be assigned, and we can identify the aircraft with the least remaining miles. Here, we apply a conservative strategy by using the lower bound of the system failure time as the actual system failure time. Suppose the least remaining miles is LF_{min}, the following theorem can be utilized to estimate the system failure time.

Theorem 6.3.1 *If* LF_{min} *is less than the minimum distance between the aircraft current location and all the airports, given its mileage consumption rate r, the time to failure is:*

$$S_{FT} = T + \frac{LF_{min}}{r} \tag{6.11}$$

where T represents the duration of the simulation.

Since LF_{min} is less than the minimum distance between its current location and all the nearby airports, in the subsequent assignments, it is impossible to make a feasible assignment. As a result, its remaining survival time determines how long the system can survive further. If LF_{min} is larger than the minimum distance, then we only know that the system survives longer than the S_{FT} in Eq. (6.11), thus S_{FT} captures the lower bound of the system failure time. In this case, the system failure time can only be expressed as an interval: $[S_{FT}, +\infty]$.

6.3.2 Variance-based Sensitivity Analysis

The sensitivity of a model output to the stochastic inputs can be measured through the relative contribution of each stochastic input to the variance of the output; the well known Sobol' indices (defined in Appendix C) are commonly used for this purpose. As mentioned in Appendix C, to compute Sobol' indices, a double-loop Mente Carlo simulation is required. There are 24 stochastic variables in our system. To calculate x_i's sensitivity, in the inner loop, we need to fix x_i and change all the other variables x_{-i}. Whereas, the outer loop requires fixing x_i at different values. Suppose both inner loop and outer loop have 100 cycles, then 10,000 simulations are needed, which in turn takes a large amount of time to collect the data. This is only sensitivity analysis for one single variable, not to mention sensitivity analysis for the remaining 23 variables. Assume that only 1000 simulations are affordable.

Fortunately, an efficient data-driven sensitivity analysis method has been recently developed [230], based on the concept of stratified sampling [231]. Suppose we divide the range of an input variable x_i into equally probable intervals $\phi = \left\{\phi^1, \cdots, \phi^M\right\}$, then the first-order Sobol' index can be computed as:

$$S_i = 1 - \frac{E_\phi\left(V_{\phi^l}(y)\right)}{V(y)}, \quad l = 1, \cdots M. \tag{6.12}$$

where $V_{\phi^l}(y)$ represents the variance of y when x_i is in the subspace ϕ^l, $V(y)$ denotes the variance of the system response y. See Ref. [230] for details of this approach.

6.3.3 SVR Surrogate Model with Precise and Imprecise Data

Generally speaking, in reliability analysis, the failure rate is quite small [232], e.g., 10^{-4}, 10^{-5}. If we aim to use simulation-based approaches to quantify the system failure probability, a large number of samples is required to estimate the failure probability. Suppose the failure probability is 10^{-4}, then we expect to obtain 1 failure data point out of 10,000 samples on average. In our re-routing simulation, each simulation lasts a duration of 2 to 10 minutes; depending on initial input variable settings, suppose we wish to collect 10,000 samples from the system, this will take 20,000 to 100,000 minutes, which is prohibitive. As a result, we need to build a surrogate model to replace the original simulation in order to efficiently build the system failure time distribution.

As mentioned earlier, system failure is not necessarily observed in all simulations. In such cases, we represent its survival time as an interval: $[S_{FT}, +\infty]$, where S_{FT} denotes the lower bound of system failure time. Suppose the dataset we have collected from the re-routing simulation is represented by $\mathbb{U}$, which we divide it into two separate groups: right-censored data, denoted by $\mathbb{U}_1$, and uncensored point targets, denoted by $\mathbb{U}_2$.

Consider a censored data point $\boldsymbol{x_i} \in \mathbb{U}_1$, in this setting, we want the predicted survival time for $\boldsymbol{x_i}$ to be within the range $[S^i_{FT}, +\infty]$, where S^i_{FT} denotes the lower bound of system failure time for $\boldsymbol{x_i}$. As long as the predicted value is larger than S^i_{FT}, there is no penalty. Otherwise, we penalize if the predicted survival time is less than S^i_{FT}. Hence, the robust ε-insensitive cost function L_ε for $\boldsymbol{x_i}$ can be updated as follows:

$$L_\varepsilon(f(\boldsymbol{x}), y) = \begin{cases} S^i_{FT} - f(\boldsymbol{x}) - \varepsilon & \text{if } S^i_{FT} - f(\boldsymbol{x}) > \varepsilon, \\ 0 \quad \text{otherwise.} \end{cases} \tag{6.13}$$

Obviously, the loss function for the right-censored data $\mathbb{U}_1$ becomes one sided, that is:

$$S_{FT}^{i} - \boldsymbol{w} \cdot \phi\left(\boldsymbol{x_i}\right) - b \leq \varepsilon + \xi_i, \quad \boldsymbol{x_i} \in \mathbb{U}_1, \tag{6.14}$$

subject to,

$$\xi_i \geq 0.$$

For the point target $\boldsymbol{x_i} \in \mathbb{U}_2$, its loss function is still two-sided, that is:

$$\begin{cases} y_i - \left(\boldsymbol{w} \cdot \phi\left(\boldsymbol{x_i}\right) + b\right) \leq \varepsilon + \xi_i, \\ \boldsymbol{w} \cdot \phi\left(\boldsymbol{x_i}\right) + b - y_i \leq \varepsilon + \xi_i^*, \\ \xi_i, \xi_i^* \geq 0. \end{cases} \tag{6.15}$$

By combining the above equations, we now propose the following formula for SVR regression in the re-routing system:

$$\min \quad C\frac{1}{N}\sum_{i=1}^{N}\left(\xi_i + \xi_i^*\right) + \frac{1}{2}\|\boldsymbol{w}\|^2 \tag{6.16}$$

subject to,

$$\begin{aligned} &S_{FT}^{i} - \boldsymbol{w} \cdot \phi\left(\boldsymbol{x_i}\right) - b \leq \varepsilon + \xi_i, \quad \text{if } \boldsymbol{x_1} \in \mathbb{U}_1, \\ &y_i - \left(\boldsymbol{w} \cdot \phi\left(\boldsymbol{x_i}\right) + b\right) \leq \varepsilon + \xi_i, \quad \text{if } \boldsymbol{x_1} \in \mathbb{U}_2, \end{aligned} \tag{6.17a}$$

$$\boldsymbol{w} \cdot \phi\left(\boldsymbol{x_i}\right) + b - y_i \leq \varepsilon + \xi_i^*, \quad \text{if } \boldsymbol{x_1} \in \mathbb{U}_2, \tag{6.17b}$$

$$\xi_i, \xi_i^* \geq 0, \quad i = 1, \ldots, N. \tag{6.17c}$$

As can be noted from the above equations, we take advantage of all the useful information available in the data. By introducing Lagrange multipliers α_i for the inequalities (6.17a), and α_i^* for the inequalities (6.17b), the dual of the above problem can be formulated as:

$$\max \quad -\varepsilon\sum_{i=1}^{N}\left(\alpha_i + \alpha_i^*\right) + \sum_{\boldsymbol{x_i}\in\mathbb{U}_2}\left(\alpha_i^* - \alpha_i\right)y_i - \sum_{\boldsymbol{x_i}\in\mathbb{U}_1}\alpha_i S_{FT}^{i} - \frac{1}{2}\sum_{i,j=1}^{N}\left(\alpha_i^* - \alpha_i\right)\left(\alpha_j^* - \alpha_j\right)\boldsymbol{K}\left(\boldsymbol{x_i}, \boldsymbol{x_j}\right) \tag{6.18}$$

subject to:

$$
\begin{aligned}
&\sum_i \alpha_i - \alpha_i^* = 0, \\
&0 \leq \alpha, \alpha^* \leq C.
\end{aligned}
\tag{6.19}
$$

where $\alpha_i^* = 0$, $\forall \boldsymbol{x_i} \in \mathbb{U}_1$. By maximizing the objective function (6.18), for a new variable $\boldsymbol{x}$, its function value is represented by $f(x) = \sum\limits_{i=1}^{N} (\alpha_i - \alpha_i^*) \boldsymbol{K}(\boldsymbol{x}, \boldsymbol{x_i}) + b$.

The performance of ε-SVR is mainly influenced by three parameters: kernel function $\boldsymbol{K}$, C, and ε. Currently, there are no unified rules for determining these parameters [233]. A common approach is to select their values by trial and error. In this study, we implement a grid search cross-validation approach to choose their values.

The prediction performance of the SVR model can be evaluated using the following performance measure, namely relative mean errors (RME):

$$
RME = \frac{1}{n} \sum_{i=1}^{n} \left| \frac{y_i - y_i^*}{y_i} \right| \tag{6.20}
$$

where y_i is the actual value, and y_i^* is the forecast value. For censored data, if $y_i^* \geq y_i$, then RME is 0. RME measures the deviation between actual and predicted values. The smaller its value is, the closer are the predicted system failure times to the values from the original simulation model.

6.4 Numerical Examples

In this section, two numerical examples are given to demonstrate the proposed method for the aircraft re-routing and system performance assessment.

6.4.1 Input Variable Settings

Table 6.1 lists the random variables, their distributions and parameters. These variables can be grouped into two classes: system variables (e.g., regional radar range, local radar range, regional radar detection angle, local radar detection angle, message delay, and space availability), and aircraft variables (remaining miles ratio, speed, and arrival rate). Besides, each radar's initial orientation follows a uniform distribution $U(0,2\pi)$. In this chapter, we assume all these stochastic variables, e.g., message delay, radar beam rotation speed, are independent from each other. If there are correlations between the stochastic variables, it can be easily included in MCS simulations. Well-established methods [220] are available in the literature to generate MCS samples with correlated factors.

6.4.2 Data Collection

In our analysis, each simulation lasts for 10 cycles, each of duration 5 minutes. Every 5 minutes, the re-routing system makes feasible assignment decisions, pairing registered aircraft with airports based on available space. Based on the probability distributions for each variable described in Table 1, we run 2000 simulations and collect 2000 data points. Among them, 71 data points are found to be right-censored.

As mentioned previously, the space availability at each nearby airport is associated with three resources: runway, gate and airspace. In Table 6.1, the availabilities are represented by three variables with their means κ, ξ, and η. As shown in Eq. (6.9), the assignment algorithm is constrained by the minimum available resources among runway, gate, and airspace. Thus, $\min(\kappa,\xi,\eta)$ is used to characterize the space availability at each nearby airport. In this way, 16 variables are employed to represent the space availability at the nearby airports. Thus, a total of 25 input variables are used to characterize the system inputs, and the system failure time is the only output.

6.4.3 Sensitivity Analysis

Due to the appearance of right-censored data, we cannot perform global sensitivity analysis directly because we do not know the exact system failure time for some of the simulations. Since we could only estimate the lower bound of the system failure time for right-censored data, to perform sensitivity analysis, we need to use a crisp number to

Table 6.1: Assumed probability distributions for the input variables.

Variables	Numbers	Distributions and parameters	Parameter ranges	Unit
Regional radar range	1	Lognormal: mean R_r, stdev 10	$R_r \sim U[40,60]$	miles
Local radar range	1	Lognormal: mean R_l, stdev 5	$R_l \sim U[14,24]$	miles
Radar beam rotation speed	1	Lognormal: mean B_s, stdev 0.3	$B_s \sim U[1.8,2.2]$	RPM (revolution per minute)
Initial orientation	16	Uniform	$U[0,2*\pi]$	
Message delay	1	Lognormal: mean m_d, stdev 4	$m_d \sim U[25,50]$	seconds
Space availability at airport k	16	Runway – Lognormal: mean κ, stdev 1	$\kappa \sim U[1,3]$	
		Gate – Lognormal: mean ξ, stdev 5	$\xi \sim U[0,24]$	
		Airspace – Lognormal: mean η, stdev 3	$\eta \sim U[0,9]$	
Arrival rate	1	Poisson: λ	$\lambda \sim U[20,30]$	five minutes
Remaining miles ratio β	1	Uniform	$\beta \sim U[0.6,1]$	
Aircraft speed s	3	Large – Lognormal: mean ν, stdev 65	$\nu \sim U[546,609]$	miles per hour
		Medium – Lognormal: mean ς, stdev 40	$\varsigma \sim U[345,414]$	miles per hour
		Small – Lognormal: mean χ, stdev 28	$\chi \sim U[226,292]$	miles per hour

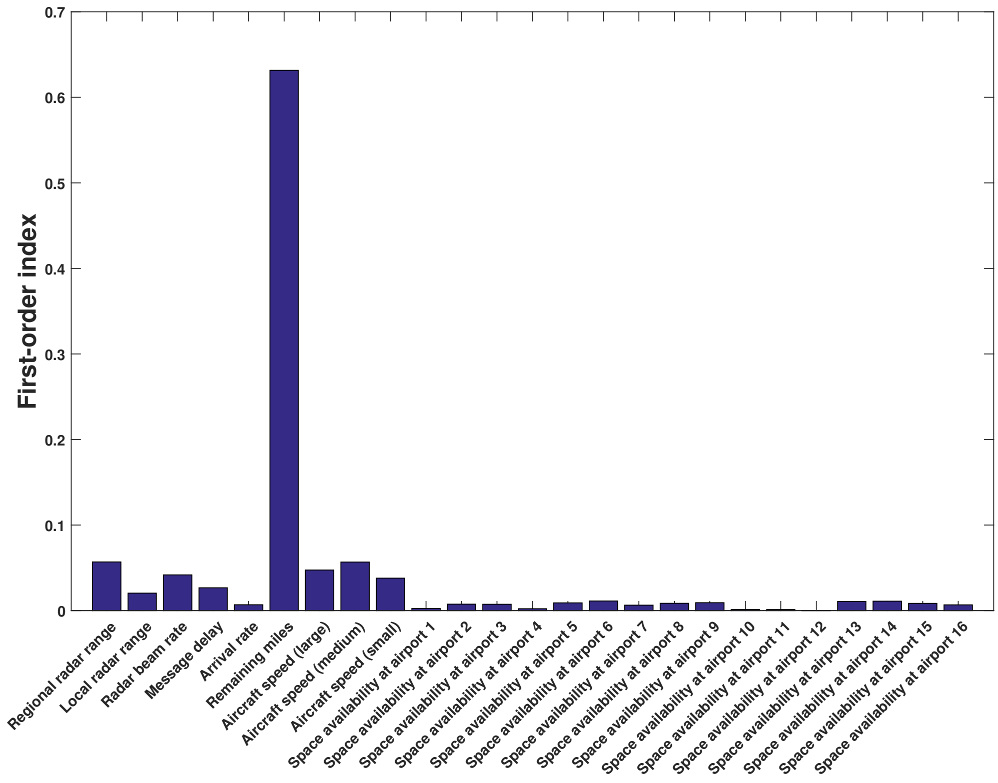

Figure 6.6: First-order Sobol' indices

represent the system failure time. There are several ways to handle censored data. We can perform sensitivity analysis on the dataset after discarding the censored data, but the system failure time characterized by the censored data is lost. Another way is to use a very large number to represent the system failure time. But which specific number to use is an issue. In this case, we use a conservative strategy to conduct the sensitivity analysis: the lower bound is used as the actual system failure time of the censored data, then we carry out global sensitivity analysis. Based on Eq. (6.12), we compute the first-order sensitivity using 2000 samples from the simulation. Fig. 6.6 shows the first-order sensitivity index for each input variable. Obviously, the remaining miles has the highest sensitivity.

Another observation is that the sensitivity of space availability varies with the location of each airport. Among all the airports, the space availabilities at airports P14 and P15 have higher sensitivity indices whereas the sensitivities at airports 4, 10, 11 and 12, are negligible. The sensitivity of space availability at each airport is greatly influenced by the complicated interactions in the system. In the assignment model, the overall travelling distance is affected by the location of the registered aircraft. But the time that an aircraft is registered is affected by other factors, e.g., its entry time and location, and the time it is detected by the radar. When the aircraft is registered determines its location, which in turn influences our assignment decision.

6.4.4 Surrogate Model Construction

Based on the sensitivity analysis result shown in Fig. 6.6, we eliminate the variables with low contribution to the overall system variance, thus reducing the problem dimension and accelerating the surrogate model construction. Among the 25 random variables considered in this study, we remove ten variables with low sensitivity indices. The 15 variables that are retained in the surrogate model are: regional radar range, local radar range, radar beam rate, message delay, remaining miles, aircraft speed (large), aircraft speed (medium), aircraft speed (small), and the space availability at airports 5, 6, 8, 9, 13, 14 and 15.

Next, cross validation is used to determine parameter values. The data is split into ten groups: nine out of ten are used to train the model, and the remaining one is used to validate the performance of the trained model. Then grid search is used to search the space of these variables using exponentially growing sequences of C and ε to identify good values of the parameters (for example, $C = 2^{-4}, 2^{-2}, 2^{0}, 2^{2}, 2^{4}$). We try three kernel functions: linear kernel, Gaussian kernel, and polynomial kernel. The kernel function $\boldsymbol{K}$, with parameter set of C and ε, which yields the minimum RME, is selected. It is found that the parameter set $C = 2^{-3}, \varepsilon = 2^{-10}$, and $\gamma = 2^{2}$ gives the best prediction result (minimizing the test RME).

Fig. 6.7 shows the comparison results between the actual simulations and the SVR surrogate model predictions for 200 data points. The SVR predictions (with polynomial kernel) show good agreement with the observed system failure time. The relative mean error is 7.3%, which indicates that the SVR model is reasonably accurate. If higher accuracy

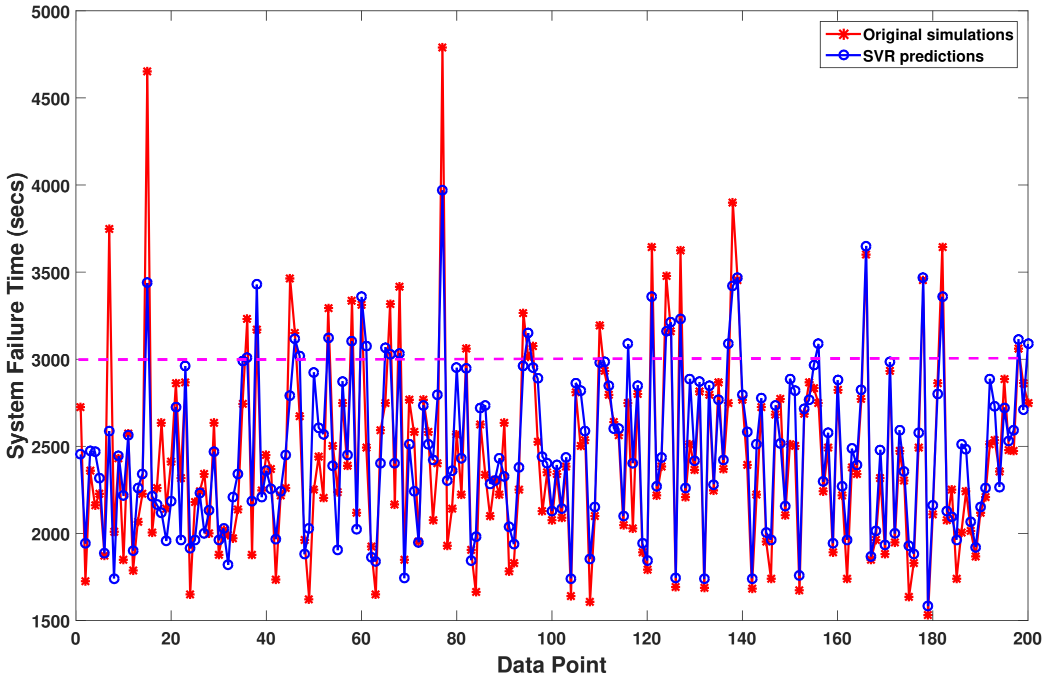

Figure 6.7: System failure time prediction with ε-SVR model

is desired, more runs of the original re-routing simulation are needed.

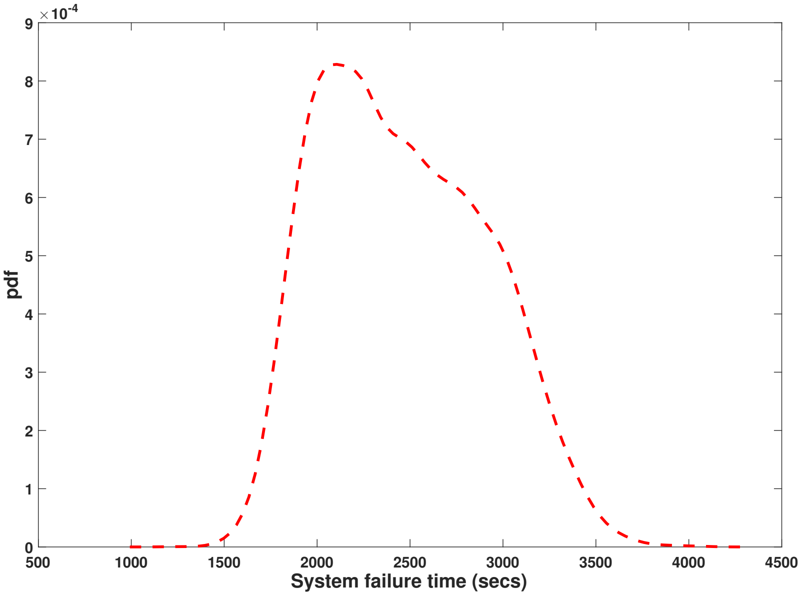

Figure 6.8: First case: System performance assessment

6.4.5 Case I

With the surrogate model constructed in the previous section, we evaluate the system performance by randomly sampling the 15 variables within their ranges. Fig. 6.8 shows the system failure time distribution based on 20,000 samples.

Given the 20,000 samples, we fit the data using five candidate distributions: Weibull, lognormal, normal, gamma, and exponential. The parameters related to these distributions are estimated by maximizing the corresponding likelihood function. Two goodness-of-fit plots are shown in Fig. 6.9 to demonstrate the performance of each candidate distribution. Fig. 6.9(a) compares the density functions of the fitted distributions along with the histogram of the empirical distribution, and Fig. 6.9(b) denotes the comparisons between the CDF plot of both the empirical distribution and the fitted distributions. As can be observed, Gamma and Lognormal distributions give reasonable agreement with the data.

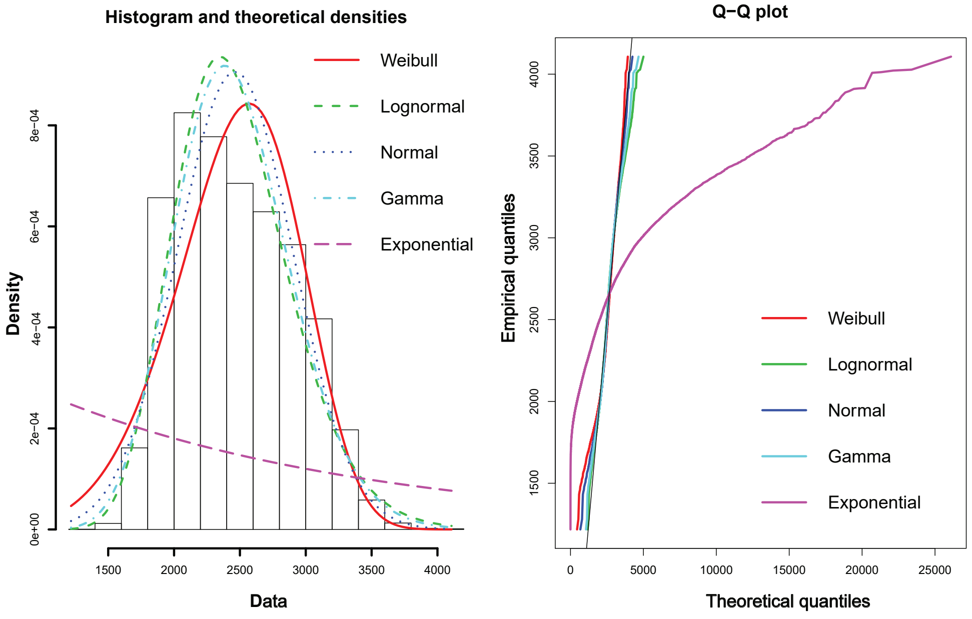

Figure 6.9: Two Goodness-of-fit plots for various distributions fitted to continuous data (Weibull, Lognormal, normal, gamma, and exponential distributions fitted to 20,000 samples)

In addition, three well-known quantitative tests are employed to quantify the goodness-

Table 6.2: Goodness-of-fitness statistics as defined by Stephens [1]

Statistic	General formula	Computational formula
Kolmogorov-Smirnov (KS)	$\sup \lvert F_n(x) - F(x) \rvert$	$\max(D^+, D^-)$ $D^+ = \max\limits_{i=1,\ldots,n}\left(\frac{i}{n} - F_i\right)$ $D^- = \max\limits_{i=1,\ldots,n}\left(F_i - \frac{i-1}{n}\right)$
Cramer-von Mises (CvM)	$n\int_{-\infty}^{+\infty}(F_n(x) - F(x))^2 dx$	$\frac{1}{12n} + \sum\limits_{i=1}^{n}\left(F_i - \frac{2i-1}{n}\right)^2$
Anderson-Darling (AD)	$n\int_{-\infty}^{+\infty}\frac{(F_n(x)-F(x))^2}{F(x)(1-F(x))}dx$	$-n - \frac{1}{n}\sum\limits_{i=1}^{n}(2i-1)\log(F_i(1-F_{n+1-i}))$

Table 6.3: Goodness-of-fit statistics.

	Weibull	Lognormal	Normal	Gamma	Exponential
Kolmogorov-Smirnov statistic	0.06790564	**0.04280514**	0.06185114	0.04557395	0.489977
Cramer-von Mises statistic	29.82418846	**15.17619515**	23.01538695	15.60813899	1322.880084
Anderson-Darling statistic	199.44501732	**95.18102060**	143.27729802	98.24155121	6221.194507

of-fitness of each candidate distribution: Kolmogorov-Smirnov, Cramer-von Mises, and Anderson-Darling, which are defined in Table 6.2. The statistical test results are shown in Table 6.3. Among the candidate distributions considered, the lognormal distribution has the lowest statistical error in all three tests. In other words, the lognormal distribution fits the data best. The parameters of the best-fitted lognormal distribution are: $\mu = 7.79$, $\sigma = 0.1786$. Suppose we want to estimate the probability that the system survives longer than 2600s; the results are shown in Table 6.4. As can be noted, there is a 6.3% deviation of the system reliability estimation between the fitted distribution and the actual simulation. But considering the two approximations in estimating the system reliability, our prediction is very precise. Specifically, when we build the surrogate model from the 2,000 simulation data, there is approximation error between the simulation data and the surrogate model, which is about 7.3%. When we fit the distributions according to the samples generated by the surrogate model, the second approximation arises. Thus, the 6.3% prediction discrepancy is within the range of the deviation caused by the two approximations.

In addition, the Kaplan-Meier estimator fits the data very well. Since the simulation lasts for 3,000s, when we estimate $P(S_{FT} > 2600)$, there is no right-censored data involved.

Table 6.4: System reliability analysis.

	Original simulation	Lognormal distribution	Kaplan-Meier estimator
$P(S_{FT} > 2600)$	0.3255	0.3408	0.3255
$P(S_{FT} > 4200)$	0.023	0.012	0.0337

In this case, the Kaplan-Meier estimator is equivalent to the empirical cdf. In contrast, when we evaluate the probability of $P(S_{FT} > 4200)$, censored data arises. It can be observed that the Kaplan-Meier estimator overestimates the probability of $P(S_{FT} > 4200)$. However, the fitted distribution gives a more conservative prediction for this example when compared with the Kaplan-Meier estimator.

6.4.6 Case 2

In this section, we broaden the range of the mean for the space availability at the nearby airports: $\kappa \sim U[1,6]$, $\xi \sim U[0,48]$, and $\eta \sim U[0,18]$. Since the upper bound in the mean values of available runways, gates, and airspace has increased, the system survives a longer time than Case I. Following the same procedure, we collect 1,000 data points, of which 600 are found to be right-censored. The system failure time of the right-censored data is represented by an interval $[S_{FT}, \infty]$. As long as the predictions of our surrogate model fall within the range, there is no penalty. In other words, the prediction can be any number in the range $[S_{FT}, \infty]$. Thus, the right-censored data contributes to the uncertainty in the surrogate model prediction. The performance of the surrogate model will deteriorate if there are more right-censored data due to the increase in uncertainty.

Table 6.5: Case 2: system reliability analysis.

	Original simulation	Surrogate model	Kaplan-Meier estimator
$P(S_{FT} > 2600)$	0.6766	0.7311	0.6747
$P(S_{FT} > 3844)$	0.5978	0.5885	0.4012

Contrary to the first case, the average error of the surrogate model has risen to 18% in

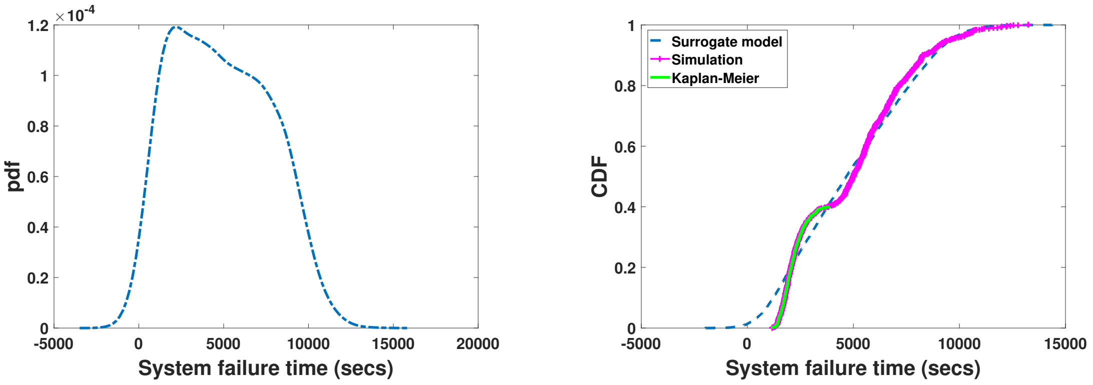

(a) Case 2: System performance assessment

(b) Case 2: Comparisons of cumulative distribution function

Figure 6.10: Performance assessment

the second case due to the increase of right-censored data. Fig. 6.10a shows the system failure time distribution. Since some of the system failure time predictions in the surrogate model are negative, we cannot fit it using the four candidate distributions. Table 6.5 shows the comparison results among original simulation, surrogate model, and Kaplan-Meier estimator. Fig. 6.10b shows the comparisons of cumulative distribution function. When the time is less than 3,844s, there are only 2 right-censored data out of 402 points. The Kaplan-Meier estimator is equivalent to the empirical CDF if there is no right-censored data. As a result, the Kaplan-Meier estimator nearly coincides with the empirical cdf. When the time is larger than 3,844s, all the system responses are right-censored. The Kaplan-Meier estimate of system reliability then becomes a constant 0.4012. However, the surrogate model still fits the cumulative distribution of system failure time very well, as shown in Fig. 6.10b and Table 6.5.

6.5 Summary

This chapter assesses system resilience through measuring the effectiveness of an algorithmic response in handling extreme events, in which system survival time is used a quantitative metric. By simulating different scenarios and configurations, we quantify the survival rate of a response strategy in mitigating the impact of extreme event. In particular, we evaluate the performance of a re-routing strategy in alleviating the impact of an airport closure caused by extreme events. We assess the effectiveness of the response action in the presence of uncertainty arising from several different sources (radar performance, communication system, aircraft characteristics, and space availability in nearby airports) and develops an support vector regression-based approach to assess the performance of the proposed methodology. A simulation-based approach is used to characterize the actual re-routing process and account for the uncertainty contributed by several heterogeneous subsystems. Based on the simulation data, we employ a data-driven sensitivity analysis method to quantify the contribution of each uncertain variable towards the overall variance of system response. The variables with the lowest importance are removed to reduce the problem dimension. A support vector regression surrogate model is built for predicting the system failure time and constructing the probability distribution for the failure time of the re-routing system.

Our contributions are several fold. First of all, since the current aircraft re-routing is operated manually, it is hard to assess the performance of aircraft re-routing operations. In this study, we develop a simulation-based model to accommodate the various uncertainties arising in this process, and it allows us to evaluate the performance of the proposed re-routing algorithm quantitatively. Secondly, based on the simulation, we perform sensitivity analysis to quantify the contribution of each stochastic variable to the system reliability. The sensitivity analysis results enable us to identify which factor affects the system performance most, thus providing a quantitative basis for decisions such as component design optimization and specific operational measures in order to improve system performance. Given limited resources to improve the system performance, the sensitivity analysis result provides the guidance to optimally allocate the limited resources. Thirdly, our study models the aircraft re-routing from a system of systems perspective considering the interactions of multiple subsystems, and integrates the uncertainties arising from each subsystem (radar detection, re-routing assignment, and communication system). In this way, we are able to view this problem from a systemic point of view, have a comprehensive understanding of the system work flow, and characterize the relationship among the subsystems. At last, the construction of surrogate model improves the computational efficiency and facilitates fast analysis of system performance, thus supporting real-time decision-making.

Our work brings several benefits to the practitioners (airline dispatcher and air traffic controller) when extreme weather affects the original aircraft routes. With the aforementioned uncertainties considered, we provide quantitative analysis on the performance of aircraft re-routing operation. In this sense, the airline dispatcher is able to make risk-averse decisions given the system failure time distribution given a specific set of system parameters. In addition, since as the technology is moving towards the Next Generation Air Transportation System (NextGen), there is a huge demand for automatic operations in order to reduce the amount of information the air crew must process at one time [234, 235]. This chapter provides a case study of evaluating the performance of a re-routing algorithm under uncertainty, and the simulation platform we have built is extendable to test the performance of other re-routing algorithms with additional constraints imposed, e.g., separation assurance.

The assessment of algorithmic response gains our insights on the effectiveness of algorithms/strategies in handling extreme events. The reliability analysis of algorithmic response illustrates the resilience of algorithmic strategy in different realizations of uncertain environment when dealing with extreme events. To increase system resilience further, more effective algorithms with robust performance in uncertain environment needs to be developed. The methodology developed in this chapter offers a general framework to evaluate the effectiveness for more advanced algorithms to be developed in the future. Since the purpose of assessing the response strategies is to make the system more resilient, in Chapter 7, we explore the design for resilience in infrastructure systems from an optimization point of view.

Chapter 7

Design Optimization for Resilience[1]

7.1 Introduction

The previous two chapters investigate the effectiveness of human and algorithmic response in dealing with extreme events in existing systems, respectively. In this chapter, we move towards designing the system for resilience. The overall goal of this chapter is to enable resilience from an optimization perspective such that the system is equipped with the capability to withstand extreme events, and we illustrate the developed method with an application in the configuration of a logistics service center system.

Over the past few years, there has been a growing interest in the design for resilience in terms of system configuration, logistics operations, and resource allocation. Likewise, when determining the configuration (location and capacity) of logistics service centers (a system consisting of multiple service centers distributed within an area to serve customers), resilience is also an important and essential consideration. Take large global companies as an example, they often distribute their manufacturing plants all over the world (global outsourcing) to reduce the operation cost and enhance business agility. In today's competitive world, the manufacturing plants distributed around the world are vulnerable to disruptions caused by various factors, such as natural disasters, strikes etc. These disruptions often result in immediate and significant loss in their revenue and market share, especially when alternative competing enterprise can offer the same product or service. A recent major fire at Ford caused the shutdown of the Dearborn truck plant and the full halt of F-150 production line in all its manufacturing plants due to parts shortages. As reported by the Detroit News [237], this disruption might have a potential damage to Ford's second-quarter performance and market share. In addition to global companies, regional service centers like

[1] An archival paper related to this chapter has been submitted to IEEE Transactions on Reliability for publication. For more details, see Ref. [236]

banks and supermarkets often perform periodic renovation and store upgrades at certain branches, which might result in congestion in other stores within the same area, thereby causing a decrease in customer satisfaction. In worse cases, the customers might divert to other companies because of the heavy congestion or long travel distance to other alternative stores. Thus, it is imperative to take such factors (i.e., planned regular renovation, and unexpected disruptive events) into consideration in determining the configuration of logistics service centers, whereas current studies considering the effect of random branch breakdown on system performance and including resilience in the selection of logistics distribution center are comparatively rare and limited.

In this chapter, we are motivated to bridge this research gap through the development of a resilience-based framework to optimize the configuration of logistics service centers with the consideration of the impact of random branch breakdown and other possible disruption scenarios. In realistic scenarios, the number, locations, and sizes of distribution centers significantly affect the quality of customer service as measured by the time that is needed for each customer to reach the service center together with the amount of waiting time in line and processing time at the service center. Hence, the distribution of service centers has a significant impact on customers' decisions in choosing the branch that he is going to be served. Whereas, from the viewpoint of the planner, the company can only afford to build a limited number of service centers due to budget constraints. Thus, service centers must be designed and distributed reasonably with the consideration of customers' behavior. The interactions between planner and customers can also be analyzed from the game theory point of view. Specifically, the planner, as a top-level decision maker, can determine where to open and deploy the service center, thereby influencing customers' service-choosing behavior, but has no control over which distribution center the customers choose to be served. From the customers' perspective, they are free to choose distribution/service centers based on their own habits and behaviors (i.e., minimum distance, minimum travel time, or other personal preferences), but do not have control over the location of the service center. The interactions between planner and customers can be represented as a leader-follower game, in which the planner acts as the leader in making an initial move at determining the locations of service center, while the customers freely choose the service center based on the decision made by the planner. Mathematically, it can be modeled as a bi-level optimization program, where the planner determines the locations and configurations of logistics centers in the upper level, while the customers take corresponding reaction based upon the decision made by the planner.

To characterize the impact of potential disruptions due to some extreme event, we randomly pick a fixed number of service centers and make them closed simultaneously. Since the impacted service centers are closed, customers shift to other alternate centers that are still in service, which might cause traffic congestion and long queues. Thus, we formulate the objective as mitigating the expected congestion incurred by the closing of certain service centers during the service center restoration period; thus, developing a resilient service center distribution subject to a fixed amount of budget. The problem is formulated as a nonlinear integer optimization problem, and our goal is to design a resilient logistics center distribution such that the expected customer service time can be minimized. Specifically, there are two decision variables in this problem: where to locate the service centers and the number of servers at each service center. A multi-level cross-entropy algorithm is developed to tackle the bi-level optimization problem to approach the near-optimal solution within limited time. In comparison with the current state-of-the-art studies, we have made the following contributions:

1. We develop a new formulation of user equilibrium traffic assignment in the service centers configuration, where the travel demand between each pair of origin and destination nodes is unknown in advance.

2. We propose an innovative method to determine the customer demand at each service center with the introduction of dummy node and auxiliary links.

3. The upper-level model not only considers the travel time of each user from different zones to the service centers, but also their average waiting time in line and processing time within each service center.

4. To tackle the challenging bi-level optimization problem formulated in this chapter, a multi-level cross entropy method is leveraged to find an importance sampling that gradually concentrates all its mass in the vicinity of the optimal state.

7.2 Problem Formulation

Logistics service center location, as a crucial issue, plays a significant role in maintaining the daily operations of societal activities ranging from financial services to grocery shopping. Typically, there are two major considerations in determining the configuration of logistic distribution centers, namely where to deploy the service center (location), and what should be the design capacity of each service center (capacity). In this chapter, we account for these two major factors in the configuration of resilient logistics center distribution so that it is able to recover from different disruptive events in an efficient manner. In practice, the configuration of service centers and customer demand distribution among the established service centers are determined by two individual entities. By varying the location and capacity of service centers, decision maker can influence customers' choice by making some service centers more attractive than others, but has no control over customers' choice behavior. Whereas, each customer compares and chooses the service center based on his/her own habit and preference (e.g., travel distance, travel time, or perceived waiting time at each service center). As can be observed, there is an explicit hierarchical relationship between the two players in this problem. The interactions between the leader (decision maker) and follower (customers) can be mathematically modeled with bi-level programming [238] as follows.

$$\begin{aligned} \text{(U0)} \quad \min_{\boldsymbol{x}} \quad & \boldsymbol{F}(\boldsymbol{x},\boldsymbol{y}) \\ \text{s.t.} \quad & \boldsymbol{G}(\boldsymbol{x},\boldsymbol{y}) \leq 0, \end{aligned} \tag{7.1}$$

where $\boldsymbol{x}$ denotes the decision variables in the upper-level model, while $\boldsymbol{y} = \boldsymbol{y}(\boldsymbol{x})$ is determined by the optimization problem in the lower-level model:

$$\begin{aligned} \text{(L0)} \quad \min_{\boldsymbol{y}} \quad & \boldsymbol{f}(\boldsymbol{x}, \boldsymbol{y}) \\ \text{s.t.} \quad & \boldsymbol{g}(\boldsymbol{x}, \boldsymbol{y}) \leq 0. \end{aligned} \tag{7.2}$$

where $\boldsymbol{y}$ represents the vector of variables resulting from the non-cooperative competition behavior among the customers in the lower-level model given the actions ($\boldsymbol{x}$) taken by the decision maker in the upper-level model. $\boldsymbol{F}$ is the objective function in the upper-level model, e.g., minimizing the system total travel cost, $\boldsymbol{f}$ is the objective function in the lower-level model, e.g., minimizing the cumulative customer travel cost, and $\mathscr{G}$ and $\boldsymbol{g}$ denote the system constraints in the upper and lower level problems, e.g., flow conservation, balanced demand and supply.

In general, the objectives that the two players have are usually conflicting with each other in the system. To be more specific, users in the lower-level model (L0) typically aim to maximize the individual utility function through the optimization of decision variable $\boldsymbol{y}$ subject to constraints $\boldsymbol{g}$ while the variable $\boldsymbol{x}$ in the upper-level model acts as parameters. Conversely, the upper-level model $\boldsymbol{F}$ aims to minimize the total system travel cost via the optimization of the location and capacity associated with each service center as represented by the decision vector $\boldsymbol{x}$, while decision variable $\boldsymbol{y}$ is regarded as parameters. The partition of the control over the two decision vectors between two ordered levels imposes to model the problem as a bi-level program. Through the response function $\boldsymbol{y} = \boldsymbol{y}(\boldsymbol{x})$, the actions of two players are coupled together, thereby influencing each other's decision. From the system design viewpoint, each decision vector $\boldsymbol{x}$ corresponds to a particular configuration of service center distribution. Given each system design, the customer selects a service center that maximizes his/her own utility function. As a result, a unique traffic flow distribution emerges in the network, which further influences the design objective formulated in the upper-level model.

7.2.1 User Equilibrium Traffic Assignment

As introduced in the previous section, given the service center configuration, each customer makes their own choice to minimize the travel cost. Suppose travel time is the only consideration for each customer, at the initial stage, all the customers choose the service center that needs the least amount of travel time. With time going on, traffic flow accumulates along the minimum-cost path, thereby resulting in congestion. Since travel cost depends on traffic flow, the emergence of congestion on certain paths leads to the increase in their travel time. Given the updated travel time along each path, customers shift to other service centers via other paths with shorter travel time. The same non-cooperative competition behavior continues until no customer can reduce his/her travel time by unilaterally shifting to other service centers through other routes. Eventually, the system converges to an ultimate traffic equilibrium state, where no customer could reduce the travel time by making other movements. Such state is also referred to as Wardrop user equilibrium [239], and one important principal can be established at the user equilibrium state: the travel time along all the used paths is the same and less than those that would be experienced by a single vehicle on any unused route.

However, in the context of service center distribution problem, its user equilibrium state differs from the user equilibrium state of transportation system in two major aspects.

1. If the locations of service distribution centers are given, there are two decisions made by each customer in choosing the service center. Specifically, the first decision is which center he/she plans to go to, and the second decision is which path he/she should take to go to the service center he/she just chooses. These two decisions are combined together and made simultaneously to achieve his/her objective in minimizing the total travel time. Whereas, in transportation system, each passenger only needs to determine which path to take to reach the target location because the destination is already known in advance.

2. Another primary difference is that the traffic demand between each origin-destination (OD) pair is explicitly given in the transportation system. While in the service center distribution problem, we only know the number of customers at each community (or region), and no explicit value is given to indicate the number of customers between each resident zone and service center.

The above two features differ the user equilibrium in the context of service center distribution problem from the classical user equilibrium defined in Section 2.3. To address the new challenges, we formulate a new user equilibrium traffic assignment for the service center configuration problem in this chapter. Consider a directed network $\mathscr{G}(V,E)$, where V and E denote the set of nodes and edges in graph $\mathscr{G}$, and $V = \{v_1, ..., v_n\}$, where $n \geq 2$. Suppose the number of customers at each node (zone) v_i is denoted by d_i, there is a set of candidate sites M, where logistics distribution centers could be established. Here, a binary variable z_m $(m \in M)$ is used to indicate whether to construct logistics distribution center at site m or not. If logistics distribution center at site m is constructed, then z_m takes the value of 1; otherwise, z_m takes the value of 0. Suppose the number of customers that each service center m serves is represented by λ_m, since all the customers should be served by some service center, then we have:

$$\sum_{i=1}^{n} d_i = \sum_{m \in M} \lambda_m \tag{7.3}$$

where λ_m denotes the amount of customers that is served by logistics distribution center m, and d_i denotes the customer demand at node v_i. Obviously, only after the logistics service center at site m is established, then it is able to serve customers, which implies the following constraint:

$$0 \leq \lambda_m \leq \omega z_m, \forall\, m \in M. \tag{7.4}$$

where ω is an arbitrarily large positive constant. When $z_m = 0$, then λ_m cannot be positive. As a result, we have $0 \leq \lambda_m \leq 0$, and it implies that λ_m can only take the value of zero because logistics distribution center m is not established. But if $z_m = 1$, then λ_m can be as large as desired.

Suppose $P^{i,m}$ denote the set of cycle-free paths from the customer at node v_i to the service center m, $q_p^{i,m}$ represent the number of customers along the path p connecting the customer at node v_i with service center m, then we have:

$$\sum_{i=1}^{n} \sum_{p \in P^{i,m}} q_p^{i,m} = \lambda_m, \quad \forall\, m \in M. \tag{7.5}$$

The above constraint imposes that the total number of customers along all the paths connecting all the customer nodes and service center m should be equal to the amount of customers that logistics distribution center m serves. Obviously, the number of customers along each path must be non-negative, thus we have:

$$q_p^{i,m} \geq 0, \quad \forall p \in P^{i,m}, \quad \text{for } i = 1, 2, \cdots, n,\ m \in M. \tag{7.6}$$

Let a $(a \in E)$ be one link in the network G, x_a denote the traffic flow along link a, then the total amount of flow along link a is expressed as:

$$x_a = \sum_{i=1}^{n} \sum_{m \in M} \sum_{p \in P^{i,m}} q_p^{i,m} \delta_{a,p}^{i,m}, \quad \forall a \in E. \tag{7.7}$$

where $\delta_{a,p}^{i,m}$ is a binary variable indicating whether link a is a segment constituting path p $(p \in P^{i,m})$. When $\delta_{a,p}^{i,m} = 1$, it reveals that link a is a segment constituting path p; otherwise, $\delta_{a,p}^{i,m} = 0$.

With the above notations, the user equilibrium traffic assignment in the context of logistics distribution center location can be formulated as the following nonlinear optimization problem:

$$
\begin{aligned}
\min \quad & f = \sum_{a \in E} \int_{0}^{x_a} t_a(x)\, dx \\
\text{s.t.} \quad & x_a = \sum_{i=1}^{n} \sum_{m \in M} \sum_{p \in P^{i,m}} q_p^{i,m} \delta_{a,p}^{i,m}, \quad \forall a \in E, \\
& \sum_{i=1}^{n} d_i = \sum_{m \in M} \lambda_m, \\
& \sum_{i=1}^{n} \sum_{p \in P^{i,m}} q_p^{i,m} = \lambda_m, \quad \forall\, m \in M, \\
& q_p^{i,m} \geq 0, \quad \forall p \in P^{i,m}, \text{ for } i = 1, 2, \cdots, n, \;\; m \in M, \\
& 0 \leq \lambda_m \leq \omega z_m, \quad \forall m \in M.
\end{aligned}
\tag{7.8}
$$

where f is a function denoting the cumulative travel cost for all the customers, $t_a(x)$ is a monotonically increasing function to represent the relationship between traffic flow and travel time, and z_m is a binary variable indicating the establishment of logistics distribution center at candidate site m ($m \in M$) or not.

7.2.2 System-level Optimization

At the system level, system planner needs to make two individual decisions simultaneously with regard to the configuration of logistics service centers subject to a fixed amount of budget, and the goal of system planner is to minimize the total travel and service time for all the customers within the city. To be specific, the first decision is with regard to where the service centers should be constructed among the set of candidate sites M given the limited amount of investment, and the second decision is what should be the design capacity of each distribution center in terms of its capability in serving how many customers on average per hour. Suppose the total budget that the system planner has is denoted by a variable T. The cost of constructing each distribution center, for the sake of simplicity, is a nonlinear monotonically increasing function of its design capacity, while the capacity of each distribution center has an explicit impact on its serving capability, thereby affecting the waiting time of each customer in line before they are served. From the previous description, the system-level optimization problem can be formulated as:

$$\begin{aligned} \min \quad & F = \sum_{a\in E} x_a t_a(x_a) + \sum_{i=1}^{m} \lambda_m \left[\mathbb{E}(\kappa_m) + \mathbb{E}(s_m)\right] \\ \text{s.t.} \quad & \tau_m = f(c_m), \quad \forall m \in M, \\ & \sum_{m\in M} \tau_m z_m \leq T, \\ & z_m \in \{0,1\}, \quad \forall m \in M. \end{aligned} \tag{7.9}$$

where z_m has a binary value indicating whether to construct a logistics distribution center at the candidate site m or not. If service center m is built, then z_m takes the value of 1, and 0 otherwise; c_m denotes the design capacity of logistics distribution center m, and τ_m is the incurred cost of constructing logistics distribution center at candidate site m, which is in turn a monotonically increasing function of its design capacity c_m. Since system planner has a limited amount of budget T, the cost of building all the distribution centers should be less than the available budget T, as formulated in the second constraint in Eq. (7.9).

With respect to the optimization objective formulated in Eq. (7.9), it has two individual parts: the first element $\sum_{a\in E} x_a t_a(x_a)$ measures the total travel time of all the customers from their origin locations to the service center they choose to be served, and the second element $\sum_{i=1}^{m} \lambda_m \left[\mathbb{E}(\kappa_m) + \mathbb{E}(s_m)\right]$ characterizes the within-service center time that consists of average waiting time and processing time for each customer at each service center, and λ_m denotes the number of customers that service center m serves in total. Specifically, the first term $\mathbb{E}(\kappa_m)$ represents the average waiting time for each customer at the logistics distribution center m given that its capacity is c_m. In general, for a fixed customer demand, if the processing capacity of service center is less than the arrival rate of customers, the smaller its capacity, the longer the waiting time per customer. The second term $\mathbb{E}(s_m)$ denotes the average processing time for each customer at service center m. As shown in Eq. (7.9), the system planner not only considers the travel time of all the customers, but also the within-service-center waiting and processing time. The optimization objective formulated in Eq. (7.9) models realistic scenarios more accurately due to the consideration of center capacity and service time at each service center, which makes the current research effort different from the state-of-the-art literature studies.

As modeled in the upper-level model of bi-level formulation for logistics distribution center location optimization, the system planner makes decisions with regard to the configuration of logistics center distribution in terms of service center location and its capacity to maximize the performance of the system in serving the customers distributed across a region. The formulated optimization objective models the significant considerations of system planner in an appropriate manner through the configuration optimization of logistics service centers.

7.3 Proposed Method

In this section, we mathematically formulate a bi-level optimization model for enabling resilience in the configuration of logistics distribution centers. The objective of the upper-level model is to maximize the resilience of the logistics center distribution system subject to disruptions, while the customers traffic assignment is characterized in the lower-level model. To tackle the traffic assignment in the lower-level model, a dummy node and auxiliary links are created to determine the corresponding customer demand allocation among the service centers, then gradient projection method is utilized to determine the traffic assignment along the links in the traffic network. In the upper-level model, the logistics distribution center optimization problem is recast as a nonlinear integer optimization problem, and a multiple level cross-entropy optimization algorithm is leveraged to identify the near-optimal solution within limited amount of time. The flowchart of the proposed methodology is summarized in Fig. 7.1.

7.3.1 Resilience-driven Optimization Model

In reality, unanticipated disruptions might lead to the shutdown of some service centers, e.g., human-induced fire in factory or extreme weather events (i.e., flood, storm). Decision

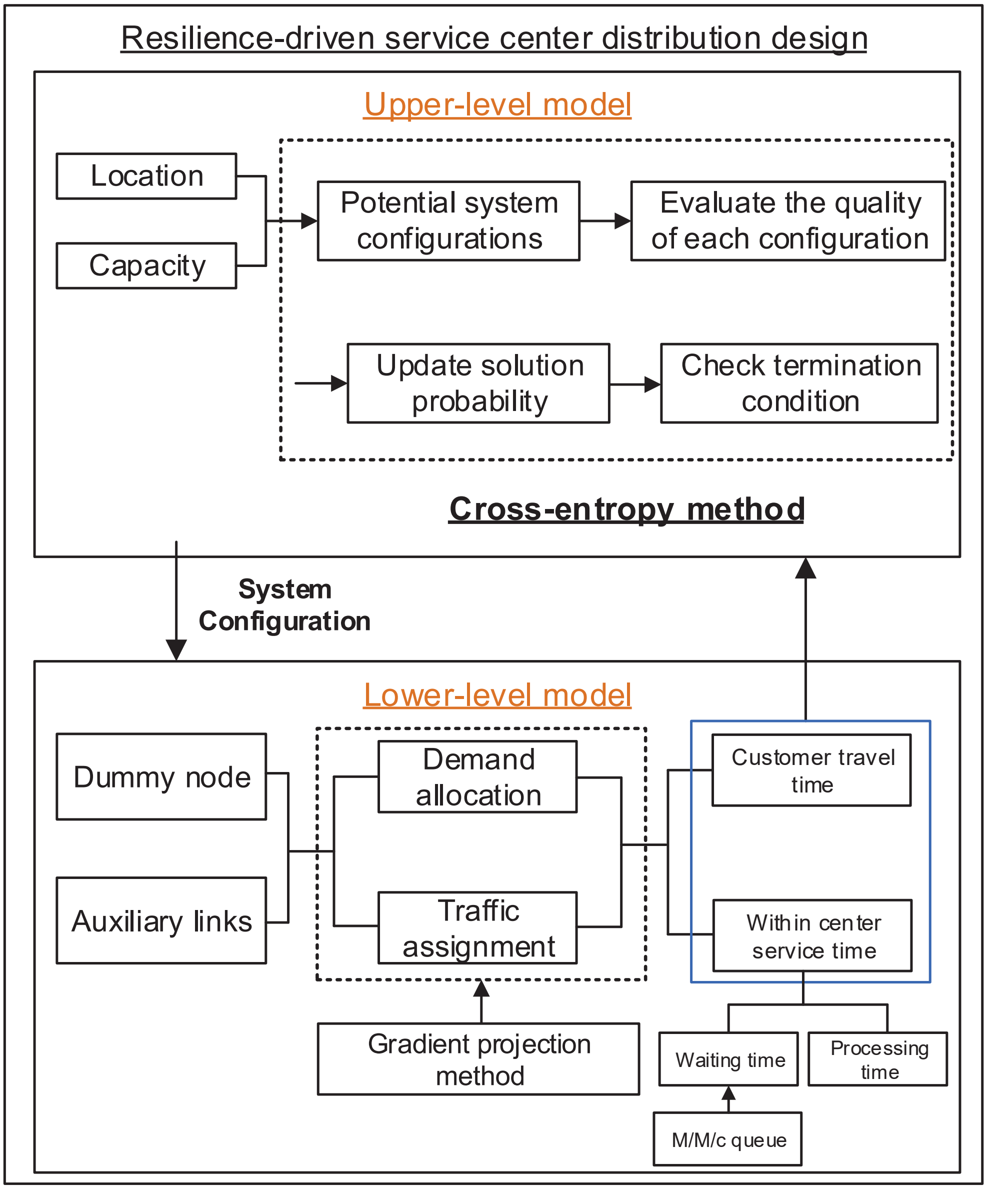
Resilience-driven service center distribution design
Upper-level model
Location
Capacity
Potential system configurations
Evaluate the quality of each configuration
Update solution probability
Check termination condition
Cross-entropy method
System Configuration
Lower-level model
Dummy node
Auxiliary links
Demand allocation
Traffic assignment
Customer travel time
Within center service time
Gradient projection method
Waiting time
Processing time
M/M/c queue

Figure 7.1: Flowchart of the proposed methodology

makers must take this into consideration when determining the configuration of logistics distribution centers such that the closure of some service centers will not result in severe congestion and abrupt degradation of customer satisfaction in the remaining service centers. In this chapter, we address this problem from a system resilience perspective with the goal to enhance the capability of the logistics center distribution configuration to stand against disruptive events. As mentioned in Chapter 2, we adopt the resilience definition developed by Henry and Ramirez-Marquez [2] as illustrated in Fig. 2.1, which is a time-dependent function of the performance of a system before, during, and after the disruptive event.

From Fig. 2.1, the system of interest experiences three different stages when disruptive event e occurs. Prior to the occurrence of the disruptive event, the system operates at an as-planned state S_0 with a stable performance $\psi(t_0)$. At time instant t_e, when disruptive event e happens, since the system is vulnerable to this disruption, its performance starts to drop down gradually from the time instant t_e due to the failure of certain system components or the loss of partial system functionality. The same performance degradation continues until the time instant t_d when its performance drops to a maximum disrupted but stable state $\psi(t_d)$. With the preparation of recovery resources at time instant t_d and the implementation of restoration action at time instant t_s, system performance starts to restore to a better level from time instant t_s until arriving a best post-disruption level $\psi\left(t_f\right)$ at time instant t_f. Considering the variation of system performance $\psi(t)$ before, during, and after the occurrence of the disruptive event e, system resilience is defined as the ratio of system performance that has been restored from the implementation of recovery action to the performance loss caused by the disruptive event e, as mathematically formulated in Eq. (2.1) in Chapter 2.

From Eq. (2.1), it can be observed that resilience measures the recoverability ability and restoration speed of a system in the presence of disruptive events. With respect to the system of service center distribution, it is susceptible to several different types of disruptive events in practice. For example, human-induced fire could cause the closure of truck manufacturing plant, as revealed in the Ford example in the introduction, which severely damages Ford's global supply chain network. Natural disasters (e.g., storm, flood) might hit a city unexpectedly and result in several service centers failing to offer services to customers. Besides, service center usually performs renovation and upgrade to enable more advanced functionality on a regular basis. All the aforementioned disruptive events lead to the closure of some of the logistics distribution service centers. Suppose W, which is a subset of M ($W \subseteq M$), denotes the set of logistics service centers that are damaged by the disruptive event e. When the disruptive event e happens, customers shift to other logistics distribution centers that are still in service, then the following mathematical model is formulated to describe the new user equilibrium under this circumstance:

$$
\begin{aligned}
\min \quad & f(e) = \sum_{a \in E} \int_0^{x_a} t_a(x)\, dx \\
\text{s.t.} \quad & x_a = \sum_{i=1}^{n} \sum_{m \in M \backslash W} \sum_{p \in P^{i,m}} q_p^{i,m} \delta_{a,p}^{i,m}, \quad \forall a \in E, \\
& \sum_{i=1}^{n} d_i = \sum_{m \in M \backslash W} \lambda_m, \\
& \sum_{i=1}^{n} \sum_{p \in P^{i,m}} q_p^{i,m} = \lambda_m, \quad \forall m \in M \backslash W, \\
& q_p^{i,m} \geq 0, \quad \forall p \in P^{i,m}, \text{ for } i = 1, 2, \ldots, n,\ m \in M \backslash W, \\
& 0 \leq \lambda_m \leq \omega z_m, \quad \forall m \in M \backslash W.
\end{aligned}
\tag{7.10}
$$

In this case, for a given service center configuration, the shutdown of certain service centers causes an increase in the customer demand allocation among remaining service centers accordingly, thereby resulting in traffic congestion in the transportation system and within-center waiting time in line and processing time. Customers may be less patient/loyal to the company when a disruptive event diminishes a system's ability to offer the service in a timely manner. As a result, it is important to account for these factors in the decision making pertaining to the configuration of service centers in a city. From a systematic point of view, given the occurrence of disruptive event e, the total travel time and service time for all the customers corresponding to the traffic flow at the new user equilibrium can be updated as follows:

$$
F(e) = \sum_{a \in E} x_a t_a(x_a) + \sum_{i=1}^{m} \lambda_m \left[E(\kappa_m) + E(s_m) \right] \quad \forall m \in M \backslash W. \tag{7.11}
$$

Since disruptive event e has an explicit impact on customers' traveling time and service time, the goal of our study is to help system planner design a resilient service center configuration with the consideration of the effect of possible disruptive events on the system in advance such that the traffic congestion and long waiting time can be mitigated when disruptive event actually happens. In this circumstance, by adopting the resilience definition developed by Henry and Ramirez-Marquez [2], the resilience of a given service center configuration is measured as below:

$$R\left(\boldsymbol{u}', e\right) = \frac{F\left(\boldsymbol{u}, e\right) - F\left(\boldsymbol{u}', e\right)}{F\left(\boldsymbol{u}, e\right) - F\left(\boldsymbol{u}\right)} \tag{7.12}$$

where $\boldsymbol{u} = (\boldsymbol{z}, \boldsymbol{c})$ is a vector consisting of two decision variables $\boldsymbol{z}$ and $\boldsymbol{c}$ corresponding to whether to construct a service center and the design capacity of each established service center at each candidate location m ($m \in M$), $\boldsymbol{u}$ and $\boldsymbol{u}^{'}$ represent two service center configurations with and without the consideration of the potential impact of disruptive event e, respectively. $F\left(\boldsymbol{u}\right)$ denotes the total time spent by all the customers before the occurrence of disruptive event e, $F\left(\boldsymbol{u}, e\right)$ measures the total time consumed by all the customers in the system configuration $\boldsymbol{u}$ after disruptive event e happens, and $F\left(\boldsymbol{u}^{'}, e\right)$ models the total consumed time in the resilient design configuration $\boldsymbol{u}^{'}$ when event e occurs.

The research goal of the proposed study is to help system operators to plan ahead and prepare for any potential disruptive event such that the configured system has enough room and buffer in response to the possible disruptive events through the optimization of decision variable $\boldsymbol{u}$.

7.3.2 User Equilibrium Traffic Assignment with Unknown Travel Demand

As mentioned earlier, unlike conventional transportation system, no specific value is given to indicate the travel demand between each resident zone and service center in the logistics service center distribution system. To address this issue, we introduce a dummy node θ and auxiliary links to determine the customer demand allocation among the already established service centers and the corresponding traffic flow assignment along each link.

As illustrated in Fig. 7.2, suppose yellow circles represent the service centers that are established in different locations, light blue solid squares denote the zones where customers

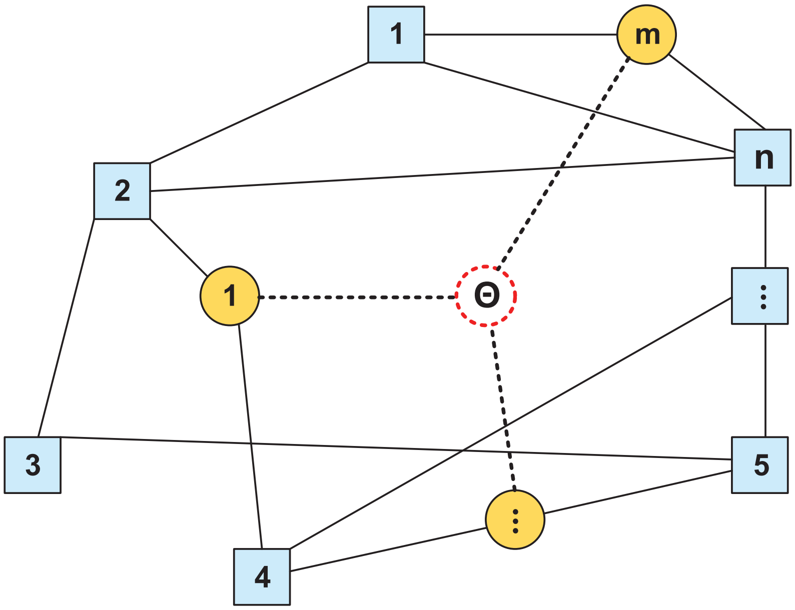

Figure 7.2: A simple network to demonstrate the proposed method to deal with user equilibrium with unknown travel demand between resident zones and service centers

are distributed, and the solid links indicate the road segments that connect customers and service centers. Given customer demand d_i at each zone, an approach needs to be developed to determine the customer demand allocation at each service center. To tackle this problem, a dummy node θ is created and added into the network. In parallel, several auxiliary links are created to connect the service centers with dummy node θ. The travel time along the artificial (dashed) links is set at a negligible value. Since all the customers' demand needs to be satisfied, then we have:

$$\sum_{i=1}^{n} d_i = \lambda_\theta \tag{7.13}$$

where λ_θ denotes the number of customers that the artificially created service center θ serves.

With the introduction of dummy node θ, the traffic assignment equilibrium with unknown demand between origins and destinations degenerates to the classical traffic assignment problem. Since the demand at node θ is now known, which is the sum of customer demand over all the city zones, a number of algorithms that are used for solving classical traffic assignment problems, such as Frank-Wolfe [240], gradient projection [241], bush-based algorithms [242, 243], and other algorithms [244, 7, 245], can be then utilized to tackle this problem thereafter. Since the dummy node θ is only connected with service centers, all the traffic flow that destinies at dummy node θ must go through one of these links connecting service centers with dummy node. As a consequence, we are able to obtain the corresponding customer demand allocation at each service center as well as the traffic flow assignment in the network when it reaches user equilibrium. Since the travel time along the artificially created links is negligible, following Wardrop's user equilibrium principle, the equilibrium state in the service center configuration problem investigated can be characterized as: the travel time along all the used paths from customer zones to all the service centers are minimized, and no customer could reduce the travel time by unilaterally switching to other service centers or taking other routes.

For the sake of completeness, we briefly introduce the gradient projection method that is leveraged to tackle the traffic assignment equilibrium problem for its efficiency and simplicity [241]. Simply speaking, gradient projection approach solves traffic assignment problem by exploiting the separability of the origin-destination (OD) pairs, and it operates directly on the space of path flows. Suppose $K(i,\theta)$ denote the set of paths with positive traffic flow between OD pair city zone i and dummy node θ. At each iteration, gradient projection method moves traffic flow to the shortest path from all the other non-shortest paths in set $K(i,\theta)$ while keeping the path flows of other OD pairs fixed. Afterwards, traffic flow along the paths is projected to the links, from which the travel time along each link is updated accordingly. The same procedures are repeated over all the other OD pairs until the predefined algorithm termination condition is met.

To be more specific, given the updated link travel cost, the shortest path among each OD pair (i,θ) is updated and added to the set of paths $K(i,\theta)$ if the found shortest path is shorter than the current shortest path. In parallel, paths that carry no flow are removed from the set $K(i,\theta)$. The aforementioned two operations correspond to line 11 in Algorithm

Algorithm 2 : Gradient Projection Algorithm for Traffic Assignment Problem

```
Initialize the network $G$, customer demand zone $i$ $(i = 1, 2, \cdots, n)$, dummy node
$\theta$, and the link cost function $\boldsymbol{t}$.
Generate initial shortest path for each OD pair
for each OD pair $(i, \theta) \in \mathbb{OD}$ do
    Find the shortest path $p$ from node $\theta$ to $i$
    Assign all the travel demand among OD pair $(i, \theta)$ to the shortest path $p$
    Store the found shortest path $p$ in the set $K(i, \theta)$
end for
Project the path flow on the links and update the link cost
while the convergence termination condition is not met do
    for each OD pair $(i, \theta) \in \mathbb{OD}$ do
        Update path cost $y_p$, $\forall p \in P^{i,\theta}$
        Improve the path set $P^{i,\theta}$
        if $P_{s,t}$ is improved or $\left|P^{i,\theta}\right| > 2$ then
            Shift the flow from the costlier paths to the shortest path
            Project the path flow on the links and update the link cost
            Remove unused paths from the set $K(i, \theta)$
        end if
    end for
end while
```

2. Afterwards, traffic flow is shifted from costlier paths to the shortest path continuously until the algorithm termination criteria is satisfied. See more details on path flow shift in Ref. [241]. With respect to the termination of the algorithm, we adopt a commonly used convergence indicator as defined in Eq. (7.14) to decide when to halt the algorithm:

$$\text{RGAP} = 1 - \frac{\sum\limits_{i \in (1,2,\cdots,m)} d^{i,\theta} \cdot p^{i,\theta}_{\min}}{\sum\limits_{a \in E} x_a \cdot t_a} \tag{7.14}$$

where $d^{i,\theta}$ denotes the total traffic flow from zone i to dummy node θ, $p^{i,\theta}_{\min}$ represents the travel time along the shortest path between OD pair (i, θ), x_a and t_a denotes the traffic flow and travel time along any given link a in the network, respectively.

A general framework of gradient projection method is briefly summarized in Algorithm 2. At the first step, traffic flow along each path is determined with the all-or-nothing (AON) operation. Since there is no traffic flow in the network, all the travel demand is assigned to the shortest path between each OD pair (i,θ), then these found shortest paths are saved in the set $K(i,\theta)$. Meanwhile, path flow is projected on the links, and the link travel cost is updated accordingly. Afterwards, the shortest path given the updated link travel cost is found, and traffic flow is shifted from all the other non-shortest path to the shortest path. The same procedures continues until the convergence termination condition is met.

7.3.3 Upper Level Optimization Model

In the upper-level model, there are two decision variables: $\boldsymbol{z}$ and $\boldsymbol{c}$ (as discussed in Section 7.3.1, see Eq. (7.12)), where $\boldsymbol{z}$ is a vector consisting of binary variables denoting whether to build a service center at the candidate site m $(m \in M)$ or not, while $\boldsymbol{c}$ represents the design capacity of each established service center, e.g., the number of tellers in a bank.

As mentioned previously, the time spent in the service center is composed of two individual parts: waiting time in the queue and service time in the system. To characterize the waiting time of each customer, we model the flow of customers as a M/M/c queue [246, 247]. In the M/M/c queue, the arrival of customers at each service center is characterized as a Markovian process (*M*) following a Poisson process with arrival rate λ; the service times are memoryless (*M*) following an exponential distribution with parameter μ; there are c identical servers to offer the same type of service $(1 \leq c \leq \infty)$, and the system has an a single queue for all the customers who cannot be served upon arrival [248]. Customers who arrive to find all the c servers busy join a single queue and wait as long as necessary for service. With the aforementioned notations, the utilization of the M/M/c service system can be computed as:

$$\rho = \frac{\lambda}{c\mu} \tag{7.15}$$

For the M/M/c queue, the mean number of customers in the queue is calculated as follows [249]:

$$L_q = \frac{P_0 \left(\frac{\lambda}{\mu}\right)^c \rho}{c!(1-\rho)^2} \tag{7.16}$$

where

$$P_0 = 1/\left[\sum_{m=0}^{c-1} \frac{(c\rho)^m}{m!} + \frac{(c\rho)^c}{c!\,(1-\rho)}\right] \tag{7.17}$$

where P_0 denotes the probability that there is zero customer in the system.

After determining L_q, the mean waiting time for the customers in the queue is calculated with Little's law [250]:

$$\mathscr{W}_q = \frac{L_q}{\lambda} = \frac{1}{\lambda} \frac{P_0 \left(\frac{\lambda}{\mu}\right)^c \rho}{c!(1-\rho)^2} \tag{7.18}$$

The total time that each customer spends in the system is the waiting time plus service time, which can be expressed as:

$$\mathscr{W} = \mathscr{W}_q + \frac{1}{\mu} \tag{7.19}$$

By combining the findings in queue theory with the optimization objective formulated in the upper-level model, it can be observed the total time in the M/M/c system depends on three factors: the mean arrival rate (λ), the number of servers (c), and the mean service rate (μ). As mentioned in the previous subsection, gradient projection algorithm provides the distribution of customer demand among all the service centers, from which we estimate the mean rate of arrival at each service center based upon the assumption that customers are uniformly distributed over the eight working hours every day. Meanwhile, the number of servers (c) corresponds to the design capacity (c) in the upper-level optimization model. Once the mean service rate is given, then the average stay of customers in the system at each service center can be estimated with Eq. (7.19).

In the formulated bi-level optimization problem, both lower-level and upper-level objective functions are nonlinear. As proved by Hansen et al. [251], bi-level optimization is strongly NP-hard, and it has been shown that merely evaluating a solution for optimality is also NP-hard task [252]. Even in the simplest case of linear bi-level programs, where the lower level problem has a unique optimal solution for all the parameters, it is not likely to find a polynomial algorithm that is capable of solving the linear bi-level program to global optimality [253]. In this chapter, to tackle the challenging bi-level optimization problem, we leverage an innovative cross entropy method, which was originally developed by Rubinstein to estimate the probability of rare event [254, 255, 256]. To date, cross-entropy method has been extensively used for mixed integer nonlinear programming [257], network reliability optimization [258, 259, 260], facility layout optimization [261], resource allocation in stochastic systems [262], and others [263, 264].

The gist of cross-entropy method is that locating an optimal or near-optimal solution with random search is a low-probability event. The cross entropy method aims to update the sampling distribution of the random search in an adaptive manner such that the rare event is more likely to happen over iterations. To accomplish this goal, the cross entropy method estimates a sequence of distributions that converges to a distribution with probability mass centered on the region of near-optimal solutions. In general, when solving an optimization problem, there are two major steps in the cross entropy method:

1. Generate random samples following a parameterised probability distribution.

2. Update the parameters of the probability distribution such that the updated distribution is able to generate “better” samples in the next iteration.

With respect to the resilient service center configuration problem, our objective is to find an optimal decision variable $\boldsymbol{u}$ to maximize the objective function defined in Eq. (7.12). Let $\boldsymbol{u}^*$ be the optimal solution and $\gamma^* = R(\boldsymbol{u}^*, e)$, the starting point of cross entropy method is to associate an estimation problem with this optimization problem, as formulated below:

$$l = \mathbb{P}(R(\boldsymbol{U},e) \geq \gamma^*) = \mathbb{E}\left[I_{\{R(\boldsymbol{U},e)\geq\gamma^*\}}\right] = \int I_{\{R(\boldsymbol{u},e)\geq\gamma^*\}} f(\boldsymbol{u};\boldsymbol{v})\, d\boldsymbol{u} \tag{7.20}$$

where the random variable $\boldsymbol{U}$ has a probability density function (pdf) $f(\cdot;\boldsymbol{v})$ parameterized by a finite-dimensional real vector $\boldsymbol{v}$ over the feasible region $\mathscr{U}$, and $I_{\{R(\boldsymbol{u},e)\geq\gamma^*\}}$ is an indicator function on $\mathscr{U}$ for threshold value $\gamma^* \in \mathbb{R}$. When $R(\boldsymbol{u}, e) \geq \gamma^*$ holds, $I_{\{R(\boldsymbol{u},e)\geq\gamma^*\}} = 1$; otherwise, $I_{\{R(\boldsymbol{u},e)\geq\gamma^*\}} = 0$.

Since γ^* is generally unknown in advance, a multiple-level cross entropy method is used to generate a sequence of reference parameters γ and $\boldsymbol{v}$ to gradually find an importance sampling distribution that concentrates all its mass in the proximity of the optimal point $\boldsymbol{u}^*$. Samples generated from such distributions are highly likely to produce high-quality solutions thereafter. Let $\{f(\cdot;\boldsymbol{v}), \boldsymbol{v} \in \mathscr{V}\}$ be a family of distributions on $\mathscr{U}$ parameterized by the real-valued parameter $\boldsymbol{v}$, since the estimation problem defined in Eq. (7.20) is a rare event, a natural way to estimate l is to identify a distribution parameter $\boldsymbol{v}^*$ that maximizes the probability of l, which is formulated in the equation below:

$$\boldsymbol{v}^* = \arg\max_{\boldsymbol{v}} \; E_{\boldsymbol{v}} I_{\{R(\boldsymbol{u},e)\geq\gamma\}} \ln f(\boldsymbol{u};\boldsymbol{v}) \tag{7.21}$$

where $I_{\{R(\boldsymbol{u},e)\geq\gamma\}}$ is an indicator function on $\mathscr{U}$ for different threshold values $\gamma \in \mathbb{R}$.

The parameter $\boldsymbol{v}^*$ can be estimated by:

$$\tilde{\boldsymbol{v}}^* = \arg\max_{\boldsymbol{v}} \; \frac{1}{N} \sum_{k=1}^{N} I_{\{R(\boldsymbol{u_k},e)\geq\gamma\}} \ln f(\boldsymbol{u_k};\boldsymbol{v}) \tag{7.22}$$

where $\boldsymbol{u_1}, \boldsymbol{u_2}, \ldots, \boldsymbol{u_N} \sim_{\text{iid}} f(\cdot;\boldsymbol{v})$. In general, the optimal parameter $\tilde{\boldsymbol{v}}$ can be obtained in closed form [256].

From the above descriptions, it can be seen that cross entropy method constructs a sequence of levels $\tilde{\gamma}_1, \tilde{\gamma}_2, \ldots, \tilde{\gamma}_T$ and reference parameters $\tilde{\boldsymbol{v}}_1, \tilde{\boldsymbol{v}}_2, \ldots, \tilde{\boldsymbol{v}}_T$ such that $\tilde{\gamma}_T$ is close to the optimal value γ^* and $\tilde{\boldsymbol{v}}_T$ centers on the region with high performance. In the resilient service center configuration problem, we develop a two step method to generate feasible solutions in the first step. As mentioned earlier, there are two decision variables $\boldsymbol{u} = (\boldsymbol{z}, \boldsymbol{c})$, where $\boldsymbol{z}$ and $\boldsymbol{c}$ correspond to whether to construct a service center and the design capacity of each established service center at each candidate location m ($m \in M$). One straight implication here is that only when a service center at a candidate site is decided to be built, then it is necessary to generate specific value as its planned capacity. Following this logic, we generate the configuration for decision vector $\boldsymbol{z}$ first with equal probability because there is no information on which service center should be built. When the samples generated in the first step indicate that service center is going to be constructed, then we generate its design capacity. Otherwise, we set its design capacity as zero for the candidate sites with no service center. Once the initial possible solutions are generated, cross entropy method is then leveraged to update the probability distribution such that the algorithm eventually converges to optimal or near optimal solutions. The structure of the cross entropy method is summarized in Algorithm 3.

Algorithm 3 : Cross Entropy Algorithm for Bi-level Optimization

```
1: Choose initial parameter vector $\tilde{\boldsymbol{v}}_0$, let $N^e = [\rho N]$, and set $t = 1$
2: Generate $\boldsymbol{u}_1, \boldsymbol{u}_2, \cdots, \boldsymbol{u}_N \sim_{\text{iid}} f\left(,;\tilde{\boldsymbol{v}}_{t-1}\right)$. Calculate the traffic assignment at user equilibrium corresponding to the randomly generated samples as well as the objective value of the upper-level model. Rank the samples from smallest to biggest based on the objective values of upper-level model: $R_{(1)} \leq R_{(2)} \leq \cdots \leq R_{(N)}$. Let $\tilde{\gamma}_t$ be the $(1-\rho)$ sample quantile of performance, which is $\tilde{\gamma}_t = R_{(N-N^e+1)}$
3: Solve the stochastic program defined in Eq. (7.22) with the same sample $\boldsymbol{u}_1, \boldsymbol{u}_2, \cdots, \boldsymbol{u}_N$, and let the solution denoted by $\tilde{\boldsymbol{v}}_t$
4: If the termination condition is met, then the algorithm ends; otherwise, set $t = t+1$, go back to Step 2
```

As illustrated in Algorithm 3, N denotes the sample size, ρ is a predetermined rarity parameter, and $[\rho N]$ denotes the minimum integer not less than ρN. Another thing worthy of mention is that a smoothing factor α is often introduced to combine the current estimated distribution parameter with the distribution parameter used in the previous iteration.

$$\tilde{\boldsymbol{v}}_t = \alpha \widetilde{\boldsymbol{v}}_t + (1-\alpha)\,\tilde{\boldsymbol{v}}_{t-1} \tag{7.23}$$

where $\widetilde{\boldsymbol{v}}_t$ denotes the solution to the optimization problem formulated in Eq. (7.22), and $0 \leq \alpha \leq 1$.

7.3.4 Summary

The methodology developed in this chapter tackles the resilient service center distribution configuration problem with a four-step procedure:

1. We formulate a logistics service center distribution problem, in which system resilience is taken into consideration to measure the potential impact caused by disruptive events.

2. Customers' path choosing behavior is characterized as a traffic assignment problem, in which a dummy node is introduced to determine the customer demand allocation among all the service centers.

3. In the upper-level model, both the travel time and within center processing time is considered. To measure the within center processing time, we model the interaction between customers and service centers as a M/M/c queue.

4. To solve the formulated bi-level optimization problem, cross entropy method is utilized to generate a family of probability distributions with probability mass gradually converging to the proximity of the optimal state.

7.4 Numerical Example and Simulation Results

In this section, a numerical example is used to demonstrate the effectiveness of the developed method in increasing the resilience of service center configuration. To solve this problem, some parameters need to be specified first. First of all, the number of servers that can be established at each service center needs to be an integer, and the maximum number of servers allowed at each service center is set as 6 in this study. Secondly, with respect to the mean service rate, it is a parameter independent of waiting time, and we assume that each server is able to serve 18 customers per hour ($\mu = 18$). In other words, each customer slightly more than 3 minutes to have service on average. To measure customer's travel time, we take the most commonly used BPR link cost function in the literature to characterize the relationship between travel time and traffic flow, which is shown in Eq. (7.24).

$$t_a(x_a) = t_a^0 \left(1 + 0.15 \left(\frac{x_a}{\chi_a} \right)^4 \right). \tag{7.24}$$

where t_a^0, x_a, and χ_a denote the free-flow travel time, the current traffic flow, and the road capacity along link a, respectively. In this study, we set the threshold value of convergence indicator RGAP as 10^{-3} to determine when to terminate the gradient projection traffic assignment algorithm.

Since there is a limit on the budget as defined in Eq. (7.9), we develop a nonlinear function as shown in Eq. (7.25) to represent the relationship between the design cost and corresponding capacity (c) for service centers.

$$\tau(c) = 8c + 0.6c^2 \tag{7.25}$$

where $\tau(c)$ represents the incurred cost.

Regarding the cross entropy method, we generate 40,000 samples in total at each iteration to represent a small portion of service center configurations. The generation of service center configurations follows a two-step procedure. In the first step, binary vectors are generated following independent Bernoulli random variables with the probability of establishing service center among all the candidate sites initialized as $\tilde{z}_0 = \mathbf{0.5}$. In the second step, with respect to each instance generated in the first step, the number of servers is assigned to each service center following a uniform distribution for the values ranging from 1 to the maximum number of server allowed at each service center. Given the randomly generated samples, we set ρ as 0.1, and the top 10% elite solutions are used to update the probability of having each specific service center constructed with specific number of servers in the configuration, and the smoothing factor α is set at a value of 0.5 to combine the distribution parameter in two consecutive iterations. The updated probabilities are used to generate better service center configurations in the next iteration. The same procedures is repeated until the probabilities converge to zero or one.

Fig. 7.3 illustrates a transportation network with 25 nodes and 40 two-way links. The nodes in green color represent the potential construction sites for establishing service centers. The area within the red solid box denotes a region susceptible to natural disasters, e.g., hurricane, flood. When the region is damaged by the extreme event, service centers established within this area is unable to offer service any more, while the road segments are still able to allow residents in this area to commute to other nearby places. The numbers along each link denotes the free flow travel time (unit: minutes) and link capacity (unit: vehicles), respectively. Take link 1 → 2 as an example, its practical capacity is 300 vehicles, and it takes passengers 3.72 minutes to drive from node 1 to node 2 when there is no congestion at all.

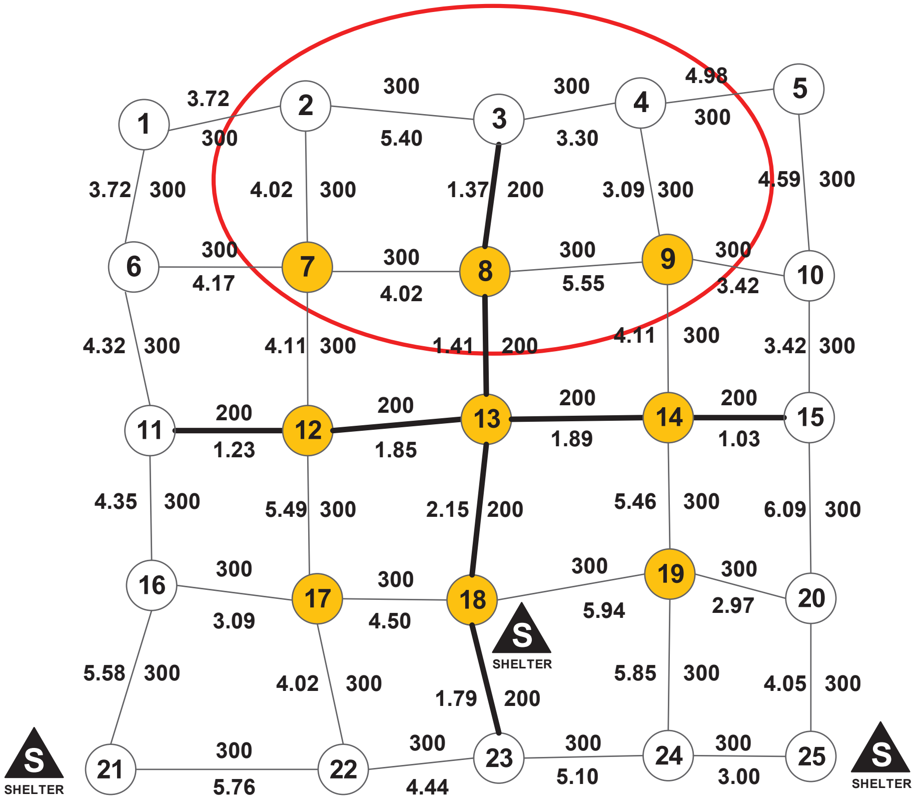

Figure 7.3: Test network 1: A 25-node transportation network

Suppose the customer demand at each resident zone (except the candidate sites to build service centers) is 100 customers per day. In other words, there are 1700 customers that need to be served by all the service centers in one day. The system planner has a total budget of $T = 240$ to construct service centers in this region. As the customer demand between each service center and resident zone is unknown, a dummy node and auxiliary edges are created to connect all the service centers with the dummy node. To illustrate this idea, Fig. 7.4 shows a network where we decide to build three service centers at node 2, 5 and 8, respectively. Although the demand between each service center and resident zone is unknown, the total customer demand at the dummy node 26 is known (1700), which is equal to the summation of customer demand over all the resident zones. One thing worthy of mention is that the free-flow travel time along the dummy links is set at a very small value (e.g., 0.0001), while the road capacity along the auxiliary links is set at a relatively large value (i.e., 10000). By adding dummy node 26 and auxiliary links into this network, the customer demand at node 26 is known now. The introduction of auxiliary node and links not only allows to estimate the customer demand at each service center, but also enables to calculate the traffic assignment along each road segment. The same idea also applies to other service center configurations.

Given the customer demand at each resident zone, the cross entropy method first generates 40,000 random samples to represent the possible service center configurations consisting of service center construction site and the corresponding number of servers at each constructed site. Afterwards, the gradient projection algorithm is used to deal with the user equilibrium traffic assignment. Fig. 7.5 shows the convergence trend for one system configuration. As can be observed, the gradient projection method converges to the predefined precision at a fast rate.

Once the customer demand allocation at each service center is determined, the average customer waiting time in line and service time for each service center configuration is calculated accordingly, where the interaction between each service center and customers is modeled as a M/M/c queue. Afterwards, the value of objective function defined in Eq.

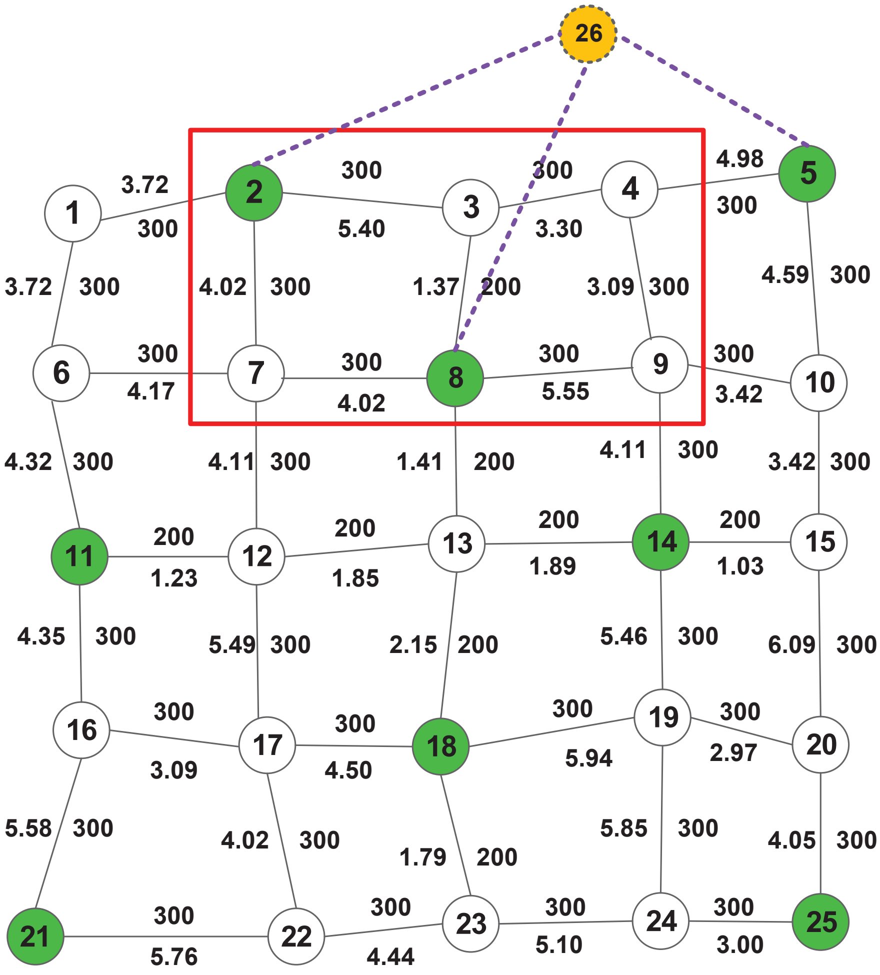

Figure 7.4: Illustration of dummy node and auxiliary links

(7.11) is acquired. Next, the top 10% feasible solutions out of the 40,000 samples is used to update the probability of having each candidate service center and corresponding number of servers established accordingly. Next, the aforementioned same procedures are repeated with the updated probability until the probability converges to zero or one. Fig. 7.6 shows the convergence of establishing service center at each candidate site. At first ($t = 1$), all the candidate sites have the same probability of 0.5 to build service center. With the increase of iterations, only the probability of site 2, 8, 11, 14, 18, and 25 converges to one, while the probability of all the other candidate sites (5, 21) reduces to zero gradually. Since all the probabilities converge to stable values within only 25 iterations, it demonstrates

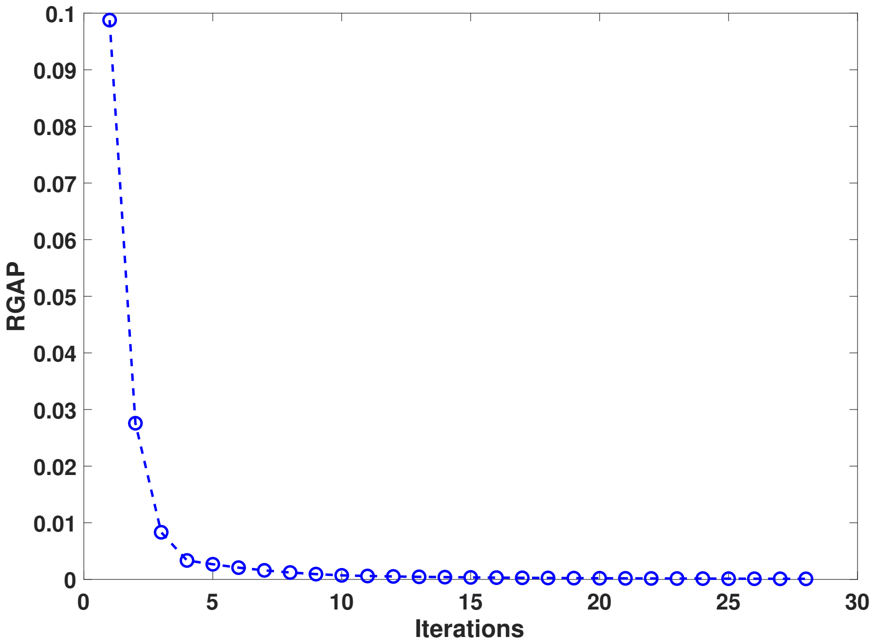

Figure 7.5: Convergence of gradient projection algorithm for one instance of service center configuration

the effectiveness of the cross entropy method in tackling the challenging combinatorial optimization problem. Fig. 7.7 shows the changing trend of objective function value over 25 iterations.

Table 7.1: Best solution found by the cross entropy method without the consideration of the impact of disruptive event *e*.

Candidate site ID	2	5	8	11	14	18	21	25
Construction of service center	✓	×	✓	✓	✓	✓	×	✓
Number of servers	3	0	4	4	5	4	0	3

If we do not account for the influence of extreme events on this region, then the best service center configuration found by the cross entropy method is reported in Table 7.1. As can be observed, service center 14 has the largest number of servers, followed by service centers 8, 11, and 18. Whereas, service centers 2 and 25 have the least number of servers. The total incurred cost for such a service center configuration is 238.6, which is slightly less than the total budget 240. The total travel time and service time for all the customers

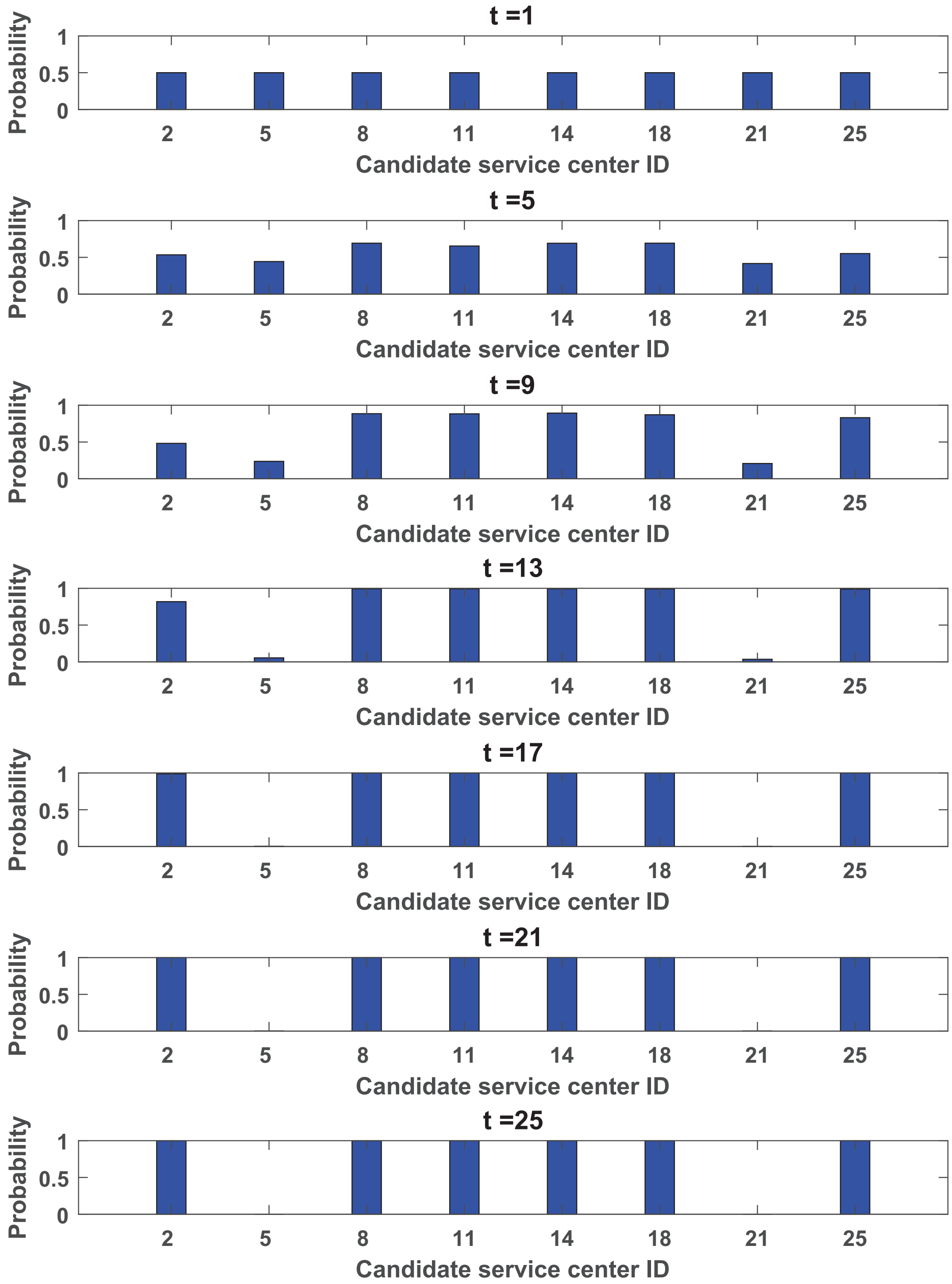

Figure 7.6: The evolution of constructing service center at each candidate site

is 12,356. If we take into consideration of the extreme event impact, it implies that service centers 2 and 8 will get closed because they fall within the disaster-prone zone. If the two

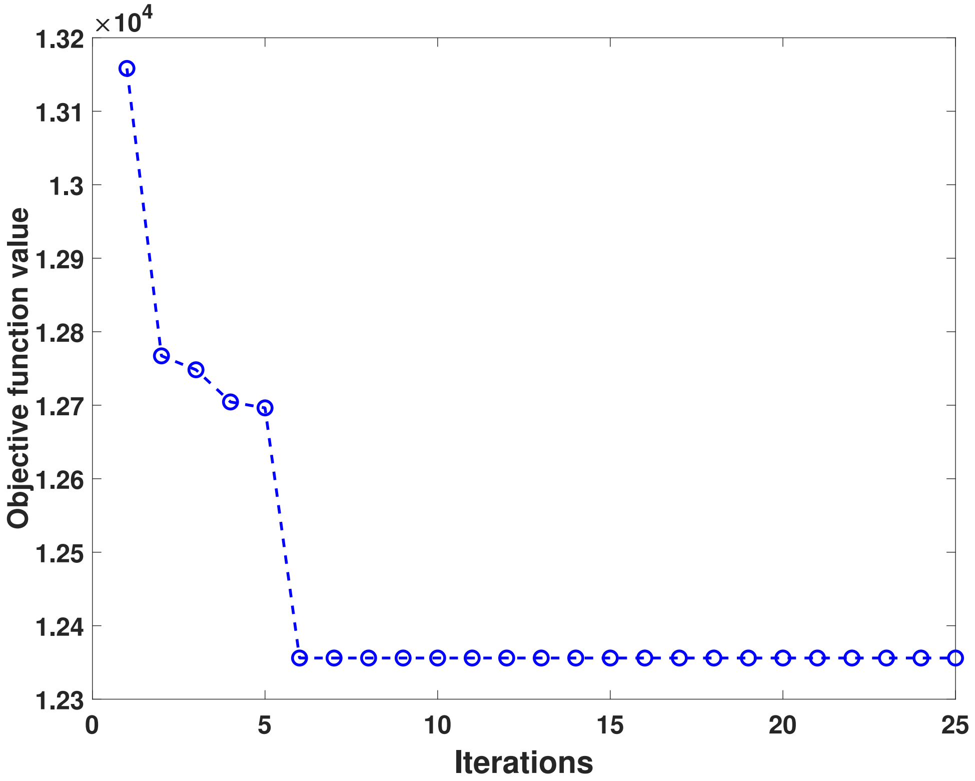

Figure 7.7: The evolution of objective function value over iterations

service centers are shut down, customers in this zone will shift to other service centers for service, which causes an abrupt increase in customer demand. As a consequence, since too many customers switch to the remaining service centers, it might cause congestion in road traffic and long line at each service center (see the following Fig. 7.8). Given the closure of service centers 2 and 8, the objective function value defined in Eq. (7.11) is recalculated with a value of 29,746. As can be observed, the objective function value is doubled in comparison with the no-disaster case due to the abrupt increase in customer demand among the remaining service centers.

Table 7.2: Best solution found by the cross entropy method when the impact of disruptive event e is considered.

Candidate site ID	2	5	8	11	14	18	21	25
Construction of service center	×	✓	×	✓	✓	✓	✓	✓
Number of servers	0	2	0	6	6	3	2	3

In contrast, if we take into account the impact of extreme event in advance, the new service center configuration should be able to absorb the negative effect of disruptive event *e*, thereby alleviating the impact of disruptive event on the performance of service centers. In this regard, the service center configuration should not only work for the regular scenario, but also for the circumstance that disruptive event *e* occurs. Hence, the regular objective function (without disaster) needs to be joined with the new objective function value in the circumstance that disruptive event *e* occurs, and these two functions have same weight (0.5). Given these considerations, the cross entropy method with same parameter settings is used to find out the best service center configuration. Table 7.2 shows the best solution found by cross entropy method after 25 iterations. As can be observed, different from the service center configuration illustrated in Table 7.1, no service center is established in candidate sites 2 and 8 in consideration of the potential impact of extreme event. Instead, two service centers are established at candidate sites 5 and 21 with the same number of servers. Besides, the number of servers in the service centers established at candidate site 11 and 14 is increased accordingly. By doing this, the new service center configuration avoids the costly consequence caused by the disruptive event. Such a design incurs a total investment of 234.8, and has an objective function value of 13,443.

Fig. 7.8 compares the travel time, service time for all the customers with and without extreme event under the two designs. In the original service center configuration, when disruptive event *e* occurs, the total service time increases substantially because too many customers shift to other service centers, which result in a dramatic rise in customers' average waiting time. On the contrary, the extreme event has no impact on the travel time and service time in the resilient service center configuration. Although the travel time for the resilient design is slightly larger than the travel time of original design in the no-disaster case, the service time remains the same level even if the extreme event occurs. Following the resilience definition formulated in Eq. (7.12), the resilience of new service center

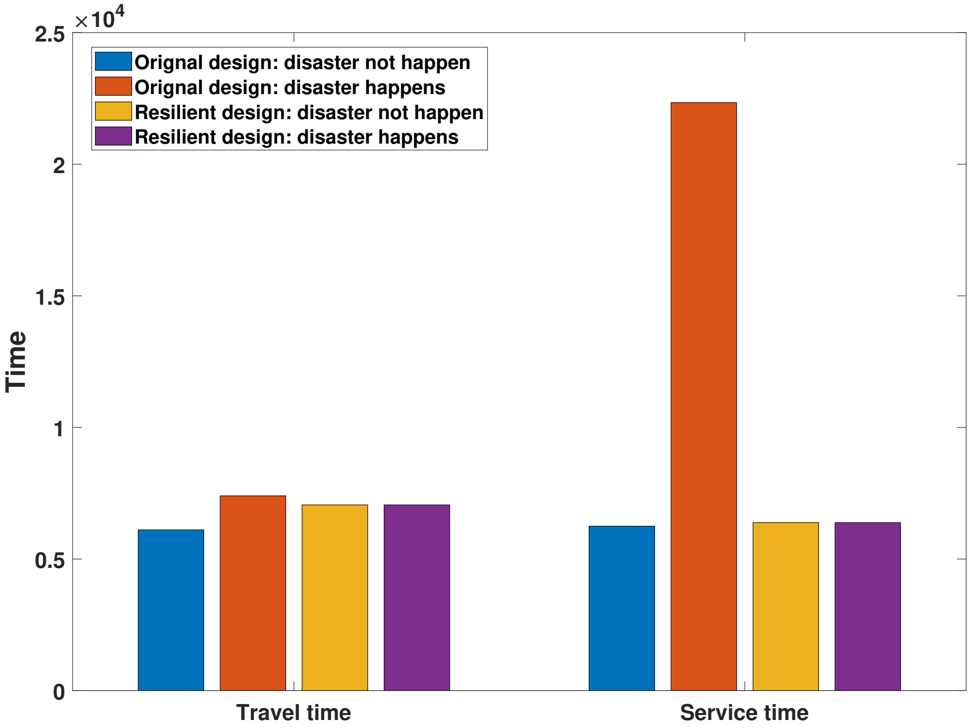

Figure 7.8: Comparison of travel time and service time in different scenarios

configuration in responding to the disruptive event e is calculated as:

$$R\left(u',e\right) = \frac{29746-13443}{29746-12356} = 0.9375 \tag{7.26}$$

7.5 Summary

In this chapter, a comprehensive bi-level optimization model is developed to optimize the service center distribution to increase its capability in withstanding the impact of an unanticipated extreme event. A bi-level program is formulated to characterize the interactions between customers and system planners. From the perspective of customers, they behave in a non-cooperative manner to pick a service center with the shortest travel time, and eventually converge to a user equilibrium state, where nobody could reduce the travel time by unilaterally shifting to other service centers or alternative routes. A dummy node and auxiliary links are introduced to find the customer demand allocation among service centers, from which a gradient projection algorithm is used to identify customer flow assignment in the traffic network. In the upper-level model, both customers' travel time and service time composed of average waiting time in a line and mean processing time, as well as the potential impact of extreme event are considered. To tackle the bi-level optimization problem, a multi-level cross entropy method is utilized to generate samples in an adaptive manner, which gradually converges probability mass towards the optimal solution. The new configuration of logistics service center in this chapter implies that the impact of natural disaster on infrastructure system can be mitigated to a large extent if the system is designed with resilience.

This chapter leverages optimization techniques to identify the optimal system configuration to enable resilience in an infrastructure system. The optimization of system configuration significantly strengthens the ability of the system against disruptive events. This chapter focused on designing an entirely new service center configuration, where none existed before. In practice, it is more common that some service centers or components already exist in the system before the design. Under this circumstance, instead of designing a new system, we need to redesign or reconfigure pre-existing system components to achieve resilience. In the next chapter, we focus on reconfiguring pre-existing components to enhance the resilience of a transportation system.

Chapter 8

System Reconfiguration to Increase System Resilience[1]

8.1 Introduction

The previous chapter addressed the design for resilience in a new system, i.e., no component exists in the system before the design. A more realistic scenario in practice is that the system has been operated for a while, and that we aim to improve the resilience in the legacy system by adding new components or other operations. In this chapter, we leverage optimization algorithms to address this problem. We optimize actions that can be taken in an already existing system to enhance the effectiveness of the system in responding to emergency situations, and illustrate the developed method in a transportation network.

In recent years, it has become a high priority for many countries to increase the resilience in existing infrastructure systems, such as, power grids [266], transportation networks [267], and telecommunication networks [268]. By implementing a variety of measures before, during, and after the occurrence of disruptive events, the outcome of the low-probability-high-consequence natural disasters can be mitigated dramatically. Typically, the approaches used to increase the resilience of any system can be grouped into three categories.

1. Increase system redundancy: System redundancy is concerned with constructing redundant paths/links to offer the same type of service, or building multiple paths/links with every path/link used for each specific scenario. It has been used as an effective way to reduce the probability of the system failing to provide the required service [269, 270]. For example, Jenelius [271] demonstrated that redundant road links played an important role as backup alternatives in transportation systems when other links in the network were disrupted. However, this strategy has been criticized for

[1] An archival paper related to this chapter is to appear in the journal Risk Analysis. For more details, see Ref. [265]

several reasons. First of all, it is usually time-consuming to construct new paths/links for infrastructure systems, especially for transportation systems. Secondly, enormous financial resources are in need to be invested to build new paths/links, while the construction of new paths/links based on previous disasters does not necessarily guarantee mitigation from unforeseen future disaster events.

2. System hardening strategies: System hardening strategies aim at making physical changes to the infrastructure system to strengthen its innate ability to resist disruptive events. Typically, retrofit/fortification actions have been investigated to protect critical system components such that they are able to withstand certain disasters [272, 273, 274]. Along this direction, research efforts have been dedicated to prioritizing project investment in hardening system components. For example, Thorisson and Lambert [275] as well as Thekdi and Lambert [276] leveraged corridor trace analysis to identify sections of transportation systems at risk when stressed in terms of increased traffic, accidents, deteriorating physical conditions, and others, thus offering insights on prioritization of projects for increasing the resilience of the transportation system. Qin et al. [277] formulated a mathematical model to solve a fortification planning problem through optimizing the location of fortified facilities, the inventory of pre-positioning emergency, and the assignment of emergency transportation for an existing logistics system with capacitated facilities and limited protection investment budget. However, system hardening usually consumes large amount of resources because it involves reinforcing the construction materials. More importantly, one hardening strategy typically can only handle certain types of extreme events.

3. Operational resilience strategies: Operational resilience is an umbrella term used to represent the activities and operations for increasing the system flexibility and reconfigurability [278]. For example, Kim et al. [279] proposed scalable computational

heuristics to determine the optimal contraflow network configuration, and demonstrated that contraflow approaches could reduce the total evacuation time by 40% percent or more. In comparison with the previous two strategies, operational resilience strategies have demonstrated promising features, and it has been extensively studied to restore power, transportation, and manufacturing system performance in the aftermath of extreme events [280, 281, 282, 283]. First of all, this strategy is economically achievable compared to the aforementioned two strategies. For example, in the power grid, we only need to install switching devices across the network, from which we are able to adjust the topology of power system in response to disruptive events. Secondly, this strategy makes the infrastructure system flexible and reconfigurable. By changing the open/close status of the switching devices in the power grid, the system has a series of possible configurations. By adopting an appropriate configuration, we are able to isolate the fault, reconnect the station with other normally operating feeders, thus recovering the power supply to the blackout area.

The above discussion indicates that among the three mainstream strategies for increasing system resilience, operational resilience strategy has advantages over the other two approaches from the economic and operational point of view. System reconfiguration, as a major means to achieve operational resilience strategy, can be an effective measure in mitigating the consequence of disruptive events. Indeed, several studies already leverage this strategy to restore system performance. For example, Daigle et al. [284] demonstrated that a robot could recover from damage to sustain performance through an autonomous process of self-modeling and self-reconfiguration [285]. Daigle et al. [284] used circuit breakers and relays to enable a number of distinct power distribution configurations for the purpose of mitigating the effect of different types of faults in a spacecraft power distribution system. Arıkan et al. [286] implemented aircraft cruise speed control in recovering system performance and mitigating delays in the presence of airline disruption. Fang and Sansavini [287] combined capacity expansion and transmission switch installation in electric systems to increase the reconfigurability for the sake of alleviating the impact of disruptive events. Recently, Yodo et al. [288] utilized control theory to adapt the configuration of the system to maintain a desirable level of system performance in response to external disturbance.

In the presence of a natural disaster, transportation networks play a vital role in evacuating the residents who live in the affected area. Evacuating a large population out of the disaster prone areas within a limited time is an important strategy in mitigating the impact of a disaster [289]. For example, Kumar, Romanski, and Van Hentenryck [290] formulated a mixed integer programming (MIP) model to determine the most effective infrastructure enhancements for evacuation planning. Another study worthy of mention conducted by Lambert et al. [291] estimated the number of evacuees in a particular region and assigned the trips to the transportation system to analyze the traffic system performance for emergency management in several disaster scenarios. One common problem arising under this circumstance is that the abrupt increase in the traffic demand results in severe traffic jam during the evacuation process. For example, traffic jams occurred along major freeways leading out of the Houston area during Hurricane Harvey [292]. Similar phenomena have been observed in past evacuations due to Hurricane Katrina and Rita [293]. As pointed out by Lambert *et al.* [291], reversed lanes and ramp metering can be used to increase traffic operations, thereby improving system performance. In this chapter, we work along this direction to investigate how to leverage system reconfiguration strategies and develop an integrated approach to reconfigure the road network for restoring the performance of the transportation system. To that end, two simple and operable strategies are considered for their simplicity and generality to be implemented in transportation systems.

1. Contraflow. Contraflow, also referred to as lane reversal, denotes reversing the direction of the lanes to increase the outbound evacuation capacity. Since it can increase the directional capacity of a roadway immediately and significantly without the need to plan, design, and construct additional lanes, this strategy has been highly effective in reallocating the road capacities to accommodate unbalanced traffic demand. In

many big cities, lane reversal has already been in operation to mitigate traffic congestion during peak hours and large sporting events [294].

2. Crossing elimination at intersections. Intersection crossing elimination was originally suggested by Cova and Johnson as a lane-based routing strategy to reduce traffic delays in emergency evacuations [295]. With this strategy, we can transform the traffic flow interrupted by the traffic signals in each intersection into a temporary uninterrupted flow, which increases the capacity of the traffic system to accommodate high traffic demand under emergency conditions. The implementation of this strategy enables the removal of stop-and-go traffic controls and greatly increases the capacity for the allowable traffic movements.

In this chapter, a mathematical model is formulated to optimize the two network reconfiguration strategies mentioned above in transportation systems for the sake of minimizing the total travel time of both the evacuees and other regular commuters. The problem is formulated as a bi-level optimization program, in which the behavior of the passengers is modeled as user equilibrium in the lower level, and the decision maker's traffic network reconfiguration decisions are represented as discrete variables in the upper level. The two system reconfiguration strategies mentioned above, namely contraflow and crossing elimination at intersections, are taken into consideration. Given each possible system configuration decision, the lower level is a user equilibrium traffic assignment problem, and we employ the gradient projection method to approach its optimal solution. Given that the upper level is a discrete optimization problem, novel approaches are developed to mathematically represent the various link reversal and cross elimination strategies, and a probabilistic solution discovery algorithm is then developed to approach the solution. Two numerical examples are used to demonstrate the effectiveness of the integrated system reconfiguration strategies in reducing the total travel time of the evacuees and the regular commuters. From a practical standpoint, during the response phase, law enforcement and traffic operators are dispatched to corresponding locations to eliminate crossings at intersections and reverse certain lanes as decided by the optimization algorithm. Meanwhile, appropriate road signs need to be placed at right locations to increase drivers' situation awareness of the new traffic patterns. During the restoration phase, after the system reconfiguration decisions are implemented, system performance gradually improves over time because the outbound capacity for emergency evacuees to travel from impacted areas to shelters are increased significantly. Compared to the current state of the art, we have made the following contributions:

1. System reconfiguration strategies (contraflow and crossing elimination at intersections) are considered for the purpose of mitigating the severe congestion caused by the evacuation of a large number of residents within the disaster impacted areas. These reconfiguration strategies facilitate the timely reorganization of the transportation system in response to the large scale evacuation, thereby strengthening emergency preparedness and increasing the system resilience.

2. Novel approaches are developed to mathematically represent the various contraflow and crossing elimination configuration options. Given the system reconfiguration representation, a bi-level optimization model is formulated to maximize the system resilience, in which users' path-choosing behavior is modeled as user equilibrium traffic assignment in the lower level optimization model, and the traffic system operators' reconfiguration decisions in terms of link reversal and crossing elimination are represented in the upper level optimization model.

3. Efficient solution algorithms are leveraged to tackle the formulated bi-level optimization problem. To be specific, the gradient projection approach is used to shift the flow among the paths connecting the same origin-destination pair continuously until the traffic assignment converges to a stable state. A probabilistic solution discovery algorithm is developed to iteratively update the probability of taking each possible system reconfiguration action at the component level, eventually finding the near-

optimal strategies for maximizing the system resilience.

8.2 Proposed Method

In this section, we mathematically formulate the bi-level optimization problem, in which the different system reconfigurations (contraflow and crossing elimination at intersections) are modeled as decision variables in the upper level model, and the user equilibrium traffic assignment based on Wardrop's first principle is characterized in the lower level model. The structure of the proposed method is illustrated in Fig. 8.1. The first step is to express the system reconfiguration strategies and the incurred link capacity change in a mathematical form. Afterwards, consider the mathematical representation, the possible system reconfiguration option with respect to each component is combined with the probability of choosing that particular option to generate candidate system reconfiguration designs. To the lower level traffic network users, such designs are perceived in the form of link reversal and roadway block. For a given particular reconfiguration, the lower level traffic assignment problem is solved by an efficient gradient projection method through shifting the flow from costlier paths to the shortest path for each origin-destination pair until the user equilibrium traffic assignment converges, from which we are able to evaluate the performance in terms of total travel time for all the network users with respect to all the randomly generated system reconfiguration designs. By utilizing a probabilistic solution discovery algorithm, we can update the probability of choosing each option at the component level based on the performance of the previously generated designs, and new candidate reconfiguration designs can be sampled based on the updated probability to approach better solution.

8.2.1 Problem Formulation

As mentioned earlier, our objective is to leverage available system reconfiguration strategies to mitigate traffic congestion and restore performance of the traffic network dur-

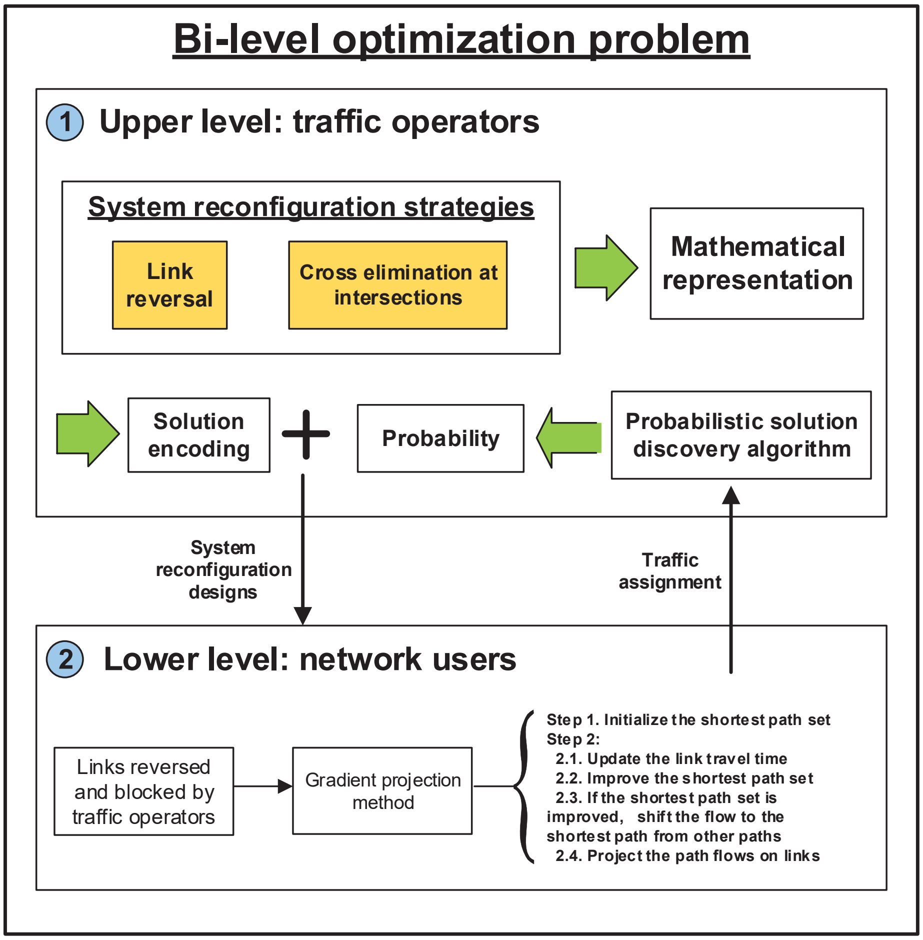
Bi-level optimization problem
1 Upper level: traffic operators
System reconfiguration strategies
Link reversal
Cross elimination at intersections
Mathematical representation
Solution encoding
Probability
Probabilistic solution discovery algorithm
System reconfiguration designs
Traffic assignment
2 Lower level: network users
Links reversed and blocked by traffic operators
Gradient projection method
Step 1. Initialize the shortest path set
Step 2:
2.1. Update the link travel time
2.2. Improve the shortest path set
2.3. If the shortest path set is improved, shift the flow to the shortest path from other paths
2.4. Project the path flows on links

Figure 8.1: Structure of the proposed method

ing evacuation. In this section, we describe the underlying mechanisms of the two system reconfiguration strategies one by one, then we formulate a bi-level optimization problem with the consideration of two network reconfiguration strategies.

First, we introduce a nonlinear function to relate travel time with link congestion level. In general, the traversal time $t_a\left(x_a\right)$ along a link a is a monotonically increasing function of the traffic flow x_a passing through it. Suppose the capacity along the link a is denoted by c_a, then a commonly used function can be expressed in the following form:

$$t_a\left(x_a\right) = t_a^0\left(1+\alpha\left(\frac{x_a}{c_a}\right)^{\beta}\right). \tag{8.1}$$

where t_a^0 denotes the free-flow travel time along link a, and α and β are scalar parameters that can be specified from statistical analysis through curve fitting on the data obtained from uninterrupted freeway.

The above function was developed by U.S. Bureau of Public Roads (BPR) [296]. Fig. 8.2 illustrates several typical shapes of link travel time functions when α and β take different values while the capacity c_a is fixed at a constant value of 5. As can be observed, travel time increases exponentially when the traffic flow exceeds link capacity c_a. To improve the traffic system efficiency, it is beneficial for us to implement different strategies to reconfigure the traffic system for the sake of adapting to the traffic demand and controlling the traffic congestion below certain level.

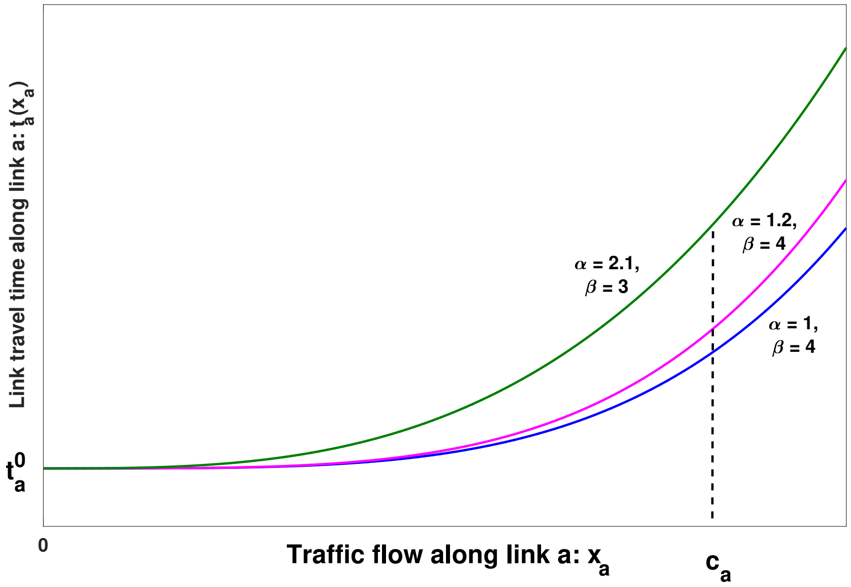

Figure 8.2: BPR function

8.2.1.1 Contraflow

Contraflow refers to reversing the direction of one or more lanes of a roadway for the sake of moving traffic in the opposite direction. In emergency situations, by reversing the inbound lanes to the outbound direction, contraflow can increase the traffic system outbound capacity significantly.

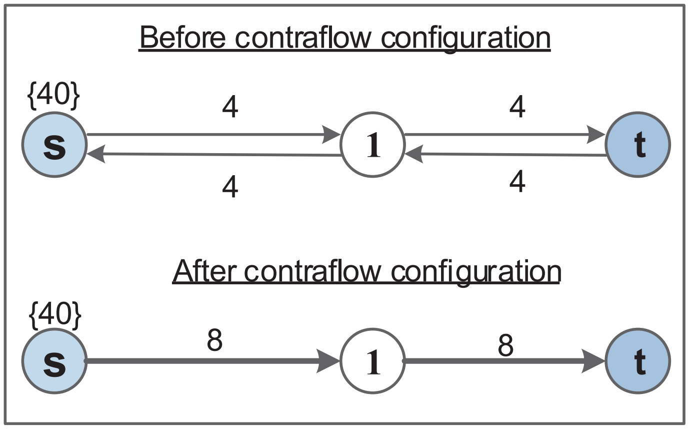
Before contraflow configuration
{40}
4
4
4
4
s
1
t
After contraflow configuration
{40}
8
8
s
1
t

Figure 8.3: Contraflow illustration

To illustrate the concept of contraflow, a simple evacuation situation is shown in Fig. 8.3. Suppose some residents need to be evacuated from node s to node t, and node 1 serves as the transshipment node. The number within the parentheses indicates the number of persons to be evacuated, and the number along each link denotes the link capacity (number of persons per minute). As can be observed, the capacity is the same for all the two-way links. Since the traffic demand (40) is much higher than the link capacity (4), there will be severe congestion along links $s \to 1$ and $1 \to t$. By reversing the direction of links $t \to 1$ and $1 \to s$, we double the system outbound evacuation capacity, as shown in the graph at the bottom of Fig. 8.3. In addition, the link congestion is reduced significantly as the travel demand to link capacity ratio drops from 10 to 5. By taking advantage of the contraflow reconfiguration strategy, one can increase the network outbound capacity, mitigate the link level congestion, and reduce the total time in evacuating people out of disaster-impacted area significantly.

8.2.1.2 Crossing Elimination at Intersections

Crossing elimination is demonstrated to be effective in improving the traffic flow movement efficiency by prohibiting certain turning movements. By doing so, the intersections that interrupt the traffic flow are removed from the system. As a result, the traffic move-

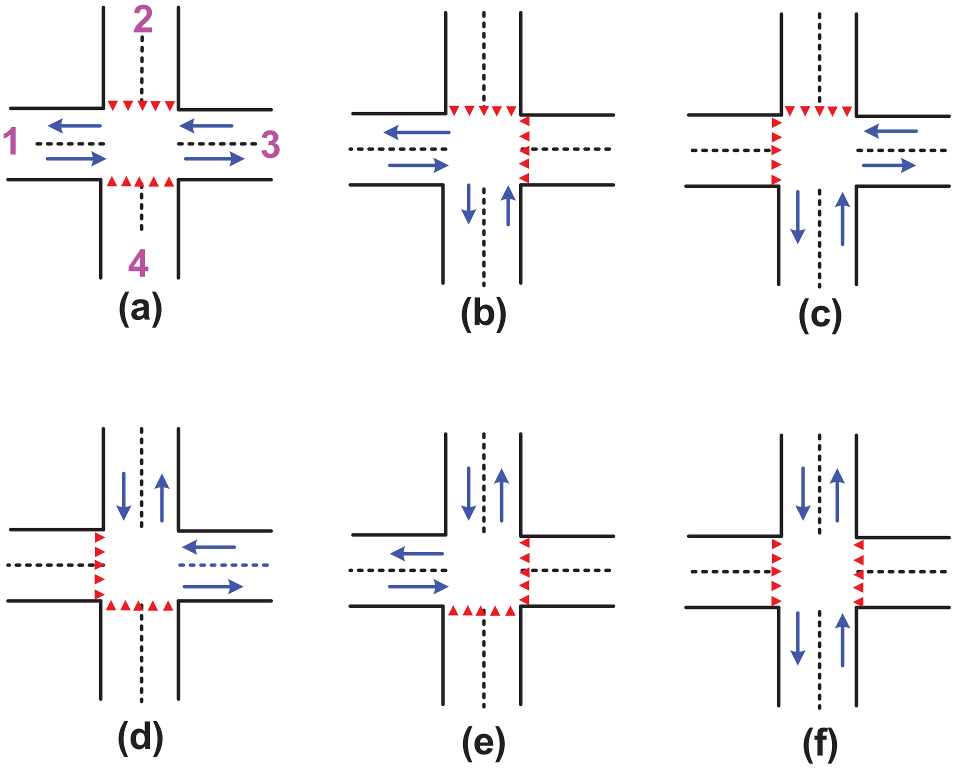

Figure 8.4: An illustration of crossing elimination at an intersection. The blue arrows denote the direction of traffic flow in each lane, the red triangles mean that the roadway is blocked, and the labels in purple represent the order that will be used to encode the problem

ments at intersections are free from the stop-and-go traffic control. The traffic movements at intersections become more smooth, and the system is capable of accommodating more traffic at the intersections within the same time.

In this study, we assume that partial crossing elimination is not allowed. In other words, when we block one roadway of an intersection, both of the two-way links are blocked. This constraint also helps to keep the problem size at a reasonable scale. Typically, all four roadways at an intersection have the same link capacity. To balance traffic and avoid traffic interaction, we impose that the number of blocked roads must be an even number. In other words, it is not allowed to block one or three roadways. In this way, the traffic signal is no longer needed at the intersection. Fig. 8.4 illustrates six possible road block configurations ($C_4^2 = 6$). Each configuration represents a unique way to block the roadways. It can be seen that the traffic flow pattern is changed due to the crossing elimination reconfiguration strategy. Without the control of the traffic signal, traffic movements will become smoother than before.

8.2.1.3 Mathematical Formulation

To represent the aforementioned two reconfiguration strategies in a mathematical form, two additional variables are introduced, which are indicated as below:

1. λ_a: the contraflow configuration of link a $(a \in E)$. If $\lambda_a = 0$, no contraflow operation is carried out on link a. If $\lambda_a = 1$, we reverse the roadway that has the opposite direction with the current roadway. If $\lambda_a = -1$, we reverse the roadway a itself. For example, with respect to the link $1 \rightarrow 2$ shown in Fig. 8.5, if $\lambda_{1\rightarrow 2} = 1$, the direction of link $2 \rightarrow 1$ is reversed; if $\lambda_{1\rightarrow 2} = -1$, the direction of link $1 \rightarrow 2$ is reversed; if $\lambda_{1\rightarrow 2} = 0$, no link is reversed and the directions of the two links remain the same.

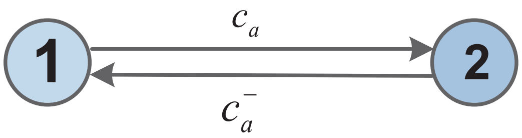

Figure 8.5: Contraflow illustration

To illustrate the mathematical representation of contraflow configuration, a simple example is given in Fig. 8.5. As can be observed, there are two-way traffic roads between node 1 and node 2. Let c_a and c_a^- denote the link capacity from node 1 to node 2 and from node 2 to node 1, respectively. As mentioned previously, when $\lambda_a = 1$, the link that has opposite orientation with the roadway $1 \rightarrow 2$ is reversed. In this example, the link from node 2 to node 1 is reversed. Thus, we have the updated link capacity along link a as follows:

$$\begin{aligned} c_a^* &= c_a + \lambda_a \cdot c_a^- = c_a + c_a^-, \\ c_a^{*-} &= c_a^- - \lambda_a \cdot c_a^- = c_a - c_a^-. \end{aligned} \tag{8.2}$$

where c_a^* and c_a^{*-} represent the updated capacity of the link from node 1 to node 2 and the link from node 2 to node 1, respectively.

If $\lambda_a = -1$, the link from node 1 to node 2 is reversed, then the capacity for link a is updated as:

$$\begin{aligned} c_a^* &= c_a + \lambda_a \cdot c_a^- = c_a - c_a^-, \\ c_a^{-*} &= c_a^- - \lambda_a \cdot c_a^- = c_a + c_a^-. \end{aligned} \tag{8.3}$$

If $\lambda_a = 0$, the above two equations still hold. In summary, no matter which roadway is reversed, the two equations always hold. Thus, they are used to represent the new link capacity after the contraflow reconfiguration. Hence, for any link a $(a \in E)$, we have:

$$\begin{cases} c_a^* = c_a + \lambda_a \cdot c_a^-, \\ c_a^{-*} = c_a^- - \lambda_a \cdot c_a^-. \end{cases} \tag{8.4}$$

2. ξ_i: the crossing elimination configuration at each intersection, where I $(i \in I)$ is the set of intersections that are reconfigured in the network G. ξ_i is a vector consisting of four binary variables, and each variable denotes whether to block one roadway of intersection i or not. When the value of the variable in ξ_i is 1, it indicates that the roadway is blocked. Otherwise, the roadway is not blocked. For example, following the order shown in Fig. 8.4 (a) to encode the problem, the crossing elimination configuration shown in Fig. 8.4(a) can be represented as: $\xi_i = \begin{bmatrix} 0 & 1 & 0 & 1 \end{bmatrix}$ because the second and fourth roadways are blocked in this configuration. The labels in purple fonts shown in Fig. 8.4(a) are used to represent the order in which the decisions related to each roadway is encoded. Likewise, the second and third crossing elimination configurations can be represented as $\xi_i = \begin{bmatrix} 0 & 1 & 1 & 0 \end{bmatrix}$ and $\xi_i = \begin{bmatrix} 1 & 1 & 0 & 0 \end{bmatrix}$, respectively. In this way, each crossing elimination configuration has a unique representation.

Given the above notations, the bi-level optimization model for reconfiguring the traffic network G can be formulated as:

$$(\underline{\text{U2}}) \quad \text{Min} \quad F = \sum_{a \in E} x_a t_a(x_a) \tag{8.5a}$$

$$s.t. \quad \sum_{j=1}^{4} \xi_i(j) = 2, \quad i \in I^*, \tag{8.5b}$$

$$I^* \subseteq I, \tag{8.5c}$$

$$\begin{cases} c_a^* = c_a + \lambda_a \cdot c_a^-, \\ c_a^{-*} = c_a^- - \lambda_a \cdot c_a^-, \end{cases} \quad \forall a \in E, \tag{8.5d}$$

$$\lambda_a = 0 \text{ or } -1 \text{ or } 1, \quad \forall a \in E, \tag{8.5e}$$

$$c_a = 0 \text{ and } c_a^- = 0, \quad \text{if } a \in \omega. \tag{8.5f}$$

$$\omega = \{m(i,j) | \, \xi_i(j) = 1, \forall i \in I, j \in \{1,2,3,4\}\}. \tag{8.5g}$$

$$(\text{L2}) \quad \text{Min} \quad f = \sum_{a \in E} \int_0^{x_a} t_a(x)\, dx, \tag{8.5h}$$

$$s.t. \quad x_a = \sum_{(s,t) \in OD} \sum_{p \in P^{s,t}} q_p^{s,t} \delta_{a,p}^{s,t}, \quad \forall a \in E, \tag{8.5i}$$

$$\sum_{p \in P^{s,t}} q_p^{s,t} = d^{s,t}, \quad \forall (s,t) \in \mathbb{OD}, \tag{8.5j}$$

$$q_p^{s,t} \geq 0, \quad \forall p \in P^{s,t}, \forall (s,t) \in \mathbb{OD}, \tag{8.5k}$$

$$x_a \leq \kappa_a, \quad \forall a \in E. \tag{8.5l}$$

where $\boldsymbol{\xi}_i(j)$ denotes the value of the j-th element in vector $\boldsymbol{\xi}_i$, I denotes the set of all the intersections in network G, I^* represents the set of intersections that are reconfigured, and ω denotes the set of roadways that are blocked in the crossing elimination strategy, and m is a function mapping the j blocked roadway at the i-th intersection to the node label space. With respect to the system constraints, Eq. (8.5b) requires that two roadways must be blocked in each intersection as introduced before, Eq. (8.5d) models the updated link capacity along link a, in which λ is a discrete variable with three possible values ($0, -1$ and $+1$), and Eq. (8.5f) denotes that the capacity along link a reduces to zero if it is blocked.

Algorithm 4 : Gradient Projection Algorithm

```
Initialize the network $G$, origin-destination demand $\mathbb{OD}$, link capacity $\boldsymbol{c}$, and the
link cost function $t_a$ $(a \in E)$.
for each OD pair $(s,t) \in \mathbb{OD}$ do
    Find the shortest path $p$ from node $s$ to $t$
    Assign all the travel demand among OD pair $(s,t)$ to the shortest path $p$
    Store the found shortest path $p$ in the set $P$
end for
Generate initial shortest path for each OD pair
while the convergence termination condition is not met do
    for each OD pair $(s,t) \in \mathbb{OD}$ do
        Update path cost $y_p$, $\forall p \in P^{s,t}$
        Improve the path set $P^{s,t}$
        if $P^{s,t}$ is improved or $|P^{s,t}| \geq 2$ then
            Shift the flow from the costlier paths to the shortest path
            Project the path flow on the links and update the link cost
            Remove unused paths from the set $P$
        end if
    end for
end while
Project the path flow on the links and update the link cost
```

8.2.2 Optimization Algorithms

In this section, we introduce two algorithms to tackle the lower level and upper level optimization problems formulated in the last section.

8.2.2.1 Lower Level Optimization Problem

Given the contraflow configuration and the crossing elimination strategies, the lower level optimization problem can be formulated as a traffic assignment problem (TAP). Many algorithms have been proposed for solving this problem [241, 245]. In this study, we choose the gradient projection method [241] due to its efficiency and simplicity. The gradient projection method exploits the separability of the origin-destination pairs, and it operates on the path space to shift the flow from costlier paths to the shortest path for each origin-destination pair during the iterations. The overall framework of the gradient projection algorithm is illustrated in Algorithm 4.

As can be seen from Algorithm 4, the gradient projection method employs an all-or-nothing (AON) assignment to initialize the traffic assignment, in which all travel demand $d^{s,t}$ is assigned to the shortest path p connecting each origin-destination pair $(s,t) \in \mathbb{OD}$. A set P is constructed to keep track of all the paths with positive traffic flow. Next, path flow is projected on all the links, and the link cost is updated accordingly. Given the updated link cost, the shortest path among each origin-destination pair is updated. Suppose the travel time along the current shortest path $u \in P^{s,t}$ connecting the origin-destination pair (s,t) is y_u. If the found shortest path is not in the set P, then we add it to this set. Next, gradient projection method moves the flow to the shortest path u from all other paths of $P^{s,t}$. Considering the travel time y_u along the shortest path, the direction of descent for other paths can be expressed as:

$$\begin{aligned} &d_p = y_u - y_p, \quad \forall p \in P^{s,t},\ p \neq u, \\ &d_u = - \sum_{p \in P^{s,t},\ p \neq u} d_p. \end{aligned} \tag{8.6}$$

where d_p measures the descent direction in terms of travel time between the current shortest path u and costlier path p. Given the direction of descent d_p, gradient projection moves a certain amount of traffic flow from costlier paths p to the current shortest path u to equilibrate their travel time.

In order to determine the appropriate amount of flow to be shifted from the costlier paths to the shortest path, a linear search along the descent direction is formulated to find the optimal step size as indicated below:

$$L_p = L_p + \gamma d_p, \quad \forall p \in P^{s,t}. \tag{8.7}$$

where γ denotes the step size.

Now the problem is how to find the optimal value for the step size γ. By projecting the descent direction of the path flow on all the links then we have:

$$\begin{aligned} g(\gamma) = \min \sum_{a \in A} \int_0^{x_a + \gamma y_a} t_a(x)\, dx \\ s.t. \quad 0 \leq \gamma \leq \gamma^{ub}. \end{aligned} \tag{8.8}$$

where $\boldsymbol{y} = \left(y_1, \ldots, y_{|A|}\right)$ is the direction of descent along the links after the projection, A is the set of links that are either in path $p \in P^{s,t}$ $(p \neq u)$ or in the shortest path u but not in both, x_a is the current flow of link a, and γ^{ub} is an upper bound on the step size that guarantees the new solution is still feasible. The value of γ^{ub} can be easily derived as $\gamma^{ub} = \min\limits_{k} \left\{ \frac{-L_p^{\max}}{d_p} \middle| d_p < 0 \right\}, \quad \forall p \in P^{s,t}$ [297], where $L_p^{\max}$ is the maximum amount of flow to be shifted on the condition that d_p is less than zero.

Obviously, problem (8.8) is a one-dimensional optimization problem. A variety of techniques are available to determine the optimal step size that is used to move the path flow. In this study, we use the bisection technique proposed in Ref. [298] to find the optimal value of γ to minimize the objective function defined in Eq. (8.8). Once the value of γ is determined, we can shift the flow to the shortest path from other costlier paths of $P^{s,t}$. After the path flow move is accomplished, we project the path flow on all the links and update the link cost. Meanwhile, the path with zero flow is eliminated from set P.

The above procedures finish one step of analysis for a single origin-destination pair, and the same process is repeated for the remaining origin-destination pairs. After the path flows among all origin-destination pairs are analyzed and optimized, one iteration of the gradient projection method is completed. The algorithm continues the same procedures until the convergence termination condition is met. In this study, we take one commonly used metric – relative gap – as a convergence measure, which is defined as below:

$$\mathrm{RGAP} = 1 - \frac{\sum\limits_{(s,t) \in \mathbb{OD}} d^{s,t} \cdot p_{\min}^{s,t}}{\sum\limits_{a \in E} f_a \cdot t_a} \tag{8.9}$$

where $d^{s,t}$ denotes the travel demand between the origin-destination pair (s,t), $p_{\min}^{s,t}$ is the travel cost of the shortest path between origin-destination pair (s,t), f_a and t_a represent the link flow and link cost associated with link a, respectively.

In this study, when the relative gap is less than a predefined threshold, the algorithm stops. When the algorithm converges, we obtain the amount of flow associated with each link, from which we compute the value of the objective function defined in Eq. (2.31).

8.2.2.2 Upper Level Optimization Problem

As mentioned previously, whenever a system reconfiguration strategy is implemented, a corresponding user equilibrium traffic assignment can be obtained by the gradient projection method. Given the user equilibrium traffic assignment, we are able to compute the total travel time for all users as indicated in the upper level objective function. In this section, our goal is to identify the optimal reconfiguration strategy that minimizes the total travel time with the consideration of users' path-choosing behavior. There are two decision variables in the upper level optimization problem, λ_a ($a \in E$) and ξ_i ($i \in I$). Both of the decision variables are discrete. Since it is computationally intractable to derive an analytical solution to this optimization problem, we leverage a powerful evolutionary method – probabilistic solution discovery algorithm – to identify the near-optimal solution within a reasonable time.

The probabilistic solution discovery algorithm was originally developed by Ramirez-Marquez and Rocco [299], and it searches for the best solution in a probabilistic manner by updating the probability of every individual element in the solution space to be a certain value. In general, there are three steps in the probabilistic solution discovery algorithm: strategy development, strategy analysis, and solution discovery. In the strategy development step, with respect to the upper level optimization problem, a large number of possible solutions are randomly generated. The values of the two decision variables are specified in the following manner.

1. With respect to the contraflow configuration, for each link a, three design values are

possible: $0, -1$, and 1. Since we do not know whether to reverse a link or not, all the three values are initially assigned with equal probability $(1/3)$. Hence, we use three separate intervals π_a: $\left[0, \frac{1}{3}\right], \left[\frac{1}{3}, \frac{2}{3}\right]$, and $\left[\frac{2}{3}, 1\right]$ to represent the probability to choose each particular decision value. Then a random number in the range $[0,1]$ is generated. If the generated number is within the range $\left[0, \frac{1}{3}\right]$, then $\lambda_a = 0$. If the generated number falls within the range $\left[\frac{1}{3}, \frac{2}{3}\right]$, then $\lambda_a = -1$. Otherwise, $\lambda_a = 1$. It is worth mentioning that only one variable λ_a is needed to represent all the contraflow configurations related to a two-way roadway.

2. Regarding the crossing elimination at the intersections, there are four binary variables in the decision vector ξ_i ($i \in I$). First, we need to determine whether to reconfigure an intersection or not. Since we do not know whether an intersection should be reconfigured at the beginning, then an uninformative probability 0.5 is used as the value of blocking each intersection. In other words, reconfiguration and no reconfiguration have the probability of 0.5 for each intersection at the beginning. With that probability, a binary value is randomly generated with the probability to represent different realizations. As indicated earlier, if an intersection is reconfigured, only two roadways are blocked at that intersection ($\sum_{j=1}^{4} \xi_i(j) = 2, \quad i \in I^*$). Likewise, the unit is divided into four equal intervals: π_i: $[0, 0.25], [0.25, 0.50], [0.50, 0.75]$ and $[0.75, 1]$. Next, two numbers in the range $[0,1]$ are randomly generated. If the two numbers fall within the same interval, only one roadway is blocked, then two other random numbers are needed to be generated. The same process repeats until the two generated random numbers fall within different intervals. Depending on which interval the value of each generated random number falls within, we decide the specific value for each binary variable in the decision vector ξ_i.

Repeating the above procedure, we utilize Monte Carlo simulation (MCS) to generate a fixed number – called SAMPLE – of potential network reconfiguration strategies. The algorithm terminates when the probability of every decision value in the solution space converges to a stable value.

In the strategy analysis step, we compute the total travel time for the network users corresponding to each potential network reconfiguration strategy generated before, denoted by $\psi(\boldsymbol{\kappa})$, where $\boldsymbol{\kappa}$ is a vector consisting of the decision variables λ_a $(a \in E)$ and $\boldsymbol{\xi}_i$ $(i \in I)$. All the generated network reconfiguration strategies are ranked in an ascending order by their objective values. By analyzing all the generated network reconfiguration strategies, we identify the best solution found so far.

In the solution discovery step, a fixed number of solutions, denoted by TOP, are saved in the set K. A small fraction of size S of ordered strategies are used to update the probability of each decision value appearing in the top-ranked solutions. After normalizing the probabilities for each decision variable, we construct the updated probability intervals π_a $(a \in E)$ and π_i $(i \in I)$ for each variable. Given the new intervals π_a and π_i, the algorithm goes back to the first step and generate new candidate solutions for the next iteration. The algorithm will terminate when π_a and π_i do not change any more. The procedures of the probabilistic solution discovery algorithm are summarized in Algorithm 5 below.

8.2.3 Summary

The proposed methodology in this section solves the bi-level optimization problem using a three-step procedure. First, the different network reconfiguration strategies are represented in a mathematical form. Given the mathematical representation, a bi-level program is formulated to characterize the complex interactions between the traffic operators and the traffic network users. Secondly, for a specified system reconfiguration, to determine the user equilibrium traffic assignment of the lower level optimization problem, a gradient projection method is used to shift the flow from costlier paths to the shortest path among each origin-destination pair, in which bisection method is used to determine the appropriate amount of flow to be shifted. Finally, a probabilistic solution discovery algorithm is developed to identify the best system reconfiguration strategy with the consideration of users'

Algorithm 5 : Probabilistic Solution Discovery Algorithm

```
Initialize SAMPLE, S, TOP, $\pi_a$ $(a \in E)$, $\pi_i$ $(i \in I)$, $\tau = 1$, $K = \Phi$;
while $\tau < T$ do
    STEP 1: (Strategy Development)
    for $h = 1$ to SAMPLE do
        Generate potential network reconfiguration strategies:
            $\boldsymbol{\kappa}_{\tau,1} = (\cdots, \lambda_a, \cdots), \quad \forall a \in E,$
            $\boldsymbol{\kappa}_{\tau,2} = (\cdots, \xi_i, \cdots), \quad \forall i \in I.$
            $\boldsymbol{\kappa}_{\tau}^{h} = \left[ \begin{array}{cc} \boldsymbol{\kappa}_{\tau,1} & \boldsymbol{\kappa}_{\tau,2} \end{array} \right]$
    end for
    STEP 2: (Strategy Analysis)
    (a): Compute the user equilibrium traffic assignment corresponding to each randomly generated strategy $\boldsymbol{\kappa}_{\tau}^{h}$ with gradient projection method as described in Algorithm 4;
    (b): Calculate the total travel time corresponding to the user equilibrium traffic assignment;
    (c): List all the solutions in an ascending order by their objective values;
    STEP 3: (Solution Discovery)
        $K \to K \cup \left\{ \psi\left(\boldsymbol{\kappa}_{\boldsymbol{\tau}}^{(1)}\right), \psi\left(\boldsymbol{\kappa}_{\boldsymbol{\tau}}^{(2)}\right), \ldots, \psi\left(\boldsymbol{\kappa}_{\boldsymbol{\tau}}^{(\mathrm{TOP})}\right) \right\}$
        $\tau \to \tau + 1$
    Update the probability of link to be present in the optimal solution
    Use the top $S$ solutions in the ordered solution set to update $\pi_a$ and $\pi_i$.
end while
```

path-choosing behavior so as to minimize the travel time of all the users across the network. By measuring the amount of total travel time that is reduced by the network reconfiguration strategies, the system resilience can be calculated in a straightforward way.

8.3 Numerical Examples

In this section, two numerical examples are used to illustrate the procedures of proposed method in alleviating the traffic congestion and improving traffic system performance. As a well-known problem, user equilibrium traffic assignment has been extensively studied. Hence, the data on many transportation networks is readily available from the literature (see Refs. [242, 300]), we use the same data and BPR link travel time function as shown in Eq. (8.10) to illustrate the effectiveness of the proposed method.

$$t_a(x_a) = t_a^0\left(1+0.15\left(\frac{x_a}{c_a}\right)^4\right). \tag{8.10}$$

where t_a^0, x_a, and c_a denote the free-flow travel time, the current flow, and the capacity along link a, respectively.

The value of relative gap is set as 10^{-3}. The parameters of probabilistic solution discovery algorithm are set as: SAMPLE = 1000, TOP = 100, and T = 5. All the algorithms are implemented in C++ under Windows 10 with 16.0 GB RAM, Intel Core i7-4790 CPU, 8 Core, 3.60 GHz.

8.3.1 Example 1

Fig. 8.6 shows the Sioux-Falls network with 24 nodes and 76 links. The characteristics of all the links in this network are available at the website: https://github.com/zxgcqupt/TransportationNetworks/blob/master/SiouxFalls/SiouxFalls_net.tntp. The Sioux-Falls is a symmetrical transportation system, in which all the two-way roadways have identical capacity and free-flow travel time. In this chapter, for the sake of simplicity, we only consider the nodes that have four outgoing and ingoing links as intersections. In this case, there are six intersections in the Sioux-Falls network at nodes 8, 11, 15, 16, 20 and 22, and they are highlighted in yellow circles.

Now suppose an extreme event is going to hit the city, and all the areas within the red circle are expected to be impacted by this disruptive event. To mitigate the consequence of this disruption, all the residents within this particular area need to be evacuated as quickly as possible. As indicated by the blue arrows, there are five primary routes to evacuate the residents out of the disaster impacted zones to the three shelters indicated by black triangles in Fig. 8.6. Before the flood, the travel demand from the nodes within the red circle to all

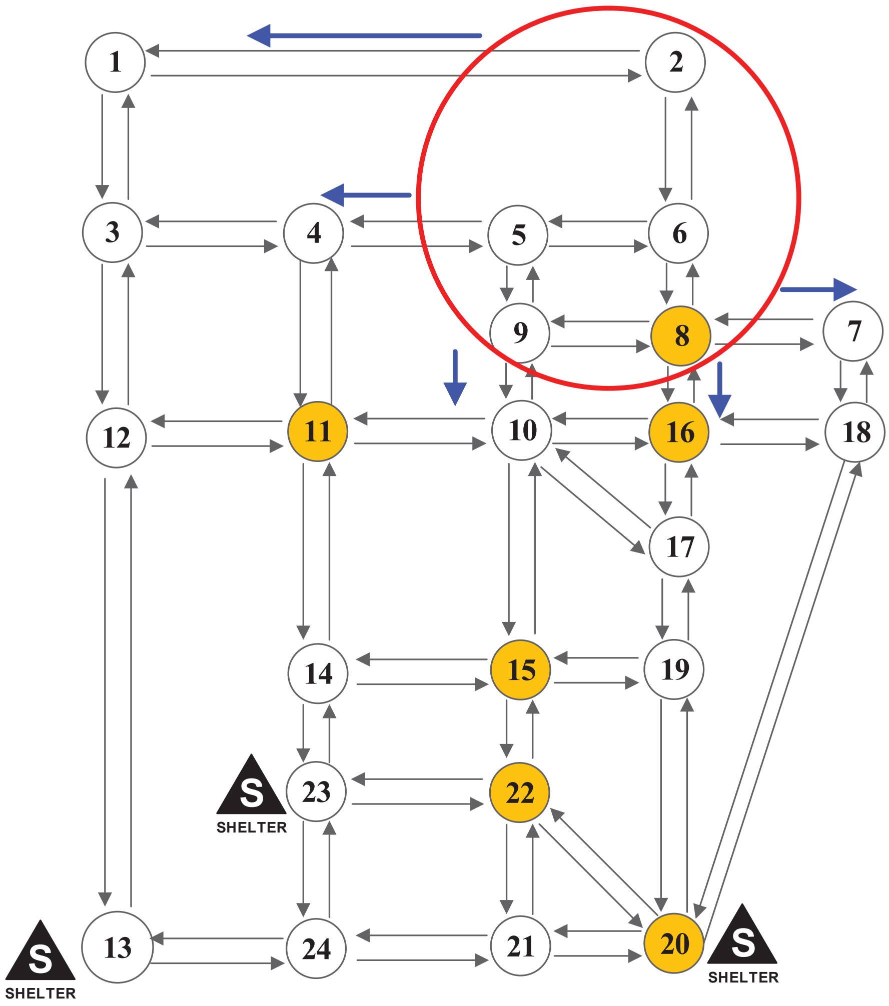

Figure 8.6: Test network 1: Sioux-Falls network

the other nodes is almost evenly distributed across the network. The detailed traffic demand data is available at the website: https://github.com/olga-perederieieva/TAsK/blob/master/Data/SiouxFalls_trips.txt. For example, the regular traffic demand between node 2 and all the other nodes is:

$$d^{2,1} = 100,\ d^{2,3} = 100,\ d^{2,4} = 200,\ d^{2,5} = 100$$
$$d^{2,6} = 400,\ d^{2,7} = 200,\ d^{2,8} = 400,\ d^{2,9} = 200$$
$$d^{2,10} = 600,\ d^{2,11} = 200,\ d^{2,12} = 100,\ d^{2,13} = 300,$$
$$\dots$$

Now, since there are a large number of vehicles moving towards the three shelters that are distributed in different locations across the network at the same time, the traffic demand between the nodes within the red circle and the shelters increases abruptly. The roadways that transport disaster-impacted residents to the designated shelters face a higher travel demand than usual and traffic congestion might occur thereafter. To simulate this effect, we assume all the travel demand that originally starts from the nodes within the red circle and ends at all the other nodes across the network now only ends at the three individual shelters. For example, as shown above, there is different traffic demand from node 2 to all the other nodes in the network. Now, all the traffic demand ends at the three nodes that the shelters are located. For the sake of simplicity, we assume the traffic demand is evenly distributed at the three shelters. Then we have:

$$
\begin{aligned}
&d^{2,13} = 1333,\ d^{2,20} = 1333,\ d^{2,23} = 1333,\\
&d^{5,13} = 2033,\ d^{5,20} = 2033,\ d^{5,23} = 2033,\\
&d^{6,13} = 2533,\ d^{6,20} = 2533,\ d^{6,23} = 2533,\\
&d^{8,13} = 5567,\ d^{8,20} = 5567,\ d^{8,23} = 5567,\\
&d^{9,13} = 5400,\ d^{9,20} = 5400,\ d^{9,23} = 5400.
\end{aligned}
$$

In addition to the travel demand from the emergency evacuations, the regular commuters who stay outside of the impacted areas still need to drive from their homes to the workplaces. To account for this, we add the travel demand among other origin-destination pairs into the origin-destination demand matrix. The final traffic demand through the network under consideration is shown in Eq. (8.11), where the numbers in bold indicate the demand arising from the emergency evacuations.

Given the traffic demand from both the evacuees and the regular commuters, we first solve the lower level optimization problem using the gradient projection algorithm. Fig. 8.7 demonstrates the convergence process of the relative gap for one system reconfiguration design. As can be observed, the gradient projection algorithm converges to the predefined

$$
\begin{array}{c|cccccccccccccccccccccccc}
 & 1 & 2 & 3 & 4 & 5 & 6 & 7 & 8 & 9 & 10 & 11 & 12 & 13 & 14 & 15 & 16 & 17 & 18 & 19 & 20 & 21 & 22 & 23 & 24 \\
\hline
1 & 0 & 0 & 0 & 0 & 0 & 0 & 0 & 0 & 0 & 0 & 0 & 0 & 0 & 300 & 500 & 500 & 400 & 100 & 300 & 300 & 100 & 400 & 300 & 100 \\
2 & 0 & 0 & 0 & 0 & 0 & 0 & 0 & 0 & 0 & 0 & 0 & 0 & \mathbf{1333} & 0 & 0 & 0 & 0 & 0 & 0 & \mathbf{1333} & 0 & 0 & \mathbf{1333} & 0 \\
3 & 0 & 0 & 0 & 0 & 0 & 0 & 100 & 0 & 0 & 300 & 300 & 200 & 100 & 100 & 100 & 200 & 100 & 0 & 0 & 0 & 0 & 100 & 100 & 0 \\
4 & 0 & 0 & 200 & 0 & 0 & 0 & 0 & 0 & 0 & 1200 & 0 & 600 & 600 & 500 & 500 & 800 & 500 & 100 & 200 & 300 & 200 & 400 & 500 & 200 \\
5 & 0 & 0 & 0 & 0 & 0 & 0 & 0 & 0 & 0 & 0 & 0 & 0 & \mathbf{2033} & 0 & 0 & 0 & 0 & 0 & 0 & \mathbf{2033} & 0 & 0 & \mathbf{2033} & 0 \\
6 & 0 & 0 & 0 & 0 & 0 & 0 & 0 & 0 & 0 & 0 & 0 & 0 & \mathbf{2533} & 0 & 0 & 0 & 0 & 0 & 0 & \mathbf{2533} & 0 & 0 & \mathbf{2533} & 0 \\
7 & 500 & 0 & 100 & 400 & 0 & 0 & 0 & 0 & 0 & 1900 & 500 & 700 & 400 & 200 & 500 & 1400 & 1000 & 200 & 400 & 500 & 200 & 500 & 200 & 100 \\
8 & 0 & 0 & 0 & 0 & 0 & 0 & 0 & 0 & 0 & 0 & 0 & 0 & \mathbf{5567} & 0 & 0 & 20 & 0 & 0 & 20 & \mathbf{5567} & 0 & 0 & \mathbf{5567} & 0 \\
9 & 0 & 0 & 0 & 0 & 0 & 0 & 0 & 0 & 0 & 0 & 0 & 0 & \mathbf{5400} & 0 & 0 & 0 & 0 & 0 & 0 & \mathbf{5400} & 0 & 0 & \mathbf{5400} & 0 \\
10 & 1300 & 0 & 300 & 1200 & 0 & 0 & 1900 & 0 & 0 & 0 & 0 & 2000 & 1900 & 2100 & 0 & 4400 & 3900 & 700 & 18000 & 2500 & 1200 & 2600 & 1800 & 800 \\
11 & 500 & 0 & 300 & 0 & 0 & 0 & 500 & 0 & 0 & 0 & 0 & 0 & 1000 & 0 & 1400 & 1400 & 1000 & 100 & 400 & 600 & 400 & 1100 & 1300 & 600 \\
12 & 200 & 0 & 200 & 600 & 0 & 0 & 700 & 0 & 0 & 2000 & 0 & 0 & 1300 & 700 & 700 & 700 & 600 & 200 & 300 & 400 & 300 & 700 & 700 & 500 \\
13 & 0 & 0 & 0 & 0 & 0 & 0 & 0 & 0 & 0 & 0 & 0 & 0 & 0 & 0 & 0 & 0 & 0 & 400 & 0 & 0 & 0 & 0 & 0 & 0 \\
14 & 300 & 0 & 100 & 0 & 100 & 0 & 200 & 0 & 0 & 2100 & 0 & 700 & 600 & 0 & 0 & 700 & 700 & 100 & 300 & 500 & 400 & 1200 & 1100 & 400 \\
15 & 500 & 0 & 100 & 500 & 0 & 0 & 500 & 0 & 0 & 0 & 1400 & 700 & 700 & 0 & 0 & 0 & 1500 & 200 & 0 & 1100 & 800 & 0 & 1000 & 400 \\
16 & 500 & 0 & 200 & 800 & 0 & 0 & 1400 & 0 & 0 & 4400 & 1400 & 700 & 600 & 700 & 1200 & 0 & 2800 & 500 & 1300 & 1600 & 600 & 1200 & 500 & 300 \\
17 & 400 & 0 & 100 & 500 & 0 & 0 & 1000 & 0 & 0 & 3900 & 1000 & 600 & 500 & 700 & 1500 & 2800 & 0 & 600 & 1700 & 1700 & 600 & 1700 & 600 & 300 \\
18 & 100 & 0 & 0 & 100 & 0 & 0 & 200 & 0 & 0 & 700 & 200 & 200 & 100 & 100 & 200 & 500 & 600 & 0 & 300 & 400 & 100 & 300 & 100 & 0 \\
19 & 300 & 0 & 0 & 300 & 0 & 0 & 500 & 0 & 0 & 2500 & 600 & 500 & 600 & 500 & 0 & 1600 & 1700 & 400 & 1200 & 0 & 1200 & 2400 & 700 & 400
\end{array}
\tag{8.11}
$$

threshold within 0.1 second. In a similar way, the gradient projection method is used to approach the user equilibrium traffic assignment for all the other randomly generated system reconfigurations.

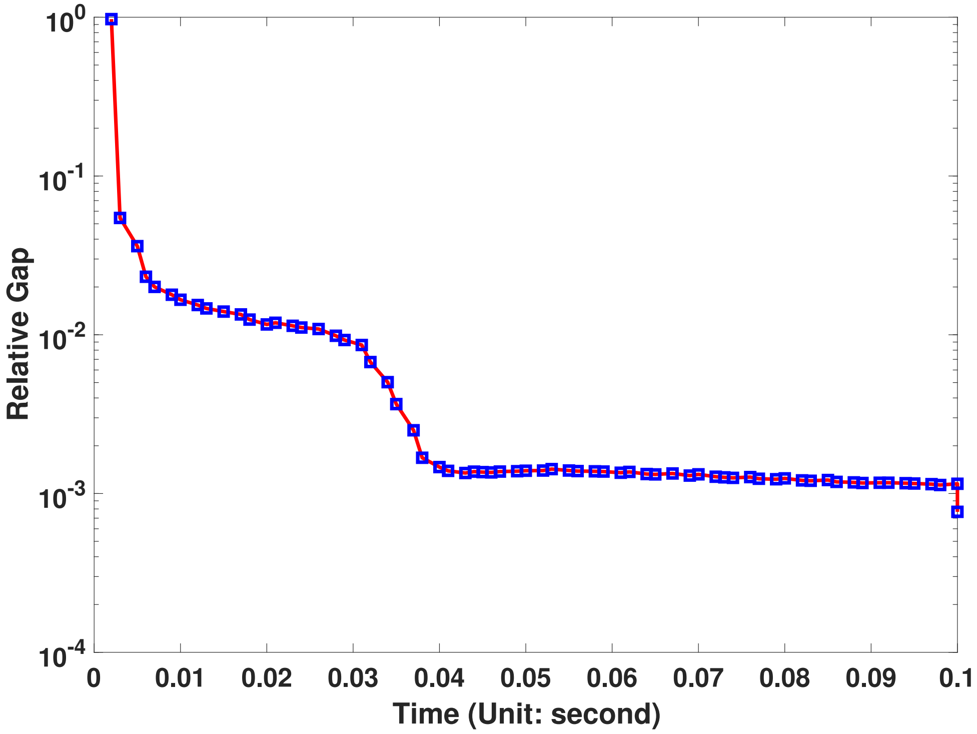

Figure 8.7: The convergence process of the relative gap when the threshold value is 10^{-3}

Given the traffic assignment at the user equilibria, we can evaluate the total travel time of all the network users. Next, the probabilistic solution discovery algorithm is used to iteratively update the probability of assigning each state to every decision variable in the solution space based on the total travel time of the randomly generated reconfiguration designs in the last iteration. Fig. 8.8 illustrates the total travel time for all the users over the iterations. To account for the waiting time of each vehicle at the intersections that are not blocked, we follow National Association of City Transportation Officials [301] and take a commonly used waiting time – 2 minutes – for every vehicle that passes the intersection. Under this consideration, the total travel time of all the users in the original traffic system is 4898226. The best reconfiguration strategy found by the algorithm is shown in Fig. 8.9.

As can be observed, the directions of two links are reversed (link 23 → 14 and 22 → 15), which are highlighted in red color. The reconfigured network has a total travel time of 4525691. Compared with the total travel time in the original system, it has been reduced by 7.6% in the reconfigured traffic system.

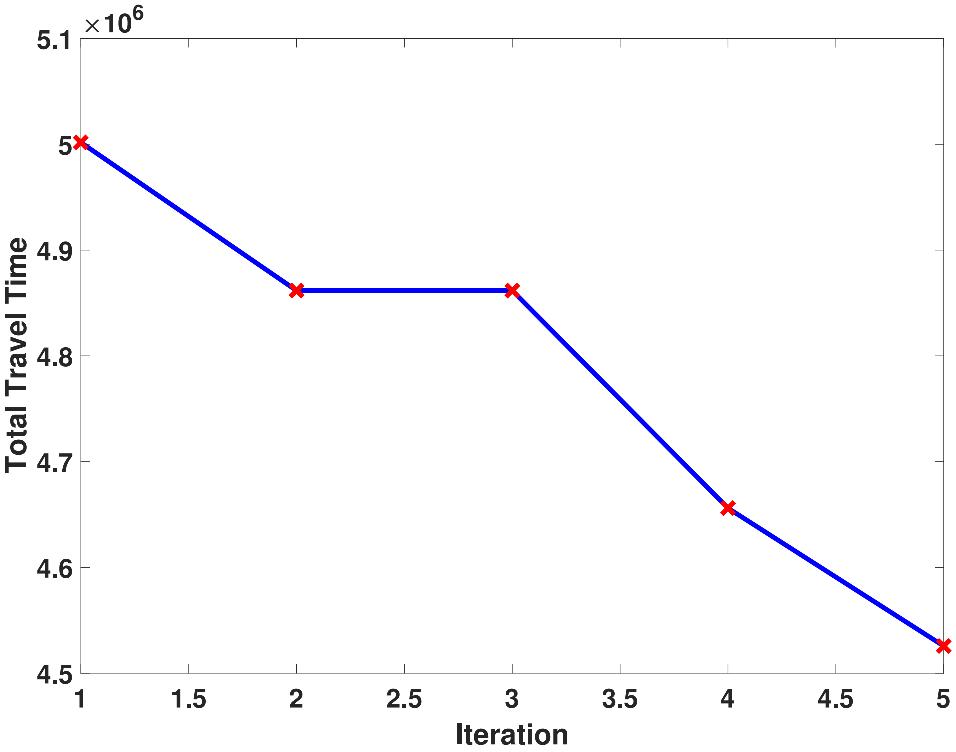

Figure 8.8: The convergence process of total travel time in the Sioux-Falls network.

If the traffic demand is as usual (the traffic demand between the nodes within the red circle and other nodes is evenly distributed), then the total travel time is 4427449. By adopting the resilience definition shown in Fig. 2.1, we have the system resilience as:

$$\mathscr{R}\left(t_f\right) = 1 - \frac{4525691 - 4427449}{4898226 - 4427449} = 0.79. \tag{8.12}$$

The above result implies that the implementation of network reconfiguration strategy has increased the system resilience from 0 to 0.79. The increase of system resilience facilitates the timely restoration of system performance as indicated by the total travel time. From this perspective, network reconfiguration is an effective approach for increasing transportation system resilience under extreme events. Fig. 8.10 demonstrates the traffic flow assignment at the user equilibria for the best system reconfiguration design found by the algorithm. It can be observed that the traffic flow along each roadway varies from 1000 to 35875. To illustrate the traffic flow distribution across the network, we divide them into four levels and represent the amount of flow by four different colors. As can be seen, a large amount of traffic demand flows into the three shelters, see link 18 → 20, 12 → 13.

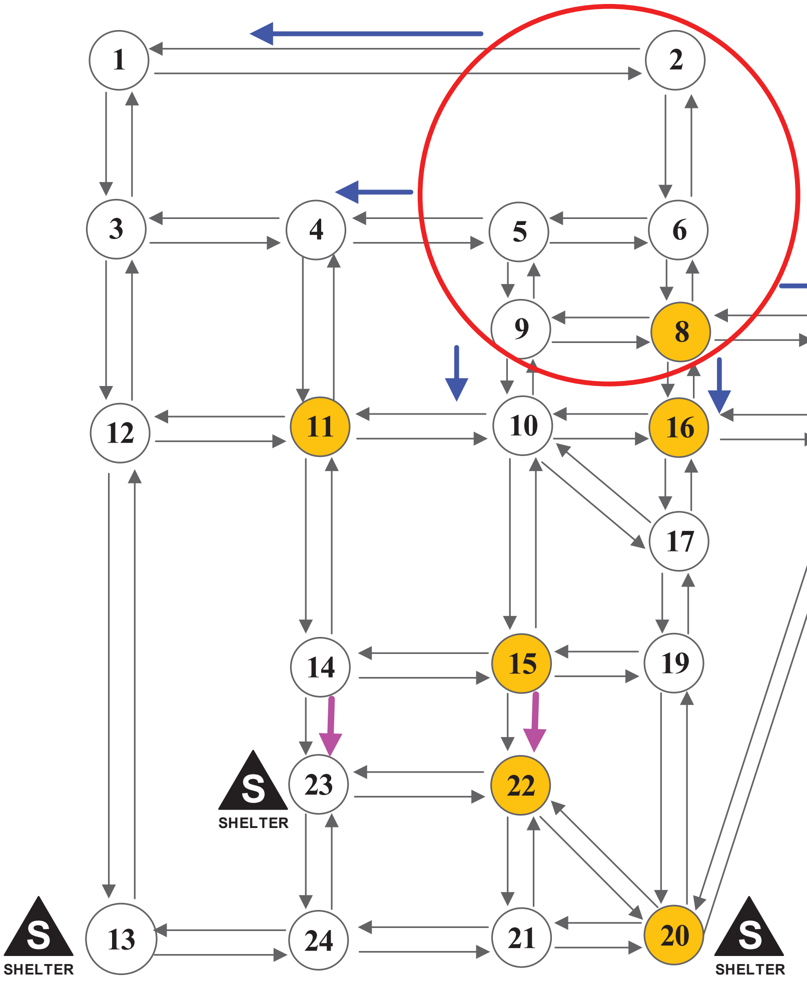

Figure 8.9: The reconfigured Sioux-Falls network

Another interesting observation is that only the first system reconfiguration strategy is utilized in this example. Since the travel demand is relatively small compared to the link capacity (see Eq. (8.11) for details), the traffic flow that goes through the intersections is only a small amount. In other words, only slight traffic congestion occurs. To enhance the

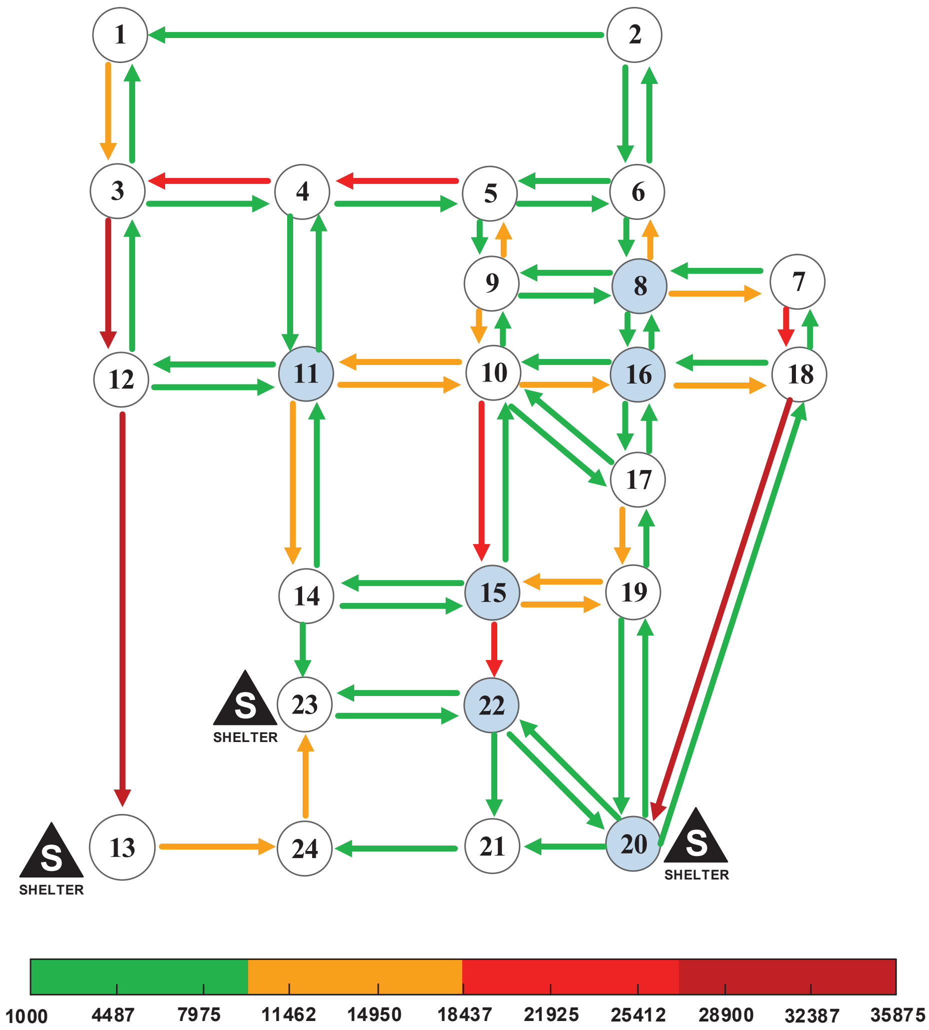

Figure 8.10: The link flow distribution of the best system reconfiguration in the Sioux-Falls network

importance of intersections in the network but without increasing the computational workload, we increase the waiting time for each vehicle going through the intersection that is not blocked from 2 to 20. In this case, the reconfigured traffic system found by the proposed method is illustrated in Fig. 8.11. In this case, both system reconfiguration strategies are used. Specifically, two intersections (intersection 8 and 22) are blocked due to the increase of waiting time: with respect to intersection 8, links connecting node 8 and node 9, node 8 to node 16, are blocked although there is a small amount of traffic demand from node 8 to node 16, and such traffic demand can be satisfied using other alternate routes; regarding intersection 22, the roadways that connect node 22 with node 20 and 21 are blocked. With respect to contraflow, the direction of three links, including 15 → 10, 11 → 12, and 20 → 18, are reversed. By implementing the above system reconfiguration, the travel time of all the network users has been reduced from 10948173 to 8266862. The significant reduction (24%) in the total travel time explicitly demonstrates that system reconfiguration is an effective strategy in improving the system performance and increasing the system resilience.

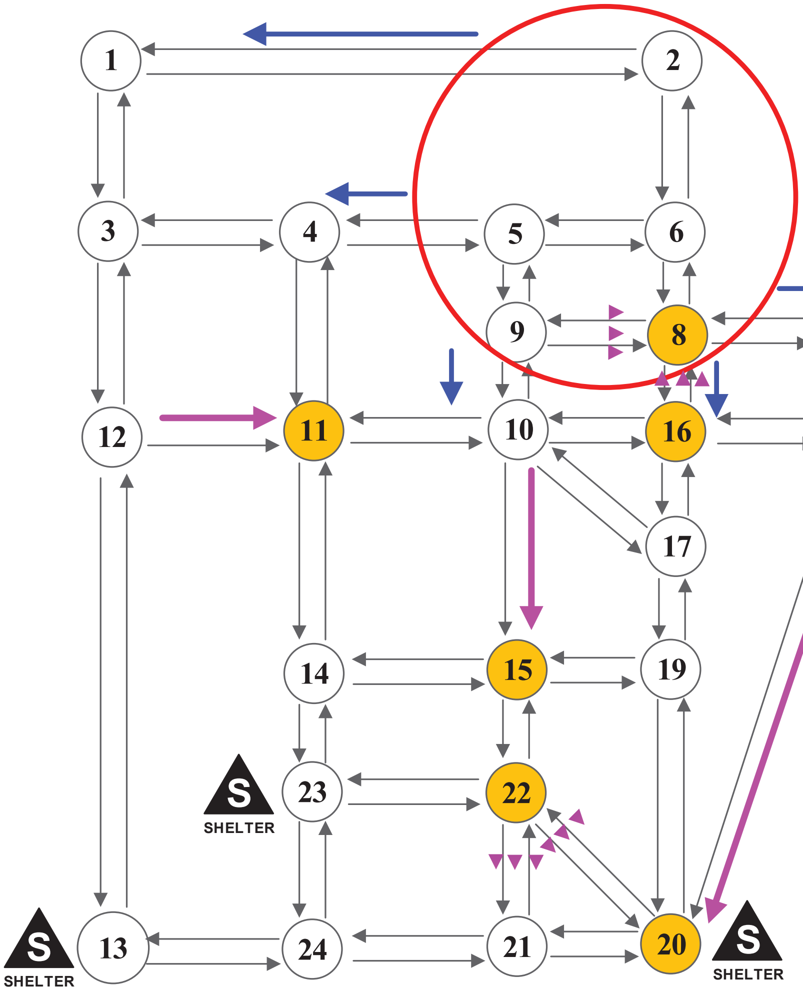

Figure 8.11: The reconfigured Sioux-Falls network when the waiting time increases from 2 to 20

8.3.2 Example 2

Fig. 8.12 shows a network with 25 nodes and 40 two-way links. All the two-way links have symmetric link capacity and travel time, which are indicated by the two numbers along each link. Each node is labeled by the number within the circle. As can be noticed, there are nine intersections in this network, and they distribute at the center of the traffic system to connect the nodes at the top and bottom layers. With respect to the links in the network, they are in two different categories: freeways indicated by the bold links have a free-flow speed of 55 mph and a practical capacity of 200 vehicles, and other links have a free-flow speed of 20 mph and a capacity of 300 vehicles.

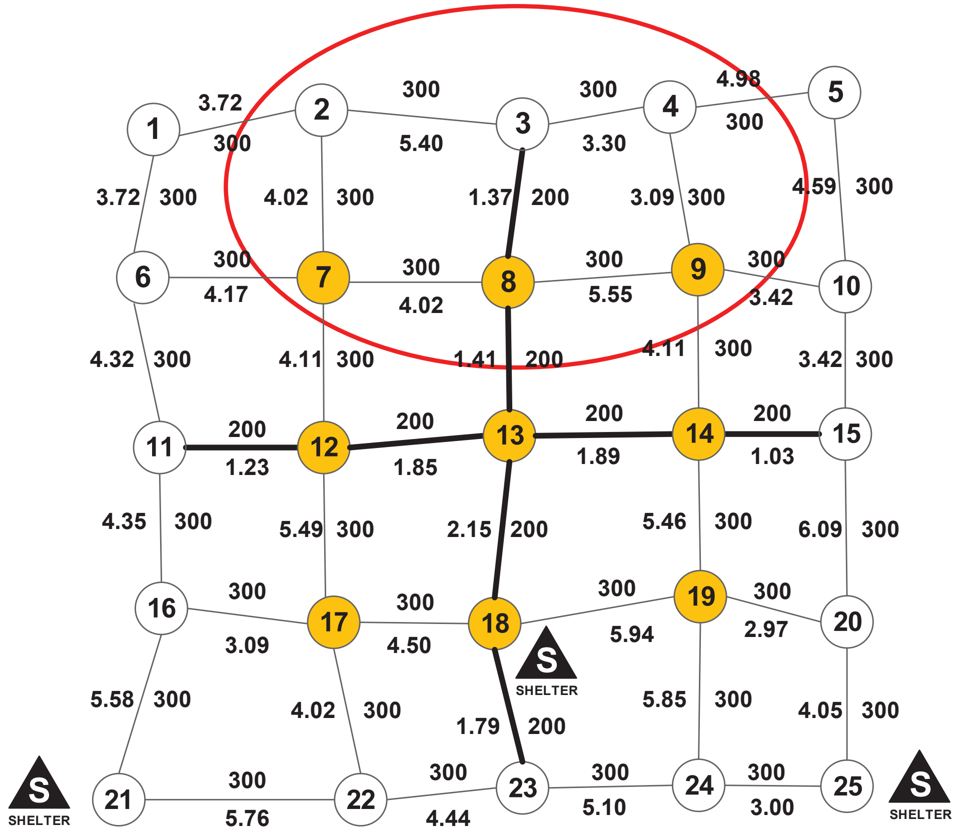

Figure 8.12: Test network 2: a 25-node artificial net

Suppose the area within the red ellipse is going to be hit by a catastrophic disaster, and all the residents need to be evacuated away from this area. Three evacuation shelter centers have been set up in three different locations across the network. All the residents within the disaster-impacted region will be evacuated to the three shelters. Similar to the last example, we assume that the travel demand from the disaster-impacted zones to the three shelters are the same, and they are given as below:

$$\begin{aligned}
&d^{2,18} = 800,\ d^{2,21} = 800,\ d^{2,25} = 800,\\
&d^{3,18} = 650,\ d^{3,21} = 650,\ d^{3,25} = 650,\\
&d^{4,18} = 780,\ d^{4,21} = 780,\ d^{4,25} = 780,\\
&d^{7,18} = 560,\ d^{7,21} = 560,\ d^{7,25} = 560,\\
&d^{8,18} = 420,\ d^{8,21} = 420,\ d^{8,25} = 420,\\
&d^{9,18} = 600,\ d^{9,21} = 600,\ d^{9,25} = 600.
\end{aligned} \tag{8.13}$$

From the travel demand shown in Eq. (8.13), it can be observed that node 2 has the highest travel demand to the three shelters, followed by node 4 and node 3. In addition to that, the traffic demand of the regular commuters among other nodes outside of the disaster-impacted zone are also taken into consideration, which are indicated as below:

$$\begin{aligned}
&d^{1,10} = 70,\ d^{1,15} = 60,\ d^{1,19} = 50,\\
&d^{6,16} = 120,\ d^{6,19} = 60,\ d^{6,25} = 70,\\
&d^{11,15} = 100,\ d^{11,20} = 80,\ d^{11,23} = 90,\\
&d^{15,12} = 50,\ d^{15,17} = 80,\ d^{15,24} = 110,\\
&d^{16,20} = 100,\ d^{16,23} = 80.
\end{aligned} \tag{8.14}$$

Considering the above travel demand, the proposed method is leveraged to reconfigure the traffic system in such a way that the total travel time for all the network users is minimized. Fig. 8.13 shows the convergence process of the total travel time. It can be seen that the total travel time converges to a stable value within five iterations. The best system reconfiguration found by the probabilistic solution discovery algorithm is illustrated in Fig. 8.14. The direction of six links are reversed, and they are 6 → 7, 11 → 6, 7 → 8, 14 → 9, 18 → 13, and 19 → 14. In other words, there are six one-way links in the reconfigured

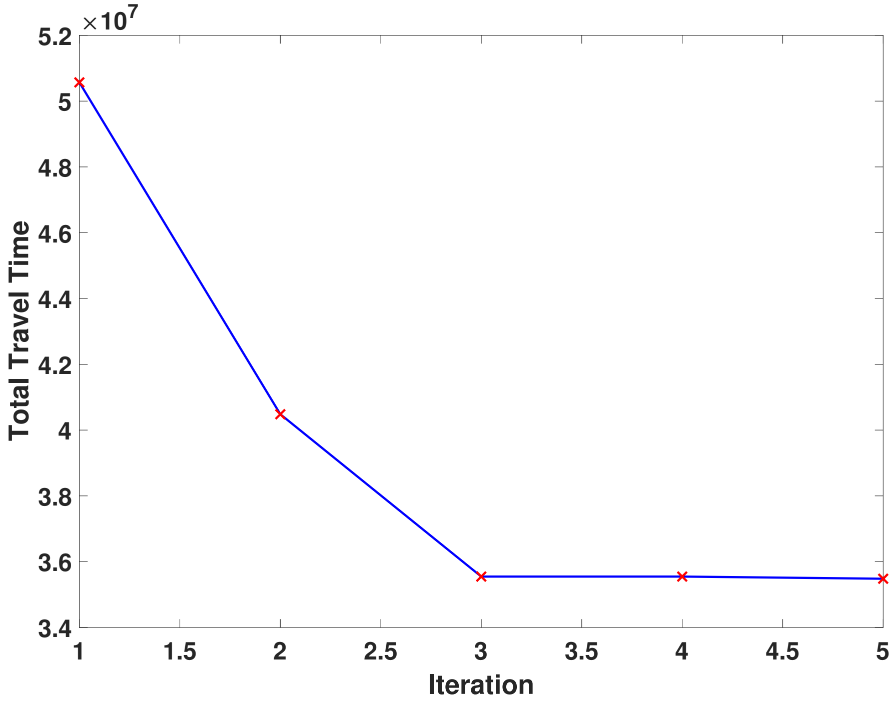

Figure 8.13: The convergence process of total travel time in the 25-node network

network, and they are highlighted in red color in Fig. 8.14. Two intersections: intersection 9 and 14 are blocked. By reconfiguring the traffic system to adapt to the abrupt increased traffic demand, the total travel time has been reduced from 91194781 to 35481005.

If we reduce the travel demand between the nodes within the red eclipse and other nodes to the normal level as shown in Eq. (8.16), then the total travel time for all the users is 172277. Considering the total travel time in the regular case, it can be noticed that the total travel time reduces by 61% after the network reconfiguration action is taken. Similarly, the system resilience is computed as:

$$\mathscr{R}\left(t_f\right) = 1 - \frac{35481005 - 172277}{91194781 - 172277} = 0.61. \tag{8.15}$$

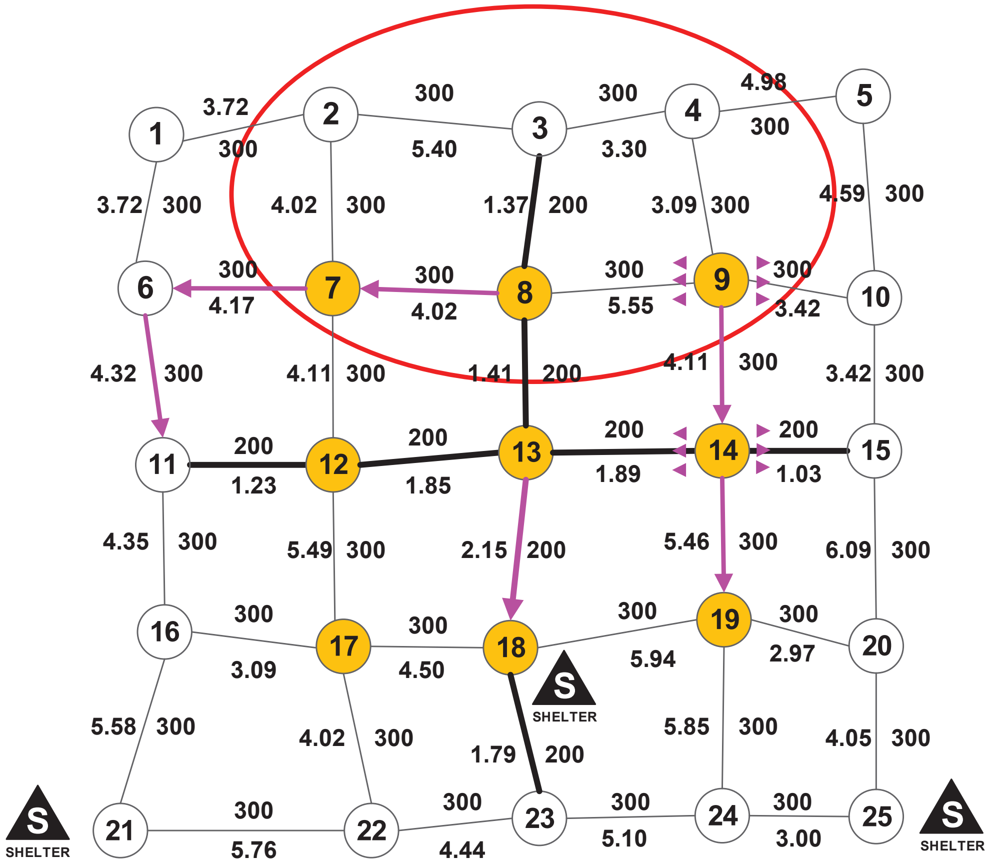

Figure 8.14: The reconfigured 25-node network

$$
\begin{aligned}
&d^{2,18} = 100,\ d^{2,21} = 100,\ d^{2,25} = 100,\\
&d^{3,18} = 150,\ d^{3,21} = 150,\ d^{3,25} = 150,\\
&d^{4,18} = 180,\ d^{4,21} = 180,\ d^{4,25} = 180,\\
&d^{7,18} = 160,\ d^{7,21} = 160,\ d^{7,25} = 160,\\
&d^{8,18} = 120,\ d^{8,21} = 120,\ d^{8,25} = 120,\\
&d^{9,18} = 100,\ d^{9,21} = 100,\ d^{9,25} = 100.
\end{aligned}
\tag{8.16}
$$

As can be observed, the system resilience is 0.61 after the system reconfiguration action is taken, which results in a significant 61% reduction in the total travel time. Thus, system reconfiguration is shown to be effective in mitigating the system-wide congestion and restoring the transportation system performance in the presence of extreme events.

8.4 Summary

In this chapter, we consider the travel demand arising from emergency evacuations out of the disaster-impacted zones. To mitigate the system-wide traffic congestion, we leverage two system reconfiguration strategies, namely lane reversal and crossing elimination at intersections, and develop an integrated approach to increase the system resilience. The objective of the proposed approach is to minimize the total travel time for both the regular commuters and emergent evacuees. The issue investigated in this chapter is formulated as a bi-level optimization problem, in which the lower level problem is modeled as user equilibrium traffic assignment, and decision maker's system-level traffic network reconfiguration decisions are characterized as discrete variables in the upper level problem. A gradient projection method is utilized to approach the traffic assignment at the user equilibria, and a probabilistic solution discovery algorithm is developed to identify the best system reconfiguration in terms of contraflow and blocking roadways at each intersection so that the total travel time of all the users is minimized. Two numerical examples have demonstrated that the developed method reduces the total travel time and restores the traffic system performance significantly.

The proposed approach and the numerical examples provide significant managerial insights on the implementation of simple yet effective operations in mitigating the severe system-wide congestion triggered by extreme events. The bi-level optimization enables managers to make timely and rational system reconfiguration decisions by accounting for the complex user driving behavior. More importantly, from a practical standpoint, the implementation of system reconfiguration does not consume a lot of resources, which significantly enhances the operational flexibility of managers and the system's quick responsiveness to a variety of emergency situations.

The reconfiguration strategy developed in this chapter has great potential to be applied into many other systems for the purpose of increasing their resilience. By optimally reconfiguring the system components and topology properly, different reconfiguration options and operation paradigms become readily available. By doing this, the system is equipped with the capability to respond to different disruptive scenarios that impair different system components. The flexibility enabled by system reconfiguration together with the relatively less investment that is needed to achieve the reconfiguration make it a promising solution to improve system resilience.

Chapter 9

Summary and Future Work

9.1 Summary of Accomplishments

The overall objective of this dissertation is to develop comprehensive machine learning and optimization models to assess and enhance the resilience of engineering systems. Towards this end, we have investigated a series of assessment, prevention, and restoration methodologies that can be taken before, during, and after the occurrence of hazardous events. This target is approached by leveraging state-of-the-art machine learning algorithms to build data-driven predictive models as well as effective sampling-based optimization algorithms to approach challenging discrete bi-level optimization problems. The measures taken to enhance system resilience in this dissertation can be broadly classified into three categories: 1. construction of predictive models to increase the operators' situation awareness on the dynamic evolution of hazardous events; 2. assessment of the effectiveness of human and algorithmic responses in handling off-nominal events; 3. utilization of optimization algorithms to enable resilience in new and legacy systems. The three sets of strategies investigated in this dissertation form a closed loop for enhancing system resilience in terms of the actions that can be taken before, during, and after the occurrence of anomalous events. With respect to each objective, the specific accomplishments and innovations made in this dissertation are summarized below.

Deep Learning Models for Early Warning of the Occurrences of Hazardous Events: In Chapter 3, an innovative methodology is developed for making long-term prediction on system behavior with high accuracy, and three critical issues are addressed in this study: (1) an efficient big data engine Apache Spark is leveraged to parse a large volume of raw data with scalable performance; (2) two deep learning models are trained to make predictions on system behavior from different views, in which Monte Carlo dropout is used to characterize model prediction uncertainty following a Bayesian approach; (3) the two models are integrated together via a discrepancy term, thereby retaining both long-term prediction capability and high prediction accuracy; (4) the integrated model is expanded to make predictions on multiple system components, and a probabilistic safety metric is defined to measure system safety. A highlight is that we characterize the uncertainty in the prediction made by the trained deep learning models. The inclusion of model prediction uncertainty not only improves the model prediction accuracy, but also significantly increases the confidence of relevant stakeholders in decision making.

Ensemble Machine Learning Models for Risk Prediction on the Consequence of Anomalous Events In Chapter 4, two conventional machine learning algorithms are used to predict the severity of the consequence associated with anomalous events in terms of their risk levels. The major innovation in this chapter is the development of a probabilistic fusion rule to determine which model prediction outcome to count on when their predictions disagree. The proposed probabilistic fusion rule considers three levels of information: record-level prediction confidence, class-level prediction accuracy, and the proportion of each class in the set of records with disagreeing predictions. By doing this, the misclassification information is further utilized to correct model predictions on the subsequent unseen test dataset. The fusion rule accounts for the various types of misclassifications that the trained model is prone to make, thereby increasing the probability of labeling the observation as the target class.

Human Reliability Analysis in Diagnosing and Correcting System Malfunctions: In Chapter 5, an information fusion methodology is developed to assess the human performance in eliminating off-nominal events. We fuse heterogeneous data with an ensemble of support vector machine-based learning models. Despite the limited amount of data, the trained model demonstrates a promising performance in predicting crew performance prediction. This ensemble model of the full heterogeneous dataset is superior to SVM models built with any subset of the heterogeneous data, and substantially better than simple correlation between performance outcome and any individual input features. The development of such an ensemble model helps to quantitatively measure the reliability in the operators' response to system malfunction events.

Performance Assessment of Algorithmic Response to Hazardous Events: In Chapter 6, we evaluate the effectiveness of an algorithmic response in dealing with anomalous event. The first crucial contribution made along this front is to construct a dynamic simulation model to characterize the complex interactions among system components, and incorporate the uncertainties arising at different stages. The dynamic simulation model facilitates the quantitative evaluation of the effectiveness of algorithmic response in mitigating the impact of airport closure caused by extreme event. The second important contribution is to develop a support vector regression-based surrogate model to handle both precise and right-censored data. The development of SVR-based surrogate model facilitates fast evaluation of the performance of algorithmic response at different configurations, thus supporting real-time decision-making.

Design Optimization for Resilience: In Chapter 7, we develop a resilience-based framework to optimize the configuration of an infrastructure system. The significant contribution made in this chapter is to account for multiple factors (i.e., travel time, waiting time, service time) in the objective function. To tackle this challenging bi-level optimization problem, a multi-level cross entropy method is leveraged to generate a family of probability distributions with probability mass gradually converging to the proximity of the optimal state, which is the second major contribution made in this chapter.

System Reconfiguration to Increase System Resilience: In Chapter 8, we address an optimization problem for reconfiguring transportation system for the sake of mitigating the traffic congestion caused by the large volume evacuation out of disaster-prone areas. The innovation in this chapter is to investigate multiple implementable and economically achievable operations to deal with different evacuation scenarios in a timely manner. Mathematical models are developed to represent system reconfiguration schemes and characterize the interactions between traffic operators and passengers. A probabilistic solution discovery algorithm is used to obtain the near-optimal solution. The proposed method offers insights for staging efficient evacuations with the reconfiguration of system typologies, and equips the transportation system with the ability to respond to different emergency scenarios quickly.

9.2 Future Work

Several areas that are worthy of further investigation are identified in this section.

For the flight trajectory prediction in Chapter 3, future work needs to develop visualization of safety assessment at the sector or national level. The visualization will greatly help operators pinpoint the position with the highest safety risk in a timely manner, thereby improving operators and controller's performance in maintaining the system safety dramatically. Another direction to move towards is to incorporate the probabilistic forecast on weather conditions into the deep learning models so as to characterize the effect of weather on flight trajectory.

With respect to the ensemble machine learning for prediction on the consequence of hazardous events in Chapter 4, if the actions taken by the pilot or other operators involved in the response to abnormal events are available, it will be useful to extend the developed hybrid model to account for such important information. The inclusion of such information helps us to identify risk mitigation actions for unforeseen events in the future by learning from the actions that have been taken in past.

For the reliability assessment of crew performance in Chapter 5, future work needs to extend the proposed method to include the plant states (i.e., process parameters in the simulator logs) for quantifying the consequences of operator actions and thus their performance. In addition, other relevant physiological indicators, such as electroencephalogram, electrocardiogram and pupillometry, can be collected for modeling to increase prediction accuracy as wearable sensors are improving in capabilities rate, battery life), comfort (i.e., size) and cost.

Regarding the performance assessment of response strategy in Chapter 6, further work is needed w.r.t. data mining techniques to construct more realistic distributions to characterize the uncertainty related to each system component. Secondly, the reliability estimation carried out in this chapter can be investigated towards reliability-based optimization of the system variables (e.g., airport capacity and message delay) in order to improve the system performance. Thirdly, we model gate capacity as a hard constraint, while planes can stop on the tarmac and be unloaded by stairway, thus it is more reasonable to model gate capacity as a soft constraint in reality. Another future direction worthy of investigation is to adapt the dynamic simulation to a more realistic situation with a higher density of radars that cover the entire region.

With respect to the resilience-driven optimization framework for logistics service centers in Chapter 7, future work needs to investigate the combined effect of multiple individual events as well as the cascading effect of an individual disruptive event in a complex engineering system. Future work can explore the implementation of the cross entropy method in high-performance computing platforms (i.e., MapReduce, Spark) in order to accelerate the computational speed for large-scale optimization. Finally, the planned distribution of service centers investigated in Chapter 7 avoids any locations that could be impacted by the unexpected extreme event, it will be worthy to investigate the case where some service center locations that could be affected are actually used.

For system reconfiguration in transportation system presented in Chapter 8, future work can increase the robustness of the system reconfiguration strategy by accommodating travel demand uncertainty. In addition, it will be helpful to investigate how the system resilience varies if the extreme event hits different locations in the transportation system. Additional traffic system control and optimization strategies (e.g., traffic flow control, ramp metering, and intelligent traffic signal) can be integrated into the framework proposed in this chapter, thereby enhancing the system reconfiguration capability and the flexibility of the system in response to different disruptive events.

The proposed strategies for response effectiveness assessment and resilience optimization in this dissertation need to be investigated and validated for large-scale infrastructure systems. One challenge arising during this process is how to resolve the large-scale optimization problems. Effective approximation optimization algorithms need to be developed to solve the formulated complex optimization problems, so that provide decision makers can respond to extreme events in a timely manner. Last but not the least, most of optimization models developed in this dissertation are deterministic. The aleatory and epistemic uncertainties arising at various stages need to be represented appropriately and included in the optimization model, thereby increasing the robustness of the optimization model.

9.3 Concluding Remarks

This dissertation focused on the investigation of measures to assess and strategies to increase the resilience of engineering systems by leveraging state-of-the-art machine learning and optimization algorithms. The proposed methodologies address several significant challenges in system resilience assessment and enhancement, and make the following contributions: (1) multiple predictive models are developed to build ensemble machine learning models, which increase the operators' situation awareness and understanding on the evolution trajectory of hazardous events, such as when the anomalous event is about to occur, and what is the consequence of an anomalous event; (2) we evaluate the response effectiveness of both human and algorithmic responses in withstanding the impact of extreme event, such as the performance of a crew in diagnosing and correcting system malfunctions, and the adopted rerouting strategy in handling inbound flights when the destination airport shuts down abruptly; (3) optimization algorithms are leveraged to achieve or improve system resilience through the design of a new system or reconfiguration of an existing system. The resilience embedded into the system together with the modeling of interactions among different players and components allows the system to restore from disruptive scenarios to normal performance in a timely manner.

The machine learning and optimization models will be of high value to decision makers. One the one hand, the predictive models significantly increase the decision maker's understanding and situation awareness regarding the system's evolution trajectory and the effect of various response actions on system performance. On the other hand, the implementation of optimization algorithms helps the system to restore closer to its original performance following the disruptive event. All of these new developments help to improve the system resilience against unanticipated events, thereby showing significant potential for practical application.

BIBLIOGRAPHY

[1] Ralph B D'Agostino. *Goodness-of-fit-techniques*, volume 68. CRC press, 1986.

[2] Devanandham Henry and Jose Emmanuel Ramirez-Marquez. Generic metrics and quantitative approaches for system resilience as a function of time. *Reliability Engineering & System Safety*, 99:114–122, 2012.

[3] Vivienne Sze, Yu-Hsin Chen, Tien-Ju Yang, and Joel S Emer. Efficient processing of deep neural networks: A tutorial and survey. *Proceedings of the IEEE*, 105(12): 2295–2329, 2017.

[4] Salman Salloum, Ruslan Dautov, Xiaojun Chen, Patrick Xiaogang Peng, and Joshua Zhexue Huang. Big data analytics on Apache Spark. *International Journal of Data Science and Analytics*, 1(3-4):145–164, 2016.

[5] Marvin Rausand and Arnljot Høyland. *System reliability theory: models, statistical methods, and applications*, volume 396. John Wiley & Sons, 2004.

[6] Xiaoge Zhang, Sankaran Mahadevan, and Xinyang Deng. Reliability analysis with linguistic data: An evidential network approach. *Reliability Engineering & System Safety*, 162:111–121, 2017.

[7] Xiaoge Zhang and Sankaran Mahadevan. A game theoretic approach to network reliability assessment. *IEEE Transactions on Reliability*, 66(3):875–892, 2017.

[8] Crawford S Holling. Resilience and stability of ecological systems. *Annual Review of Ecology and Systematics*, 4(1):1–23, 1973.

[9] Mayada Omer, Roshanak Nilchiani, and Ali Mostashari. Measuring the resilience of the trans-oceanic telecommunication cable system. *IEEE Systems Journal*, 3(3): 295–303, 2009.

[10] Hiba Baroud, Jose E Ramirez-Marquez, Kash Barker, and Claudio M Rocco. Stochastic measures of network resilience: Applications to waterway commodity flows. *Risk Analysis*, 34(7):1317–1335, 2014.

[11] Mathaios Panteli and Pierluigi Mancarella. Modeling and evaluating the resilience of critical electrical power infrastructure to extreme weather events. *IEEE Systems Journal*, 11(3):1733–1742, 2015.

[12] Lijuan Shen, Beatrice Cassottana, and Loon Ching Tang. Statistical trend tests for resilience of power systems. *Reliability Engineering & System Safety*, 177:138–147, 2018.

[13] Xiaoge Zhang, Zili Zhang, Yajuan Zhang, Daijun Wei, and Yong Deng. Route selection for emergency logistics management: A bio-inspired algorithm. *Safety Science*, 54:87–91, 2013.

[14] Yacov Y Haimes, Kenneth Crowther, and Barry M Horowitz. Homeland security preparedness: Balancing protection with resilience in emergent systems. *Systems Engineering*, 11(4):287–308, 2008.

[15] Zhen Hu and Sankaran Mahadevan. Resilience assessment based on time-dependent system reliability analysis. *Journal of Mechanical Design*, 138(11):111404, 2016.

[16] Michel Bruneau, Stephanie E Chang, Ronald T Eguchi, George C Lee, Thomas D ORourke, Andrei M Reinhorn, Masanobu Shinozuka, Kathleen Tierney, William A Wallace, and Detlof Von Winterfeldt. A framework to quantitatively assess and enhance the seismic resilience of communities. *Earthquake Spectra*, 19(4):733–752, 2003.

[17] Hiba Baroud, Kash Barker, Jose E Ramirez-Marquez, et al. Importance measures for inland waterway network resilience. *Transportation Research Part E: Logistics and Transportation Review*, 62:55–67, 2014.

[18] Hossein Fotouhi, Seksun Moryadee, and Elise Miller-Hooks. Quantifying the resilience of an urban traffic-electric power coupled system. *Reliability Engineering & System Safety*, 163:79–94, 2017.

[19] Seyedmohsen Hosseini, Kash Barker, and Jose E Ramirez-Marquez. A review of definitions and measures of system resilience. *Reliability Engineering & System Safety*, 145:47–61, 2016.

[20] Kash Barker, Jose Emmanuel Ramirez-Marquez, and Claudio M Rocco. Resilience-based network component importance measures. *Reliability Engineering & System Safety*, 117:89–97, 2013.

[21] Xiaoge Zhang, Sankaran Mahadevan, Shankar Sankararaman, and Kai Goebel. Resilience-based network design under uncertainty. *Reliability Engineering & System Safety*, 169:364–379, 2018.

[22] Rahul Nair, Hakob Avetisyan, and Elise Miller-Hooks. Resilience framework for ports and other intermodal components. *Transportation Research Record: Journal of the Transportation Research Board*, (2166):54–65, 2010.

[23] Vladimir Vapnik. *The nature of statistical learning theory*. Springer Science & Business Media, 2013.

[24] Zhiquan Qi, Yingjie Tian, and Yong Shi. Robust twin support vector machine for pattern classification. *Pattern Recognition*, 46(1):305–316, 2013.

[25] Xiang-Yang Wang, Ting Wang, and Juan Bu. Color image segmentation using pixel wise support vector machine classification. *Pattern Recognition*, 44(4):777–787, 2011.

[26] Chia-Feng Juang and Guo-Cyuan Chen. A TS fuzzy system learned through a sup-

port vector machine in principal component space for real-time object detection. *IEEE Transactions on Industrial Electronics*, 59(8):3309–3320, 2012.

[27] Xiaoge Zhang and Sankaran Mahadevan. Aircraft re-routing optimization and performance assessment under uncertainty. *Decision Support Systems*, 96:67–82, 2017.

[28] Chi-Jie Lu, Tian-Shyug Lee, and Chih-Chou Chiu. Financial time series forecasting using independent component analysis and support vector regression. *Decision Support Systems*, 47(2):115–125, 2009.

[29] Chun-Hsin Wu, Jan-Ming Ho, and Der-Tsai Lee. Travel-time prediction with support vector regression. *IEEE Transactions on Intelligent Transportation Systems*, 5 (4):276–281, 2004.

[30] Yann LeCun, Yoshua Bengio, and Geoffrey Hinton. Deep learning. *Nature*, 521 (7553):436–444, 2015.

[31] Jürgen Schmidhuber. Deep learning in neural networks: An overview. *Neural Networks*, 61:85–117, 2015.

[32] Sepp Hochreiter and Jürgen Schmidhuber. Long short-term memory. *Neural Computation*, 9(8):1735–1780, 1997.

[33] Radford M Neal. *Bayesian learning for neural networks*, volume 118. Springer Science & Business Media, 2012.

[34] Yarin Gal and Zoubin Ghahramani. Dropout as a bayesian approximation: Representing model uncertainty in deep learning. In *International Conference on Machine Learning*, pages 1050–1059, 2016.

[35] Yarin Gal and Zoubin Ghahramani. A theoretically grounded application of dropout in recurrent neural networks. In *Advances in Neural Information Processing Systems*, pages 1019–1027, 2016.

[36] Yarin Gal. *Uncertainty in deep learning*. PhD thesis, PhD thesis, University of Cambridge, 2016.

[37] Andreas Damianou and Neil Lawrence. Deep Gaussian processes. In *Artificial Intelligence and Statistics*, pages 207–215, 2013.

[38] Heinrich Von Stackelberg. *Market structure and equilibrium*. Springer Science & Business Media, 2010.

[39] John Glen Wardrop. Some theoretical aspects of road traffic research. *Proceedings of the Institution of Civil Engineers*, 1(3):325–362, 1952.

[40] John D Murchland. Braess's paradox of traffic flow. *Transportation Research*, 4(4): 391–394, 1970.

[41] Richard Steinberg and Willard I Zangwill. The prevalence of braess' paradox. *Transportation Science*, 17(3):301–318, 1983.

[42] Armen Der Kiureghian and Ove Ditlevsen. Aleatory or epistemic? does it matter? *Structural Safety*, 31(2):105–112, 2009.

[43] Saideep Nannapaneni and Sankaran Mahadevan. Reliability analysis under epistemic uncertainty. *Reliability Engineering & System Safety*, 155:9–20, 2016.

[44] Kyle Neal, Zhen Hu, Sankaran Mahadevan, and Jon Zumberge. Discrepancy prediction in dynamical system models under untested input histories. *Journal of Computational and Nonlinear Dynamics*, 14(2):021009, 2019.

[45] Glenn Shafer. *A mathematical theory of evidence*, volume 42. Princeton university press, 1976.

[46] Lotfi A Zadeh. Fuzzy sets. *Information and control*, 8(3):338–353, 1965.

[47] Xiaoge Zhang, Yong Deng, Felix TS Chan, Peida Xu, Sankaran Mahadevan, and Yong Hu. IFSJSP: a novel methodology for the job-shop scheduling problem based on intuitionistic fuzzy sets. *International Journal of Production Research*, 51(17): 5100–5119, 2013.

[48] Didier Dubois and Henri Prade. *Possibility theory*. Springer, 2012.

[49] Andrea Saltelli, Marco Ratto, Terry Andres, Francesca Campolongo, Jessica Cariboni, Debora Gatelli, Michaela Saisana, and Stefano Tarantola. *Global sensitivity analysis: the primer*. John Wiley & Sons, 2008.

[50] Bruno Sudret. Global sensitivity analysis using polynomial chaos expansions. *Reliability Engineering & System Safety*, 93(7):964–979, 2008.

[51] Pan Wang, Zhenzhou Lu, and Zhangchun Tang. An application of the Kriging method in global sensitivity analysis with parameter uncertainty. *Applied Mathematical Modelling*, 37(9):6543–6555, 2013.

[52] Biagio Ciuffo, Jordi Casas, Marcello Montanino, Josep Perarnau, and Vincenzo Punzo. Gaussian process metamodels for sensitivity analysis of traffic simulation models: Case study of AIMSUN mesoscopic model. *Transportation Research Record*, 2390(1):87–98, 2013.

[53] Søren Nymand Lophaven, Hans Bruun Nielsen, and Jacob Søndergaard. Dace-A Matlab Kriging toolbox, version 2.0. 2002.

[54] Stefano Tarantola, Debora Gatelli, and Thierry Alex Mara. Random balance designs for the estimation of first order global sensitivity indices. *Reliability Engineering & System Safety*, 91(6):717–727, 2006.

[55] Andrea Saltelli and Ricardo Bolado. An alternative way to compute Fourier am-

plitude sensitivity test (FAST). *Computational Statistics & Data Analysis*, 26(4): 445–460, 1998.

[56] Gregory J McRae, James W Tilden, and John H Seinfeld. Global sensitivity analysisa computational implementation of the Fourier amplitude sensitivity test (FAST). *Computers & Chemical Engineering*, 6(1):15–25, 1982.

[57] Sergei Kucherenko, Balazs Feil, Nilay Shah, and Wolfgang Mauntz. The identification of model effective dimensions using global sensitivity analysis. *Reliability Engineering & System Safety*, 96(4):440–449, 2011.

[58] J-Y Tissot and Clémentine Prieur. A randomized orthogonal array-based procedure for the estimation of first-and second-order Sobol'indices. *Journal of Statistical Computation and Simulation*, 85(7):1358–1381, 2015.

[59] Clémentine Prieur and Stefano Tarantola. Variance-based sensitivity analysis: Theory and estimation algorithms. *Handbook of Uncertainty Quantification*, pages 1217–1239, 2017.

[60] Michael Armbrust, Reynold S Xin, Cheng Lian, Yin Huai, Davies Liu, Joseph K Bradley, Xiangrui Meng, Tomer Kaftan, Michael J Franklin, Ali Ghodsi, et al. Spark SQL: Relational data processing in Spark. In *Proceedings of the 2015 ACM SIGMOD International Conference on Management of Data*, pages 1383–1394. ACM, 2015.

[61] Joseph E Gonzalez, Reynold S Xin, Ankur Dave, Daniel Crankshaw, Michael J Franklin, and Ion Stoica. GraphX: Graph processing in a distributed dataflow framework. In *11th USENIX Symposium on Operating Systems Design and Implementation (OSDI 14)*, pages 599–613, 2014.

[62] Matei Zaharia, Tathagata Das, Haoyuan Li, Timothy Hunter, Scott Shenker, and Ion Stoica. Discretized streams: Fault-tolerant streaming computation at scale. In *Pro-*

ceedings of the Twenty-fourth ACM Symposium on Operating Systems Principles, pages 423–438. ACM, 2013.

[63] Xiangrui Meng, Joseph Bradley, Burak Yavuz, Evan Sparks, Shivaram Venkataraman, Davies Liu, Jeremy Freeman, DB Tsai, Manish Amde, Sean Owen, et al. Mllib: Machine learning in Apache Spark. *The Journal of Machine Learning Research*, 17 (1):1235–1241, 2016.

[64] Joseph E Gonzalez. From graphs to tables the design of scalable systems for graph analytics. In *Proceedings of the 23rd International Conference on World Wide Web*, pages 1149–1150. ACM, 2014.

[65] Xiaoge Zhang and Sankaran Mahadevan. Bayesian neural networks for flight trajectory prediction and safety assessment. *Decision Support Systems*, Under Review, 2019.

[66] IATA forecasts passenger demand to double over 20 years. http://www.iata.org/pressroom/pr/Pages/2016-10-18-02.aspx, Accessed: 2017-12-28.

[67] EU ROCONTROL. European organisation for the safety of air navigation. 1997.

[68] Shankar Sankararaman, Indranil Roychoudhury, Xiaoge Zhang, and Kai Goebel. Preliminary investigation of impact of technological impairment on trajectory-based operation. In *17th AIAA Aviation Technology, Integration, and Operations Conference*, page 4488, 2017.

[69] Xiaoge Zhang and Sankaran Mahadevan. Ensemble machine learning models for aviation incident risk prediction. *Decision Support Systems*, 116:48–63, 2019.

[70] Federal Aviation Administration, U.S. Department of Transportation. The future of the nas, June 2016. https://www.faa.gov/nextgen/media/futureofthenas.pdf.

[71] Javier Lovera Yepes, Inseok Hwang, and Mario Rotea. New algorithms for aircraft intent inference and trajectory prediction. *Journal of Guidance, Control, and Dynamics*, 30(2):370–382, 2007.

[72] Xavier Prats, Vicenç Puig, Joseba Quevedo, and Fatiha Nejjari. Multi-objective optimisation for aircraft departure trajectories minimising noise annoyance. *Transportation Research Part C: Emerging Technologies*, 18(6):975–989, 2010.

[73] Arjen de Leege, Marinus van Paassen, and Max Mulder. A machine learning approach to trajectory prediction. In *AIAA Guidance, Navigation, and Control (GNC) Conference*, page 4782, 2013.

[74] Chester Gong and Dave McNally. A methodology for automated trajectory prediction analysis. In *AIAA Guidance, Navigation, and Control Conference and Exhibit*, page 4788, 2004.

[75] Antonio Franco, Damián Rivas, and Alfonso Valenzuela. Probabilistic aircraft trajectory prediction in cruise flight considering ensemble wind forecasts. *Aerospace Science and Technology*, 82:350–362, 2018.

[76] Matthew Daigle, Indranil Roychoudhury, Liljana Spirkovska, Kai Goebel, Shankar Sankararaman, John Ossenfort, and Chetan S Kulkarni. Real-time prediction of safety margins in the national airspace. In *17th AIAA Aviation Technology, Integration, and Operations Conference*, page 4388, 2017.

[77] Angela Nuic, Damir Poles, and Vincent Mouillet. BADA: An advanced aircraft performance model for present and future ATM systems. *International Journal of Adaptive Control and Signal Processing*, 24(10):850–866, 2010.

[78] Xiangmin Guan, Renli Lv, Liang Sun, and Yang Liu. A study of 4D trajectory prediction based on machine deep learning. In *2016 12th World Congress on Intelligent Control and Automation (WCICA)*, pages 24–27. IEEE, 2016.

[79] Samet Ayhan and Hanan Samet. Aircraft trajectory prediction made easy with predictive analytics. In *Proceedings of the 22nd ACM SIGKDD International Conference on Knowledge Discovery and Data Mining*, pages 21–30. ACM, 2016.

[80] Richard Alligier and David Gianazza. Learning aircraft operational factors to improve aircraft climb prediction: A large scale multi-airport study. *Transportation Research Part C: Emerging Technologies*, 96:72–95, 2018.

[81] Claudio Di Ciccio, Han Van der Aa, Cristina Cabanillas, Jan Mendling, and Johannes Prescher. Detecting flight trajectory anomalies and predicting diversions in freight transportation. *Decision Support Systems*, 88:1–17, 2016.

[82] Mohammad Assaad, Romuald Boné, and Hubert Cardot. A new boosting algorithm for improved time-series forecasting with recurrent neural networks. *Information Fusion*, 9(1):41–55, 2008.

[83] Florent Altché and Arnaud De La Fortelle. An LSTM network for highway trajectory prediction. In *2017 IEEE 20th International Conference on Intelligent Transportation Systems (ITSC)*, pages 353–359. IEEE, 2017.

[84] Zhiyuan Shi, Min Xu, Quan Pan, Bing Yan, and Haimin Zhang. LSTM-based flight trajectory prediction. In *International Joint Conference on Neural Networks*, 2018.

[85] Mina Moradi Kordmahalleh, Mohammad Gorji Sefidmazgi, and Abdollah Homaifar. A sparse recurrent neural network for trajectory prediction of Atlantic hurricanes. In *Proceedings of the Genetic and Evolutionary Computation Conference 2016*, pages 957–964. ACM, 2016.

[86] Alexandre Alahi, Kratarth Goel, Vignesh Ramanathan, Alexandre Robicquet, Li Fei-Fei, and Silvio Savarese. Social LSTM: Human trajectory prediction in crowded spaces. In *Proceedings of the IEEE Conference on Computer Vision and Pattern Recognition*, pages 961–971, 2016.

[87] Hao Wu, Ziyang Chen, Weiwei Sun, Baihua Zheng, and Wei Wang. Modeling trajectories with recurrent neural networks. In *Proceedings of the 26th International Joint Conference on Artificial Intelligence*, pages 3083–3090. AAAI Press, 2017.

[88] Zoubin Ghahramani. Probabilistic machine learning and artificial intelligence. *Nature*, 521(7553):452, 2015.

[89] Charles Blundell, Julien Cornebise, Koray Kavukcuoglu, and Daan Wierstra. Weight uncertainty in neural network. In *International Conference on Machine Learning*, pages 1613–1622, 2015.

[90] Yarin Gal and Zoubin Ghahramani. Bayesian convolutional neural networks with bernoulli approximate variational inference. *arXiv preprint arXiv:1506.02158*, 2015.

[91] Lingxue Zhu and Nikolay Laptev. Deep and confident prediction for time series at Uber. In *2017 IEEE International Conference on Data Mining Workshops (ICDMW)*, pages 103–110, 2017.

[92] Nikolay Laptev, Jason Yosinski, Li Erran Li, and Slawek Smyl. Time-series extreme event forecasting with neural networks at Uber. In *International Conference on Machine Learning*, number 34, pages 1–5, 2017.

[93] Alex Kendall and Roberto Cipolla. Modelling uncertainty in deep learning for camera relocalization. In *2016 IEEE International Conference on Robotics and Automation (ICRA)*, pages 4762–4769. IEEE, 2016.

[94] Matei Zaharia, Reynold S Xin, Patrick Wendell, Tathagata Das, Michael Armbrust, Ankur Dave, Xiangrui Meng, Josh Rosen, Shivaram Venkataraman, Michael J Franklin, et al. Apache Spark: A unified engine for big data processing. *Communications of the ACM*, 59(11):56–65, 2016.

[95] Marianela García Lozano, Jonah Schreiber, and Joel Brynielsson. Tracking geographical locations using a geo-aware topic model for analyzing social media data. *Decision Support Systems*, 99:18–29, 2017.

[96] Ahmad Usmani. System wide information management. In *2010 Integrated Communications Navigation and Surveillance Conference (ICNS)*, pages 1–17. IEEE, 2010.

[97] James G Shanahan and Laing Dai. Large scale distributed data science using Apache Spark. In *Proceedings of the 21th ACM SIGKDD International Conference on Knowledge Discovery and Data Mining*, pages 2323–2324. ACM, 2015.

[98] Spark-xml. https://github.com/databricks/spark-xml, Accessed: 2019-02-12.

[99] Haonan Yu, Jiang Wang, Zhiheng Huang, Yi Yang, and Wei Xu. Video paragraph captioning using hierarchical recurrent neural networks. In *Proceedings of the IEEE Conference on Computer Vision and Pattern Recognition*, pages 4584–4593, 2016.

[100] Alex Graves and Navdeep Jaitly. Towards end-to-end speech recognition with recurrent neural networks. In *International Conference on Machine Learning*, pages 1764–1772, 2014.

[101] Alex Graves, Abdel-rahman Mohamed, and Geoffrey Hinton. Speech recognition with deep recurrent neural networks. In *2013 IEEE International Conference on Acoustics, Speech and Signal Processing*, pages 6645–6649. IEEE, 2013.

[102] Shujie Liu, Nan Yang, Mu Li, and Ming Zhou. A recursive recurrent neural network for statistical machine translation. In *Proceedings of the 52nd Annual Meeting of the Association for Computational Linguistics*, volume 1, pages 1491–1500, 2014.

[103] Joerg Evermann, Jana-Rebecca Rehse, and Peter Fettke. Predicting process behaviour using deep learning. *Decision Support Systems*, 100:129–140, 2017.

[104] Ming Liang and Xiaolin Hu. Recurrent convolutional neural network for object recognition. In *Proceedings of the IEEE Conference on Computer Vision and Pattern Recognition*, pages 3367–3375, 2015.

[105] Bharat Singh, Tim K Marks, Michael Jones, Oncel Tuzel, and Ming Shao. A multi-stream bi-directional recurrent neural network for fine-grained action detection. In *Proceedings of the IEEE Conference on Computer Vision and Pattern Recognition*, pages 1961–1970, 2016.

[106] Lucio Flavio Vismari and João Batista Camargo Junior. A safety assessment methodology applied to CNS/ATM-based air traffic control system. *Reliability Engineering & System Safety*, 96(7):727–738, 2011.

[107] Fedja Netjasov and Milan Janic. A review of research on risk and safety modelling in civil aviation. *Journal of Air Transport Management*, 14(4):213–220, 2008.

[108] ALC Roelen, R Wever, AR Hale, L Goossens, R Cooke, R Lopuhaä, M Simons, and PJL Valk. Causal modeling for integrated safety at airports. In *Proceedings of ESREL*, pages 1321–1327, 2003.

[109] Douglas A Wiegmann and Scott A Shappell. *A human error approach to aviation accident analysis: The human factors analysis and classification system*. Routledge, 2017.

[110] Huan-Jyh Shyur. A quantitative model for aviation safety risk assessment. *Computers & Industrial Engineering*, 54(1):34–44, 2008.

[111] Xi Chen, Indranil Bose, Alvin Chung Man Leung, and Chenhui Guo. Assessing the severity of phishing attacks: A hybrid data mining approach. *Decision Support Systems*, 50(4):662–672, 2011.

[112] Kathleen L McFadden and Elizabeth R Towell. Aviation human factors: a framework for the new millennium. *Journal of Air Transport Management*, 5(4):177–184, 1999.

[113] Nikunj Oza, J Patrick Castle, and John Stutz. Classification of aeronautics system health and safety documents. *IEEE Transactions on Systems, Man, and Cybernetics, Part C (Applications and Reviews)*, 39(6):670–680, 2009.

[114] Suratna Budalakoti, Ashok N Srivastava, and Matthew E Otey. Anomaly detection and diagnosis algorithms for discrete symbol sequences with applications to airline safety. *IEEE Transactions on Systems, Man, and Cybernetics, Part C (Applications and Reviews)*, 39(1):101–113, 2009.

[115] ASRS program briefing. https://asrs.arc.nasa.gov/docs/ASRS_ProgramBriefing2016.pdf, Accessed: 2017-12-28.

[116] Yao Liu, Cuiqing Jiang, and Huimin Zhao. Using contextual features and multi-view ensemble learning in product defect identification from online discussion forums. *Decision Support Systems*, 105:1–12, 2018.

[117] Thorsten Joachims. Text categorization with support vector machines: Learning with many relevant features. In *European Conference on Machine Learning*, pages 137–142. Springer, 1998.

[118] Yibo Wang and Wei Xu. Leveraging deep learning with LDA-based text analytics to detect automobile insurance fraud. *Decision Support Systems*, 105:87–95, 2018.

[119] Feng Wang, Tianhua Xu, Tao Tang, MengChu Zhou, and Haifeng Wang. Bilevel feature extraction-based text mining for fault diagnosis of railway systems. *IEEE Transactions on Intelligent Transportation Systems*, 18(1):49–58, 2017.

[120] Runyu Chen, Yitong Zheng, Wei Xu, Minghao Liu, and Jiayue Wang. Secondhand seller reputation in online markets: A text analytics framework. *Decision Support Systems*, 108:96–106, 2018.

[121] Alan S Abrahams, Weiguo Fan, G Alan Wang, Zhongju John Zhang, and Jian Jiao. An integrated text analytic framework for product defect discovery. *Production and Operations Management*, 24(6):975–990, 2015.

[122] Gongde Guo, Hui Wang, David Bell, Yaxin Bi, and Kieran Greer. Using kNN model for automatic text categorization. *Soft Computing*, 10(5):423–430, 2006.

[123] Min-Ling Zhang and Zhi-Hua Zhou. Multilabel neural networks with applications to functional genomics and text categorization. *IEEE Transactions on Knowledge and Data Engineering*, 18(10):1338–1351, 2006.

[124] Man Lan, Chew Lim Tan, Jian Su, and Yue Lu. Supervised and traditional term weighting methods for automatic text categorization. *IEEE Transactions on Pattern Analysis and Machine Intelligence*, 31(4):721–735, 2009.

[125] Simon Tong and Daphne Koller. Support vector machine active learning with applications to text classification. *Journal of Machine Learning Research*, 2(Nov):45–66, 2001.

[126] Vladimir Naumovich Vapnik and Vlamimir Vapnik. *Statistical learning theory*, volume 1. Wiley New York, 1998.

[127] Nan Li and Desheng Dash Wu. Using text mining and sentiment analysis for online forums hotspot detection and forecast. *Decision Support Systems*, 48(2):354–368, 2010.

[128] Yuchun Tang, Yan-Qing Zhang, Nitesh V Chawla, and Sven Krasser. SVMs model-

ing for highly imbalanced classification. *IEEE Transactions on Systems, Man, and Cybernetics, Part B*, 39(1):281–288, 2009.

[129] Weinan Zhang, Tianming Du, and Jun Wang. Deep learning over multi-field categorical data. In *European Conference on Information Retrieval*, pages 45–57. Springer, 2016.

[130] Yelong Shen, Xiaodong He, Jianfeng Gao, Li Deng, and Grégoire Mesnil. A latent semantic model with convolutional-pooling structure for information retrieval. In *Proceedings of the 23rd ACM International Conference on Conference on Information and Knowledge Management*, pages 101–110. ACM, 2014.

[131] Victoria López, Alberto Fernández, Salvador García, Vasile Palade, and Francisco Herrera. An insight into classification with imbalanced data: Empirical results and current trends on using data intrinsic characteristics. *Information Sciences*, 250: 113–141, 2013.

[132] José F Díez-Pastor, Juan J Rodríguez, César García-Osorio, and Ludmila I Kuncheva. Random balance: ensembles of variable priors classifiers for imbalanced data. *Knowledge-Based Systems*, 85:96–111, 2015.

[133] Nitesh V Chawla, Kevin W Bowyer, Lawrence O Hall, and W Philip Kegelmeyer. SMOTE: synthetic minority over-sampling technique. *Journal of Artificial Intelligence Research*, 16:321–357, 2002.

[134] Shulong Tan, Yang Li, Huan Sun, Ziyu Guan, Xifeng Yan, Jiajun Bu, Chun Chen, and Xiaofei He. Interpreting the public sentiment variations on Twitter. *IEEE Transactions on Knowledge and Data Engineering*, 26(5):1158–1170, 2014.

[135] Andrew McCallum, Kamal Nigam, et al. A comparison of event models for Naïve Bayes text classification. In *AAAI-98 Workshop on Learning for Text Categorization*, volume 752, pages 41–48. Citeseer, 1998.

[136] Joseph Lilleberg, Yun Zhu, and Yanqing Zhang. Support vector machines and word2vec for text classification with semantic features. In *2015 IEEE 14th International Conference on Cognitive Informatics & Cognitive Computing (ICCI* CC)*, pages 136–140. IEEE, 2015.

[137] Shenghuo Zhu, Xiang Ji, Wei Xu, and Yihong Gong. Multi-labelled classification using maximum entropy method. In *Proceedings of the 28th Annual International ACM SIGIR Conference on Research and Development in Information Retrieval*, pages 274–281. ACM, 2005.

[138] Dino Isa, Lam H Lee, VP Kallimani, and Rajprasad Rajkumar. Text document preprocessing with the Bayes formula for classification using the support vector machine. *IEEE Transactions on Knowledge and Data Engineering*, 20(9):1264–1272, 2008.

[139] Soumen Chakrabarti, Shourya Roy, and Mahesh V Soundalgekar. Fast and accurate text classification via multiple linear discriminant projections. *The VLDB Journal*, 12(2):170–185, 2003.

[140] Natural language toolbox. https://www.nltk.org/, Accessed: 2018-04-02.

[141] Karen Spärck Jones. IDF term weighting and IR research lessons. *Journal of Documentation*, 60(5):521–523, 2004.

[142] Alex Krizhevsky, Ilya Sutskever, and Geoffrey E Hinton. Imagenet classification with deep convolutional neural networks. In *Advances in Neural Information Processing Systems*, pages 1097–1105, 2012.

[143] Geoffrey Hinton, Li Deng, Dong Yu, George E Dahl, Abdel-rahman Mohamed, Navdeep Jaitly, Andrew Senior, Vincent Vanhoucke, Patrick Nguyen, Tara N Sainath, et al. Deep neural networks for acoustic modeling in speech recognition:

The shared views of four research groups. *IEEE Signal Processing Magazine*, 29 (6):82–97, 2012.

[144] Ronan Collobert, Jason Weston, Léon Bottou, Michael Karlen, Koray Kavukcuoglu, and Pavel Kuksa. Natural language processing (almost) from scratch. *Journal of Machine Learning Research*, 12:2493–2537, 2011.

[145] Michał Woźniak, Manuel Graña, and Emilio Corchado. A survey of multiple classifier systems as hybrid systems. *Information Fusion*, 16:3–17, 2014.

[146] Bianca Zadrozny and Charles Elkan. Transforming classifier scores into accurate multiclass probability estimates. In *Proceedings of the Eighth ACM SIGKDD International Conference on Knowledge Discovery and Data Mining*, pages 694–699. ACM, 2002.

[147] Shankar Sankararaman and Sankaran Mahadevan. Model validation under epistemic uncertainty. *Reliability Engineering & System Safety*, 96(9):1232–1241, 2011.

[148] Per Ahlgren and Cristian Colliander. Document–document similarity approaches and science mapping: Experimental comparison of five approaches. *Journal of Informetrics*, 3(1):49–63, 2009.

[149] Diederik P Kingma and Jimmy Ba. Adam: A method for stochastic optimization. In *International Conference on Learning Representation*, pages 1–13. ACM, 2015.

[150] Jason DM Rennie and Nathan Srebro. Loss functions for preference levels: Regression with discrete ordered labels. In *Proceedings of the IJCAI Multidisciplinary Workshop on Advances in Preference Handling*, pages 180–186. Kluwer Norwell, MA, 2005.

[151] Fabian Pedregosa-Izquierdo. *Feature extraction and supervised learning on fMRI: from practice to theory*. PhD thesis, Université Pierre et Marie Curie-Paris VI, 2015.

[152] Zhi-Hua Zhou. *Ensemble methods: foundations and algorithms*. Chapman and Hall/CRC, 2012.

[153] Xiaoge Zhang, Sankaran Mahadevan, Nathan Lau, and Matthew B Weinger. Multi-source information fusion to assess control room operator performance. *Reliability Engineering & System Safety*, doi: 10.1016/j.ress.2018.10.012, 2019.

[154] Catherine M Burns, Gyrd Skraaning Jr, Greg A Jamieson, Nathan Lau, Jordanna Kwok, Robin Welch, and Gisle Andresen. Evaluation of ecological interface design for nuclear process control: situation awareness effects. *Human Factors*, 50(4):663–679, 2008.

[155] Paulo VR Carvalho, Isaac L dos Santos, Jose Orlando Gomes, Marcos RS Borges, and Stephanie Guerlain. Human factors approach for evaluation and redesign of human–system interfaces of a nuclear power plant simulator. *Displays*, 29(3):273–284, 2008.

[156] Nathan Lau, Greg A Jamieson, Gyrd Skraaning Jr, and Catherine M Burns. Ecological interface design in the nuclear domain: An empirical evaluation of ecological displays for the secondary subsystems of a boiling water reactor plant simulator. *IEEE Transactions on Nuclear Science*, 55(6):3597–3610, 2008.

[157] Jeffrey C Joe and Ronald L Boring. Using the human systems simulation laboratory at idaho national laboratory for safety focused research. In *Advances in Human Factors in Energy: Oil, Gas, Nuclear and Electric Power Industries*, pages 193–201. Springer, 2017.

[158] A Mosleh, JA Forester, RL Boring, SM Hendrickson, AM Whaley, SH Shen, DL Kelly, JYH Chang, VN Dang, JH Oxstrand, et al. A model-based human reliability analysis framework. In *Proceedings of the International Conference on Probabilistic Safety Assessment and Management (PSAM10)*, 2010.

[159] Sheue-Ling Hwang, Yi-Jan Yau, Yu-Ting Lin, Jun-Hao Chen, Tsun-Hung Huang, Tzu-Chung Yenn, and Chong-Cheng Hsu. Predicting work performance in nuclear power plants. *Safety Science*, 46(7):1115–1124, 2008.

[160] Jennifer A Healey and Rosalind W Picard. Detecting stress during real-world driving tasks using physiological sensors. *IEEE Transactions on Intelligent Transportation Systems*, 6(2):156–166, 2005.

[161] Yulan Liang and John D Lee. A hybrid Bayesian network approach to detect driver cognitive distraction. *Transportation Research Part C: Emerging Technologies*, 38: 146–155, 2014.

[162] Bob Bailey, Carl Elks, Nathan Lau, and Matt Demas. Progress and lessons learned in establishing the integrated control room and operator performance laboratory (in-control) for digital instrumentation and control and human factors research in nuclear power. *Proc. of the 9th American Nuclear Society International Topical Meeting on Nuclear Plant Instrumentation, Control and Human-Machine Interface Technologies*, pages 2109–2120, 2015.

[163] Matt Demas, Nathan Lau, and Carl Elks. Advancing human performance assessment capabilities for integrated system validation-A human-in-the-loop experiment. *Proc. of the 9th American Nuclear Society International Topical Meeting on Nuclear Plant Instrumentation, Control and Human-Machine Interface Technologies*, pages 1051–1064, 2015.

[164] Gyrd Skraaning Jr. The operator performance assessment system (OPAS). Technical report, Institutt for Energiteknikk, 1998.

[165] Per Øivind Braarud. Subjective task complexity and subjective workload: Criterion validity for complex team tasks. *International Journal of Cognitive Ergonomics*, 5 (3):261–273, 2001.

[166] Nathan Lau, Greg A Jamieson, and Gyrd Skraaning Jr. Situation awareness acquired from monitoring process plants–the process overview concept and measure. *Ergonomics*, 59(7):976–988, 2016.

[167] GSE systems. http://www.gses.com/training-applications/, Accessed: 2017-05-17.

[168] The observer XT. http://www.noldus.com/human-behavior-research/products/the-observer-xt, Accessed: 2017-05-17.

[169] I Elaine Allen and Christopher A Seaman. Likert scales and data analyses. *Quality Progress*, 40(7):64, 2007.

[170] Tobii eye tracking glass. https://www.tobii.com/, Accessed: 2017-05-17.

[171] BN-PPGED. http://www.biopac.com/product/bionomadix-ppg-and-eda-amplifier/, Accessed: 2017-05-17.

[172] Bionomadix respiration transducer. https://www.biopac.com/product/respiration-transducer-bionomadix/, Accessed: 2017-05-17.

[173] J M O'Hara, J C Higgins, S A Fleger, and P A Pieringer. Human factors engineering program review model NUREG-0711, rev 3. *US Nuclear Regulatory Commission*, 2012.

[174] Per Oeivind Braarud. Subjective task complexity in the control room. Technical report, Institutt for Energiteknikk, 2000.

[175] Nathan Lau, Greg A Jamieson, and Gyrd Skraaning Jr. Inter-rater reliability of query/probe-based techniques for measuring situation awareness. *Ergonomics*, 57 (7):959–972, 2014.

[176] Nathan Lau, Greg A Jamieson, and Gyrd Skraaning Jr. Empirical evaluation of the process overview measure for assessing situation awareness in process plants. *Ergonomics*, 59(3):393–408, 2016.

[177] Michael J Skinner and Peter A Simpson. Workload issues in military tactical airlift. *The International Journal of Aviation Psychology*, 12(1):79–93, 2002.

[178] Curtis S Ikehara and Martha E Crosby. Assessing cognitive load with physiological sensors. In *System Sciences, 2005. HICSS'05. Proceedings of the 38th Annual Hawaii International Conference on*, pages 295a–295a. IEEE, 2005.

[179] Jun Su Ha and Poong Hyun Seong. A human–machine interface evaluation method: A difficulty evaluation method in information searching (DEMIS). *Reliability Engineering & System Safety*, 94(10):1557–1567, 2009.

[180] James G May, Robert S Kennedy, Mary C Williams, William P Dunlap, and Julie R Brannan. Eye movement indices of mental workload. *Acta Psychologica*, 75(1): 75–89, 1990.

[181] Mary M Hayhoe. Advances in relating eye movements and cognition. *Infancy*, 6(2): 267–274, 2004.

[182] Esa M Rantanen and Joseph H Goldberg. The effect of mental workload on the visual field size and shape. *Ergonomics*, 42(6):816–834, 1999.

[183] Chih-Chung Chang and Chih-Jen Lin. LIBSVM: a library for support vector machines. *ACM Transactions on Intelligent Systems and Technology (TIST)*, 2(3):27, 2011.

[184] Jan Kodovsky, Jessica Fridrich, and Vojtěch Holub. Ensemble classifiers for steganalysis of digital media. *IEEE Transactions on Information Forensics and Security*, 7(2):432–444, 2012.

[185] Piero Baraldi, Francesca Mangili, and Enrico Zio. A Kalman filter-based ensemble approach with application to turbine creep prognostics. *IEEE Transactions on Reliability*, 61(4):966–977, 2012.

[186] Ali Mosleh and YH Chang. Model-based human reliability analysis: prospects and requirements. *Reliability Engineering & System Safety*, 83(2):241–253, 2004.

[187] IS Kim. Human reliability analysis in the man–machine interface design review. *Annals of Nuclear Energy*, 28(11):1069–1081, 2001.

[188] Guo-Feng Liang, Jhih-Tsong Lin, Sheue-Ling Hwang, Fei-Hui Huang, Tzu-Chung Yenn, and Chong-Cheng Hsu. Evaluation and prediction of on-line maintenance workload in nuclear power plants. *Human Factors and Ergonomics in Manufacturing & Service Industries*, 19(1):64–77, 2009.

[189] Xiaoyan Su, Sankaran Mahadevan, Peida Xu, and Yong Deng. Dependence assessment in human reliability analysis using evidence theory and AHP. *Risk Analysis*, 35(7):1296–1316, 2015.

[190] Jussi K Vaurio. Human factors, human reliability and risk assessment in license renewal of a nuclear power plant. *Reliability Engineering & System Safety*, 94(11): 1818–1826, 2009.

[191] Bruce Hallbert, David Gertman, Erasmia Lois, Julie Marble, Harold Blackman, and James Byers. The use of empirical data sources in HRA. *Reliability Engineering & System Safety*, 83(2):139–143, 2004.

[192] Jing Xiong and Mark Hansen. Value of flight cancellation and cancellation decision modeling: ground delay program postoperation study. *Transportation Research Record: Journal of the Transportation Research Board*, (2106):83–89, 2009.

[193] Benjamin G Thengvall, Jonathan F Bard, and Gang Yu. Balancing user preferences for aircraft schedule recovery during irregular operations. *IIE Transactions*, 32(3): 181–193, 2000.

[194] Matthew E Berge, Michael L Carter, Aslaug Haraldsdottir, Bruno Repetto, and Laura Kang. Airline schedule recovery in flow management: An application for departure re-routing. In *25th Digital Avionics Systems Conference, 2006 IEEE/AIAA*, pages 1–9. IEEE, 2006.

[195] Virot Chiraphadhanakul and Cynthia Barnhart. Robust flight schedules through slack re-allocation. *EURO Journal on Transportation and Logistics*, 2(4):277–306, 2013.

[196] Andrea D'Ariano, Marco Pistelli, and Dario Pacciarelli. Aircraft retiming and rerouting in vicinity of airports. *Intelligent Transport Systems, IET*, 6(4):433–443, 2012.

[197] Jens Clausen, Allan Larsen, Jesper Larsen, and Natalia J Rezanova. Disruption management in the airline industry–concepts, models and methods. *Computers & Operations Research*, 37(5):809–821, 2010.

[198] Amedeo R Odoni. The flow management problem in air traffic control. *Flow Control of Congested Networks*, 38:269, 2012.

[199] Dimitris Bertsimas and Sarah Stock Patterson. The air traffic flow management problem with enroute capacities. *Operations Research*, 46(3):406–422, 1998.

[200] Dimitris Bertsimas and Sarah Stock Patterson. The traffic flow management rerouting problem in air traffic control: A dynamic network flow approach. *Transportation Science*, 34(3):239–255, 2000.

[201] Paula Leal De Matos and Richard Ormerod. The application of operational research to european air traffic flow management–understanding the context. *European Journal of Operational Research*, 123(1):125–144, 2000.

[202] PA Leal de Matos and PL Powell. Decision support for flight re-routing in Europe. *Decision Support Systems*, 34(4):397–412, 2003.

[203] Jonathan F Bard, Gang Yu, and Michael F Arguello. Optimizing aircraft routings in response to groundings and delays. *IIE Transactions*, 33(10):931–947, 2001.

[204] CH van Balen, Cees Bil, et al. Optimal re-routing of aircraft around closed airspace in free flight. In *26th American Institute of Aeronautics and Astronautics Applied Aerodynamics Conference*, pages 1–10, 2008.

[205] Dimitris Bertsimas, Guglielmo Lulli, and Amedeo Odoni. An integer optimization approach to large-scale air traffic flow management. *Operations Research*, 59(1): 211–227, 2011.

[206] Andrew M Churchill, David J Lovell, and Michael O Ball. Evaluating a new formulation for large-scale traffic flow management. In *Proceedings of the 8th USA/Europe Air Traffic Seminar (ATM09)*, volume 310, 2009.

[207] A Agustı, Antonio Alonso-Ayuso, Laureano F Escudero, Celeste Pizarro, et al. On air traffic flow management with rerouting. part ii: Stochastic case. *European Journal of Operational Research*, 219(1):167–177, 2012.

[208] Jay M Rosenberger, Ellis L Johnson, and George L Nemhauser. Rerouting aircraft for airline recovery. *Transportation Science*, 37(4):408–421, 2003.

[209] Maryam Kamgarpour, Vera Dadok, and Claire Tomlin. Trajectory generation for aircraft subject to dynamic weather uncertainty. In *2010 49th IEEE Conference on Decision and Control (CDC)*, pages 2063–2068. IEEE, 2010.

[210] Gillian Clare and Arthur Richards. Air traffic flow management under uncertainty: application of chance constraints. In *Proceedings of the 2nd International Conference on Application and Theory of Automation in Command and Control Systems*, pages 20–26. IRIT Press, 2012.

[211] Nikolas Pyrgiotis, Kerry M Malone, and Amedeo Odoni. Modelling delay propagation within an airport network. *Transportation Research Part C: Emerging Technologies*, 27:60–75, 2013.

[212] Flavien Balbo and Suzanne Pinson. Dynamic modeling of a disturbance in a multi-agent system for traffic regulation. *Decision Support Systems*, 41(1):131–146, 2005.

[213] Surya Pathak, Mark McDonald, and Sankaran Mahadevan. A framework for designing policies for networked systems with uncertainty. *Decision Support Systems*, 49 (2):121–131, 2010.

[214] Sang Won Yoon, Juan D Velasquez, BK Partridge, and Shimon Y Nof. Transportation security decision support system for emergency response: A training prototype. *Decision Support Systems*, 46(1):139–148, 2008.

[215] Maria Prandini, Luigi Piroddi, Stephane Puechmorel, and Silvie Luisa Brázdilová. Toward air traffic complexity assessment in new generation air traffic management systems. *IEEE Transactions on Intelligent Transportation Systems*, 12(3):809–818, 2011.

[216] Bernard P Zeigler, Herbert Praehofer, and Tag Gon Kim. *Theory of modeling and simulation: integrating discrete event and continuous complex dynamic systems*. Academic press, 2000.

[217] Controller-pilot data link communications. https://en.wikipedia.org/wiki/Controller-pilot_data_link_communications, Accessed: 2016-09-24.

[218] Esa M Rantanen, Jason S McCarley, and Xidong Xu. Time delays in air traffic control communication loop: effect on controller performance and workload. *The International Journal of Aviation Psychology*, 14(4):369–394, 2004.

[219] Francis T Durso and Carol A Manning. Air traffic control. *Reviews of Human Factors and Ergonomics*, 4(1):195–244, 2008.

[220] A Haldar and Sankaran Mahadevan. *Probability, reliability and statistical methods in engineering design*. John Wiley & Sons, New York, 2000.

[221] Soren W Henriksen. Radar-range equation. In *IEEE Proceedings*, volume 63, page 813, 1975.

[222] Brian L Bosart, Wen-Chau Lee, and Roger M Wakimoto. Procedures to improve the accuracy of airborne doppler radar data. *Journal of Atmospheric and Oceanic Technology*, 19(3):322–339, 2002.

[223] James Farrell. *Integrated aircraft navigation*. Elsevier, 2012.

[224] Fredrik Gustafsson, Fredrik Gunnarsson, Niclas Bergman, Urban Forssell, Jonas Jansson, Rickard Karlsson, and P-J Nordlund. Particle filters for positioning, navigation, and tracking. *IEEE Transactions on Signal Processing*, 50(2):425–437, 2002.

[225] Krishna Sampigethaya, Radha Poovendran, and Linda Bushnell. A framework for securing future e-enabled aircraft navigation and surveillance. In *AIAA Proceedings*, pages 1–10, 2009.

[226] ADSB over satellite. https://directory.eoportal.org/web/eoportal/satellite-missions/a/ads-b, Accessed: 2016-12-13.

[227] Controller-pilot communications. http://virtualskies.arc.nasa.gov/communication/11.html, Accessed: 2016-02-16.

[228] Mike C Bartholomew-Biggs, Steven C Parkhurst, and Simon P Wilson. Global optimization approaches to an aircraft routing problem. *European Journal of Operational Research*, 146(2):417–431, 2003.

[229] Mohamed Haouari, Najla Aissaoui, and Farah Zeghal Mansour. Network flow-based approaches for integrated aircraft fleeting and routing. *European Journal of Operational Research*, 193(2):591–599, 2009.

[230] Chenzhao Li and Sankaran Mahadevan. An efficient modularized Monte Carlo method to estimate the first order Sobol' index. *Reliability Engineering and System Safety*, 153:110–121, 2016.

[231] Bertrand Iooss and Mathieu Ribatet. Global sensitivity analysis of computer models with functional inputs. *Reliability Engineering & System Safety*, 94(7):1194–1204, 2009.

[232] Rüdiger Rackwitz. Reliability analysisa review and some perspectives. *Structural Safety*, 23(4):365–395, 2001.

[233] Vladimir Cherkassky and Yunqian Ma. Practical selection of SVM parameters and noise estimation for SVM regression. *Neural Networks*, 17(1):113–126, 2004.

[234] Thomas Prevot, Jeffrey Homola, and Joey Mercer. Initial study of controller/automation integration for nextgen separation assurance. In *AIAA Guidance, Navigation, and Control (GNC) Conference and Exhibit*, 2008.

[235] Joey Mercer, Jeffrey Homola, Christopher Cabrall, Lynne Martin, Susan Morey, Ashley Gomez, and Thomas Prevôt. Human-automation cooperation for separation assurance in future nextgen environments. In *Proceedings of the International Conference on Human-Computer Interaction in Aerospace*, page 1. ACM, 2014.

[236] Xiaoge Zhang, Zhen Hu, and Sankaran Mahadevan. A resilience-driven optimization model for the configuration of logistics service centers. *IEEE Transactions on Reliability*, Under Review, 2019.

[237] Ford halts F-150 production over parts shortage. https://www.detroitnews.com/story/business/autos/ford/2018/05/09/ford-trucks-production-halted/34718903/. Accessed: 2018-06-10.

[238] T John Kim and Sunduck Suh. Toward developing a national transportation planning model: a bilevel programming approach for korea. *The Annals of Regional Science*, 22(1):65–80, 1988.

[239] Stella C Dafermos and Frederick T Sparrow. The traffic assignment problem for a general network. *Journal of Research of the National Bureau of Standards B*, 73(2): 91–118, 1969.

[240] Maria Mitradjieva and Per Olov Lindberg. The stiff is movingconjugate direction Frank-Wolfe methods with applications to traffic assignment. *Transportation Science*, 47(2):280–293, 2013.

[241] Olga Perederieieva, Matthias Ehrgott, Andrea Raith, and Judith YT Wang. A framework for and empirical study of algorithms for traffic assignment. *Computers & Operations Research*, 54:90–107, 2015.

[242] Yu Marco Nie. A class of bush-based algorithms for the traffic assignment problem. *Transportation Research Part B: Methodological*, 44(1):73–89, 2010.

[243] Guido Gentile. Local user cost equilibrium: a bush-based algorithm for traffic assignment. *Transportmetrica A: Transport Science*, 10(1):15–54, 2014.

[244] Larry J LeBlanc, Edward K Morlok, and William P Pierskalla. An efficient approach to solving the road network equilibrium traffic assignment problem. *Transportation Research*, 9(5):309–318, 1975.

[245] Xiaoge Zhang and Sankaran Mahadevan. A bio-inspired approach to traffic network

equilibrium assignment problem. *IEEE Transactions on Cybernetics*, 48(4):1304–1315, 2018.

[246] M Yasin Ulukus. The m/m/s queue. *Wiley Encyclopedia of Operations Research and Management Science*, 2010.

[247] Zeynep Aksin, Mor Armony, and Vijay Mehrotra. The modern call center: A multi-disciplinary perspective on operations management research. *Production and Operations Management*, 16(6):665–688, 2007.

[248] Robert B Cooper. *Introduction to queueing theory*. North Holland,, 1981.

[249] Laurence A Baxter. Probability, statistics, and queueing theory with computer sciences applications, 1992.

[250] John DC Little. A proof for the queuing formula: L= λ w. *Operations Research*, 9 (3):383–387, 1961.

[251] Pierre Hansen, Brigitte Jaumard, and Gilles Savard. New branch-and-bound rules for linear bilevel programming. *SIAM Journal on Scientific and Statistical Computing*, 13(5):1194–1217, 1992.

[252] Luis Vicente, Gilles Savard, and Joaquim Júdice. Descent approaches for quadratic bilevel programming. *Journal of Optimization Theory and Applications*, 81(2):379–399, 1994.

[253] Ankur Sinha, Pekka Malo, and Kalyanmoy Deb. A review on bilevel optimization: from classical to evolutionary approaches and applications. *IEEE Transactions on Evolutionary Computation*, 22(2):276–295, 2018.

[254] Reuven Y Rubinstein. Optimization of computer simulation models with rare events. *European Journal of Operational Research*, 99(1):89–112, 1997.

[255] Pieter-Tjerk De Boer, Dirk P Kroese, Shie Mannor, and Reuven Y Rubinstein. A tutorial on the cross-entropy method. *Annals of Operations Research*, 134(1):19–67, 2005.

[256] Reuven Y Rubinstein and Dirk P Kroese. *Simulation and the Monte Carlo method*, volume 10. John Wiley & Sons, 2016.

[257] Rishabh P Kothari and Dirk P Kroese. Optimal generation expansion planning via the cross-entropy method. In *Simulation Conference (WSC), Proceedings of the 2009 Winter*, pages 1482–1491. IEEE, 2009.

[258] K-P Hui, Nigel Bean, Miro Kraetzl, and Dirk P Kroese. The cross-entropy method for network reliability estimation. *Annals of Operations Research*, 134(1):101, 2005.

[259] Dirk P Kroese, Kin-Ping Hui, and Sho Nariai. Network reliability optimization via the cross-entropy method. *IEEE Transactions on Reliability*, 56(2):275–287, 2007.

[260] Fulya Altiparmak and Berna Dengiz. A cross entropy approach to design of reliable networks. *European Journal of Operational Research*, 199(2):542–552, 2009.

[261] Xiu Ning and Pingke Li. A cross-entropy approach to the single row facility layout problem. *International Journal of Production Research*, 56(11):3781–3794, 2017.

[262] Izack Cohen, Boaz Golany, and Avraham Shtub. Resource allocation in stochastic, finite-capacity, multi-project systems through the cross entropy methodology. *Journal of Scheduling*, 10(3):181–193, 2007.

[263] Andre Costa, Owen Dafydd Jones, and Dirk Kroese. Convergence properties of the cross-entropy method for discrete optimization. *Operations Research Letters*, 35(5): 573–580, 2007.

[264] Basima Elshqeirat, Sieteng Soh, Suresh Rai, and Mihai Lazarescu. Topology design

with minimal cost subject to network reliability constraint. *IEEE Transactions on Reliability*, 64(1):118–131, 2015.

[265] Xiaoge Zhang, Sankaran Mahadevan, and Kai Goebel. Network reconfiguration for increasing transportation system resilience under extreme events. *Risk Analysis*, doi:10.1111/risa.13320, 2019.

[266] Zhaohong Bie, Yanling Lin, Gengfeng Li, and Furong Li. Battling the extreme: A study on the power system resilience. *Proceedings of the IEEE*, 105(7):1253–1266, 2017.

[267] Elise Miller-Hooks, Xiaodong Zhang, and Reza Faturechi. Measuring and maximizing resilience of freight transportation networks. *Computers & Operations Research*, 39(7):1633–1643, 2012.

[268] Korn Vajanapoom, David Tipper, and Sira Akavipat. Risk based resilient network design. *Telecommunication Systems*, 52(2):799–811, 2013.

[269] Min Ouyang. A mathematical framework to optimize resilience of interdependent critical infrastructure systems under spatially localized attacks. *European Journal of Operational Research*, 262(3):1072–1084, 2017.

[270] Jian Gang Jin, Loon Ching Tang, Lijun Sun, and Der-Horng Lee. Enhancing metro network resilience via localized integration with bus services. *Transportation Research Part E: Logistics and Transportation Review*, 63:17–30, 2014.

[271] Erik Jenelius. Redundancy importance: Links as rerouting alternatives during road network disruptions. *Procedia Engineering*, 3:129–137, 2010.

[272] Abdullahi M Salman, Yue Li, and Mark G Stewart. Evaluating system reliability and targeted hardening strategies of power distribution systems subjected to hurricanes. *Reliability Engineering & System Safety*, 144:319–333, 2015.

[273] Yanling Lin and Zhaohong Bie. Tri-level optimal hardening plan for a resilient distribution system considering reconfiguration and dg islanding. *Applied Energy*, 210:1266–1279, 2018.

[274] James H Lambert, Joshua L Tsang, and Shital A Thekdi. Risk-informed investment for tropical cyclone preparedness of highway signs, signals, and lights. *Journal of Infrastructure Systems*, 19(4):384–394, 2012.

[275] Heimir Thorisson and James H Lambert. Multiscale identification of emergent and future conditions along corridors of transportation networks. *Reliability Engineering & System Safety*, 167:255–263, 2017.

[276] Shital A Thekdi and James H Lambert. Integrated risk management of safety and development on transportation corridors. *Reliability Engineering & System Safety*, 138:1–12, 2015.

[277] Xuwei Qin, Xiao Liu, and Lixin Tang. A two-stage stochastic mixed-integer program for the capacitated logistics fortification planning under accidental disruptions. *Computers & Industrial Engineering*, 65(4):614–623, 2013.

[278] David L Alderson, Gerald G Brown, and W Matthew Carlyle. Operational models of infrastructure resilience. *Risk Analysis*, 35(4):562–586, 2015.

[279] Sangho Kim, Shashi Shekhar, and Manki Min. Contraflow transportation network reconfiguration for evacuation route planning. *IEEE Transactions on Knowledge and Data Engineering*, 20(8):1115–1129, 2008.

[280] Cristinel Ababei and Rajesh Kavasseri. Efficient network reconfiguration using minimum cost maximum flow-based branch exchanges and random walks-based loss estimations. *IEEE Transactions on Power Systems*, 26(1):30–37, 2011.

[281] B Amanulla, Saikat Chakrabarti, and SN Singh. Reconfiguration of power distribution systems considering reliability and power loss. *IEEE Transactions on Power Delivery*, 27(2):918–926, 2012.

[282] Pavel Vrba and Vladimír Marik. Capabilities of dynamic reconfiguration of multiagent-based industrial control systems. *IEEE Transactions on Systems, Man, and Cybernetics-Part A: Systems and Humans*, 40(2):213–223, 2010.

[283] Kyu-Han Kim and Kang G Shin. Self-reconfigurable wireless mesh networks. *IEEE/ACM Transactions on Networking (TON)*, 19(2):393–404, 2011.

[284] Matthew J Daigle, Indranil Roychoudhury, Gautam Biswas, Xenofon D Koutsoukos, Ann Patterson-Hine, and Scott Poll. A comprehensive diagnosis methodology for complex hybrid systems: A case study on spacecraft power distribution systems. *IEEE Transactions on Systems, Man, and Cybernetics-Part A: Systems and Humans*, 40(5):917–931, 2010.

[285] Josh Bongard, Victor Zykov, and Hod Lipson. Resilient machines through continuous self-modeling. *Science*, 314(5802):1118–1121, 2006.

[286] Uğur Arıkan, Sinan Gürel, and M Selim Aktürk. Flight network-based approach for integrated airline recovery with cruise speed control. *Transportation Science*, 51(4): 1259–1287, 2017.

[287] Yiping Fang and Giovanni Sansavini. Optimizing power system investments and resilience against attacks. *Reliability Engineering & System Safety*, 159:161–173, 2017.

[288] Nita Yodo, Pingfeng Wang, and Melvin Rafi. Enabling resilience of complex engineered systems using control theory. *IEEE Transactions on Reliability*, 67(1):53–65, 2018.

[289] Ziyou Gao, Yunchao Qu, Xingang Li, Jiancheng Long, and Hai-Jun Huang. Simulating the dynamic escape process in large public places. *Operations Research*, 62 (6):1344–1357, 2014.

[290] Kunal Kumar, Julia Romanski, and Pascal Van Hentenryck. Optimizing infrastructure enhancements for evacuation planning. In *Proceedings of the Thirtieth AAAI Conference on Artificial Intelligence*, pages 3864–3870. AAAI Press, 2016.

[291] James H Lambert, Ayse I Parlak, Qian Zhou, John S Miller, Michael D Fontaine, Thomas M Guterbock, Janet L Clements, and Shital A Thekdi. Understanding and managing disaster evacuation on a transportation network. *Accident Analysis & Prevention*, 50:645–658, 2013.

[292] Traffic jams during hurricane evacuations are entirely preventable. https://qz.com/1073562/hurricane-irma-evacuations-are-not-doomed-to-create-traffic-jams-if-done-right/, 2017. Accessed: 2017-11-19.

[293] Todd Litman. Lessons from katrina and rita: What major disasters can teach transportation planners. *Journal of Transportation Engineering*, 132(1):11–18, 2006.

[294] Jing Zhao, Wanjing Ma, Yue Liu, and Xiaoguang Yang. Integrated design and operation of urban arterials with reversible lanes. *Transportmetrica B: Transport Dynamics*, 2(2):130–150, 2014.

[295] Thomas J Cova and Justin P Johnson. A network flow model for lane-based evacuation routing. *Transportation Research Part A: Policy and Practice*, 37(7):579–604, 2003.

[296] Bureau of public roads. *Traffic Assignment Manual. U.S. Department of Commerce, Urban Planning Division, Washington, DC*, 1964.

[297] Lin Cheng, Xiangdong Xu, and Songlin Qiu. Constrained newton methods for transport network equilibrium analysis. *Tsinghua Science & Technology*, 14(6):765–775, 2009.

[298] Y Sheffy. *Urban transportation networks: equilibrium analysis with mathematical programming methods*. Traffic Engineering Control. Prentice-Hall, ISBN: 0-13-93-972, 1985.

[299] José Emmanuel Ramirez-Marquez and Claudio M Rocco. All-terminal network reliability optimization via probabilistic solution discovery. *Reliability Engineering & System Safety*, 93(11):1689–1697, 2008.

[300] Robert B Dial. A path-based user-equilibrium traffic assignment algorithm that obviates path storage and enumeration. *Transportation Research Part B: Methodological*, 40(10):917–936, 2006.

[301] Signal cycle lengths. https://nacto.org/publication/urban-street-design-guide/intersection-design-elements/traffic-signals/signal-cycle-lengths/, 2018. Accessed: 2018-11-14.